



CONSTRUCTION MATERIALS CONSULTANTS, INC.

## Pyrrhotite Epidemic in Eastern Connecticut: A Case Study From Tolland, CT



Tolland Board of Education  
Birch Grove School  
247 Rhodes Road  
Tolland, CT 06084

January 10, 2019  
CMC 1218175



TABLE OF CONTENTS

Executive Summary ..... 1
List of Figures, Tables, and Appendices..... 8
Introduction ..... 9
Background Information ..... 9
Field Photographs..... 9
Map Cracking in Concrete Foundation Wall..... 9
Purpose of Present Investigation ..... 13
Methodologies..... 14
Optical Microscopy ..... 14
X-Ray Diffraction..... 15
Scanning Electron Microscopy and Energy-Dispersive X-Ray Spectroscopy (SEM-EDS) ..... 16
Energy-Dispersive X-Ray Fluorescence Spectroscopy (ED-XRF)..... 17
Ion Chromatography ..... 18
Samples ..... 19
Photographs, Identification, Integrity, and Dimensions ..... 19
End Surfaces..... 19
Cracking & Other Visible Distress ..... 19
Embedded Items..... 19
Resonance ..... 19
Petrographic Examinations ..... 24
Lapped Cross Sections of Cores..... 24
Photomicrographs of Lapped Cross Sections ..... 28
Photomicrographs of Lapped Cross Sections Showing Iron Sulfide Minerals ..... 32
Thin Sections ..... 35
Photomicrographs of Thin Sections ..... 36
Coarse Aggregates ..... 40
Fine Aggregates ..... 40
Paste..... 41
Air ..... 42
SEM-EDS Studies ..... 43
Microstructural Evidence of Pyrrhotite-Oxidation & Related Cracking..... 48
Microstructural Evidence of Internal Sulfate Attack By Released Sulfates ..... 48
Mineralogical Compositions and Pyrrhotite Contents of Concretes and Aggregates from XRD ..... 49
Chemical Compositions and Sulfate Contents of Concretes and Aggregates from XRF ..... 51
Ion Chromatography for Potential Sulfate Release from Concretes and Aggregates in Accelerated Oxidation Test ..... 52
Discussion ..... 54
Iron Sulfide Minerals in Concrete Aggregates..... 54
Background ..... 54
Mechanism of Distress By: (1) Oxidation of Iron Sulfides (Primary Expansion Causing Surface Staining, Popout, Cracking), (2) Release of Sulfates and Internal Sulfate Attack (Secondary Expansion Causing Further Cracking) ..... 55
Pyrrhotite Limit ..... 57
Case Studies of Concrete Deterioration Due to Oxidation of Iron Sulfide Minerals in Aggregates ..... 57
Pyrrhotite Epidemic In Eastern Connecticut..... 60
Conclusions ..... 66
References..... 68
Appendix A..... 71
Appendix B ..... 93
Appendix C..... 122
Appendix D..... 159
Appendix E..... 202
Appendix F..... 224



## EXECUTIVE SUMMARY

Widespread outbreak of deterioration of many residential concrete foundations due to oxidation of an iron sulfide mineral 'pyrrhotite' in the quarried aggregate stones has occurred in the state of Connecticut with many thousands of homes being affected. Pyrrhotite (from Greek *pyrrhos* i.e. flame-colored or redness) commonly occurs in many mafic igneous, sedimentary, and metamorphic rocks, or in high temperature hydrothermal and replacement veins as a minor accessory mineral having a chemical formula of  $Fe_{1-x}S$ , where  $x$  varies from 0 to 0.125. It is commonly associated with pyrite ( $FeS_2$ ) but is distinguished by its bronze rather than brass color of pyrite, its lower hardness, decomposition in HCl (Deer et al., 2008), lower S/Fe ratio, and weakly magnetic nature. All these features along with X-ray diffraction of rocks containing both iron sulfide minerals help to determine the pyrrhotite content, whereas XRF analysis of rocks determine the sulfur (as  $SO_3$ ) content from all iron sulfide minerals. Currently, much of the information available on pyrrhotite-related concrete deterioration in northeastern Connecticut is limited to news media, but the cause of deterioration has been attributed by investigations conducted at the University of Connecticut (Wille and Zhong, 2016) and Jana (2018) as oxidation of pyrrhotite present in the coarse aggregate in the presence of moisture and oxygen in concrete. Manifestation of damage has taken as much as 10 to 20 years. Typical visual deterioration is in the form of map cracking, some causing deformation of the wall, reddish-brown discoloration as rust stains, whitish formation of sodium sulfate salts (thenardite and mirabilite) in the vicinity of surface cracking, and in some severe cases crumbling of concrete. Most of the damage to date has been linked to aggregates supplied from one square-shaped quarry (Becker's quarry) in Willington, CT that sits in a weathered hydrothermal vein of metamorphic rocks containing significant pyrrhotite mineralization. The geology in the vicinity of the quarry is made up of metamorphic rocks predominately from two to three formations consisting predominantly of foliated schists and gneissic rock, granofels, and foliated quartz diorite. Quartz, plagioclase or oligoclase are primary minerals with micas, and noted are garnet and pyrrhotite as common accessory minerals. Most findings of concrete deterioration around the world due to pyrrhotite oxidation, including the ones in northeastern Connecticut (e.g., Moum and Rosenqvist 1959 from Norway, Tagnit-Hamou, et.al. 2005 and Rodrigues et al. 2012 from Canada, Oliveira, et al. 2014 from Spain, and Wille and Zhong 2016 and Jana 2018 from USA) indicated the following two-stage mechanisms of distress due to: (a) primary expansions associated with oxidation of pyrrhotite in the presence of oxygen, moisture, and high pH in concrete to form ferric oxy-hydroxides, e.g., ferrihydrite [ $Fe(OH)_3$ ] causing cracking of the unsound aggregates, followed by (b) secondary expansions from internal sulfate attacks by the sulfates released from pyrrhotite oxidation to cement hydration and carbonation products forming secondary ettringite and thaumasite, respectively causing further cracking in the paste. The former expansion is contributed from the pyrrhotite-bearing aggregates, whereas, the latter expansion is contributed from internal sulfate attacks within the confined spaces of the released sulfate-contaminated hydrated cement paste.

In light of this known problem of pyrrhotite in concrete aggregate from around the world, and particularly from the Becker's quarry in CT, and the resulting distress in many residential foundations in northeastern Connecticut, the observed map cracking of concrete foundation walls in Birch Grove School located at 247 Rhodes Road in Tolland, Connecticut i.e. within the known high-risk zone of 'pyrrhotite epidemic' that has affected more than 50 residential foundations as of April of 2018 has steered concern of: (a) whether or not the deteriorated concrete foundation contains pyrrhotite in its aggregate, and, if detected, (b) if pyrrhotite has played the primary role for the observed cracking and crumbling as in the case of other cracked foundations.

As a result, fifteen (15) hardened concrete cores measuring 6 in. (150 mm) to 8<sup>1/2</sup> in. (220 mm) in nominal lengths and 3<sup>3/4</sup> in. (95 mm) in diameters were drilled from the foundation walls around the school encompassing two different constructions – ten cores (of A-series through D-series) came from 1998 constructions, and, five additional cores (of F-series) came from 2001 construction. Cores from 1998 construction showed variable degrees of visible cracking from: (a) minor localized cracking within some potentially unsound crushed stone coarse aggregates (e.g., Cores A-3, B-1, C-3) to (b) moderate cracking from unsound aggregates and mostly at the exposed surface ends (e.g., Cores A-2, D-2, D-3) to (c) extensive through-depth cracking all throughout the recovered depths of the cores affecting the overall integrity (e.g., Cores A-1, C-1, C-2, D-1). By contrast (d) cores of F-series (F-1 through F-5) from 2001 construction do not show any visible cracking. Absence of visible cracking in the 2001 construction could be a combination of: (i) use of different crushed stones from different quarry, and/or (ii) lack of moisture needed for pyrrhotite-related distress to occur, e.g., collection of cores from high elevation of wall where moisture intrusion



may not have occurred. The former possibility is not found to be the case as the crushed stone coarse aggregates in the cores from 2001 construction are found to be compositionally similar to the aggregates used in the 1998 construction, which is further corroborated by reported supplier of concrete (J.J. Morris) in the 2001 construction in the concrete batch tickets, who also supplied the distressed concretes of 1998 construction, and, in fact, in many other foundations in the eastern CT that are currently suffering pyrrhotite-related deteriorations.

Field photographs of concrete conditions at the locations of fifteen cores showed: (a) map cracking of foundation at the location of Cores A-1, D-1, D-2, and D-3, (b) a few long vertical cracks across the thickness of foundation at the location of Core C-1, and (c) a few isolated vertical cracks at the location of Core F-4. Amongst the 1998 construction, foundation walls at the locations of Cores A-1, D-1, D-2, and D-3 showed most visible map cracking, which are consistent with the observed through-depth cracks in those cores when received. Extensive cracking in Cores C-1 and C-2, however are found when received but no corresponding visible cracking are found in the field photos of those locations on the exposed surfaces of foundations. Moderate cracking mostly at the exposed end of Core A-2, and minimal cracking in Cores A-3, B-1, and C-3 when received are also not seen on the exposed foundation walls of their locations in the field photos, indicating initiation of cracking in the interior concretes.

All fifteen cores were studied extensively for investigations of all possible causes for cracking, including the possible presence of pyrrhotite in concretes, and, its potentially deleterious role in concrete deterioration. Pyrrhotite's presence along with overall condition of concrete and aggregates were examined by detailed petrographic examinations (optical microscopy) *a la* ASTM C 856, whereas possible roles of pyrrhotite, its potential oxidation products and sulfate levels, and microstructures of deteriorated concrete around pyrrhotite-bearing aggregates are examined by scanning electron microscopy and energy-dispersive X-ray microanalysis (SEM-EDS) of multiple thin sections of concrete (*a la* ASTM C 1723), X-ray diffraction (XRD) and X-ray fluorescence (XRF) of concrete and pyrrhotite-bearing coarse aggregate particles extracted from the concrete, and ion chromatography (IC *a la* ASTM D 4327) of concrete and extracted aggregate particles digested in water (for concrete) or a strong oxidant of 35% hydrogen peroxide solution for several days in an accelerated oxidation test (for aggregates), then diluted in distilled water to determine levels of sulfates released by these aggregates in relation to a control aggregate without any iron sulfide mineral. Detection of pyrrhotite by optical microscopy and XRD, along with detection of its oxidation products by SEM-EDS and XRD, reaction microstructures and evidence of distress by SEM-EDS, and measurement of release of sulfate levels by IC have provided a good assessment of potential role of pyrrhotite in causing the observed distress.

Petrographic examinations have determined the concretes from both 1998 and 2001 constructions to be compositionally similar, and made using: (a) metamorphic crushed stone coarse aggregates, which are a mixture of a predominant dark gray garnetiferous quartzo-feldspathic and micaceous gneiss (having quartz, albite feldspar, biotite mica, and almandine garnet) with a subordinate amount of metamorphosed gabbro (having ortho and/or clino-pyroxenes, oligoclase plagioclase, garnet, and minor biotite having granulitic texture), and, a subordinate light brown garnetiferous quartz-feldspar-mica gneiss (having a higher quartz content than the dark gray gneiss) - all having nominal maximum sizes of  $\frac{3}{4}$  in. (19 mm) showing the typical gneissose texture of alternating bands of quartz-albitic feldspar and micaceous (mostly biotite and less muscovite) minerals that often contain almandine garnet poikiloblast, and equigranular granoblastic texture for metamorphosed gabbro; (b) natural siliceous sand fine aggregates having nominal maximum sizes of  $\frac{3}{8}$  in. (9.5 mm) and containing major amounts of quartz and quartzite, and subordinate amounts of feldspar, mica, ferruginous rock, and mafic minerals; (c) hardened pastes of Portland cement as the sole cementitious component having estimated cement contents of 6 to  $6\frac{1}{2}$  bags per cubic yard that are similar in all cores, and estimated water-cement ratios (*w/c*) of 0.45 to 0.50, and (d) estimated air contents as low as 3 to as high as 8 percent; concretes in all fifteen cores are air-entrained.

Lapped cross sections of cores from 1998 construction showed minor localized cracking within some potentially unsound crushed stone coarse aggregates in Cores A-3, B-1, C-3, and moderate to extensive through-depth cracking from unsound aggregates in Cores A-1, A-2, C-1, C-2, D-1, D-2, D-3, and no visible cracking in the cores of F-series (F-1 through F-5) from 2001 construction. All these are consistent with observations from visible cracks on the cores when received, but showed more cracking in the interior concrete in many cores than apparently sound conditions in many of their locations in the field (e.g., A-2, C-2). Therefore cracking has initiated in the interior concrete of foundation walls in many of these cores' locations but have not yet appeared on the exposed surfaces. Cracks are



random, up to 1 to 2 mm in width, tapered down from the exposed faces of the wall to depths of 10 to 20 mm when visible on the exposed surfaces, transected and/or circumscribed the crushed gneiss coarse aggregate particles, and show patterns that cannot be formed by typical concrete shrinkage or settlement of the wall but more likely due to a chemical deterioration in line with the suspected expansions from oxidation of pyrrhotite-bearing aggregates and subsequent possible internal sulfate attack by the released sulfates in concrete. Irrespective of the mechanism(s), such severe and pervasive cracking of the wall is judged to be the reason for the reported distress of the foundation. Textural associations of many of these cracks with unsound crushed gneiss coarse aggregate particles have suggested their formation by unsoundness of the associated particles.

As mentioned, petrographic examinations detected two types of crushed gneiss coarse aggregate particles – a predominant dark gray garnetiferous quartzo-feldspathic and micaceous gneiss (having quartz, albite feldspar, biotite mica, and almandine garnet) with a subordinate amount of metamorphosed gabbro (having ortho and/or clino-pyroxenes, oligoclase plagioclase, garnet, and minor biotite), and, a subordinate light brown garnetiferous quartz-feldspar-mica gneiss (having a higher quartz content than the dark gray gneiss). Both gneiss types contained iron sulfide minerals (but more common in the predominant dark gray gneiss particles) as small equant to irregular-shaped to elongated particles with characteristic metallic luster appearance and optically opaque natures. Multiple lapped cross sections of cores show many such iron sulfide inclusions mostly concentrated in the dark gray crushed gneiss and lesser in light brown coarse aggregate (probably due to more oxidation of sulfide in the latter) throughout the entire depths of the cross sections. Clearly, abundant iron sulfide mineralization in the quarried stone coarse aggregate is established in the concrete, as was reportedly found in many other foundations from northeast CT (including our previous case study from Ellington, CT) that has shown pyrrhotite-oxidation related cracking.

XRD analyses of concretes and coarse aggregates extracted from the cores have confirmed the iron sulfide minerals to be pyrrhotite, along with ferrihydrite as its oxidation product, which are, again, in line with previous findings from other deteriorated foundations (Wille and Zhong, 2016, Jana 2018). XRD analyses showed mineralogical similarities between 1998 and 2001 concretes all containing quartz, albite feldspar as two common minerals in crushed stones, followed by biotite, almandine garnet in gneiss, augite in metamorphosed gabbro, and pyrrhotite as one of the opaque phases responsible for the distress by forming its oxidation product, ferrihydrite.

XRF analysis of bulk concretes and aggregates extracted from concrete showed compositional similarities amongst concretes and differences from aggregate as seen for the minerals in XRD, all in having major amount of silica, followed by oxides of calcium, aluminum, iron, magnesium, and alkalis. Sulfate contents (as  $\text{SO}_3$ ) of bulk concretes range from 0.5 to 1.6 percent, whereas that from a crushed stone coarse aggregate that has created radial cracking in Core D-3 showed 2.43 percent sulfate. Iron oxide contents in concretes are in the range of 5 to 8.5 percent, whereas in the unsound crushed stone it is up to 25.6 percent due to oxidation of pyrrhotite.

Microcracking within many pyrrhotite-bearing crushed gneiss coarse aggregates due to pyrrhotite oxidation, often extending from unsound aggregates to paste is the first sign of distress due to primary expansion of unsound aggregate *per se* that are distinct in numerous photomicrographs of thin and lapped cross sections. Many times, microcracks simply followed the micaceous bands in gneiss due to the internal plane of weakness along the micaceous bands of gneissose-textured rock. The gneissose texture of crushed gneiss coarse aggregate particles consisting of alternating bands of denser quartzo-feldspathic minerals and flaky (cleavable) biotitic mica provided additional inherent planes of weakness (foliation) in the aggregate that are susceptible to develop cracking along the internal planes of weakness along the biotite bands during expansions from pyrrhotite oxidation. As a result, a lot of cracks within the gneiss coarse aggregate particles are found along the weak bands of mica flakes. In many particles, however, no such preferential path of aggregate cracking is noticed.

Petrographic examinations also detected abundant secondary ettringite crystallization lining or filling many air voids and occasionally lining some microcracks that are indicative of prolonged presence of moisture in the concrete during service, which is an essential pre-requisite for pyrrhotite oxidation. It also indicates availability of sulfates for ettringite crystallization, which, however, may or may not have necessarily derived from pyrrhotite oxidation since ettringite-filled air-voids are a very common microstructural feature in a concrete exposed to moisture without even any iron sulfide contaminant. Any Portland cement concrete exposed to moisture during service forms secondary ettringite deposits lining and filling air voids. To establish the source of secondary ettringite i.e. from Portland



cement's sulfate and/or from oxidation of pyrrhotite-bearing aggregates require determination of sulfate levels in concrete i.e. if the level is higher than that expected from a typical Portland cement concrete where sulfate (as  $\text{SO}_3$ ) content in cement is around 3 weight percent i.e. giving about 0.45 percent sulfate in concrete for a usual cement content of 15 percent by mass of a normal weight concrete. Excess sulfate in concrete above 0.45 percent from cement's contribution would then correspond to the pyrrhotite-aggregate source if no other sulfate source were present. To determine the sulfate ( $\text{SO}_3$ ) level of bulk concrete, a thin slice of concrete was sectioned through the entire length of the core traversing the full thickness of the foundation wall and pulverized for XRF analysis, which showed 1.45 percent bulk sulfate ( $\text{SO}_3$ ) by weight of concrete, which is more than 3 times the sulfate that is normally contributed from Portland cement. Clearly, some of the secondary ettringite crystallization in air-voids and microcracks were derived from sulfates other than Portland cement having the most likely source from oxidation of pyrrhotite in coarse aggregate.

To establish secondary expansion of paste from internal sulfate attacks by reactions between sulfates released from pyrrhotite oxidation and cement hydration products, microstructural evidence for expansion of the sulfate-contaminated hydrated cement paste has to be established. A common microstructural evidence of paste expansion commonly attributed to delayed ettringite formation (DEF) in many steam-cured precast concrete elements is gaps or separations around aggregates due to direct expansion of paste relative to aggregate (Jana 2008), where widths of the gaps are usually proportional to the size of the aggregates around which the gaps are formed from paste expansion. Optical microscopy did not detect many such gaps around aggregates, or, similar features as found in many cracked precast concrete members deteriorated by delayed ettringite formation. Another feature common in sulfate attacks from internal or external sulfates is ettringite filled cracks, which is seen in the present cracked concretes, especially in the interior cracked regions. Therefore, the possibility of paste expansion from an internal sulfate attack by reactions between excess (i.e. beyond cement's contribution) sulfates released from pyrrhotite oxidation and cement hydration products are diagnosed both by optical microscopy and subsequently by SEM-EDS.

However, the most interesting microstructural feature detected in many other pyrrhotite-related distress of residential concrete foundations of eastern Connecticut (e.g., from a case study from Ellington, CT, Jana 2018) but not that distinct in the present study is poorly crystalline (perhaps some colloidal form) secondary ettringite in the confined (or relatively less dense) areas of paste than the well-formed acicular or fibrous secondary ettringite in voids or cracks. The former type i.e. poorly crystalline secondary ettringite in paste areas (called ettringite infested paste, EIP) are judged to be the breeding grounds for internal sulfate attack that have caused secondary expansion of paste, and associated cracking. The main mechanism of paste expansion from internal sulfate attack is judged to be not so much due to precipitation of secondary ettringite in voids and cracks but more due to formation of poorly crystalline ettringite in relatively confined areas in paste. Ettringite-lined voids or cracks are most probably the result not the cause of internal sulfate attack, whereas poorly crystalline ettringite in confined areas of paste (EIP) are the direct cause for expansion and cracking of paste and around aggregate-paste interfaces. EIP is directly responsible for high sulfate content of paste detected in SEM-EDS studies described below, which is the more powerful evidence for internal sulfate attack than simple secondary ettringite-filled cracks. Ettringite-infested paste and subsequent high sulfate level in the paste *per se* was found in other case studies, e.g., from Ellington, CT but not in the present case where secondary ettringite is found extensively forming within air-voids, cracks, and porous areas of paste but not within the confined spaces at least to see as ettringite-infested paste.

SEM-EDS studies found well-developed secondary ettringite crystallization mostly in air-voids and only occasionally in microcracks including in gaps around aggregates and at aggregate-paste interfaces, which are more common microstructures of other DEF-distressed concretes. Most of the microcracks are empty, and gaps around aggregates due to paste expansion are not as frequent as in other DEF-affected concretes. However, EDS analyses of sulfate contents of paste are noticeably less (mostly less than 0.1% similar to common Portland cement pastes) than that found in other case studies (e.g., in the range of 4 to 6.5% as  $\text{SO}_3$  found in the paste of pyrrhotite-distress of foundation from Ellington, CT, Jana 2018), which is indicative of probably an initial stage of distress where most secondary ettringite formed from pyrrhotite oxidation found voids, cracks, and porous areas to be deposited rather than forming within the confined areas of paste. In other case studies, e.g., from Ellington, CT sulfate contents of paste *per se* were noticeably higher than less than 1% sulfate ( $\text{SO}_3$ ) commonly found in the paste of a normal Portland cement concrete prepared using a Portland cement containing 3 percent sulfate at a similar water-cement ratio and cement content of the present core but containing no iron sulfide contaminant.



For pyrrhotite-oxidation distress from Ellington, CT, the high sulfate content of paste detected from EDS analyses was consistent with the ettringite-infested paste found in thin section photomicrographs during optical microscopy, as well as overall high bulk sulfate ( $\text{SO}_3$ ) content of concrete, indicating sulfate release from pyrrhotite oxidation. For the present study, however, lack of high sulfate in paste is consistent with lack of ettringite-infested paste, but, however, high bulk sulfate content of concrete (similar to the bulk sulfate of concrete in Ellington, CT) – thus indicating an initial stage of deterioration in the present case where sulfate has not yet deposited within the paste *per se* to cause direct expansion but rather found its way into the voids, cracks, and porous areas to be precipitated as innocuous deposits rather than potentially deleterious. Most of the cracks seen in the present cores are, therefore, judged more due to *in situ* oxidation of pyrrhotite than expansions from both pyrrhotite oxidation followed by internal sulfate attack of released sulfates in paste.

SEM-EDS analyses (Jana 2018) of pyrrhotite-related cracking in foundations across eastern CT found three different optically opaque iron species in gneiss, e.g., iron sulfide (pyrrhotite), oxidation products of pyrrhotite measured in the EDS as iron oxide (determined in XRD as ferrihydrite), and iron-titanium oxide (rutile and ilmenite). Present case study was no exception, where both pyrrhotite and ilmenite were found and ferrihydrite is determined from XRD studies.

In the case of Ellington, CT cracked concrete foundation showed clear microstructural evidence of (a) primary expansion of concrete due to oxidation of pyrrhotite in crushed gneiss coarse aggregate causing cracking within the unsound aggregate particles often extending into paste, and (b) secondary expansion of paste due to formation of poorly crystalline (perhaps also colloidal formed) secondary ettringite in relatively confined areas in sulfate-contaminated paste (called ettringite infested paste) that are the breeding ground for internal sulfate attack causing paste expansion and associated cracking. The present study, however, showed the former i.e. pyrrhotite-oxidation related cracking from ferrihydrite formation more than subsequent distress from internal sulfate attack from ettringite infestation in paste. Relatively well-developed secondary ettringite in voids and few in cracks are judged to be the consequence of exposure of ettringite to moisture during service causing dissolution and precipitation of secondary ettringite in open spaces.

Accelerated pyrrhotite oxidation test of unsound crushed gneiss coarse aggregate from Core D-3 showed high sulfate levels compared to sulfate determined from filtrates of water-digested pulverized concretes. Concretes and aggregates were pulverized to pass No. 50 sieve, then immersed in distilled water for 24 hours (for concrete) or in a 35% hydrogen peroxide (strong oxidant) solution for several days (for extracted unsound aggregate). Sulfates released from concrete and aggregates to the filtrates were measured (as  $\text{SO}_4^{2-}$ ) in anion exchange chromatography. All samples showed noticeable release of sulfates, with unsound aggregate showing more than three times more sulfates relative to the bulk concretes, all contrary to no sulfate released from a control gneiss aggregate containing no pyrrhotite. The high pH environment of Portland cement concrete is also known to enhance pyrrhotite oxidation (Divet and Davy 1996).

All these studies have confirmed and contributed further evidence to the continuously developing clear mechanisms of the common consensus that the observed cracking and reported crumbling of concrete foundation walls in eastern Connecticut are due to: (a) oxidation of pyrrhotite in crushed garnetiferous quartzo-feldspathic gneiss coarse aggregate particles in the presence of oxygen and moisture during service in concrete with the formation of ferrihydrite causing expansion of the unsound aggregates and formation of cracks from unsound aggregates to paste, which was then followed by (b) additional expansion in the paste from reactions between sulfates released from pyrrhotite oxidation and cement hydration products (internal sulfate attack) and formation of poorly crystalline or perhaps colloidal ettringite within the confined spaces in paste. Microcracks from the primary expansion of unsound aggregates are more frequent in these cores than that from secondary expansion of paste by internal sulfate attack. Whether or not both mechanisms are well-developed depends on factors such as availability of moisture during service, age, porosity and permeability of concrete to moisture, etc.



Based on this comprehensive case study, the following conclusions are drawn:

1. Observed cracking of concrete foundation walls around the Birch Grove School in Tolland, CT is determined to be due *oxidation of unsound pyrrhotite grains in crushed garnetiferous quartzo-feldspathic and biotitic gneiss coarse aggregate* particles in the presence of oxygen and moisture during service.
2. The host rock for pyrrhotite mineralization used as coarse aggregate in concrete is metamorphic crushed stone coarse aggregates, which are a mixture of a predominant dark gray garnetiferous quartzo-feldspathic and micaceous gneiss (having quartz, albite feldspar, biotite mica, and almandine garnet) with a subordinate amount of metamorphosed gabbro (having ortho and/or clino-pyroxenes, oligoclase plagioclase, garnet, and minor biotite), and, a subordinate light brown garnetiferous quartz-feldspar-mica gneiss (having a higher quartz content than the dark gray gneiss) - all having nominal maximum sizes of  $3/4$  in. (19 mm) showing the typical gneissose texture of alternating bands of quartz-albitic feldspar and micaceous (mostly biotite and less muscovite) minerals that often contain almandine garnet poikiloblast, and equigranular granoblastic texture for metamorphosed gabbro. Amount of pyrrhotite grains varied widely amongst different crushed gneiss particles, irrespective of the host rock mineralogy.
3. Sulfur (as  $SO_3$ ) contents in the pyrrhotite-bearing crushed gneiss aggregates are variable amongst various case studies e.g., from Ellington (where  $SO_3$  contents were 2 percent in light brown gneiss to as high as 10 percent in predominant dark gray gneiss particles, or perhaps even higher, giving a total bulk sulfate ( $SO_3$ ) content of 1.45 percent in the concrete, which is more than 3 times the sulfate in a normal Portland cement concrete without any iron sulfide contaminant) to the present study in Tolland where  $SO_3$  content in unsound crushed gneiss in a core from cracked foundation is 2.43 percent and bulk sulfate contents of concretes across the cores varied from 0.5 to 1.6 percent. As high as 8 percent pyrrhotite was found from XRD analysis of dark gray gneiss in Ellington, CT indicating significant pyrrhotite mineralization.
4. Oxidation of pyrrhotite has formed *ferrihydrate* with an expansion of unsound crushed gneiss coarse aggregate causing extensive cracking in many particles having cracks extending from the affected particles to paste. The typical gneissose texture of quarried aggregates has facilitated crack formation during expansion due to the presence of inherent planes of weakness along the micaceous bands in gneiss. Reddish brown rust stain found in many distressed foundations are due to pyrrhotite (and also pyrite) oxidation and formation of iron oxy-hydroxides (e.g., goethite, limonite) and ferrihydrates. The present cores from Tolland, however, do not show any rusty brown discoloration from pyrrhotite oxidation, or popout from expansion of near-surface unsound pyrrhotite.
5. Evidence of pyrrhotite oxidation is confirmed from: (a) detection of ferrihydrate in XRD, and, (b) from SEM-EDS studies of lower than stoichiometric S/Fe ratio of many pyrrhotite grains (mostly  $<0.50$ ) indicating advanced oxidation. Microstructural evidence of oxidation-related expansion of unsound aggregate is found from extensive cracking of many of these crushed gneiss aggregates often extending into the paste.
6. Pyrrhotite oxidation has readily released sulfates and either contaminated the Portland cement paste by *in situ* infestation of ettringite as in the case of Ellington, CT, or simple secondary precipitation in voids, cracks, and porous areas though more than that usually occur in a normal Portland cement paste exposed to moisture as in the present case of Tolland. Ready release of sulfate and continued exposure to moisture promotes internal sulfate attack and subsequent secondary expansion of paste with additional cracking.
7. To determine the potential for release of sulfate in an oxidizing environment, bulk concretes from multiple cores as well as two unsound crushed gneiss aggregates from a core (D-3) from visibly cracked foundation were pulverized to pass No. 50 sieve, then immersed in distilled water for 24 hours (for concrete) or in a 35% hydrogen peroxide (strong oxidant) solution for several days (for extracted unsound aggregate). Sulfates released from concrete and aggregates to the filtrates were measured (as  $SO_4^{2-}$ ) in an anion exchange chromatograph. All samples showed noticeable release of sulfates with unsound aggregate showing more



than three times more sulfate relative to the bulk concretes, all contrary to no sulfate released from a control gneiss aggregate containing no pyrrhotite.

8. Sulfates released from pyrrhotite oxidation have reacted with cement hydration products (e.g., calcium hydroxide, calcium aluminate hydrate, calcium monosulfoaluminate) and formed poorly crystalline or perhaps colloidal form of ettringite within the confined spaces in paste with the resultant secondary expansion of paste and additional cracking within the paste and around aggregate-paste interfaces. Presence of excess sulfates, moisture, and open spaces of air-voids and cracks – all three conditions have facilitated dissolution and precipitation of well-crystallized fibrous secondary ettringite in voids and occasionally in cracks that were visible in optical microscopy and SEM analyses.
9. Evidence of internal sulfate attack in paste came first from the paste chemistry i.e. (a) very high sulfate ( $\text{SO}_3$ ) content of paste from SEM-EDS studies as in the case of Ellington, CT, and/or from various microstructural evidences in optical and scanning electron microscopy, e.g., (b) ettringite-infested paste containing poorly crystalline (perhaps some colloidal) form of ettringite, (c) well-formed secondary ettringite crystallization in aggregate-paste interfaces, microcracks, and air-voids, often due to moisture-induced dissolution of ettringite from ettringite-infested confined areas of paste and precipitation of relatively well-formed ettringite in voids and cracks, and (d) gaps between aggregates due to expansion of paste (more common in many other concrete distresses due to internal sulfate attack than the present one).
10. Relative roles of primary expansion of unsound aggregates due to pyrrhotite oxidation and secondary expansion of paste due to internal sulfate attack in the overall distress of foundation depend on various factors, e.g., proportion of pyrrhotite (and total available sulfate), moisture condition during service, consolidation and degree of impermeability of concrete to moisture ingress, etc. In the case of Ellington both mechanism were prominent where in the present case of Tolland former is more evident than latter.
11. In light of the observed cracking of foundation walls, particularly in some cores where cracks are seen extended all throughout their recovered lengths (e.g., A-1, A-2, C-1, C-2, D-1, D-2, D-3), and its anticipated progress with potential worsening of condition with time especially in continued presence of moisture at the ground level, repair of the walls showing visible cracks are necessary along with similar precautions for walls where visible cracking has not developed yet even though concrete inside shows cracking (e.g., Cores A-2, A-3, C-2). A close monitoring is needed for walls of F-series cores from 2001 construction.
12. If the pyrrhotite-bearing crushed gneiss coarse aggregate found in this concrete was indeed from the Becker's quarry in Ellington, CT (as reported for other foundations undergoing similar pyrrhotite-oxidation-related distress including the ones in Ellington), then due to the known geology of pyrrhotite mineralization in the hydrothermal vein in which this quarry is situated, and its known devastating effects when used in concrete from case studies of multiple foundations (Wille and Zhong 2016, Jana 2018) including the present one, use of crushed stone from this quarry for concrete aggregate should be abandoned, or should only be used after extensive evaluation of aggregates for the presence of pyrrhotite (e.g., from magnetic test, total sulfur test from XRF, XRD detection of pyrrhotite amount) and its potential release of sulfate in an accelerated oxidation test of aggregates.
13. Aggregate to be used in a new foundation from other quarries must be evaluated for the possible presence of any unsound constituents, including iron sulfide minerals, e.g., (a) from XRD analysis of quarried stones to detect the amount and speciation of iron sulfide minerals present, (b) from XRF analysis to detect the total sulfur (as  $\text{SO}_3$ ) content of quarried stones, and (d) from accelerated oxidation test to detect the rate and level of sulfates that can be released from aggregates.
14. Since there is no industry specification on the threshold pyrrhotite limit above which potential for oxidation-related distress can occur, and, in fact as low as 0.3% pyrrhotite by mass of aggregate in the host rock has reportedly shown severe distress in concrete (e.g., in Quebec Canada), the best solution is to avoid aggregates containing pyrrhotite without further laboratory verification of its potential unsoundness in concrete (e.g., from expansion of mortar bar, e.g. Rodrigues *et al.* 2015).



**LIST OF FIGURES, TABLES, AND APPENDICES**

| Figures, Tables, Appendices | Description  |
|-----------------------------|--|
| Fig. 1                      | Birch Grove School, Tolland’s place within the high-risk zone, core locations, classification of cores from visible cracks   |
| Fig. 2                      | Field photographs at the locations of Cores A-1 to A-3, B-1, and C-1 to C-3  |
| Fig. 3                      | Field photographs at the locations of Cores D1- to D-3   |
| Fig. 4                      | Field photographs at the locations of Cores F-series   |
| Fig. 5                      | Optical Microscopes used in investigation  |
| Fig. 6                      | Siemens D5000 X-ray diffractometer used for determination of mineralogy of concretes and aggregates  |
| Fig. 7                      | Cambridge CamScan Series II Scanning Electron Microscope   |
| Fig. 8                      | Rigaku NEX-CG bench-top ED-XRF unit used for bulk chemical compositions of concretes and aggregates  |
| Fig. 9                      | Metrohm 861 Advanced IC with 788 Sample processor used for analyses of sulfates released from concrete and aggregate   |
| Fig. 10                     | Exposed formed end surfaces, and cylindrical side views of Cores A-1 through A-3, B-1, and C-1, as received  |
| Fig. 11                     | Exposed formed end surfaces, and cylindrical side views of Cores C-2, D-1 through D-3, as received   |
| Fig. 12                     | Exposed formed end surfaces, and cylindrical side views of F-series cores from 2001 construction, as received  |
| Fig. 13                     | Lapped cross sections of the Cores A-1 to A-3, B-1, and C-1  |
| Fig. 14                     | Lapped cross sections of the Cores C-2, C-3, D-1 through D-3   |
| Fig. 15                     | Lapped cross sections of the Cores F-1 to F-5 from 2001 construction   |
| Fig. 16                     | Fluorescent dye-mixed epoxy-impregnated lapped cross sections of cores highlighting visible and invisible cracks   |
| Fig. 17                     | Photomicrographs of lapped cross sections of Cores A-1 to A-3, B-1, and C-1  |
| Fig. 18                     | Photomicrographs of lapped cross sections of Cores C-2, D-1 through D-3  |
| Fig. 19                     | Photomicrographs of lapped cross section of Core D-3 having two unsound aggregate particles that have cracked  |
| Fig. 20                     | Photomicrographs of lapped cross sections of Cores F-1 to F-5  |
| Fig. 21                     | Pyrrhotite grains in coarse aggregates in Cores of A-series  |
| Fig. 22                     | Pyrrhotite grains in coarse aggregates in Cores of C-1, C-2, and F-5   |
| Fig. 23                     | Pyrrhotite grains in coarse aggregates in Cores of D-series  |
| Fig. 24                     | Blue dye-mixed epoxy-impregnated large area (50 mm by 75 mm) thin sections of all fifteen cores  |
| Fig. 25                     | Thin section photomicrographs of Cores A-1 to A-3, and B-1   |
| Fig. 26                     | Thin section photomicrographs of Cores C-1 to C-3  |
| Fig. 27                     | Thin section photomicrographs of Cores D-1 to D-3  |
| Fig. 28                     | Thin section photomicrographs of Cores F-1 to F-5  |
| Fig. 29                     | SEM-EDS study of Core A-1 showing pyrrhotite and secondary ettringite  |
| Fig. 30                     | SEM-EDS study of Core C-2 showing pyrrhotite and EDS oxide compositions of Portland cement paste   |
| Fig. 31                     | SEM-EDS study of D-series cores showing disseminated pyrrhotite grains in aggregates from elemental maps   |
| Fig. 32                     | SEM-EDS study of F-series cores showing disseminated pyrrhotite grains in aggregates from elemental maps   |
| Fig. 33                     | Quantitative proportions of minerals in concretes in Cores A-1, B-1, C-1 to C-3, D-1 to D-3, and F-1 from XRD  |
| Fig. 34                     | X-ray diffraction pattern and quantitative proportions of minerals in two unsound aggregates in Core D-3   |
| Fig. 35                     | Ion chromatography of sulfates released from Cores A-1, B-1, C-1 to C-3, D-1 to D-3, and F-5, and two aggregates in D-3  |
| Fig. 36                     | Mechanisms of oxidation of iron sulfide minerals in concrete   |
| Fig. 37                     | Reported incidences of pyrrhotite-related concrete deterioration in the northeastern Connecticut   |
| Figs. 38-41                 | Cracking of concrete foundations in Connecticut due to oxidation of pyrrhotite bearing aggregates in concrete  |
| Table 1                     | Classification of fifteen cores received based on the degree of visible cracking   |
| Table 2                     | Overall dimensions and conditions of the fifteen cores, as received  |
| Table 3                     | Properties of coarse and fine aggregates of concretes  |
| Table 4                     | Compositions and properties of paste   |
| Table 5                     | Air contents and air-void systems of concretes   |
| Table 6                     | Quantitative mineralogical compositions and pyrrhotite contents of concretes and aggregates from XRD   |
| Table 7                     | Bulk oxide compositions and sulfate (SO <sub>3</sub> ) contents of concretes and aggregates from XRF   |
| Table 8                     | Case studies on concrete deteriorations due to oxidation of iron sulfide minerals in aggregates  |
| Appendix A                  | A1 to A21: Photographs of project location, conditions of concrete, and conditions of 15 cores as received   |
| Appendix B                  | B1 to B28: Photographs of lapped cross sections of 15 cores, traces of cracks on lapped cross sections, and depth of carbonation of concrete after treatment of lapped cross sections with phenolphthalein alcoholic solutions, as well as fluorescent dye-mixed epoxy-impregnated lapped cross sections of all 15 cores |
| Appendix C                  | C1 to C36: Photomicrographs of lapped cross sections of all 15 cores   |
| Appendix D                  | D1 to D42: Thin section photomicrographs of concrete and aggregates in all 15 cores  |
| Appendix E                  | E1 to E21: SEM-EDS studies of Cores A-1, C-1, C-2, D-1, D-2, D-3, and F-5  |
| Appendix F                  | F1 to F10: XRD studies of Cores A-1, B-1, C-1, C-2, C-3, D-1, D-2, D-3, two unsound aggregates in D-3, and F-1   |



## INTRODUCTION

Oxidation of an iron sulfide mineral 'pyrrhotite' ( $\text{Fe}_{1-x}\text{S}$ ,  $x$  varies from 0 to 0.125) in the quarried aggregate stones has caused deterioration of concrete foundations across thousands of homes in eastern Connecticut. In light of this known problem of pyrrhotite, visible cracking of some concrete foundation walls across Birch Grove School located at 247 Rhodes Road in Tolland, Connecticut has steered serious concerns especially since Tolland is located within the known high-risk zone of 'pyrrhotite epidemic' that has affected more than 50 residential foundations as of April of 2018. As a result, fifteen concrete cores were drilled from the foundation walls around the school encompassing two different constructions – ten cores (of A-series through D-series) came from 1998 constructions, and, five additional cores (of F-series) came from 2001 construction. Cores were examined in the laboratory to investigate: (a) whether or not the deteriorated concrete foundation contains pyrrhotite in its aggregate, and, if detected, (b) if pyrrhotite has played the primary role for the observed cracking and crumbling as in the case of other cracked foundations.

## BACKGROUND INFORMATION

Figure 1 shows the Birch Grove School in Tolland, and its location on a map of eastern Connecticut where Tolland falls within the high-risk zone having more than 50 reported incidences of pyrrhotite-related deterioration of concrete foundations. Also shown is a schematic diagram of locations of all fifteen cores across the school, ten cores from A-series, B-1, C and D series are from 1998 construction and the remaining five cores of F-series from 2001 construction. Cores were grouped into four classes based on occurrences of visible cracking when received from extensive cracking all throughout the recovered depths of cores marked as A-1, C-1, C-2, and D-1 to moderate cracking in Cores A-2, D-2, and D-3, to minimal cracking in Cores A-3, B-1, and C-3 to no visible cracking in the F-series cores from 2001 construction.

## FIELD PHOTOGRAPHS

### Map Cracking in Concrete Foundation Wall

Field photographs of concrete conditions at the locations of fifteen cores show map cracking of foundation at the location of Core A-1 (Figure 2), D-1, D-2, D-3 (Figure 3), a few long vertical cracks across the thickness of foundation at the location of Core C-1 (Figure 2), and a few isolated vertical cracks at the location of Core F-4. Amongst the 1998 construction, foundation walls at the locations of Cores A-1, D-1, D-2, and D-3 showed most visible map cracking, which are consistent with the observed through-depth cracks in those cores when received. Extensive cracking in Cores C-1 and C-2, however are found when received but no corresponding visible cracking are found in the field photos of those locations on the exposed surfaces of foundations. Moderate cracking mostly at the exposed end of Core A-2, and minimal cracking in Cores A-3, B-1, and C-3 when received are also not seen on the exposed foundation walls of their locations in the field photos (Figures 2 to 4).

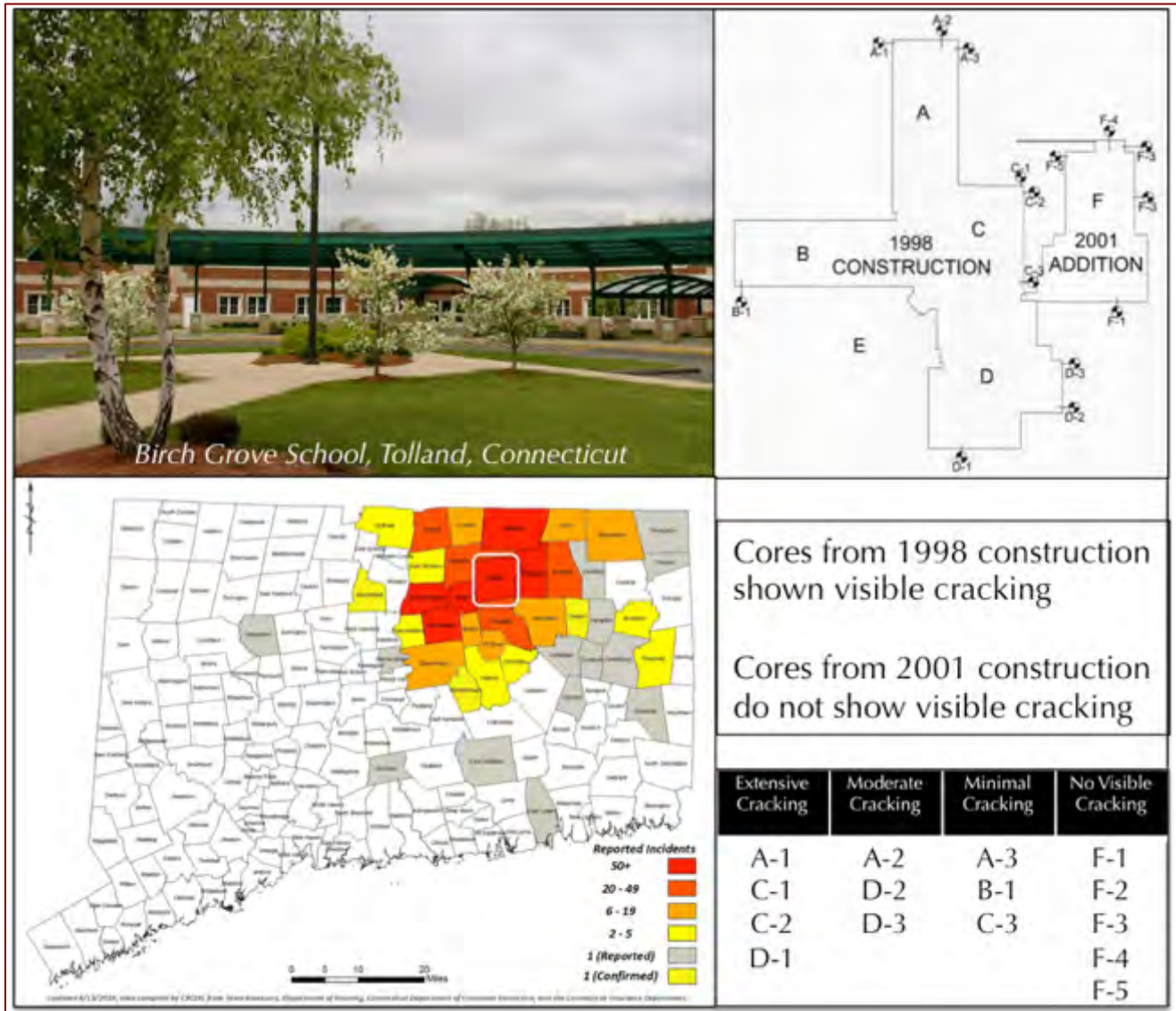


Figure 1: Shown are the Birch Grove School at 247 Rhodes Road, Tolland, CT, location of Tolland within the high-risk zone of pyrrhotite-related distress, locations of concrete cores collected from the foundations around the school, and degrees of visible cracking on the cores received. See Appendix A for details.

Figures 10 to 12 show all fifteen cores as received where visible cracks on the exposed surfaces as well as side cylindrical surfaces are marked to show variations in crack intensities to classify them into four groups. Based on observations of cracking in field photos as well as the cores received it is, therefore, confirmed that cracking of foundation walls have occurred in A, C, and D-series cores in varying degrees, whereas no visible cracking on the wall at the location of Core B-1, or, in the 2001 construction (except a few isolated vertical cracks not similar to the typical map cracking found in the walls of 1998 construction. Map cracking is the common manifestation of pyrrhotite-related deterioration as observed in many other foundations across eastern Connecticut.

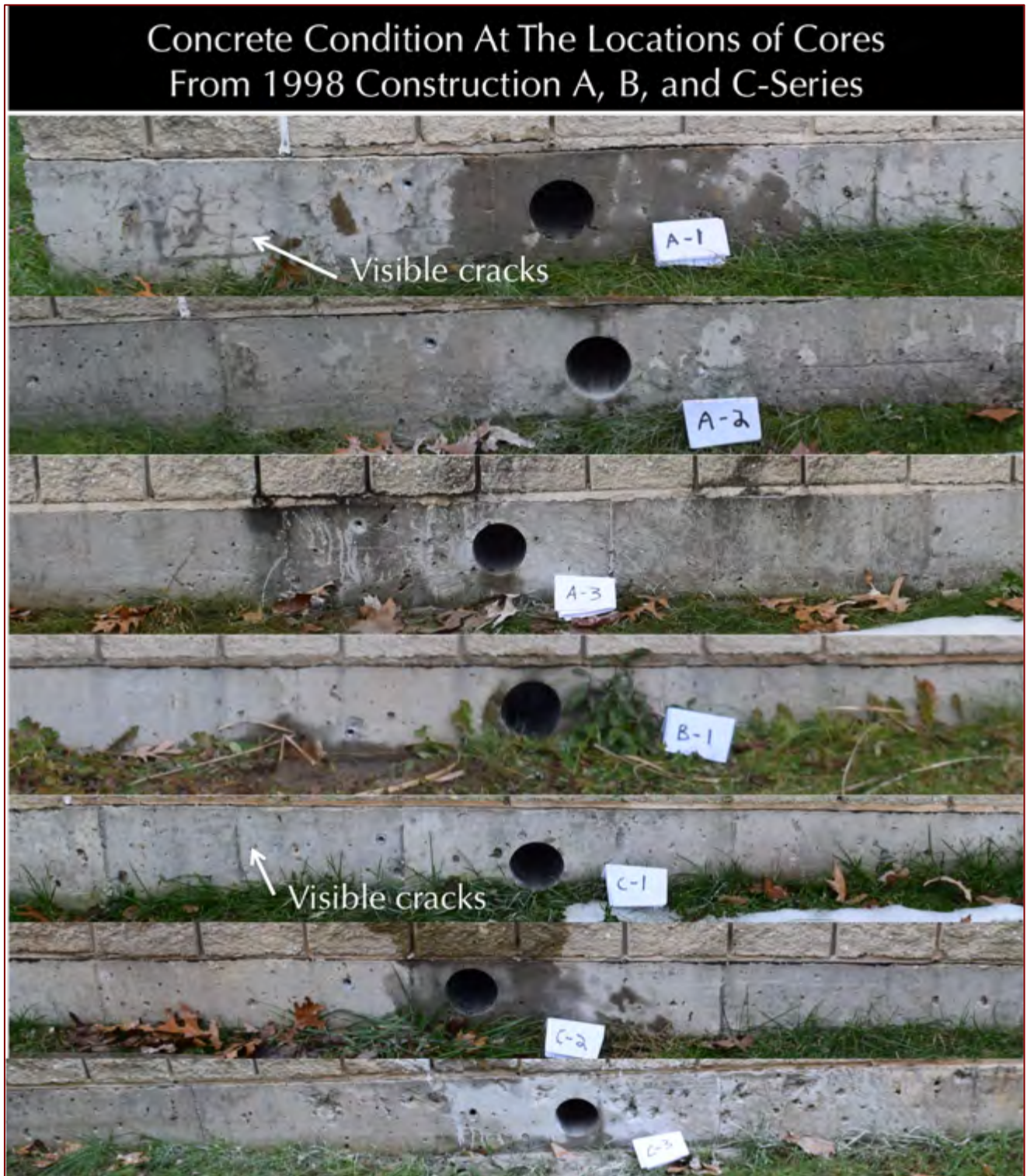


Figure 2: Field photographs at the locations of Cores A-1 to A-3, B-1, and C-1 to C-3 showing visible cracking of the foundation wall at the locations of A-1 and C-1, but no discernable cracks in other locations. Cracking of foundation wall at the location of Core A-1 is similar to typical map cracking pattern, which is common in many pyrrhotite-related deteriorations of foundation walls across eastern Connecticut. See Appendix A for details.



Figure 3: Field photographs at the locations of Cores D-1 to D-3 showing visible cracking of the foundation wall at the locations of all three cores. Map cracking is visible at the locations of all three cores, which is common in many pyrrhotite-related deteriorations of foundation walls across eastern Connecticut. See Appendix A for details.



Figure 4: Field photographs at the locations of Cores F-series showing isolated vertical visible cracking of the foundation wall at the location of F-4 but no discernable cracks in other locations, or map cracking found in the walls from 1998 construction. See Appendix A for details.

#### PURPOSE OF PRESENT INVESTIGATION

Based on the background information, the purposes of the present investigation, therefore, are to determine: (a) the composition, quality, and overall condition of concrete in the walls as represented by the cores; and particularly (b) detection of any possible physical or chemical deterioration of concrete that may have contributed to the reported cracking of the foundation walls; and (c) detection of any pyrrhotite presence in the concrete aggregates, and, if such mineral has caused the reported distress due to its known deleterious effects on durability of concrete from other studies in the region.



## METHODOLOGIES

### OPTICAL MICROSCOPY (FOR OVERALL CONDITION OF CONCRETE AND AGGREGATES)

The cores were tested and examined by following the methods of ASTM C 856 “Standard Practice for Petrographic Examination of Hardened Concrete.” Details of petrographic examinations and sample preparation are described in Jana (2006). The steps of petrographic examinations include (Jana 2006):

- i. Visual examinations of the cores, as received to trace all visible cracks;
- ii. Low-power stereomicroscopical examinations of as-received, saw-cut and freshly fractured sections, and lapped cross sections of cores for evaluation of concrete composition, condition, extent of cracking, detection of iron sulfide minerals, etc.;
- iii. Low-power stereomicroscopical examinations of air contents and air-void systems of concretes as well as detection of iron sulfide minerals (amount and distribution) in the lapped cross sections;
- iv. Examinations of oil immersion mounts in a petrographic microscope for mineralogical compositions of specific areas of interest;
- v. Examinations of un-treated and fluorescent-dye-mixed (to highlight open spaces, cracks, etc.) epoxy-impregnated treated lapped cross sections of concretes in a stereomicroscope for detailed compositional and microstructural analyses;
- vi. Examinations of blue dye-mixed (to highlight open spaces, cracks, etc.) epoxy-impregnated large area (50 mm × 75 mm) thin sections of concrete in a stereomicroscope and a petrographic microscope for detailed compositional and microstructural analyses;
- vii. Photographing samples as received, and during preparation with a digital camera and a flatbed scanner;
- viii. Photomicrographs of full-length lapped cross sections and thin sections of cores taken with stereomicroscope and petrographic microscope, respectively to provide detailed compositional, microstructural, and mineralogical information of concrete;
- ix. Detailed compositional, mineralogical, and microstructural examinations of concrete in a petrographic microscope from thin sections;
- x. Selection of areas of interest in the thin sections for subsequent examinations in scanning electron microscope;
- xi. A Nikon Eclipse 600 POL petrographic microscope attached to a Jenoptik Progres GRYPHAX high-resolution digital camera were used for petrographic examinations and collecting photomicrographs of thin sections of concretes (Figure 5). A Nikon SMZ-10A stereomicroscope (Figure 5) and an Olympus SZH stereozoom microscope (equipped with transmitted polarizing light facilities) were used for examinations of fresh fractured and lapped sections and transmitted-light examinations of thin sections, respectively.



Figure 5: Optical Microscopy: Left - A Nikon Eclipse E600 POL polarizing (petrographic) microscope at left with reflected, transmitted, polarized-light, and fluorescent-light capabilities; Middle – An Olympus SZH reflected/transmitted/polarized-light Stereozoom microscope; and Right – A Nikon SMZ-10A Stereozoom microscope. All microscopes are equipped with Jenoptik Gryphax and Lumenera Infinity digital cameras.

**X-RAY DIFFRACTION (FOR MINERALOGY OF UNSOUND AGGREGATE, IDENTIFICATION OF IRON SULFIDE PHASES & THEIR OXIDATION PRODUCTS)**

Representative portions of cores from the top 2 inches of exposed surfaces containing many unsound aggregates, as well as a few unsound crushed stone coarse aggregate particles that have caused radial cracking were extracted from the cores, pulverized, and used for X-ray diffraction to determine the sulfide species in the aggregate.



Figure 6: XRD: Siemens D5000 X-ray diffractometer and MDI Jade search/match software used for determination of mineralogical compositions of concretes and extracted concrete aggregates. Left to right: Rocklab pulverizer for initial grinding of aggregate with anhydrous alcohol; McCrone micronizing mill for final grinding; Spex 25-ton press for pellet preparation; Siemens D5000 X-ray diffractometer; and custom-made sample holder to place a 32-mm diameter pellet on sample stage.



A Rocklab pulverizer was used to grind the concrete and extracted aggregate particles down to finer than 100 microns. Usually, a few drops of anhydrous alcohol are added to reduce decomposition of any hydrous phases from the heat generated from grinding. Approximately 10 grams of sample was ground first in the Rockland pulverizer, from which about 8.0 grams of sample was selected, mixed with three binder tablets (total binder weight of 0.6 grams, for a fixed binder proportion of 7.5%), the mixture is then further ground in Rocklab pulverizer and in a McCrone micronizing mill down to finer than 44 micron size. Approximately 7.0 grams of binder-mixed pulverized sample thus prepared was weighed into a stainless steel die to prepare the sample pellet. A 25-ton Spex X-press was used to prepare 32 mm pellet from the pulverized sample. The same pellet is used for XRD to determine the mineralogies and XRF to determine the chemical compositions of concretes and aggregates.

X-ray diffraction was carried out in a Siemens D5000 Powder diffractometer ( $\theta$ - $2\theta$  goniometer, Figure 6) employing a long line focus Cu X-ray tube, divergent and anti-scatter slits fixed at 1 mm, a receiving slit (0.6 mm), diffracted and incident beam Soller slits (0.04 rad), a curved graphite diffracted beam monochromator, and a sealed proportional counter. Generator settings used are 40 kV and 30mA. Sample was placed in a custom-made circular sample holder and excited with the copper radiation of 1.54 angstroms. Tests were scanned at  $2\theta$  from  $4^\circ$  to  $64^\circ$  with a step of  $0.02^\circ$   $2\theta$  integrated at 1 sec.  $\text{step}^{-1}$  dwell time.

The resulting diffraction patterns were collected by DataScan 4 software of Materials Data, Inc. (MDI), analyzed by Jade software of MDI with ICDD PDF-4 (Minerals 2017) diffraction data. Phase identification, and quantitative analyses were carried out with MDI's Search/Match, Easy Quant, and Rietveld modules, respectively.

### SCANNING ELECTRON MICROSCOPY AND ENERGY-DISPERSIVE X-RAY SPECTROSCOPY (SEM-EDS) (FOR MICROSTRUCTURE & COMPOSITION OF DETERIORATED CONCRETE & UNSOUND AGGREGATE)

Products of oxidation of iron sulfide minerals and associated possible secondary ettringite reaction products and reaction microstructures were examined in detail by SEM-EDS. Procedures for SEM examinations are described in ASTM C 1723.

Polished and gold-palladium coated thin sections of cores already examined by optical microscopy were selected for SEM-EDS studies and examined in a Cambridge CamScan Series II scanning electron microscope equipped with a backscatter detector, a secondary electron detector, and x-ray fluorescence spectrometer (Figure 7) to observe pyrrhotite or other potentially unsound constituents in concretes and aggregates and their effect on the performance and durability of concrete, as well as evidence of internal sulfate attack and secondary ettringite formation in the paste from released sulfate.



Figure 7: SEM-EDS: Cambridge CamScan Series II Scanning Electron Microscope and 4Pi Revolution software, backscatter detector, secondary electron detector, and energy-dispersive X-ray fluorescence spectrometer used for microstructural and microchemical analyses of concretes and aggregates.

ENERGY-DISPERSIVE X-RAY FLUORESCENCE SPECTROSCOPY (ED-XRF) (FOR OXIDE COMPOSITIONS & SULFUR (SO<sub>3</sub>) LEVELS OF UNSOUND AGGREGATES & CONCRETES)



Figure 8: XRF: Rigaku NEX-CG bench-top ED-XRF unit used for bulk chemical compositions of concretes and aggregates.

An energy-dispersive bench-top X-ray fluorescence unit from Rigaku Americas Corporation (NEX-CG, Figure 8) was used for determination of bulk chemical (oxide) compositions and sulfur (as  $SO_3$ ) contents of concretes and unsound aggregate particles on pressed pellets, which were previously examined in XRD. The instrument is calibrated by using various certified (CCRL, NIST, GSA, and Brammer) reference standards of rocks. The sample pellet prepared for X-ray diffraction is used for X-ray fluorescence studies as well. The main focus of this analysis was to determine the sulfur contents (as  $SO_3$ ) in the aggregate particles as well as bulk sulfate contents (as  $SO_3$ ) in concretes.

### ION CHROMATOGRAPHY (FOR RELEASED SULFATES FROM UNSOUND AGGREGATES & CONCRETES)

Pulverized concretes, and pyrrhotite-bearing coarse aggregate particles extracted from the cores were pulverized to pass No. 20 sieve, then digested in distilled water for 24 hours (for concretes), and in hydrogen peroxide (35%) solution (for aggregates) for various days for accelerated oxidation, then filtered through 0.45-micron micro-filter paper under vacuum. The filtrates were then diluted to 250 mL with distilled water to be analyzed by Metrohm’s 861 Advanced Ion Chromatograph (Figure 9) for determination of released sulfates from oxidation of sulfides. Procedures followed in Ion chromatography are described in ASTM D 4327 “Standard Test Method for Anions in Water by Chemically Suppressed Ion Chromatography.” The IC was calibrated against different custom-made Metrohm anion standard solutions having sulfate from 1-ppm to 500-ppm levels.

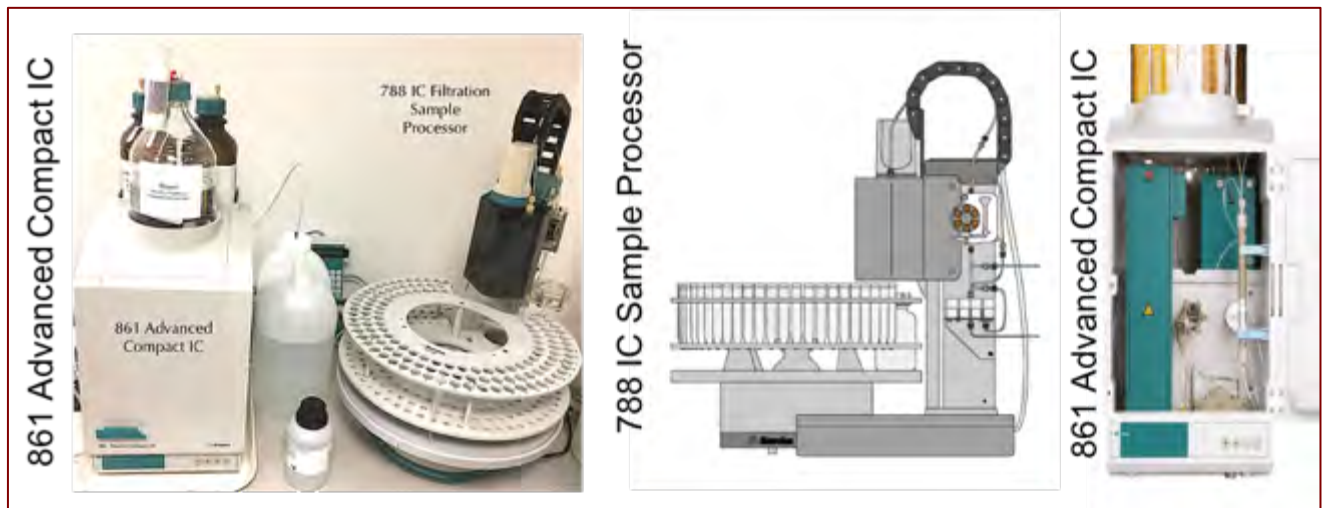


Figure 9: Metrohm 861 Advanced IC with 788 Sample processor used for analysis of sulfates released from concrete and aggregate.



**SAMPLES**

**PHOTOGRAPHS, IDENTIFICATION, INTEGRITY, AND DIMENSIONS**

Figures 10 to 12 and Appendix A show the exposed and opposite ends of the cores as well as the cylindrical surfaces, where visible cracks when noticed are marked. Figures 10 to 12 show the nominal lengths of the cores. Table 1 shows various degrees of cracking observed in the cores when received. Table 2 provides dimensions, opposite surfaces, integrity, and embedded items.

**END SURFACES**

Exposed surfaces of cores from 1998 construction show the formed surfaces of concrete foundation walls with visible cracks in some cores (e.g., A-2, B-1, C-1, C-2, C-3, D-2). All cores have fresh fractured opposite surfaces, indicating partial depth/thickness retrieval of cores from the foundation walls. Five cores from 2001 construction, however, showed a trowel-finished thin dark gray cementitious protective skim coat well-bonded to the concrete beneath.

**CRACKING & OTHER VISIBLE DISTRESS**

Figures 10 to 12, Appendix A and Table 1 provide visible cracking in ten cores from 1998 construction. Cracking is most visible (both in field photos and in cores received) in A-1, C-1 and all three cores of D-series. All visible cracks in field photos show the typical map cracking, which is common in many pyrrhotite-related distress of concrete foundations in eastern Connecticut.

**EMBEDDED ITEMS**

There is no evidence of any fibers or other embedded items found in the cores.

**RESONANCE**

The cores have a ringing resonance, when hammered.

| Extensive Cracking | Moderate Cracking | Minimal Cracking | No Cracking |
|--------------------|-------------------|------------------|-------------|
| A-1                | A-2               | A-3              | F-1         |
| C-1                | D-2               | B-1              | F-2         |
| C-2                | D-3               | C-3              | F-3         |
| D-1                |                   |                  | F-4         |
|                    |                   |                  | F-5         |

Table 1: Classification of fifteen cores received based on the degree of visible cracking.



| Core ID | Length                                   | Diameter         | Exposed Surface                              | Embedded Items   | Integrity   |
|---------|--|------------------|--|--|---|
| A-1     | 8½ in.<br>(220 mm)                       | ¾ in.<br>(95 mm) | Formed, Coarse voids,<br>No visible Cracking | Two No. 6 reinforcing steels at depths of 1¼ in. and 1¾ in. from the exposed surface | Broken into multiple pieces due to extensive cracking all throughout the depth of the core    |
| A-2     | 8¼ in.<br>(215 mm)                       | ¾ in.<br>(95 mm) | Formed, Coarse voids,<br>Visible cracking    | No. 6 reinforcing steel at a depth of 2 in. from the exposed surface                 | Broken into two unequal pieces along a reinforcing steel at 2 in. depth from exposed surface  |
| A-3     | 8 in.<br>(205 mm)                        | ¾ in.<br>(95 mm) | Formed, Coarse voids,<br>No visible cracking | No. 6 reinforcing steel at a depth of 2¼ in. from the exposed surface                | Intact  |
| B-1     | 8 in.<br>(205 mm)                        | ¾ in.<br>(95 mm) | Formed, Coarse voids,<br>Visible cracking    | None   | Intact  |
| C-1     | 7 in.<br>(175 mm)                        | ¾ in.<br>(95 mm) | Formed, Coarse voids,<br>Visible cracking    | No. 6 reinforcing steel at a depth of 1¾ in. from the exposed surface                | Broken into two unequal pieces along a reinforcing steel at 1¾ in. depth from exposed surface |
| C-2     | 8½ in.<br>(220 mm)                       | ¾ in.<br>(95 mm) | Formed, Fine voids,<br>Visible cracking      | No. 6 reinforcing steel at a depth of 2 in. from the exposed surface                 | Broken into two unequal pieces along a reinforcing steel at 2 in. depth from exposed surface  |
| C-3     | 7½ in.<br>(195 mm)                       | ¾ in.<br>(95 mm) | Formed, Coarse voids,<br>Visible cracking    | No. 6 reinforcing steel at a depth of 1¼ in. from the exposed surface                | Intact  |
| D-1     | 8¼ in.<br>(215 mm)                       | ¾ in.<br>(95 mm) | Formed, Coarse voids,<br>Visible cracking    | No. 6 reinforcing steel at a depth of 1½ in. from the exposed surface                | Broken into two unequal pieces along a reinforcing steel at 3 in. depth from exposed surface  |
| D-2     | 7 in.<br>(180 mm)                        | ¾ in.<br>(95 mm) | Formed, Coarse voids,<br>Visible cracking    | None   | Intact  |
| D-3     | 5 in.<br>(130 mm)                        | ¾ in.<br>(95 mm) | Formed, Fine voids,<br>No Visible cracking   | None   | Intact  |
| F-1     | 3½ in. +<br>4 in.<br>(90 mm +<br>100 mm) | ¾ in.<br>(95 mm) | 1 mm thick skim coat,<br>No Visible cracking | No. 6 reinforcing steel at a depth of 2 in. from the exposed surface                 | Two separate layers   |
| F-2     | 8 in.<br>(200 mm)                        | ¾ in.<br>(95 mm) | 1 mm thick skim coat,<br>No Visible cracking | None   | Intact  |
| F-3     | 8¼ in.<br>(210 mm)                       | ¾ in.<br>(95 mm) | 1 mm thick skim coat,<br>No Visible cracking | No. 6 reinforcing steel at a depth of 4 in. from the exposed surface                 | Intact  |
| F-4     | 8½ in.<br>(215 mm)                       | ¾ in.<br>(95 mm) | 1 mm thick skim coat,<br>No Visible cracking | No. 6 reinforcing steel at a depth of 3¼ in.   | Intact  |
| F-5     | 6 in.<br>(150 mm)                        | ¾ in.<br>(95 mm) | 1 mm thick skim coat,<br>No Visible cracking | No. 6 steel at a depth of 1¼ in. from the exposed surface                            | Intact  |

Table 2: Overall dimensions and conditions of the fifteen cores, as received.



Figure 10: Shown are the exposed formed end surfaces (left), and cylindrical side views of Cores A-1 through A-3, B-1, and C-1 (right), as received. Red arrows in the right column point to the formed exposed ends. Small black arrows on cylindrical side surfaces indicate visible cracks. Nominal lengths of cores are given at right. Reinforcing steels are marked. See Appendix A for details.



Figure 11: Shown are the exposed formed end surfaces (left), and cylindrical side views of Cores C-2, C-3, D-1 through D-3 (right), as received. Red arrows in the right column point to the formed exposed ends. Small black arrows on cylindrical side surfaces indicate visible cracks. Nominal lengths of cores are given at right. Reinforcing steels are marked. See Appendix A for details.



Figure 12: Shown are the exposed formed end surfaces of Cores from F-series from 2001 construction where a thin (1 mm thick) dark gray cementitious protective skim coat is detected (left), and cylindrical side views of cores (right), as received. Red arrows in the right column point to the formed exposed ends. Reinforcing steels are marked. Black arrows in Core F-1 indicate a possible construction joint. Nominal lengths of cores are given at right. See Appendix A for details.

**PETROGRAPHIC EXAMINATIONS**

**LAPPED CROSS SECTIONS OF CORES**

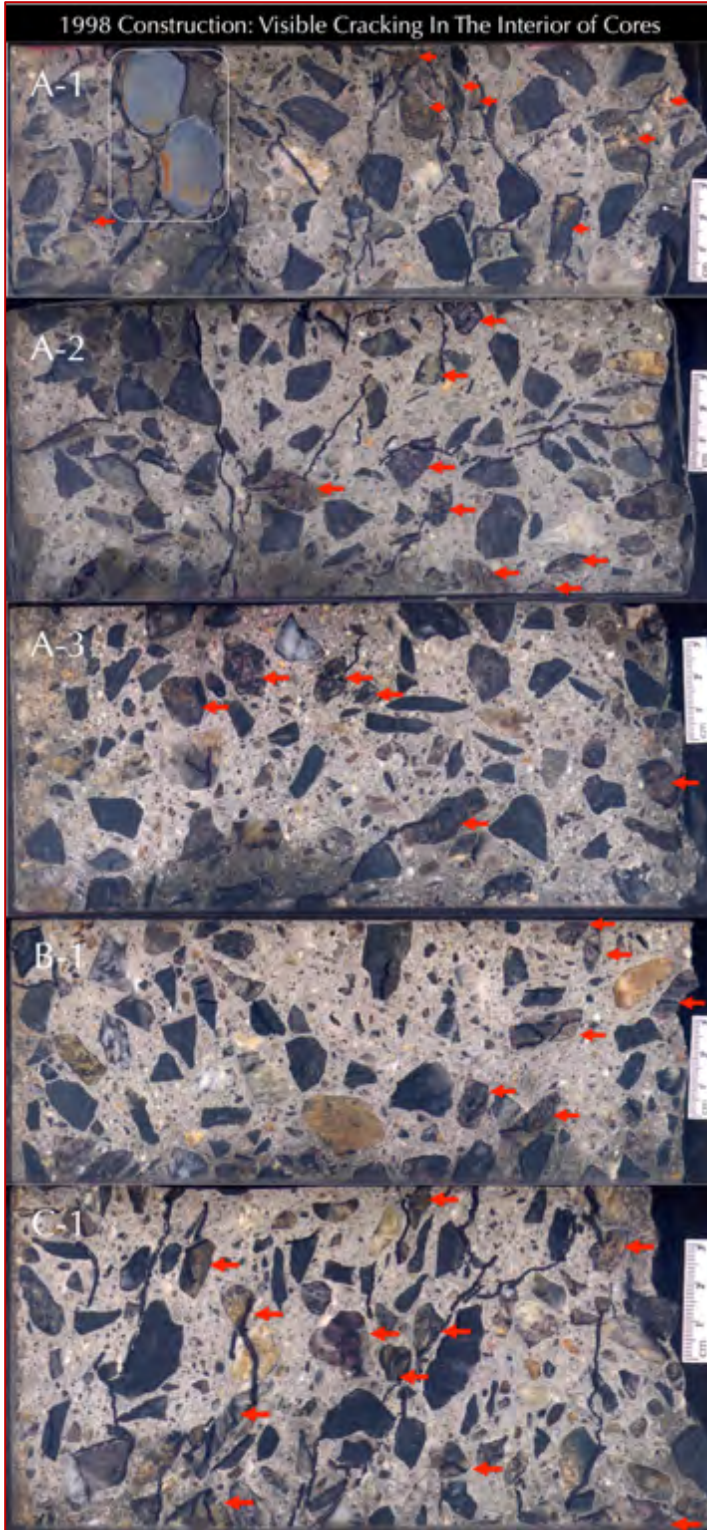


Figure 13: Lapped cross sections of Cores A-1 to A-3, B-1, and C-1 showing:

- (a) Extensive cracking (marked in black marker pen) all throughout the recovered depths of the Cores A-1, A-2, and C-1;
- (b) Some localized cracking within some unsound crushed stone aggregates in Cores A-3, and B-1 many of which are highlighted by black lines;
- (c) Potentially unsound pyrrhotite-bearing crushed stone particles many of which are marked with red arrows;
- (d) Good grading and well-distribution of the crushed stone coarse aggregate particles;
- (e) Light beige discoloration of concrete at the exposed surface ends due to atmospheric carbonation that are measured to be less than 5 to 15 mm; and,
- (f) Overall dense, well-consolidated nature of concrete in the foundation despite visible cracking.
- (g) See Appendix B for details.

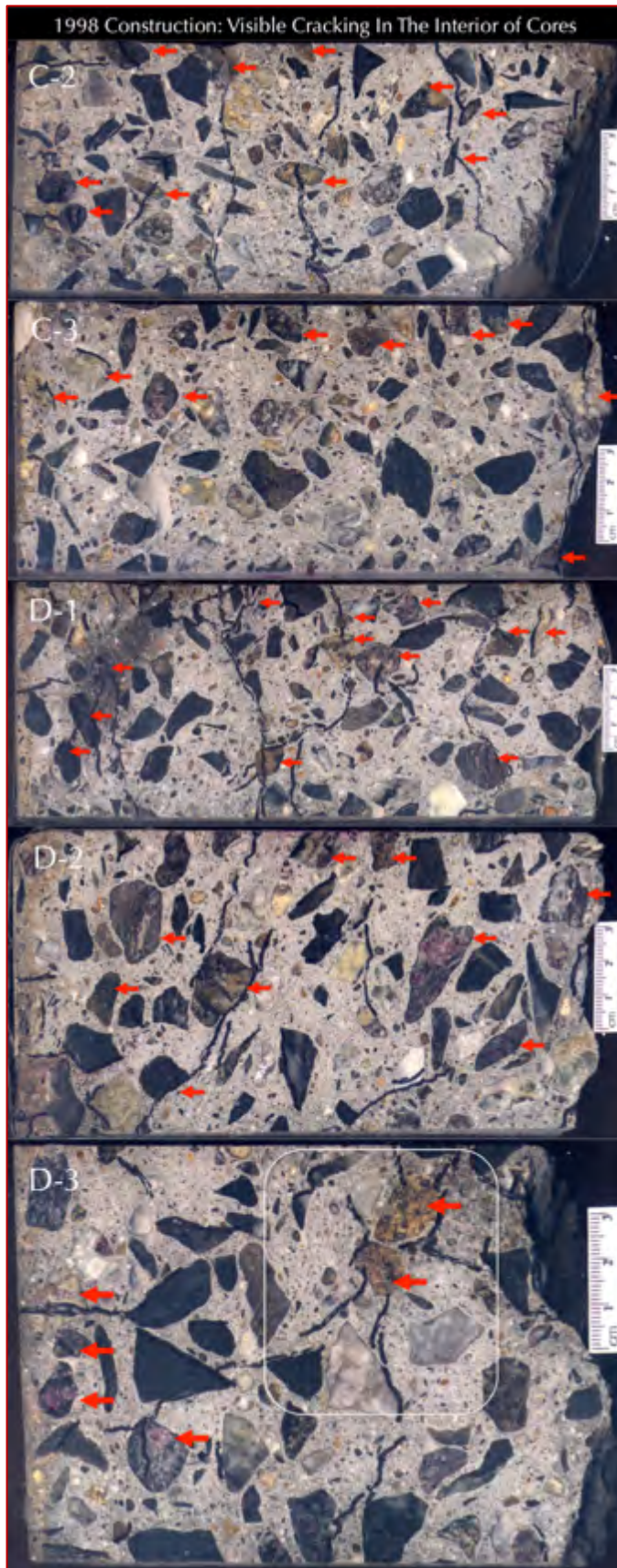


Figure 14: Lapped cross sections of Cores C-2, C-3, D-1 to D-3 showing:

- (a) Extensive cracking (marked in black marker pen) all throughout the depth of the Cores C-2, D-1, D-2, and D-3;
- (b) Some localized cracking within some unsound crushed stone aggregates in Core C-3 many of which are highlighted by black lines;
- (c) Potentially unsound pyrrhotite-bearing crushed stone particles many of which are marked with red arrows;
- (d) Radial and concentric cracking around two unsound crushed stone coarse aggregates in Core D-3 (boxed);
- (e) Good grading and well-distribution of the crushed stone coarse aggregate particles;
- (f) Light beige discoloration of concrete at the exposed surface ends due to atmospheric carbonation that are measured to be less than 5 to 15 mm; and,
- (g) Overall dense, well-consolidated nature of concrete in the foundation despite visible cracking.
- (h) See Appendix B for details.

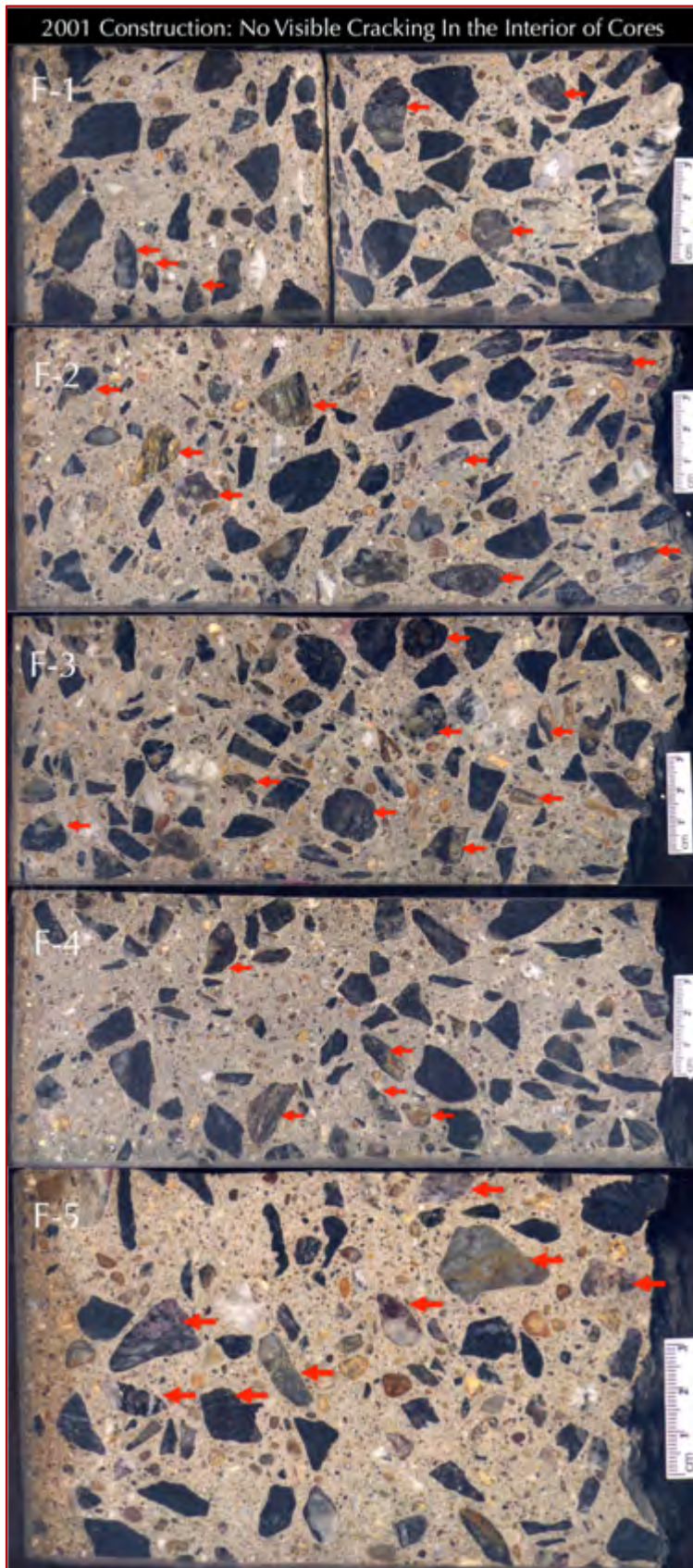


Figure 15: Lapped cross sections of Cores F-1 to F-5 showing:

- (a) Lack of visible cracking except some localized cracking within some unsound crushed stone aggregates;
- (b) Potentially unsound pyrrhotite-bearing crushed stone particles many of which are marked with red arrows that are compositionally similar to unsound stones used in 1998 construction;
- (c) Good grading and well-distribution of the crushed stone coarse aggregate particles;
- (d) Thin dark gray cementitious protective skim coat on the exposed ends of the cores that were well-bonded to the main concrete body;
- (e) Light beige discoloration of concrete at the exposed surface ends due to atmospheric carbonation that are measured to be less than 5 to 15 mm; and,
- (f) Overall dense, well-consolidated nature of concrete in the foundation.
- (g) See Appendix B for details.

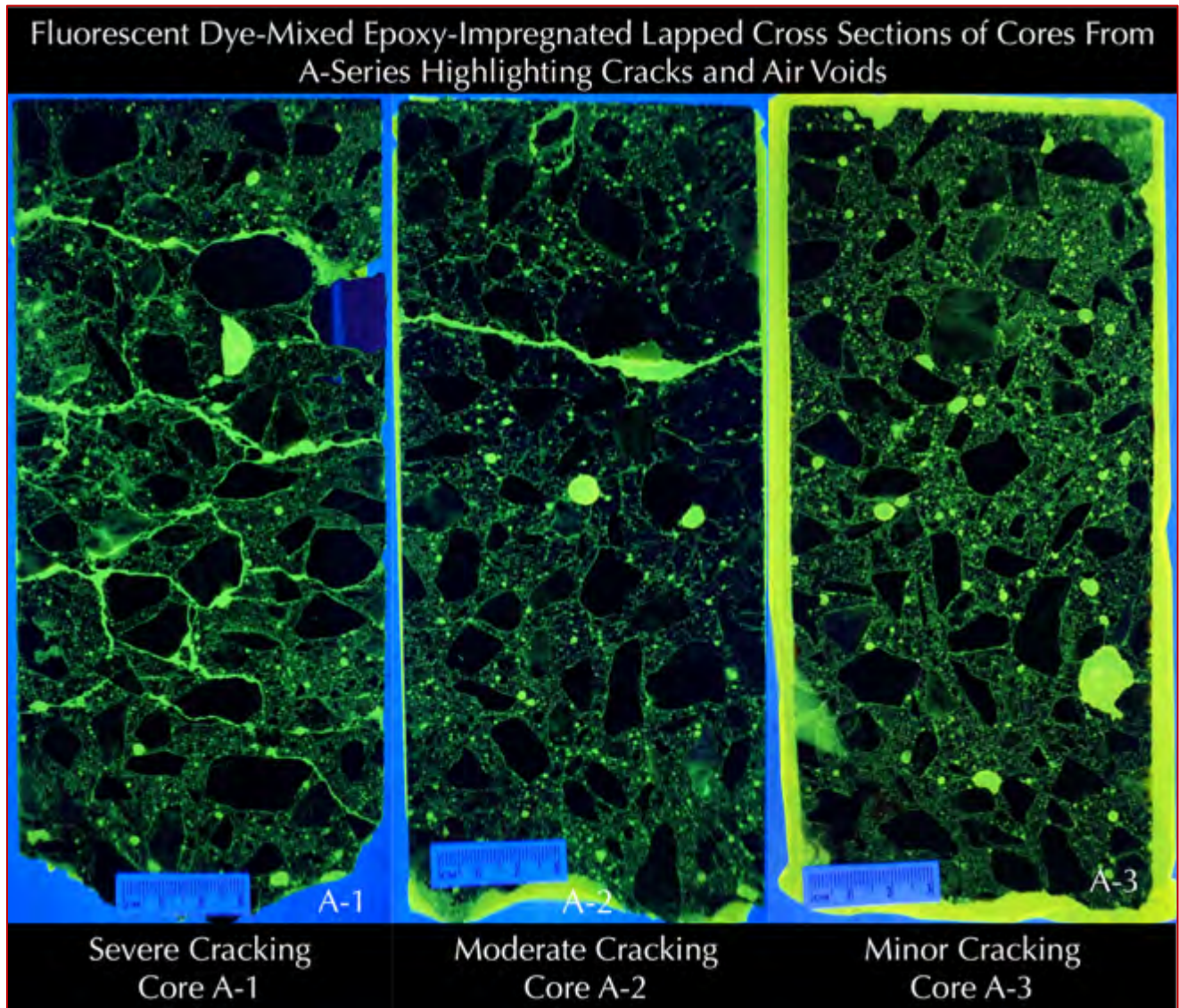


Figure 16: Fluorescent dye-mixed epoxy-impregnated lapped cross sections of three cores from A-series showing extensive cracking in Core A-1 where cracks are highlighted by the fluorescent dye (when viewed in ultraviolet light), moderate cracking in Core A-2, and minor cracking in Core A-3. See Appendix B for details.

Figure 16 shows lapped cross sections of cores from A-series that were impregnated with fluorescent dye-mixed low viscosity epoxy to highlight cracks and void spaces against everything else in dark when viewed in an ultraviolet light. Notice variations in degrees of cracking from A-1 through A-2 to A-3 (see Appendix B for other cores).

Appendix B (B1 to B28) shows photographs of lapped cross sections of 15 cores, traces of cracks on lapped cross sections, depths of carbonation of concrete after treatment of lapped cross sections with phenolphthalein alcoholic solutions, as well as fluorescent dye-mixed epoxy-impregnated lapped cross sections.

PHOTOMICROGRAPHS OF LAPPED CROSS SECTIONS

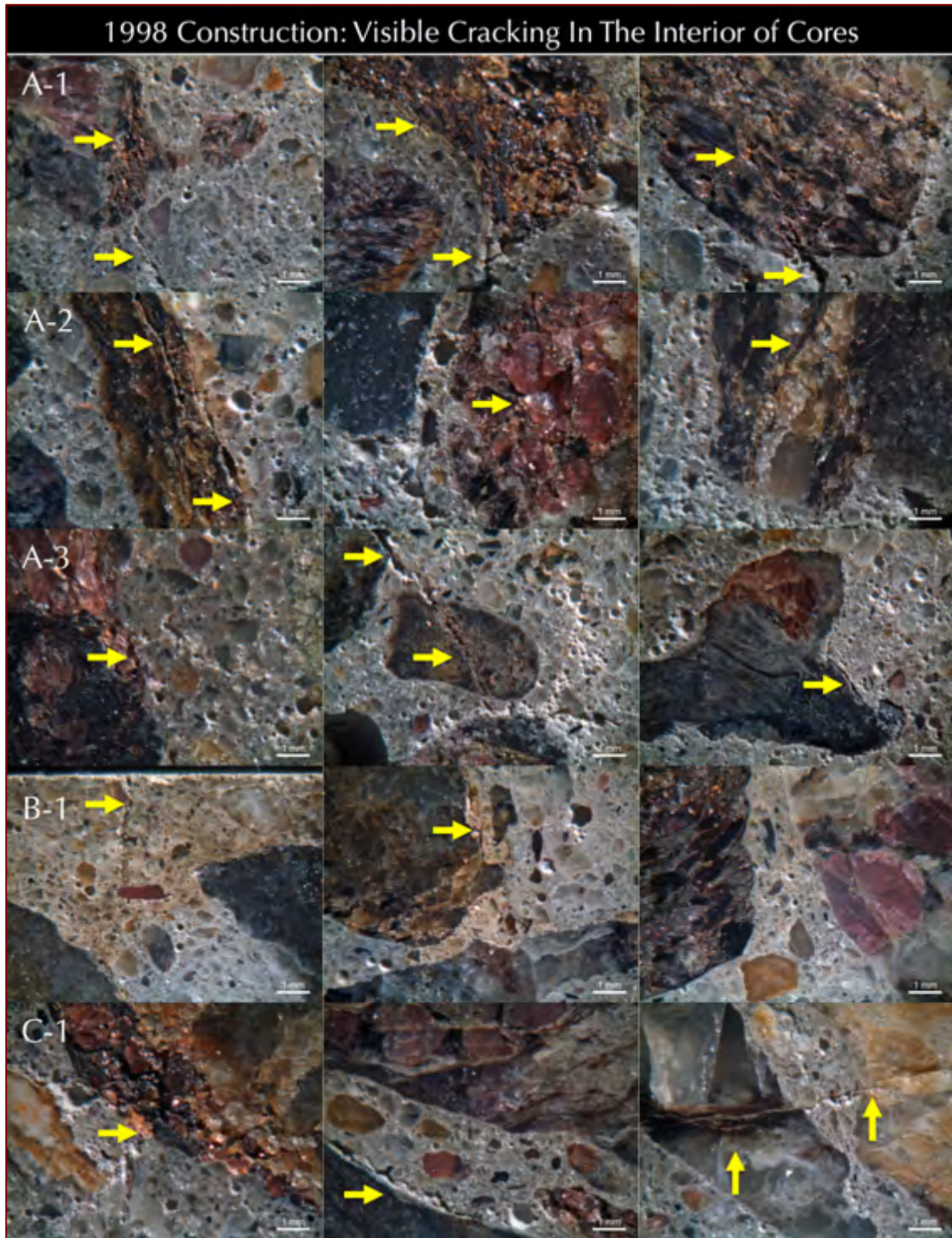


Figure 17: Photomicrographs of lapped cross sections of Cores A-1 to A-3, B-1, and C-1 showing: (a) air-entrained natures of concretes in all cores having many fine, discrete, spherical and near-spherical air voids; (b) crushed stone coarse aggregates consisting of light brown, reddish-brown colored garnetiferous quartz-feldspar-biotite gneiss (many showing red almandine garnet) and darker gray crushed metamorphosed gabbro; and (c) cracking in many unsound aggregates. See Appendix C for details.

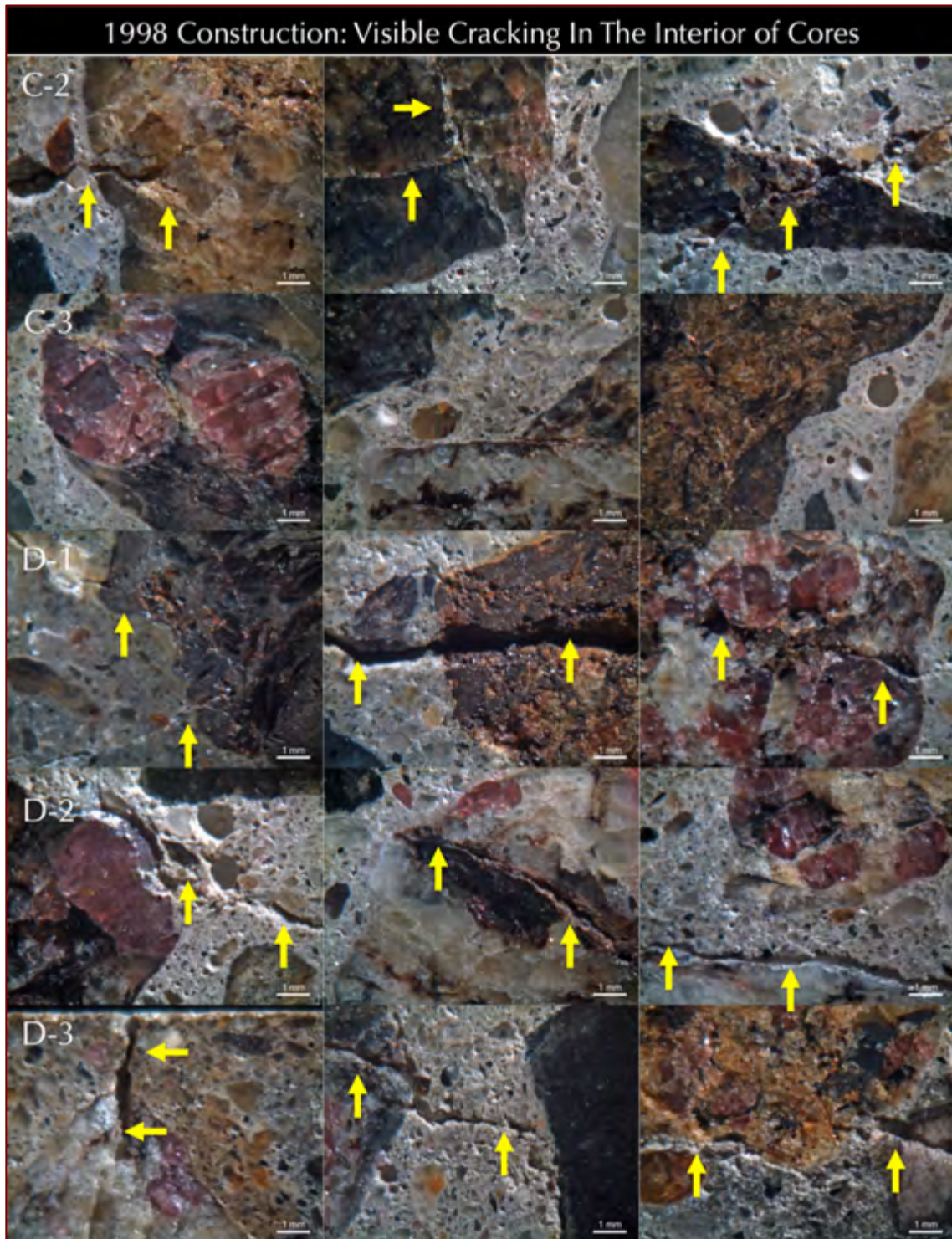


Figure 18: Photomicrographs of lapped cross sections of Cores C-2, C-3, D-1 to D-3 showing: (a) air-entrained natures of concretes in all cores having many fine, discrete, spherical and near-spherical air voids; (b) crushed stone coarse aggregates consisting of light brown, reddish-brown colored garnetiferous quartz-feldspar-biotite gneiss (many showing red almandine garnet) and darker gray crushed metamorphosed gabbro; and (c) cracking in many unsound aggregates. See Appendix C for details.

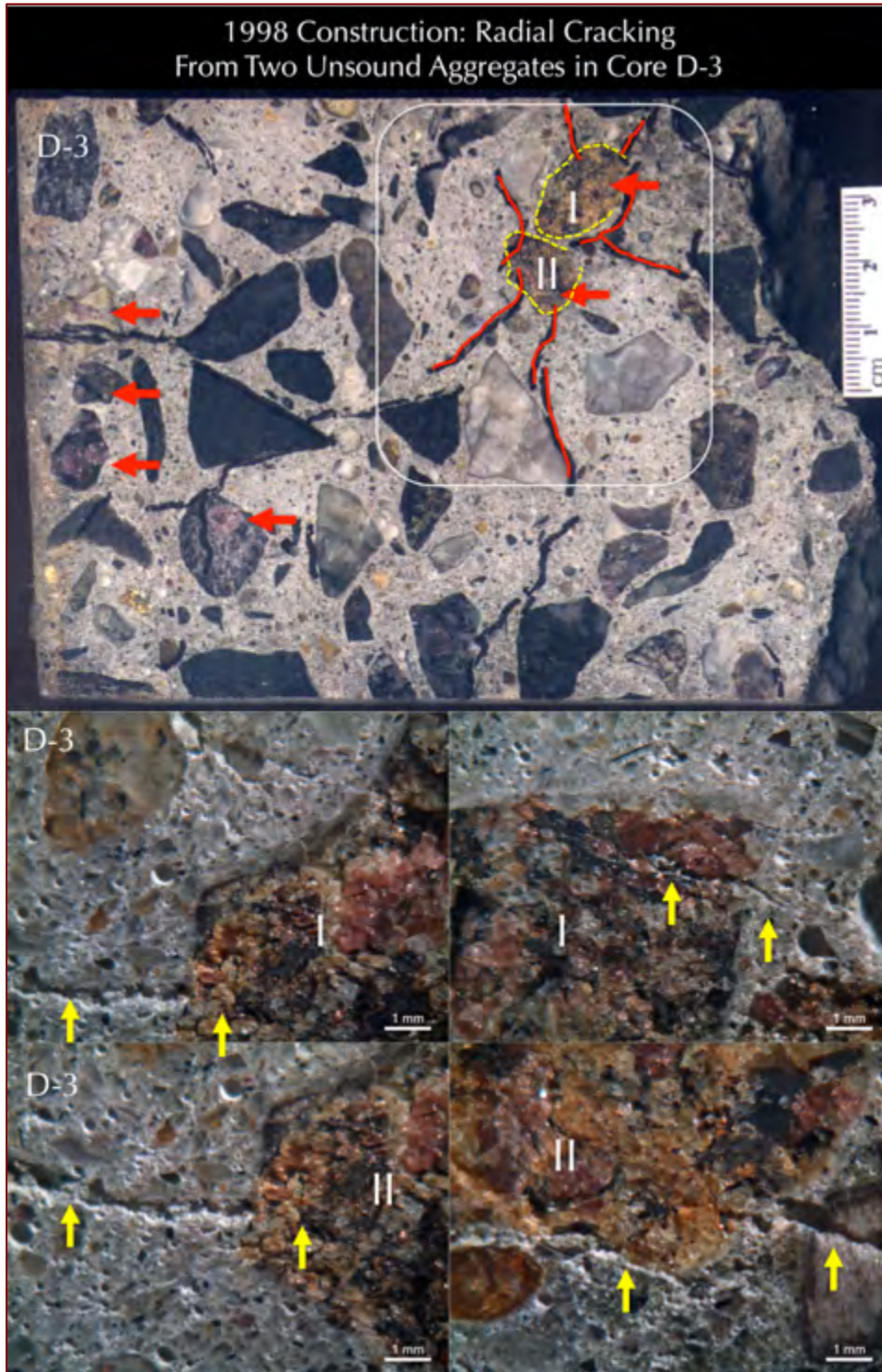


Figure 19: Photomicrographs of lapped cross section of Core D-3 having two unsound aggregate particles that have created classic radial and concentric cracks from expansions due to oxidation of pyrrhotite. Bottom four photomicrographs show these two particles and associated cracks. See Appendix C for details.

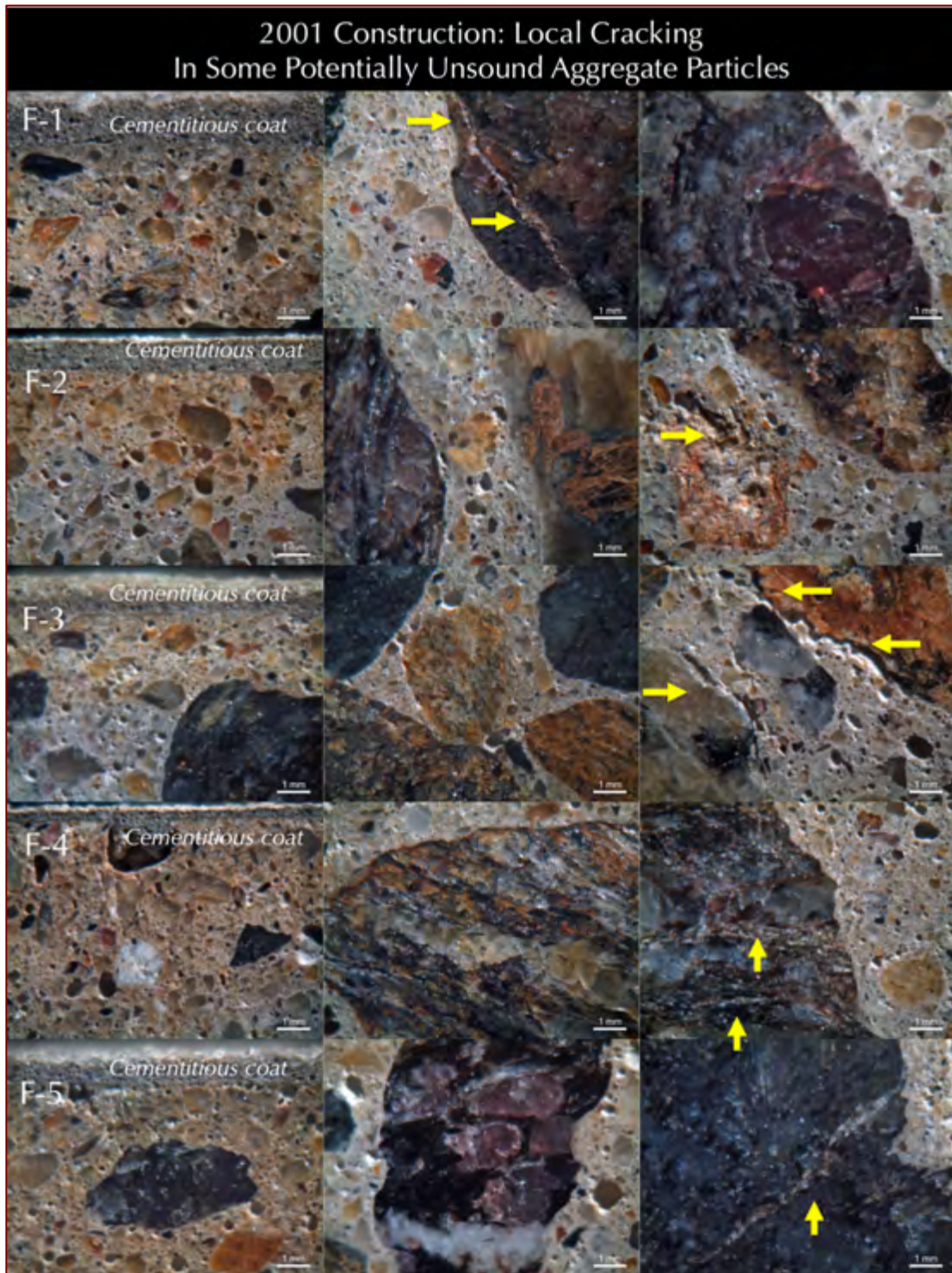


Figure 20: Photomicrographs of lapped cross sections of Cores F-1 to F-5 showing: (a) air-entrained natures of concretes in all cores having many fine, discrete, spherical and near-spherical air voids; (b) crushed stone coarse aggregates consisting of light brown, reddish-brown colored garnetiferous quartz-feldspar-biotite gneiss (many showing red almandine garnet) and darker gray crushed metamorphosed gabbro; and (c) cracking in many unsound aggregates. See Appendix C for details.

PHOTOMICROGRAPHS OF LAPPED CROSS SECTIONS SHOWING IRON SULFIDE MINERALS

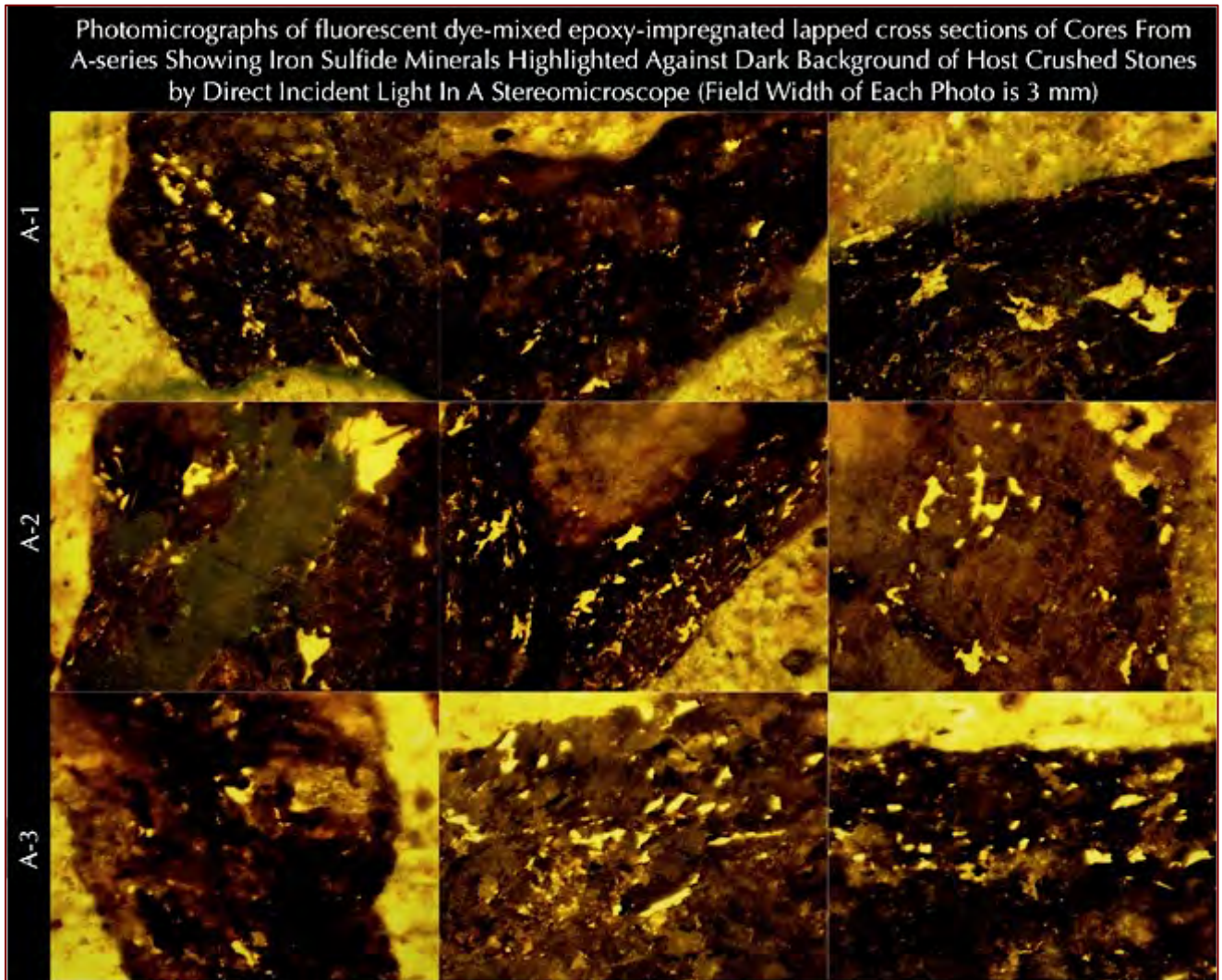


Figure 21: Photomicrographs of fluorescent dye-mixed lapped cross sections of Cores A-1 to A-3 showing fine, disseminated iron sulfide minerals (pyrrhotite) and their oxidation products that are distinguished by their high reflectivity and metallic luster against the host crushed gneiss aggregate particles (that appear dark) when viewed in a vertical incident-light source of a stereomicroscope. Fine striations in many pyrrhotite grains are due to oxidation to ferrihydrites.

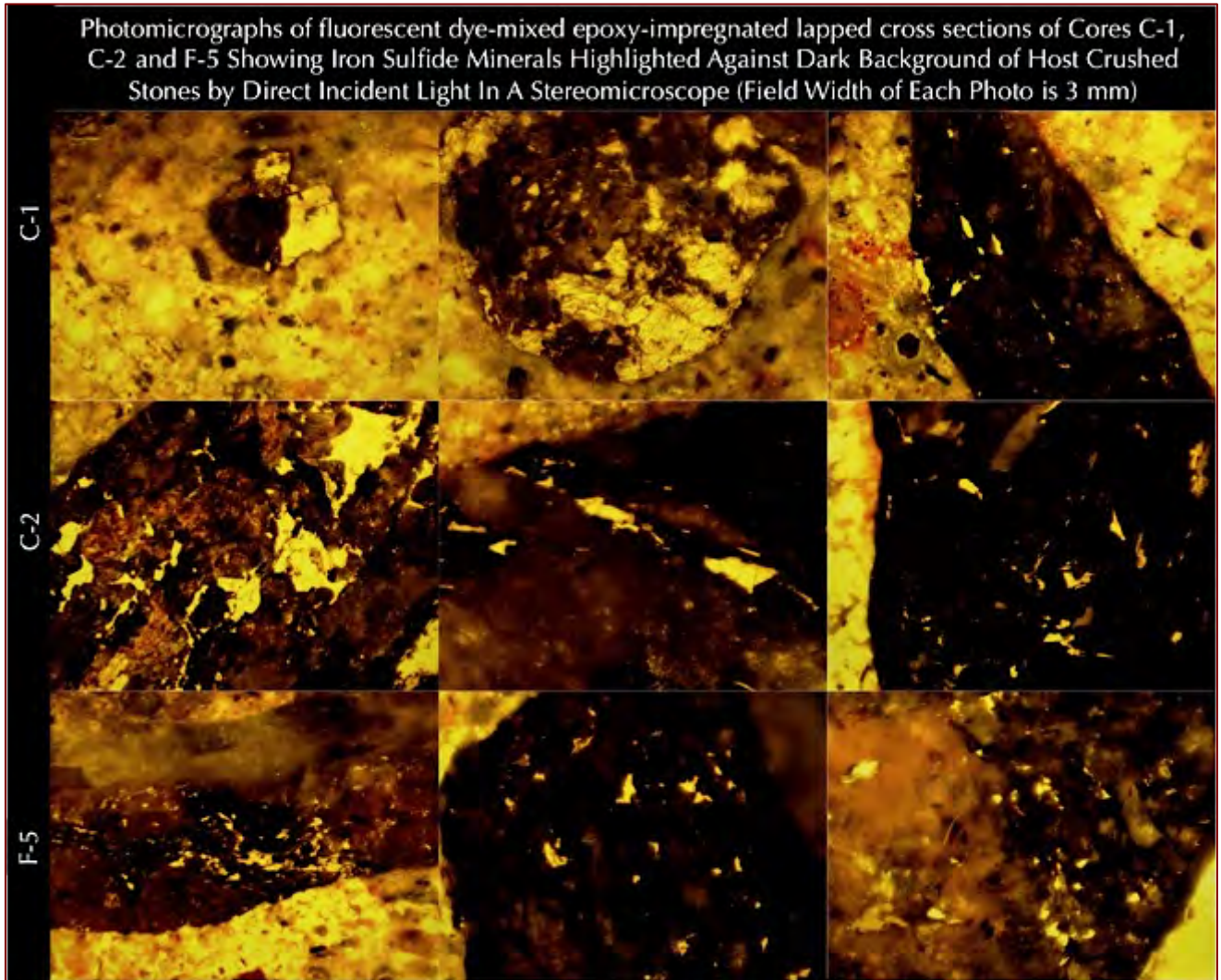


Figure 22: Photomicrographs of fluorescent dye-mixed lapped cross sections of Cores C-1, C-2, and F-5 showing fine, disseminated iron sulfide minerals (pyrrhotite) and their oxidation products that are distinguished by their high reflectivity and metallic luster against the host crushed gneiss aggregate particles (that appear dark) when viewed in a vertical incident-light source of a stereomicroscope. Fine striations in many pyrrhotite grains are due to oxidation to ferrihydrites.

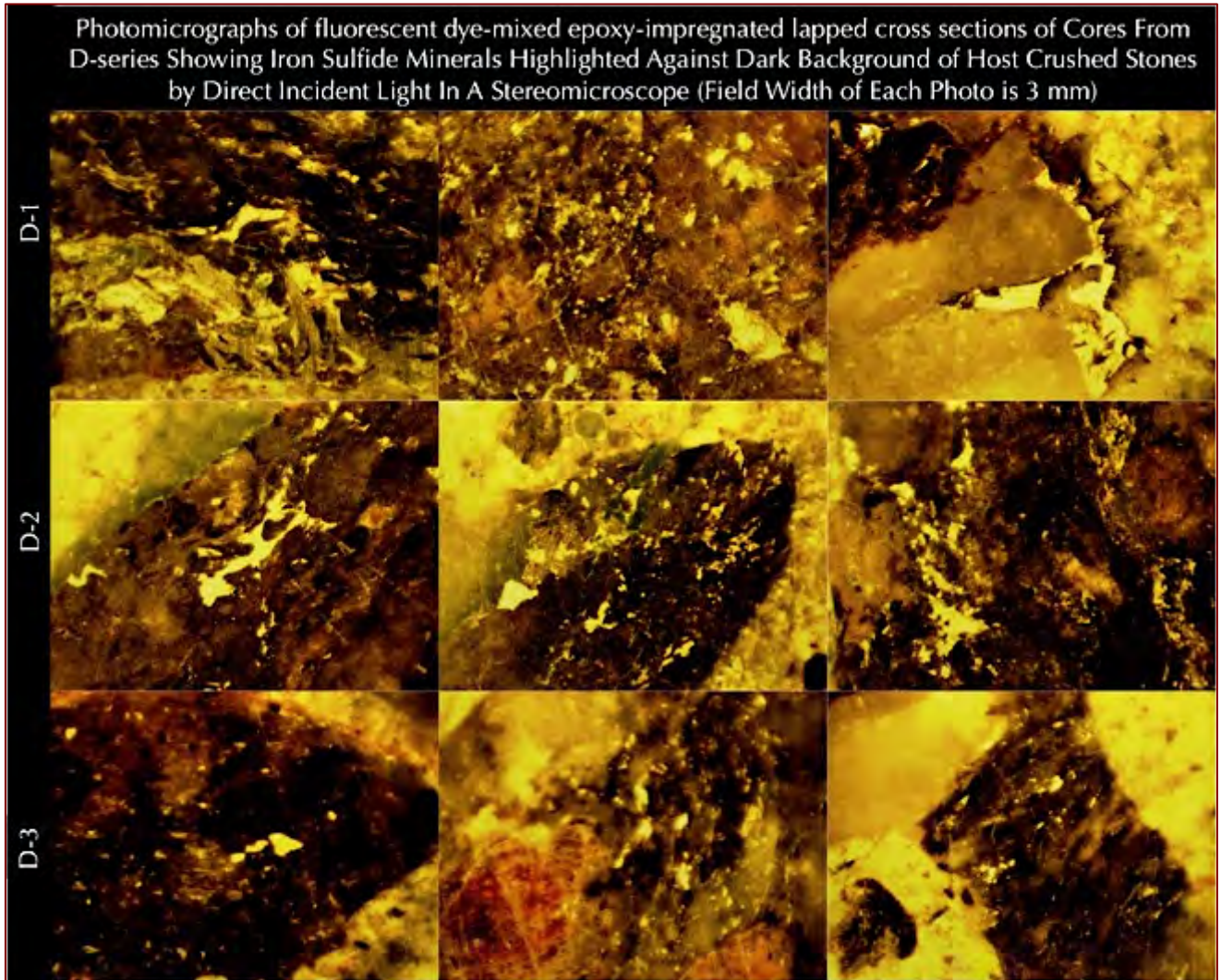


Figure 23: Photomicrographs of fluorescent dye-mixed lapped cross sections of Cores D-1 to D-3 showing fine, disseminated iron sulfide minerals (pyrrhotite) and their oxidation products that are distinguished by their high reflectivity and metallic luster against the host crushed gneiss aggregate particles (that appear dark) when viewed in a vertical incident-light source of a stereomicroscope. Fine striations in many pyrrhotite grains are due to oxidation to ferrihydrites.

THIN SECTIONS

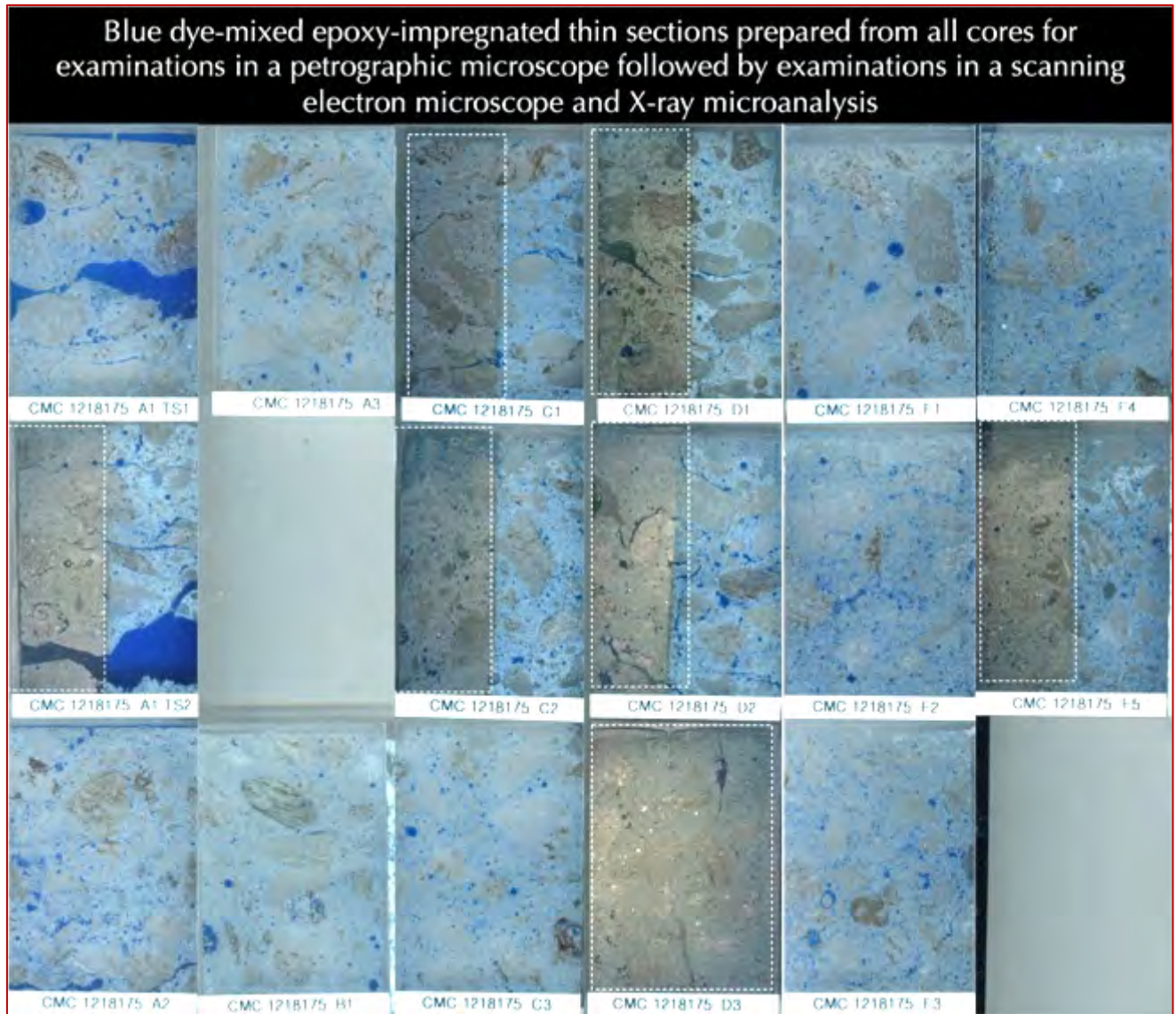


Figure 24: Blue dye-mixed epoxy-impregnated large area (50 mm × 75 mm) thin sections prepared for all cores for examinations in optical and scanning electron microscopes. Portions of thin sections after optical microscopical examinations were coated with thin gold-palladium film (boxed with dashed white lines) for further SEM-EDS studies. See Appendix D for details.

Figure 24 shows blue dye-mixed epoxy-impregnated thin sections of all fifteen cores prepared from the top 3 inches of their exposed surfaces (Core A-1 has two thin sections made from the exposed surface end and interior to cover the full-depth cracking seen). Blue dye, like fluorescent dye used in lapped cross sections, highlights all cracks, voids, and porous areas in paste. After optical microscopical examinations, portions of thin sections were coated with a thin conductive gold-palladium film to be used for subsequent SEM-EDS studies (shown in white dashed boxes).

PHOTOMICROGRAPHS OF THIN SECTIONS

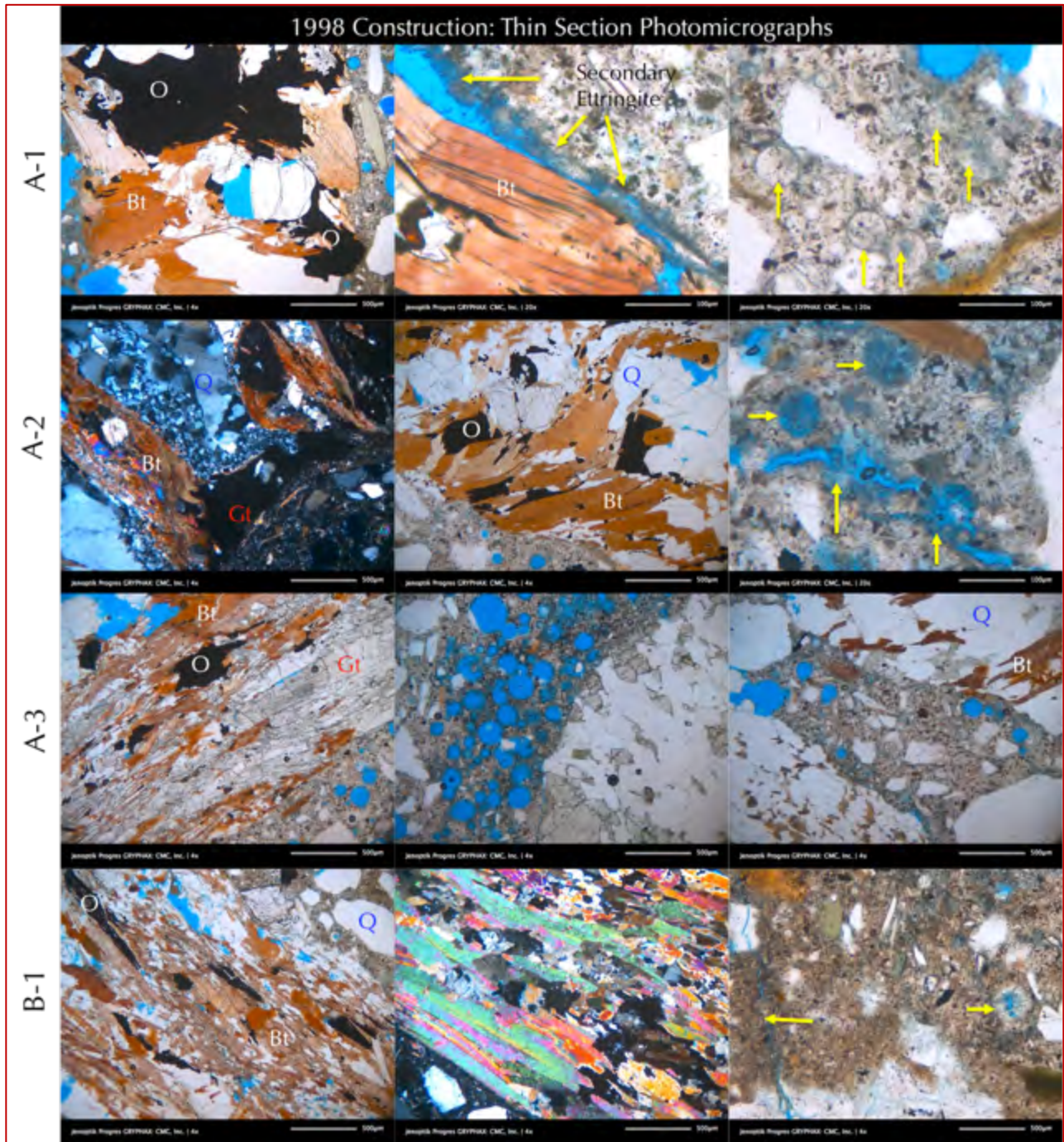


Figure 25: Thin section photomicrographs of Cores A-1 to A-3 and B-1 showing: (a) garnetiferous quartz (Q)-feldspar (albite, Pl)-biotite (Bt) gneiss coarse aggregate having alternate banding of light-colored quartzo-feldspathic and dark brown colored biotite bands defining the gneissose texture along with disseminated dark opaque grains (O) of pyrrhotite and iron titanium oxide; (b) dense Portland cement paste; and (c) secondary ettringite deposits in air voids, cracks, and porous areas of paste that are the taletell microstructural features of concretes affected by pyrrhotite oxidation, where sulfates released from oxidation react with aluminat phases of cement hydration products and form ettringite, which, upon continuous moisture exposures eventually precipitates in open spaces. See Appendix D for details.

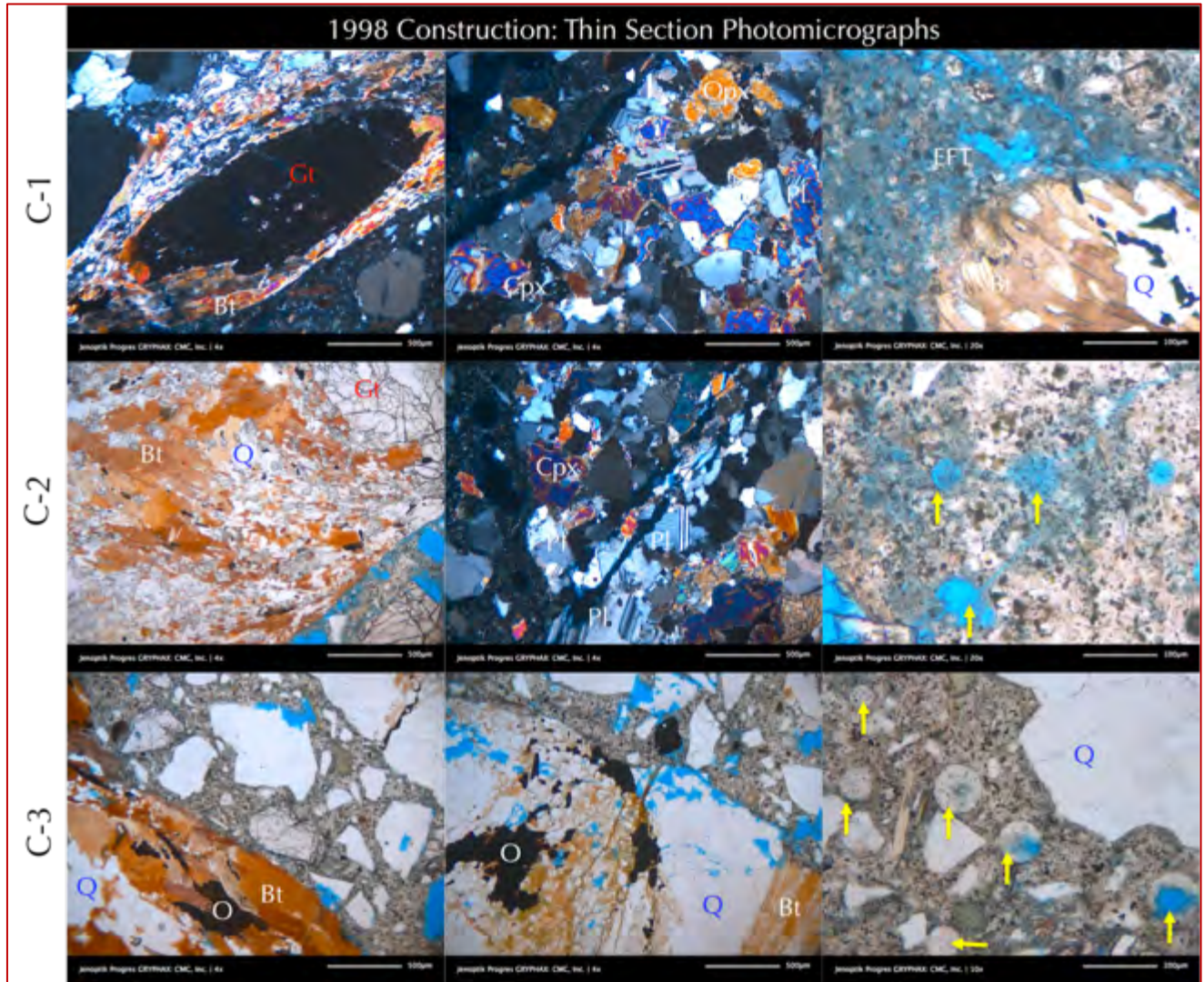


Figure 26: Thin section photomicrographs of Cores C-1 to C-3 showing: (a) garnetiferous quartz (Q)-feldspar (albite, Pl)-biotite (Bt) gneiss coarse aggregate having alternate banding of light-colored quartzo-feldspathic and dark brown colored biotite bands defining the gneissose texture along with disseminated dark opaque grains (O) of pyrrhotite and iron titanium oxide, and pyroxene granulite (metamorphosed gabbro) aggregate having enstatite (Opx), augite (Cpx), and plagioclase (oligoclase, Pl); (b) dense Portland cement paste; and (c) secondary ettringite deposits in air voids, cracks, and porous areas of paste that are the taletell microstructural features of concretes affected by pyrrhotite oxidation, where sulfates released from oxidation react with aluminates phases of cement hydration products and form ettringite, which, upon continuous moisture exposures eventually precipitates in open spaces. See Appendix D for details.

The light brown crushed stone particles seen in the lapped cross sections are found to be garnetiferous quartz-feldspar-biotite gneiss showing classic gneissose texture characterized by alternating bands of quartzo-feldspathic and micaceous layers with occasional garnet porphyroblasts that sometimes enclose poikilitic inclusions of quartz and other minerals. Biotite is the most common mica found with some muscovite and chloritic alterations.

The other darker gray crushed stone is found to be a metamorphosed gabbro, showing pyroxene granulite texture and composition consisting of equigranular texture of pyroxenes (mostly clinopyroxene, augite and a few orthopyroxene, enstatite) and plagioclase (oligoclase).

The dark disseminated opaque grains are found to be both iron sulfide minerals (pyrrhotite) and some iron titanium oxides (ilmenite), which are present in both types of crushed stones.

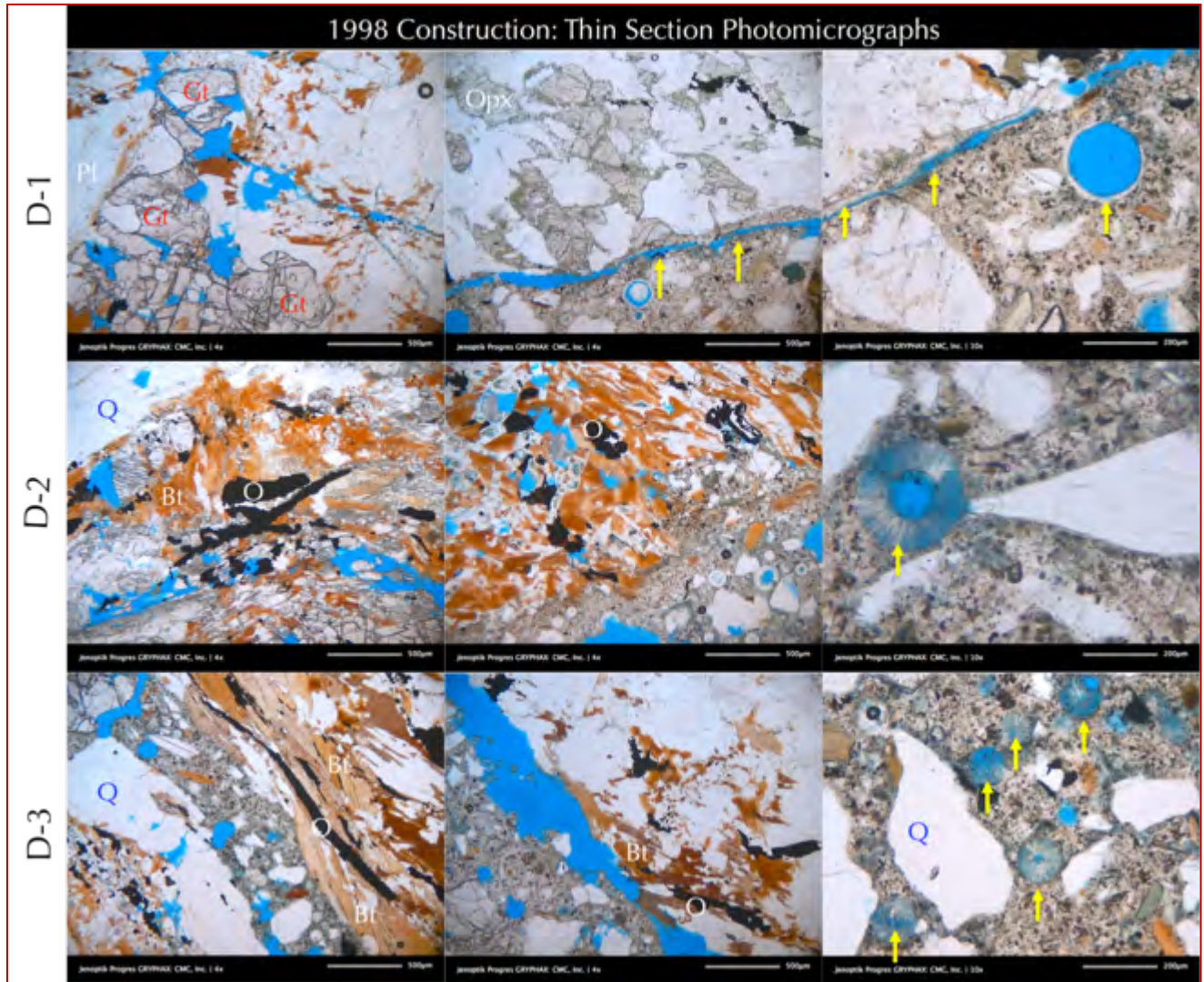


Figure 27: Thin section photomicrographs of Cores D-1 to D-3 showing: (a) garnetiferous quartz (Q)-feldspar (albite, Pl)-biotite (Bt) gneiss coarse aggregate having alternate banding of light-colored quartzo-feldspathic and dark brown colored biotite bands defining the gneissose texture along with disseminated dark opaque grains (O) of pyrrhotite and iron titanium oxide, and pyroxene granulite (metamorphosed gabbro) aggregate having enstatite (Opx), augite (Cpx), and plagioclase (oligoclase, Pl); (b) dense Portland cement paste; and (c) secondary ettringite deposits in air voids, cracks, and porous areas of paste that are the taletell microstructural features of concretes affected by pyrrhotite oxidation, where sulfates released from oxidation react with aluminates phases of cement hydration products and form ettringite, which, upon continuous moisture exposures eventually precipitates in open spaces. See Appendix D for details.

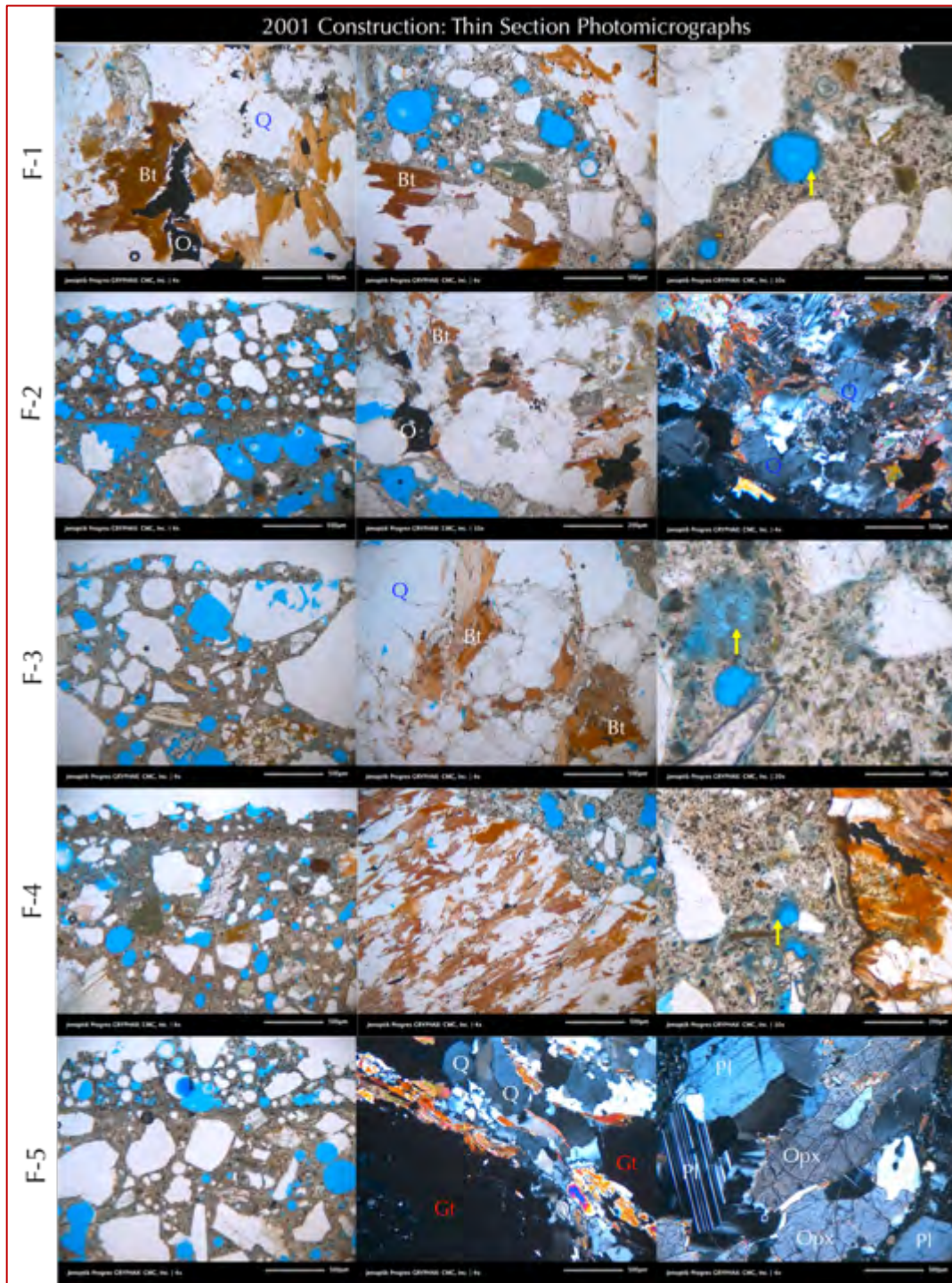


Figure 28: Thin section photomicrographs of Cores F-1 to F-5 showing: (a) garnetiferous quartz (Q)-feldspar (albite, Pl)-biotite (Bt) gneiss coarse aggregate having alternate banding of light-colored quartzo-feldspathic and dark brown colored biotite bands defining the gneissose texture along with disseminated dark opaque grains (O) of pyrrhotite and iron titanium oxide, and pyroxene granulite (metamorphosed gabbro) aggregate having enstatite (OpX), augite (Cpx), and plagioclase (oligocene, Pl); (b) dense Portland cement paste; and (c) secondary ettringite deposits in air voids, cracks, and porous areas of paste that are the taletell microstructural features of concretes affected by pyrrhotite oxidation, where sulfates released from oxidation react with aluminate phases of cement hydration products and form ettringite, which, upon continuous moisture exposures eventually precipitates in open spaces. See Appendix D for details.



### COARSE AGGREGATES

Coarse aggregates are compositionally similar across all fifteen cores from 1998 and 2001 constructions, indicating the same source of crushed stones, which was further confirmed to be provided by the same supplier (JJ Morris). All cores contain metamorphic crushed stone coarse aggregates, which is a mixture of a predominant dark gray garnetiferous quartzo-feldspathic and micaceous gneiss (having quartz, albite feldspar, biotite mica, and almandine garnet) with a subordinate amount of metamorphosed gabbro (having ortho and/or clino-pyroxenes, oligoclase plagioclase, and minor biotite), and, a subordinate light brown garnetiferous quartz-feldspar-mica gneiss (having a higher quartz content than the dark gray gneiss) all having nominal maximum sizes of 3/4 in. (19 mm) showing the typical gneissose texture of alternating bands of quartz-albitic feldspar and micaceous (mostly biotite and less muscovite) minerals that often contain almandine garnet poikiloblast, and equigranular granoblastic texture for metamorphosed gabbro. All coarse aggregates show the presence of fine, isolated anhedral/subhedral, or disseminated (often elongated along the gneissosity planes) opaque grains that are found to be both iron sulfide mineral pyrrhotite, and iron-titanium oxide (rutile, ilmenite). Coarse aggregate particles are angular, dense, hard, and light to medium to dark gray, gneissose-textured (or granoblastic textured for minor metamorphosed gabbro), equidimensional to elongated, variably altered, uncoated, and variably cracked. Coarse aggregate particles are well-graded and well-distributed. There is no evidence of alkali-aggregate reactions of coarse aggregate particles in the concretes. However, particles have been unsound during their service in the concretes due to observed cracking and microcracking in many particles often extending into paste that are determined to be due to oxidation of pyrrhotite minerals in these particles.

### FINE AGGREGATES

Fine aggregates are natural siliceous sands having nominal maximum sizes of 3/8 in. (9.5 mm). Particles contain major amounts of quartz and quartzite, and subordinate amounts of feldspar, mica, ferruginous rock, and mafic minerals. Particles are variably colored, subangular to subrounded, dense, hard, equidimensional to elongated, unaltered, uncoated, and uncracked. Fine aggregate particles are well-graded and well-distributed. There is no evidence of alkali-aggregate reaction of fine aggregate. Particles are sound during their service in the concretes.

| Properties and Compositions of Aggregates | All fifteen cores from 1998 and 2001 constructions  |
|---|---|
|   | Coarse Aggregates   |
| Types                                     | Metamorphic Crushed Stones  |
| Nominal maximum size (in.)                | 3/4 in. (19 mm)   |
| Rock Types                                | Mixture of a predominant dark gray garnetiferous quartzo-feldspathic and micaceous gneiss (having quartz, albite feldspar, biotite mica, and almandine garnet) with a subordinate amount of metamorphosed gabbro (having ortho and/or clino-pyroxenes, oligoclase plagioclase, and minor biotite), and, a subordinate light brown garnetiferous quartz-feldspar-mica gneiss (having a |



| Properties and Compositions of Aggregates                 | All fifteen cores from 1998 and 2001 constructions   |
|---|--|
|   | higher quartz content than the dark gray gneiss) all having nominal maximum sizes of 3/4 in. (19 mm) showing the typical gneissose texture of alternating bands of quartz-albitic feldspar and micaceous (mostly biotite and less muscovite) minerals that often contain almandine garnet poikiloblast, and equigranular granoblastic texture for metamorphosed gabbro |
| Angularity, Density, Hardness, Color, Texture, Sphericity | Angular, dense, hard, and light to medium to dark gray, gneissose-textured (or granoblastic textured for minor metamorphosed gabbro), equidimensional to elongated   |
| Cracking, Alteration, Coating                             | Variably altered, Uncoated, and variably cracked   |
| Grading & Distribution                                    | Well-graded and Well-distributed   |
| Soundness   | Many particles show unsoundness as radial and concentric cracking around the particles or from the particles to neighboring paste  |
| Alkali-Aggregate Reactivity                               | None   |
| <b>Fine Aggregates</b>                                    |  |
| Types   | Natural siliceous sands  |
| Nominal maximum size (in.)                                | 3/8 in. (9.5 mm)   |
| Rock Types  | Major amounts of quartz and quartzite, and subordinate amounts of feldspar, mica, ferruginous rock, and mafic minerals   |
| Cracking, Alteration, Coating                             | Variably colored, subangular to subrounded, dense, hard, equidimensional to elongated  |
| Grading & Distribution                                    | Well-graded and Well-distributed   |
| Soundness   | Sound  |
| Alkali-Aggregate Reactivity                               | None   |

Table 3: Properties of coarse and fine aggregates of concretes.

### PASTE

Properties and composition of hardened cement pastes are summarized in Table 4. Pastes at the near-surface carbonated zones are beige-toned, but interior bodies are medium gray, dense and hard; freshly fractured surfaces have subvitreous lusters and subconchoidal textures. Residual and relict Portland cement particles are present and estimated to constitute 8 to 10 percent of the paste volumes. Hydration of Portland cement is normal. The textural and compositional features of the pastes are indicative of cement contents of 6 to 6<sup>1</sup>/<sub>2</sub> bags per cubic yard that are similar in all cores, and estimated water-cement ratios (w/c) of 0.45 to 0.50. Secondary ettringite deposits found in all cores lining or filling air voids, cracks and often found in porous areas of paste (latter for C and D series cores from 1998 construction). Bonds between the coarse and fine aggregate particles and paste are tight to moderately tight to weak. There are evidence of microcracking due to deleterious reactions. The overall quality and condition of the concretes in the 1998 cores, especially for A-1, C and D series are judged to be poor and unsound with evidence of chemical deterioration due to internal sulfate attack. The interior concretes are dense and consolidated but cracked variably in micro to macro scales due to pyrrhotite oxidation and internal sulfate attacks.



| Properties and Compositions of Paste   | All fifteen cores from 1998 and 2001 constructions  |
|--|---|
| Color, Hardness, Porosity, Luster  | Gray, dense and hard, Subtranslucent vitreous   |
| Residual Portland Cement Particles   | Normal, 8 to 10 percent by paste volume   |
| Calcium hydroxide from cement hydration  | Normal, 10 to 14 percent by paste volume  |
| Pozzolans, Slag, etc.  | None  |
| Water-cement ratio (w/c), estimated  | 0.45 to 0.50  |
| Cementitious materials contents, estimated (equivalent to bags of cement per cubic yard) | 6 to 6 <sup>1</sup> / <sub>2</sub>  |
| Secondary Deposits   | Secondary ettringite deposits found in all cores lining or filling air voids, cracks and often found in porous areas of paste |
| Depth of Carbonation, mm   | Less than 5 to 25 mm from inside surface of wall, and 20 to 30 mm from outside surface (see Appendix B)                       |
| Microcracking  | Present   |
| Aggregate-paste Bond   | Tight to moderately tight to weak (gaps)  |
| Bleeding, Tempering  | None  |
| Chemical deterioration   | Internal sulfate attack due to oxidation of pyrrhotite in crushed gneiss coarse aggregate during service                      |

Table 4: Compositions and properties of pastes.

**AIR**

Air occurs as: (a) numerous fine, discrete, spherical and near-spherical voids having sizes of 1 mm; and (b) a few coarse near-spherical and irregularly shaped voids that are characteristic of entrapped air. Concretes in all fifteen cores are air-entrained having estimated air contents provide below:

| Core ID    | Estimated Air Content | Air Entrainment | Air-Void Systems   |
|------------|-----------------------|-----------------|--|
| A-1        | 5 to 6 percent        | Air-entrained   | Moderate air-void system, coarse voids, lower than recommended specific surface and higher than recommended spacing factor |
| A-2        | 7 to 8 percent        | Air-entrained   | Very good air-void system i.e. within the recommended specific surface and spacing factor                                  |
| A-3        | 8 to 9 percent        | Air-entrained   | Very good air-void system  |
| B-1        | 3 to 4 percent        | Air-entrained   | Marginal air-void system, coarse voids   |
| C-1        | 7 to 8 percent        | Air-entrained   | Very good air-void system  |
| C-2        | 7 to 8 percent        | Air-entrained   | Very good air-void system  |
| C-3        | 3 to 4 percent        | Air-entrained   | Marginal air-void system, coarse voids   |
| D-1        | 4 to 5 percent        | Air-entrained   | Moderate to good air-void system, nonuniform distribution  |
| D-2        | 5 to 6 percent        | Air-entrained   | Moderate to good air-void system, nonuniform distribution  |
| D-3        | 6 to 7 percent        | Air-entrained   | Moderate to good air-void system, nonuniform distribution  |
| F-1 to F-5 | 6 to 7 percent        | Air-entrained   | Good air-void system   |

Table 5: Air contents and air-void systems of concretes.



## SEM-EDS STUDIES

Figures 29 to 32 and more detailed figures in Appendix E provide SEM-EDS analyses of concrete to investigate the following:

1. Composition of iron sulfide minerals in aggregates – from X-ray elemental map, backscatter electron image, secondary electron image, and energy-dispersive x-ray fluorescence spectroscopy;
2. Composition of paste to determine sulfate levels in paste from released sulfates from aggregates;
3. Microstructure of unsound pyrrhotite-bearing aggregate including cracking and extension of cracks from unsound aggregates to paste;
4. Secondary ettringite crystallization along aggregate-paste interfaces – from backscatter and secondary electron images, X-ray elemental maps, and energy-dispersive x-ray fluorescence spectroscopy;
5. Secondary ettringite crystallization in air-voids; and,
6. Gaps around aggregate due to expansion of sulfate-contaminated paste

All these microstructural and microchemical studies are helpful for:

1. Identifying iron sulfide mineral present in aggregate, e.g., lower S/Fe atomic ratio than pyrite to indicate pyrrhotite;
2. Evidence of oxidation of pyrrhotite from lower S/Fe atomic ratio compared to non-oxidized stoichiometric S/Fe ratio of pyrrhotite;
3. Evidence of unsoundness of pyrrhotite-bearing aggregate from expansion and cracking;
4. Evidence of internal sulfate attack in paste from high sulfur (as SO<sub>3</sub>) level of paste compared to normal Portland cement paste, due to secondary ettringite infestation in confined areas in paste; and,
5. Evidence of internal sulfate attack in paste from gaps around aggregates due to expansion of paste and secondary ettringite crystallization along aggregate-paste interfaces.

SEM-EDS studies found well-developed secondary ettringite crystallization mostly in air-voids and only occasionally in microcracks including in gaps around aggregates and at aggregate-paste interfaces. EDS analyses of sulfate contents of pastes, however, are noticeably less (mostly less than 0.1% similar to common Portland cement pastes) than that found in other case studies (e.g., in the range of 4 to 6.5% as SO<sub>3</sub> found in the paste of pyrrhotite-distress of foundation from Ellington, CT, Jana 2018), which is indicative of probably an initial stage of distress where most secondary ettringite formed from pyrrhotite oxidation found voids, cracks, and porous areas to be deposited rather than forming within the confined areas of paste. In other case studies, e.g., from Ellington, CT sulfate contents of paste *per se* were noticeably higher than less than 1% sulfate (SO<sub>3</sub>) commonly found in the paste of a normal Portland cement concrete prepared using a Portland cement containing 3 percent sulfate at a similar water-cement ratio and cement content of the present core but containing no iron sulfide contaminant.

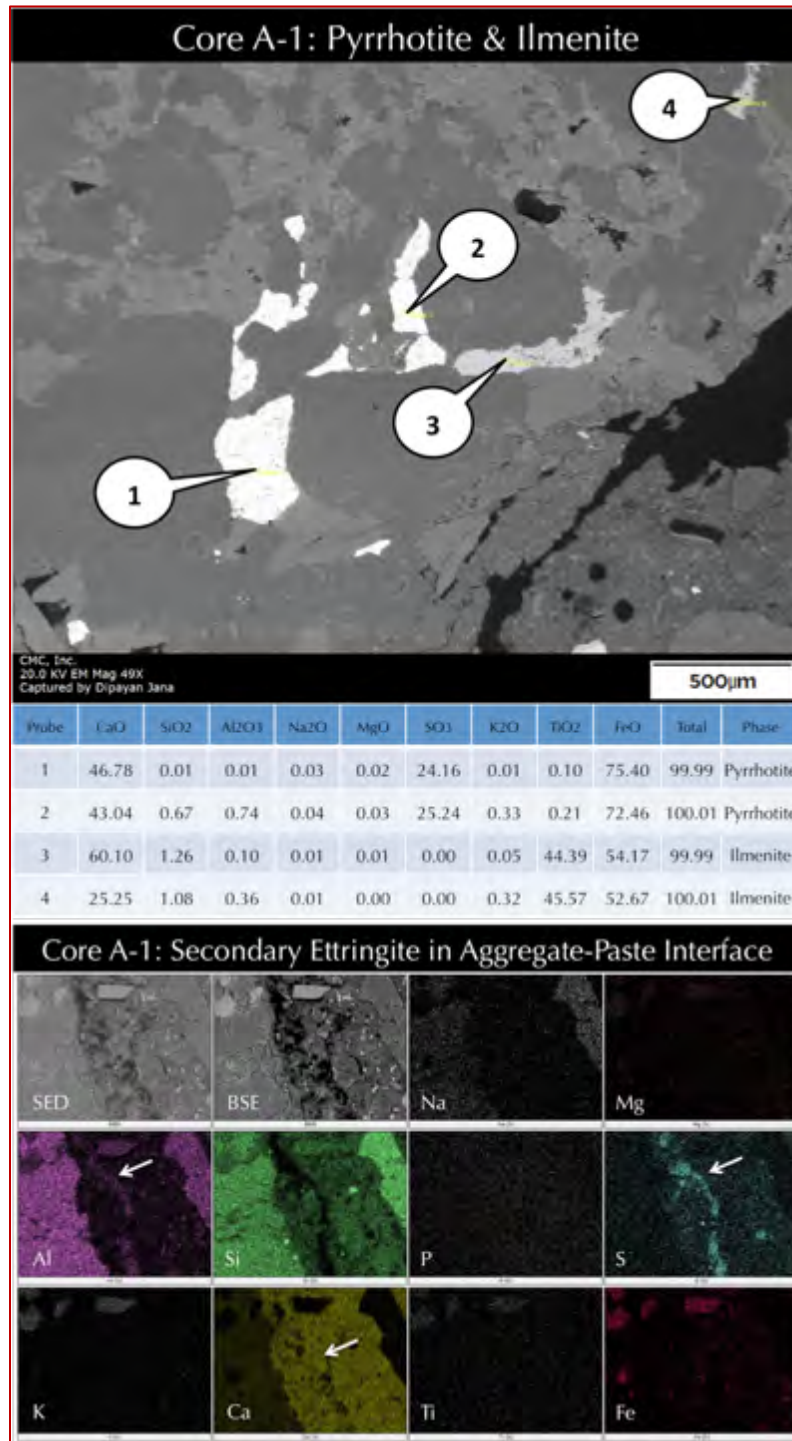


Figure 29: Top: Backscatter electron image (top) and compositional analyses of selected areas (at the tips of callouts) by energy-dispersive X-ray fluorescence spectroscopy of a portion of concrete microstructure in Core A-1 showing pyrrhotite and associated ilmenite opaque grains with their typical compositions of Fe-S and Fe-Ti-O, respectively. Bottom: Secondary electron image (top left), corresponding backscatter electron image (top 2<sup>nd</sup> from left), and corresponding X-ray elemental maps of sodium (Na), magnesium (Mg), aluminum (Al), silicon (Si), phosphorus (P), sulfur (S), potassium (K), calcium (Ca), titanium (Ti), and iron (Fe) of microstructure of concrete in Core A-1 showing: (a) disseminated pyrrhotite grains in aggregate highlighted by Fe and S maps, (b) feldspar grains in gneiss coarse aggregate highlighted by Na, K, Al, Si maps, (c) calcium silicate hydrate paste from Portland cement hydration highlighted in Ca map, (d) siliceous sand fine aggregate highlighted in Si map, (e) iron-titanium grains in aggregate highlighted in Fe and Ti maps, and (f) secondary ettringite deposits in microcracks (arrows) and in paste highlighted in Ca, Al, and S maps. See Appendix E for details.

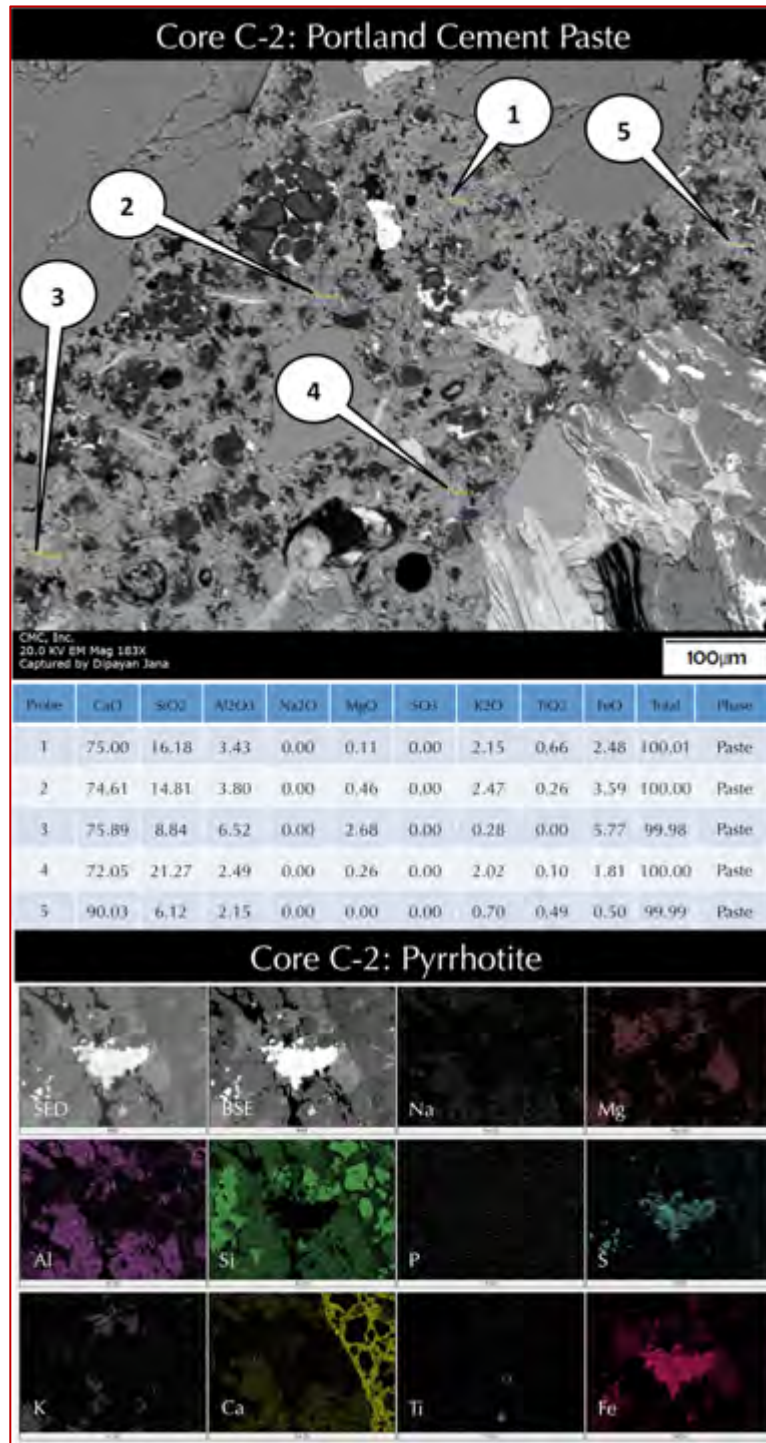


Figure 30: Top: Backscatter electron image (BSE, top) and compositional analyses of selected areas (at the tips of callouts) by energy-dispersive X-ray fluorescence spectroscopy of a portion of concrete microstructure in Core C-2 showing Portland cement paste having typical calcium silicate (hydrate) composition. Scattered residual Portland cement particles having subhedral alite grains, and ferrite remains (latter appear brighter in BSE image) are seen in the paste. Bottom: Secondary electron image (top left), corresponding backscatter electron image (top 2<sup>nd</sup> from left), and corresponding X-ray elemental maps of sodium (Na), magnesium (Mg), aluminum (Al), silicon (Si), phosphorus (P), sulfur (S), potassium (K), calcium (Ca), titanium (Ti), and iron (Fe) of microstructure of concrete in Core C-2 showing: (a) disseminated pyrrhotite grains in aggregate highlighted by Fe and S maps, (b) feldspar grains in gneiss coarse aggregate highlighted by Na, K, Al, Si maps, (c) calcium silicate hydrate paste from Portland cement hydration highlighted in Ca map, (d) siliceous sand fine aggregate highlighted in Si map, and (e) iron-titanium grains in aggregate highlighted in Fe and Ti maps. See Appendix E for details.

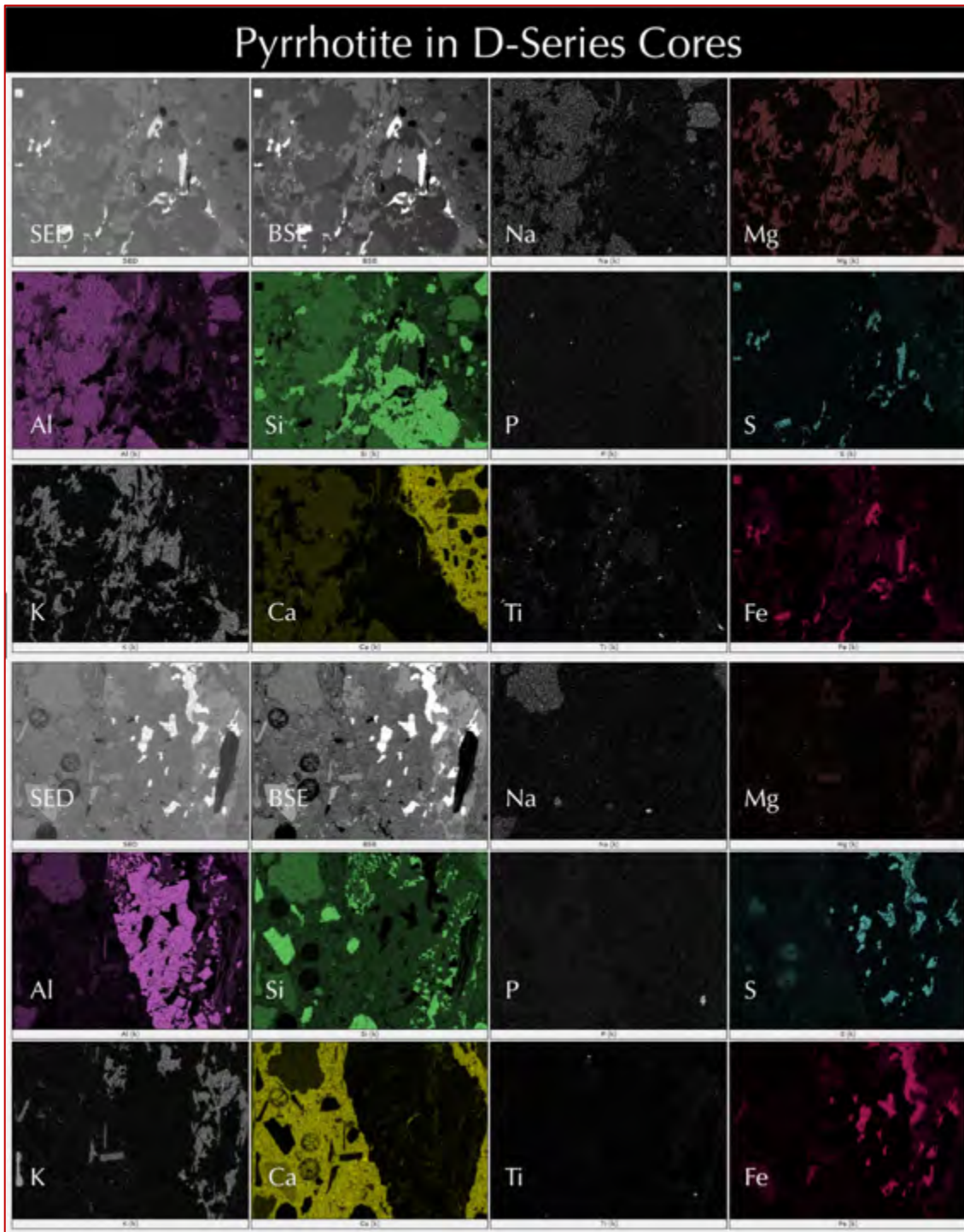


Figure 31: Secondary electron images (top left), corresponding backscatter electron images (top 2<sup>nd</sup> from left), and corresponding X-ray elemental maps of sodium (Na), magnesium (Mg), aluminum (Al), silicon (Si), phosphorus (P), sulfur (S), potassium (K), calcium (Ca), titanium (Ti), and iron (Fe) of microstructure of concrete in D-series cores showing: (a) disseminated pyrrhotite grains in aggregate highlighted by Fe and S maps, (b) feldspar grains in gneiss coarse aggregate highlighted by Na, K, Al, Si maps, (c) calcium silicate hydrate paste from Portland cement hydration highlighted in Ca map, (d) siliceous sand fine aggregate highlighted in Si map, and (e) iron-titanium grains in aggregate highlighted in Fe and Ti maps. See Appendix E for details.

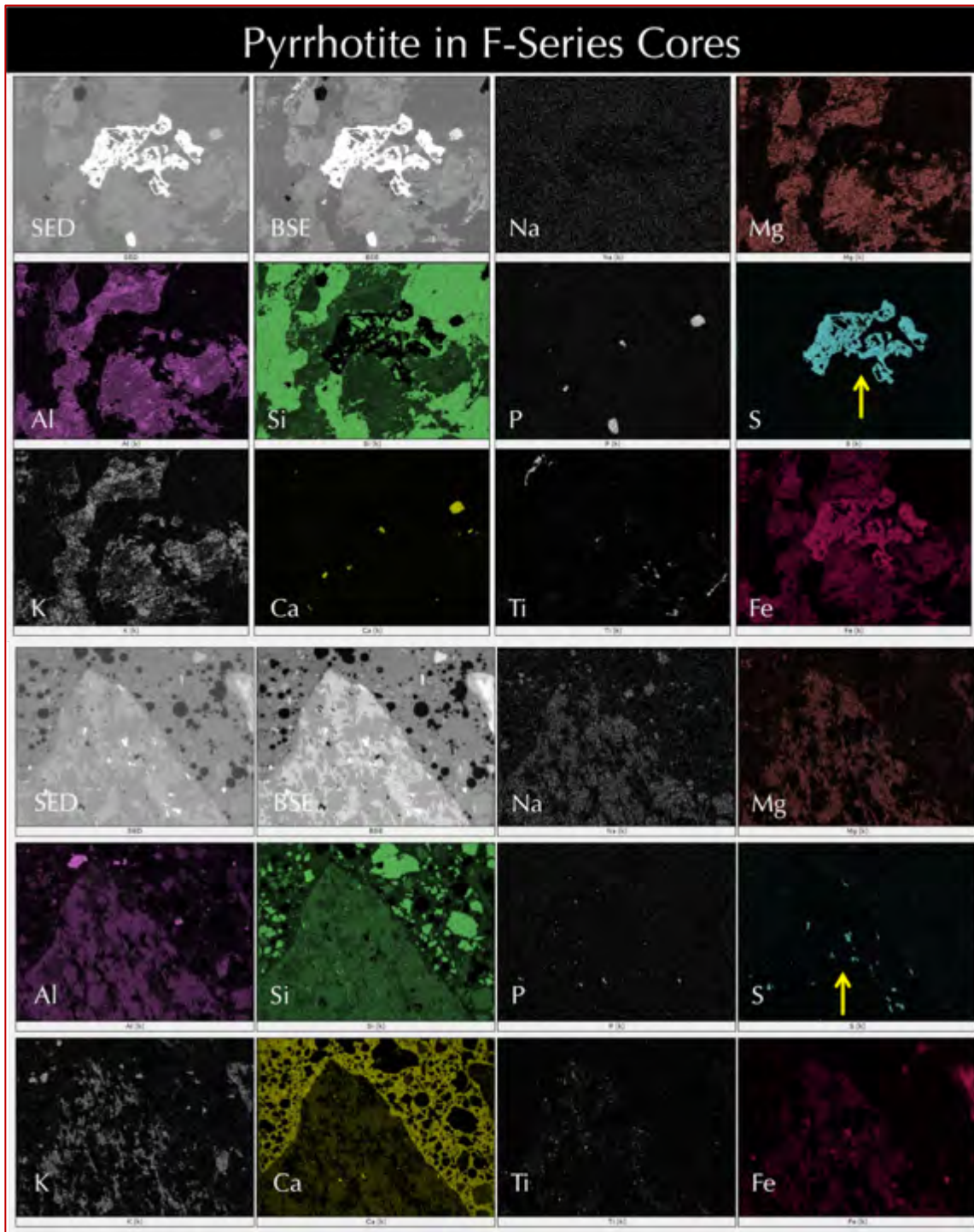


Figure 32: Secondary electron images (top left), corresponding backscatter electron images (top 2<sup>nd</sup> from left), and corresponding X-ray elemental maps of sodium (Na), magnesium (Mg), aluminum (Al), silicon (Si), phosphorus (P), sulfur (S), potassium (K), calcium (Ca), titanium (Ti), and iron (Fe) of microstructure of concrete in F-series cores showing: (a) disseminated pyrrhotite grains in aggregate highlighted by Fe and S maps, (b) feldspar grains in gneiss coarse aggregate highlighted by Na, K, Al, Si maps, (c) calcium silicate hydrate paste from Portland cement hydration highlighted in Ca map, (d) siliceous sand fine aggregate highlighted in Si map, and (e) iron-titanium grains in aggregate highlighted in Fe and Ti maps. See Appendix E for details.



The following conclusions are drawn from the SEM-EDS analyses:

- a) SEM-EDS studies found secondary ettringite crystallization mostly in air-voids and only occasionally in microcracks including in gaps around aggregates and at aggregate-paste interfaces, which are not as common as in other DEF-distressed concretes. Most of the microcracks are empty and gaps around aggregates due to paste expansion are not as frequent as in other DEF-affected concretes.
- b) However, EDS analyses of sulfate contents of paste in the cores showed negligible amounts, less than 0.1 percent as opposed to paste in the case of Ellington, CT where 4 to 6.5% (as  $\text{SO}_3$ ) were found, which were noticeably higher than less than 1% sulfate ( $\text{SO}_3$ ) commonly found in the paste of a normal Portland cement concrete prepared using a Portland cement containing 3 percent sulfate at a similar water-cement ratio and cement content of the present core but containing no iron sulfide contaminant. For the case of Ellington, CT, the high sulfate content of paste detected from EDS analyses was consistent with the overall high bulk sulfate content of concrete, indicating sulfate release from pyrrhotite oxidation. In the present case however, bulk concrete as well as unsound aggregates showed high sulfate and noticeable pyrrhotite contents, but sulfates released from pyrrhotite oxidation are mostly seen in air voids, cracks, and porous areas of pastes opposed to *in situ* infestation of paste *per se* to cause direct expansions of paste.
- c) SEM-EDS analyses found three different optically opaque iron species in gneiss, e.g., iron sulfide (pyrrhotite), oxidation products of pyrrhotite measured in the EDS as iron oxide (determined in XRD as ferrihydrite), and iron-titanium oxide (rutile and ilmenite).

#### MICROSTRUCTURAL EVIDENCE OF PYRRHOTITE-OXIDATION & RELATED CRACKING

- a. Visible and invisible cracking in pyrrhotite-bearing crushed gneiss aggregates, many extending from aggregates to paste;
- b. Lower S/Fe ratio ( $< 0.50$ ) of oxidized pyrrhotite in SEM-EDS analyses than that from stoichiometry of non-oxidized pyrrhotite.

#### MICROSTRUCTURAL EVIDENCE OF INTERNAL SULFATE ATTACK BY RELEASED SULFATES

- a. High sulfate ( $\text{SO}_3$ ) content in paste - in the case of Ellington, CT but not in the present case
- b. Ettringite infested paste – the breeding ground for internal sulfate attack – in the case of Ellington, CT
- c. Secondary ettringite crystallization in microcracks - in the present case as well as in Ellington, CT
- d. Secondary ettringite crystallization in aggregate-paste interfaces - in the present case and in Ellington, CT
- e. Gaps around aggregates due to expansion of paste - in the present case as well as in Ellington, CT.

MINERALOGICAL COMPOSITIONS AND PYRRHOTITE CONTENTS OF CONCRETES AND AGGREGATES FROM XRD

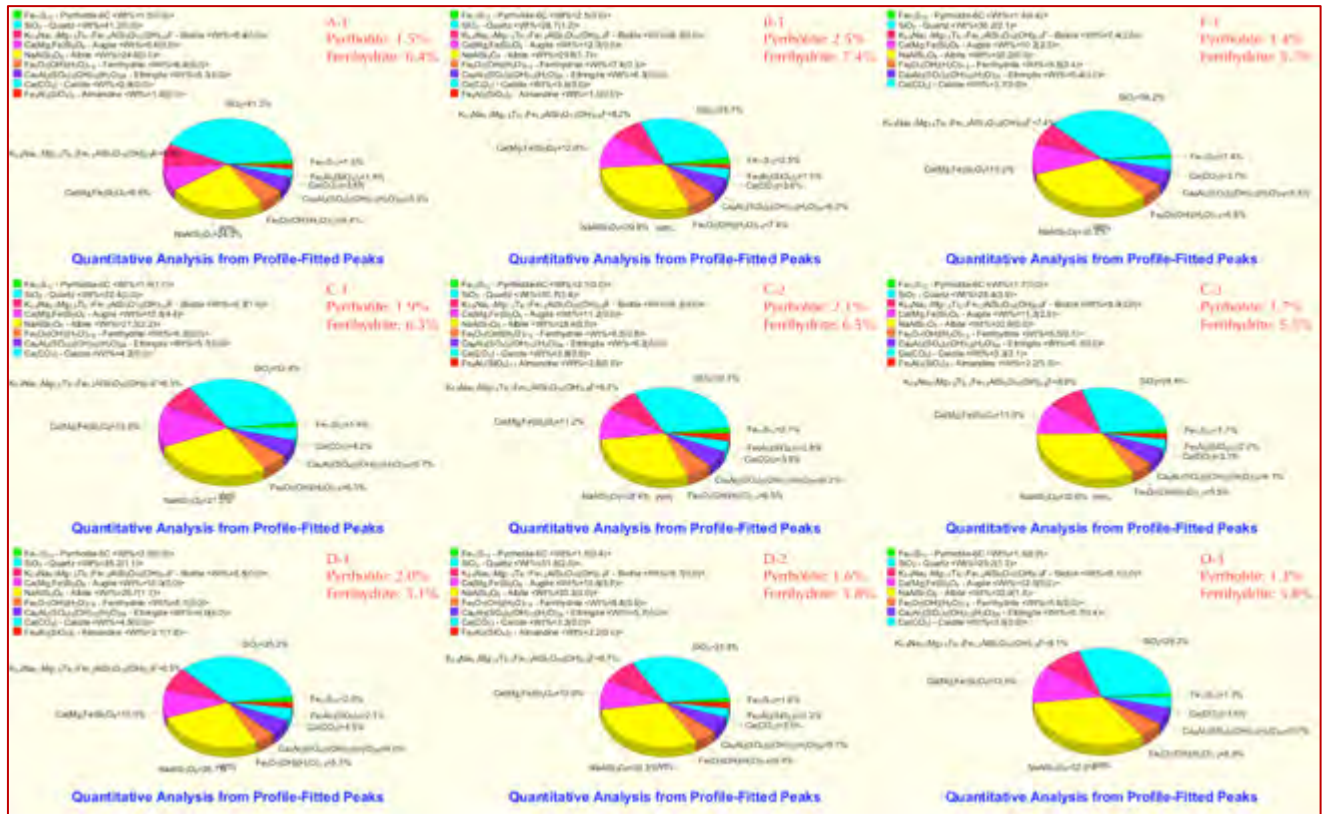


Figure 33: Quantitative proportions of minerals in bulk concretes in Cores A-1, B-1, C-1 to C-3, D-1 to D-3, and F-1 determined from XRD, showing the presence of pyrrhotite, and its oxidation product ferrihydrite, along with major minerals of aggregates, e.g., quartz, albite, and biotite from gneiss, augite pyroxene from metamorphosed gabbro, secondary ettringite from paste and calcite from carbonated paste and aggregates. See Appendix F for details.

| Minerals from XRD | A-1  | B-1  | C-1  | C-2  | C-3  | D-1  | D-2  | D-3  | F-1  | D-3* |
|-------------------|------|------|------|------|------|------|------|------|------|------|
| Quartz            | 41.2 | 28.7 | 32.4 | 30.7 | 28.4 | 35.2 | 31.8 | 29.2 | 36.2 | 4.0  |
| Albite            | 24.0 | 29.8 | 27.3 | 28.4 | 32.6 | 26.7 | 30.3 | 32.9 | 30.2 | 32.1 |
| Garnet            | 1.8  | 1.5  | <1   | 2.8  | 2.2  | 2.1  | 2.2  | <1   | <1   | 23.0 |
| Biotite           | 8.4  | 8.2  | 8.3  | 8.3  | 8.9  | 8.5  | 8.7  | 9.1  | 7.4  | 24.2 |
| Pyrrhotite        | 1.5  | 2.5  | 1.9  | 2.1  | 1.7  | 2.0  | 1.6  | 1.3  | 1.4  | 1.9  |
| Ferrihydrite      | 6.4  | 7.4  | 6.3  | 6.5  | 5.5  | 5.1  | 5.8  | 5.8  | 5.5  | 2.7  |
| Augite            | 8.6  | 12.0 | 13.8 | 11.2 | 11.3 | 10.0 | 10.6 | 12.5 | 10.2 | 2.6  |
| Calcite           | 2.8  | 3.6  | 4.2  | 3.8  | 3.3  | 4.5  | 3.3  | 3.6  | 3.7  | 2.6  |
| Ettringite        | 5.3  | 6.3  | 5.7  | 6.2  | 6.1  | 6.0  | 5.7  | 5.7  | 5.4  | 6.9  |

Table 6: Quantitative mineralogical compositions and pyrrhotite contents of concretes and aggregates from XRD. D-3 with an asterisk is for two unsound aggregate particles extracted from Core D-3 that are shown in Figure 19.

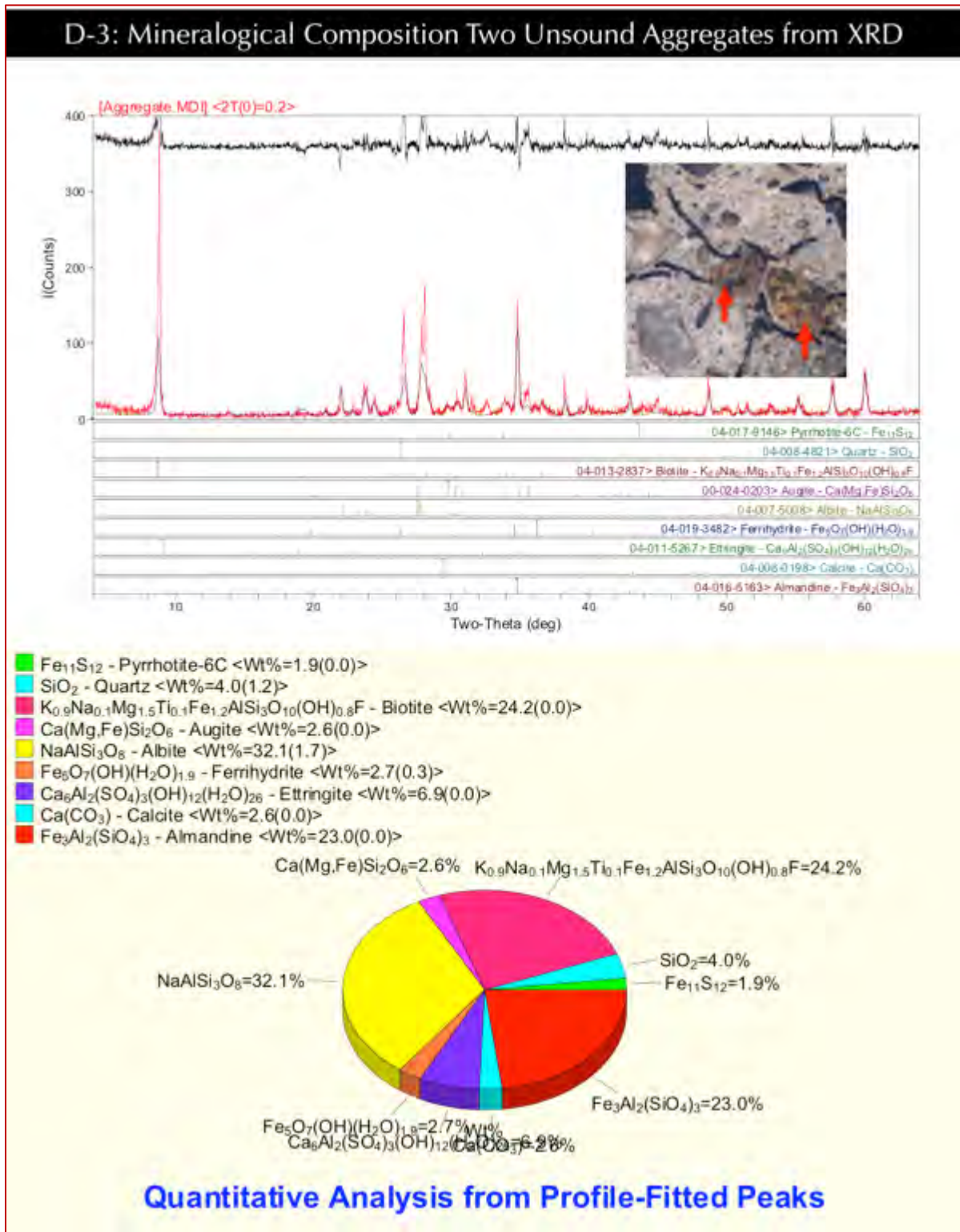


Figure 34: X-ray diffraction pattern (top) and quantitative proportions of minerals (bottom) in two unsound aggregates in Core D-3 (Figure 19). See Appendix F for details.



XRD analyses of concretes and coarse aggregates extracted from the cores have confirmed the iron sulfide minerals to be pyrrhotite, along with ferrihydrite as its oxidation product, which are, again, in line with previous findings from other deteriorated foundations (Jana 2018). XRD analyses showed mineralogical similarities between 1998 and 2001 concretes all containing quartz, albite feldspar as two common minerals in crushed stones, followed by biotite, almandine garnet in gneiss, augite in metamorphosed gabbro, and pyrrhotite as one of the opaque phases responsible for the distress by forming its oxidation product, ferrihydrite.

Two unsound crushed gneiss particles in Core D-3 that have created radial and concentric cracks (Figure 19) showed 1.9 percent pyrrhotite and its oxidation product constituting 2.7 percent ferrihydrite. Oxidation of pyrrhotite to ferrihydrite has caused radial and concentric cracking as shown in Figures 19 and 34.

**CHEMICAL COMPOSITIONS AND SULFATE CONTENTS OF CONCRETES AND AGGREGATES FROM XRF**

| Oxide (wt.%)<br>from<br>XRF    | A-1   | B-1   | C-1   | C-2   | C-3   | D-1   | D-2   | D-3   | F-1   | D-3*  |
|--------------------------------|-------|-------|-------|-------|-------|-------|-------|-------|-------|-------|
| SiO <sub>2</sub>               | 40.4  | 37.1  | 42.2  | 40.6  | 41.6  | 33.5  | 41.5  | 42    | 43    | 28.4  |
| Al <sub>2</sub> O <sub>3</sub> | 8.54  | 9.08  | 8.54  | 8.82  | 7.01  | 8.38  | 6.79  | 8.44  | 8.9   | 10.7  |
| Fe <sub>2</sub> O <sub>3</sub> | 5.93  | 8.02  | 6.62  | 8.48  | 5.9   | 7.49  | 7.63  | 7.17  | 5.81  | 25.6  |
| CaO                            | 11.1  | 10.7  | 10.3  | 10.5  | 11.9  | 10    | 9.6   | 10.4  | 10.2  | 6.45  |
| MgO                            | 2.62  | 3.43  | 2.76  | 2.96  | 2.67  | 3.52  | 2.61  | 3.73  | 2.94  | 9.07  |
| K <sub>2</sub> O               | 1.56  | 1.15  | 1.4   | 1.42  | 1.12  | 1.17  | 1.14  | 1.45  | 1.61  | 1.21  |
| TiO <sub>2</sub>               | 0.612 | 1.21  | 0.75  | 0.884 | 0.625 | 0.947 | 1.21  | 0.834 | 0.913 | 4.35  |
| P <sub>2</sub> O <sub>5</sub>  | 0.081 | 0.094 | 0.066 | 0.06  | 0.064 | 0.061 | 0.058 | 0.084 | 0.059 | 0.020 |
| SO <sub>3</sub>                | 0.509 | 1.58  | 0.991 | 1.1   | 1.1   | 0.859 | 1.39  | 0.698 | 0.821 | 2.43  |
| Balance                        | 23.9  | 26    | 24.6  | 23.5  | 27.6  | 24.1  | 35.2  | 23.9  | 24.5  | 9.43  |
| Total                          | 100   | 100   | 100   | 100   | 100   | 100   | 100   | 100   | 100   | 100   |

Table 7: Bulk oxide compositions and sulfate (SO<sub>3</sub>) contents of concretes and aggregates from XRF. D-3 with an asterisk is for two unsound aggregate particles extracted from Core D-3 that are shown in Figure 19.

XRF analysis of bulk concretes and aggregates extracted from concrete showed compositional similarities amongst concretes and their differences from coarse aggregates as seen for the minerals in XRD, in having major amount of silica, followed by oxides of calcium, aluminum, iron, magnesium, and alkalis. Sulfate contents (as SO<sub>3</sub>) of bulk concretes range from 0.5 to 1.6 percent, whereas that from a crushed stone coarse aggregate that has created radial cracking in Core D-3 showed 2.43 percent sulfate. Iron oxide contents in concretes are in the range of 5 to 8.5 percent, whereas in the unsound crushed stone it is up to 25.6 percent due to oxidation of pyrrhotite.



## ION CHROMATOGRAPHY FOR POTENTIAL SULFATE RELEASE FROM CONCRETES AND AGGREGATES IN ACCELERATED OXIDATION TEST

Two unsound crushed gneiss coarse aggregate particles in Core D-3 that have created radial and concentric cracks were carefully extracted from the core and cleaned of all adhering paste to be crushed and immersed in a strong oxidant (35% hydrogen peroxide) solution. Bulk concretes of cores A-1, B-1, C-1 to C-3, D-1 to D-3 and F-5 pulverized for XRD and XRF studies were also selected for digestion in water so that water-soluble sulfate contents of filtrates can be determined. A separate crushed gneiss aggregate from a different project with no known iron sulfide mineral from XRD study was included as a 'control' sample.

For extracted aggregates, after crushing, two 1-gram aliquots were selected for determining released sulfate contents at two different days (3 and 7 days). Pulverized aggregate sample (finer than 0.3 mm) was immersed in a 50-mL hydrogen peroxide (35%) solution, then at the end of digestion, filtered all solid residues with two 2.5-micron filter papers, the filtrate was then re-filtered through two 0.45-micron filter papers. The filtrate thus prepared was then diluted with deionized water to 250 mL to be analyzed in IC. For concrete powders, approximately 1-gram powder was immersed in deionized water, digested below boiling with a magnetic stirrer for 15 minutes followed by ambient temperature digestion for 24 hours. The filtrate thus prepared was then diluted with distilled water to 100 mL to be analyzed in IC.

Figure 35 shows water-soluble sulfate contents of filtrates of concretes and extracted aggregates tested in accelerated oxidation test, along with no or minimal release of any sulfate from a control aggregate without any sulfide.

The bottom photo in Figure 35 incorporated results of accelerated oxidation tests of quarried rocks by Wille and Zhong (2016) as well as the present study of released sulfates from two unsound aggregates at various days. As seen in both photos, all pyrrhotite-bearing aggregates show noticeable release of sulfates in an oxidizing environment even after service in concrete, compared to a control aggregate of no sulfide. Apparently, released sulfates have contaminated the paste, and formed the seeds for internal sulfate attack by reactions with cement hydration products.

Compared to the study of Wille and Zhong (2016), this study showed a large range of released sulfate from two unsound coarse aggregate particles, indicating various amounts of pyrrhotite present in the aggregate particles.

Due to these clear signals of sulfates released from pyrrhotite-bearing aggregates, accelerated oxidation test of potential pyrrhotite-bearing aggregates followed by ion chromatography of filtrate to determine the sulfate contents are helpful techniques for evaluation of quarried aggregates for potential pyrrhotite-related distress by internal sulfate attacks.

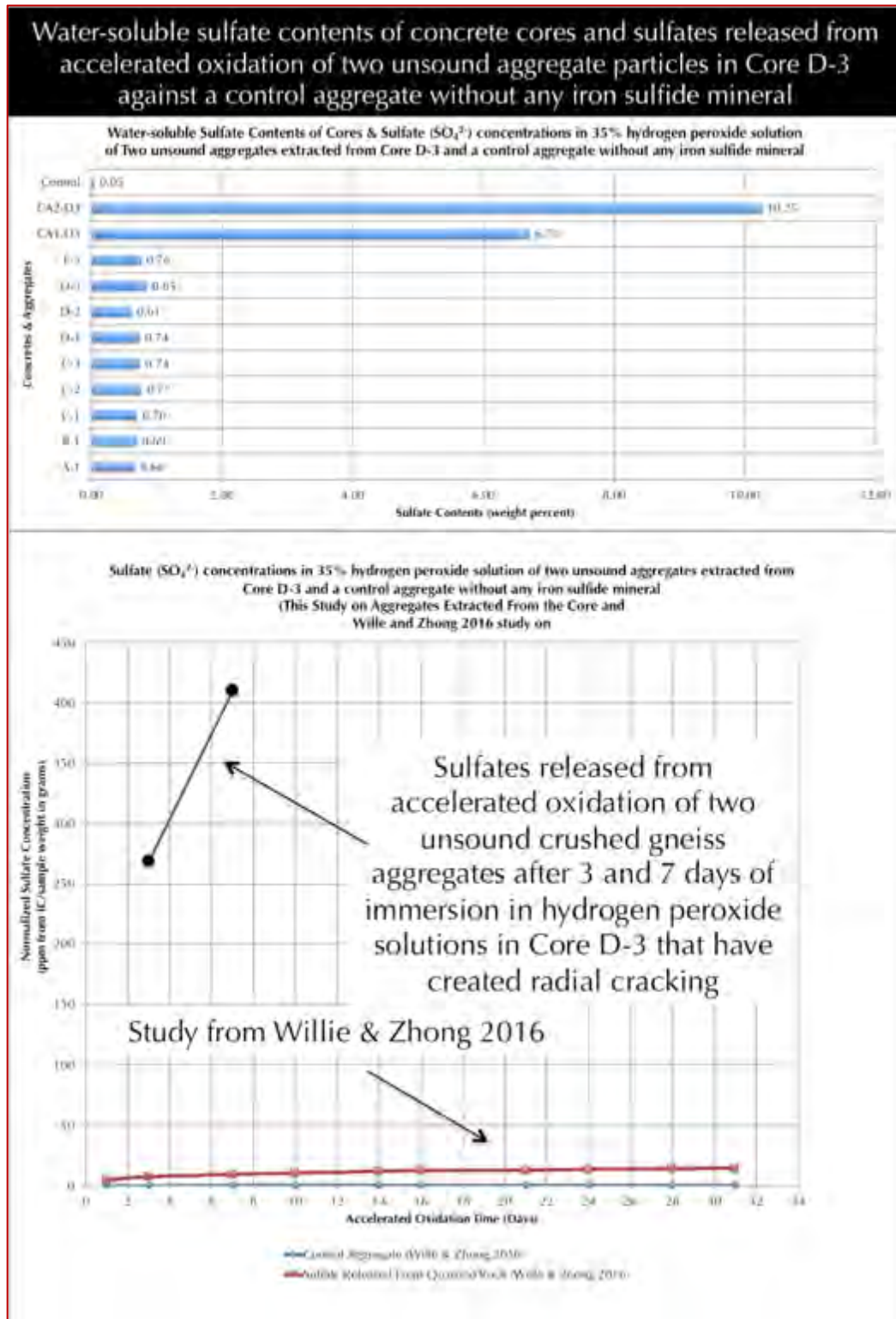


Figure 35: Results of accelerated oxidation test of two crushed gneiss coarse aggregate particles from Core D-3 at 3-day (CA1-D3) and 7-day (CA2-D3), along with water-soluble sulfates released from Cores A-1, B-1, C-1 to C-3, D-1 to D-3 and F-5 as measured from anion chromatography. Bottom graph included results of Wille and Zhong (2016) of quarried stones all showing sulfate release from pyrrhotite-bearing aggregates. Compared to Wille and Zhong (2014) this study showed a large range of released sulfates from extracted crushed gneiss coarse aggregate.



## DISCUSSION

### IRON SULFIDE MINERALS IN CONCRETE AGGREGATES<sup>1</sup>

Iron sulfide minerals (e.g., pyrite  $\text{FeS}_2$ , or pyrrhotite  $\text{Fe}_{1-x}\text{S}$ ,  $x$  varies from 0 to 0.125) occurring mostly as ‘accessory’ minerals in many concrete aggregates are known to cause various deteriorations in concrete in service. **Oxidation of iron sulfide minerals in concrete** can cause various deteriorations from **unsightly staining** on the exposed surface to **popouts** of near-surface unsound aggregates (Jana 2008) and associated local fracturing to in extreme cases severe **cracking, microcracking, and loss of strength** of concrete from **internal sulfate attacks** by reactions between released sulfate and hydrogen ion (sulfuric acid) from oxidation reactions with cement hydration products – all resulting in expansive reactions leading to structural instability. The mineral pyrrhotite has been found to be the most reactive and detrimental to the durability of concrete. If a suspicion arises regarding a possible pyrrhotite-related distress in a concrete structure then identification of the type of iron sulfide mineral responsible for the distress, and quantification of the total sulfur content in the pyrrhotite-bearing aggregate would be prudent to determine whether the mineral may have an effect on the durability of concrete.

#### Background

Iron sulfide minerals occur commonly as minor, but significant accessory minerals in a variety of rocks. Pyrite is the most common of all sulfide minerals. It is a common accessory mineral in igneous, metamorphic, and sedimentary rocks, and is a major phase in many sulfide ore bodies. In hand sample, this mineral has a metallic luster and pale-yellow color. Microscopically, pyrite is a cubic isotropic mineral with a yellowish-white color in reflected light (Deer et al., 1992). Pyrite, with the chemical formula  $\text{FeS}_2$ , is composed of 46.6% Fe and 53.5% S.

Pyrrhotite is the second most common iron sulfide in nature, found as a primary accessory mineral in ultra-mafic and mafic rocks, metamorphosed igneous and sedimentary rocks, and as a secondary mineral in hydrothermal deposits. It is mostly found with other iron sulfides, particularly pentlandite ( $(\text{Fe,Ni})_9\text{S}_8$ ), but also commonly found associated with pyrite, marcasite (orthorhombic  $\text{FeS}_2$ ), magnetite ( $\text{Fe}_3\text{O}_4$ ), and chalcopyrite ( $\text{CuFeS}_2$ ) (Deer et al, 1992; Belzile et al, 2004). These different minerals can all coexist within a grain of pyrrhotite or in contact with the grain (Uytenbogaardt, Burke, 1971). In hand sample, this mineral has a metallic luster and bronze brown, yellow, or reddish color. Microscopically, pyrrhotite is a monoclinic or pseudohexagonal anisotropic mineral with a pink cream or skin color in reflected light (Deer et al, 1992). Pyrrhotite has an unbalanced chemical formula  $\text{Fe}_{1-x}\text{S}$ , with  $x$  ranging from 0 ( $\text{FeS}$ ) to 0.125 ( $\text{Fe}_7\text{S}_8$ ).

---

<sup>1</sup> Excerpts from American Concrete Institute’s technical notes on pyrrhotite-related distress in concrete, plus author’s own addition.



Mechanism of Distress by: (1) Oxidation of Iron Sulfides (Primary Expansion Causing Surface Staining, Popout, Cracking), (2) Release of Sulfates and Internal Sulfate Attack (Secondary Expansion Causing Further Cracking)

It is well known from the literature that sulfide minerals are unstable in oxidizing conditions. According to Divet and Davy (1996), high pH conditions, such as those found in concrete, enhance iron sulfide oxidation. Upon exposure to water and oxygen, sulfide minerals (pyrite, pyrrhotite) oxidize to form acidic, iron oxides/hydroxides, and sulfate-rich by-products with an increase in solid volumes from the sulfide minerals to their oxidized products (Belzile et al. 2004, Rodrigues et al. 2012). The oxidation of ferrous iron ( $\text{Fe}^{2+}$ ) produces ferric ions ( $\text{Fe}^{3+}$ ) that can precipitate out of solution to form ferric hydroxide, if pH is not too low.  $\text{Fe}^{2+}$  is oxidized and precipitated as ferric oxyhydroxides, principally **ferrihydrate** [ $\text{Fe}(\text{OH})_3$ ] and **goethite** [ $\text{FeO}(\text{OH})$ ]. The sulfuric acid (sulfate and hydrogen ion,  $\text{H}_2\text{SO}_4$ ) generated through oxidation reactions reacts with cement hydration products, e.g., with the portlandite [ $\text{Ca}(\text{OH})_2$ ], to form **gypsum** [ $\text{CaSO}_4 \cdot 2\text{H}_2\text{O}$ ] (Grattan-Bellew and Eden 1975, Shayan 1998, Rodrigues et al. 2012), with calcium aluminate or monosulfoaluminate hydrates to form **ettringite** [ $\text{Ca}_6\text{Al}_2(\text{SO}_4)_3(\text{OH})_{12} \cdot 26\text{H}_2\text{O}$ ], or **thaumasite** [ $\text{Ca}_6[\text{Si}(\text{OH})_6]_2(\text{CO}_3)_2(\text{SO}_4)_2(\text{H}_2\text{O})_{22}$ ] latter one if carbonate minerals are present. Both the processes of *oxidation of iron sulfides*, and *reactions between released sulfates and cement hydration products* are expansive in nature resulting in concrete deteriorations.

Figure 36 from various authors (e.g., Rodrigues et al. 2012, Oliveira et al., 2014, Willi and Zhoing 2016) summarizes mechanism of two-stage expansions resulting in concrete deterioration from: (a) *primary expansion due to oxidation of iron sulfide minerals to ferric oxyhydroxides, principally goethite and ferrihydrate and associated solid volumes' increases*, and (b) *secondary expansion due to internal sulfate attacks of released sulfate and hydrogen ions (sulfuric acid) from oxidation to cement hydration products, e.g., calcium hydroxide and calcium sulfoaluminate hydrate to form gypsum (with a solid volume increase of 42) or more commonly due to formation of ettringite (with a solid volume increase of 172).*

The above expansive mineral formation results in **rust staining and pop-outs at the aggregate site in milder cases most commonly associated with pyrite, to severe cracking and decreased strength due to internal sulfate attack in paste from released sulfates in the most severe cases associated with pyrrhotite.**

In the case of pyrrhotite, the degree of cracking damage correlates with the deterioration of the mineral and the quantity of resultant expansive sulfates in the paste. **Not all concretes with pyrrhotite in aggregates, however, result in deterioration.** As shown in the case studies in Table 8, the rate and extent of damage can be variable. The rate and severity of damage are dependent on a number of factors including: (a) the interaction between the particle and the surrounding host rock that forms the aggregate (Oliveira et al. 2014) and the concrete paste, (b) the concrete quality, (c) the environmental conditions to which the concrete element is exposed to (exposure to oxygen, moisture, and temperature), (d) crystal structure, (e) the mineral associations (more than one sulfide minerals present), (f)

concrete pH, (g) trace metal content, and (h) bacterial activity (Belzile et al. 2004). The extents of controlling factors are not yet fully understood in light of the limitations of reproducing the deterioration in the laboratory.

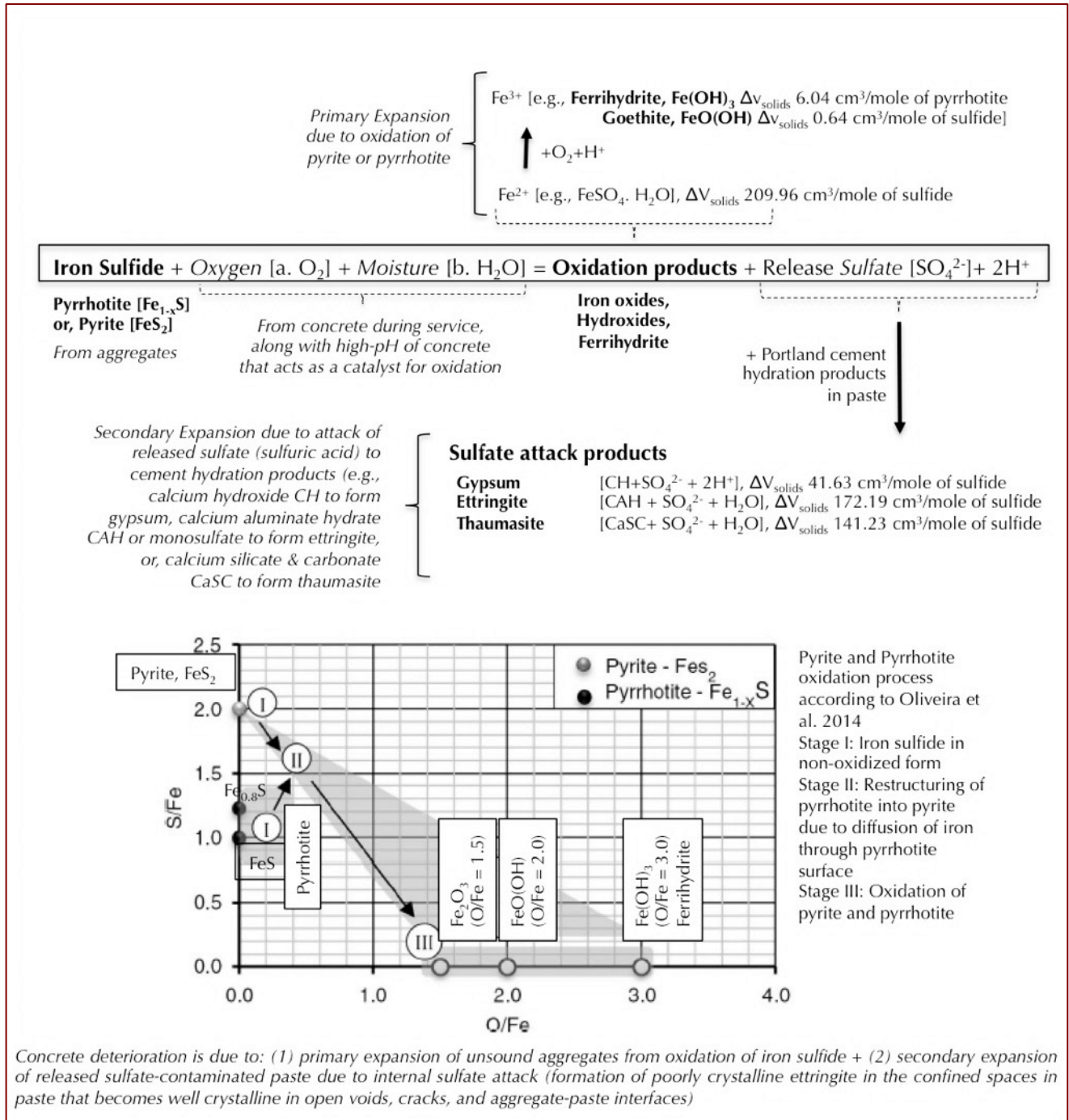


Figure 36: Mechanisms of oxidation of iron sulfide minerals in concrete according to various authors, and primary expansion due to oxidation of iron sulfide to various forms of iron oxides, hydroxides, ferrihydrite, followed by secondary expansions due to reactions between the released sulfates and hydrogen ions from oxidation reactions (sulfuric acid) and cement hydration products (calcium hydroxide, calcium aluminate, and monosulfoaluminate hydrate) to form ettringite (or thaumasite if carbonate ions are present).



## Pyrrhotite Limit

**Standardization of the amount of iron sulfide minerals that are considered acceptable in concrete aggregates is not well established.** American, Canadian, British, and French standards for concrete aggregates mention iron sulfides and their related problems with use in concrete, but have not established acceptable limits of iron sulfide contents in aggregates. Limits have been established for total sulfur ( $S_T$ ) by mass in French at 0.4%, European at 1%, or 0.1% if pyrrhotite is present. The limits as to the amount of pyrrhotite that would lead to damage has not been identified to date; this may be quite difficult because the reactivity of pyrrhotite may vary according to its crystallographic characteristics, while many factors are involved in this deleterious mechanism. No precise guidelines or methods have been proposed to evaluate the potential reactivity of sulfide containing aggregates.

Recently, an extensive investigation was carried out over a four-year period by researchers from four Canadian organizations aimed at developing an evaluation protocol for iron sulfide bearing aggregate (Rodrigues et al., 2016). The resulting recommended protocol involved a three-phase testing program including (a) measurement of total sulfur, (b) oxygen consumption determination, and (c) accelerated mortar bar expansion test. Limits are proposed for each phase of the protocol, but are in need of additional validation. These tests can be used as a general screening, but would need to be supplemented by further testing to identify the sulfate sulfur and the sulfate mineral type. Significant research is still needed to identify appropriate limits.

## CASE STUDIES OF CONCRETE DETERIORATION DUE TO OXIDATION OF IRON SULFIDE MINERALS IN AGGREGATES

Examples of deterioration of concrete structures due to oxidation corrosion of iron sulfate minerals, with pyrrhotite date back to 1955, and span a range of aggregate types. Structural damage to buildings due to pyrite or pyrrhotite breakdown has been observed in many places around the world since the mid-1950s, including Ireland, Wales, Spain, Canada, Namibia, and Japan. In the United States, pyrite-induced swelling has been observed in Ohio, West Virginia, Pennsylvania, Missouri, Kansas, and Kentucky, and more recently thousands of homes in Connecticut have been affected by pyrrhotite in concrete foundations.

Following are summaries of cases studies on concrete deterioration around the world that are described due to unsoundness of aggregates containing iron sulfide minerals, all of which have concluded that expansions associated with oxidation of iron sulfide minerals followed by additional expansions associated with internal sulfate attacks between the released sulfates and cement hydration products have caused the deterioration in form of map cracking, heaving, displacement of affected elements, and in severe cases crumbling of concrete elements. The last row is for oxidation of pyritic shale in the substrate causing heaving of structural elements, or, blistering of floor tiles when pyritic is present in the concrete aggregates at the surface of floor slab, but all other case studies are from pyrrhotite-oxidation related damages.



| <ul style="list-style-type: none"> <li>• Locality (References)</li> </ul>  | <ul style="list-style-type: none"> <li>• Pyrrhotite containing rocks</li> <li>• Associated sulfide minerals</li> </ul>  | <ul style="list-style-type: none"> <li>• Average sulfur content in aggregate</li> <li>• Pyrrhotite content</li> </ul>   | <ul style="list-style-type: none"> <li>• Structure affected</li> <li>• Type of Damage</li> <li>• Time taken to manifest the damage</li> </ul>  | <p>Proposed Mechanisms of Distress</p>  |
|--|---|---|--|---|
| <ul style="list-style-type: none"> <li>• <i>Oslo, Norway</i> (Moum and Rosenqvist 1959)</li> </ul>   | <ul style="list-style-type: none"> <li>• Sedimentary rocks (alum shales some with slight metamorphism)</li> <li>• Pyrite occurred with pyrrhotite</li> </ul>  | <ul style="list-style-type: none"> <li>• 6% (highly variable), all shales that weathered ‘explosively’ due to oxidation contained more than 0.2% sulfur as monoclinic pyrrhotite.</li> <li>• Pyrrhotite content is related to rate of alteration of pyrite and rate of weathering of shale</li> </ul>   | <ul style="list-style-type: none"> <li>• Foundation</li> <li>• Upheaval of foundation, cracking, crumbling, yellowish deposit of jarosite <math>[KFe_3(OH)_6(SO_4)_2]</math> and brown-iron oxide <math>(Fe_2O_3 \cdot nH_2O)</math> on weathered shales.</li> <li>• Within 9 months</li> </ul>  | <p>Swelling of shale due to oxidation of pyrrhotite and internal sulfate attack from released sulfate; reactivity of alum shale and resultant damage increased with increasing pyrrhotite content, with no occurrence of damage when alum shale was free of pyrrhotite; acidic and sulfate-rich water percolated through alum shale has caused acid attack and internal sulfate attack in concrete</p>  |
| <ul style="list-style-type: none"> <li>• <i>Trois-Rivières area, Quebec, Canada</i> (Tagnit-Hamou, et.al. 2005; Rodrigues, et.al. 2012; Duchesne and Benoit 2013)</li> </ul> | <ul style="list-style-type: none"> <li>• Quarried intrusive igneous rock anorthositic gabbro (norite) with different degrees of metamorphism</li> <li>• Pyrite and chalcopyrite. Only pyrrhotite showed signs of oxidation but pyrite and chalcopyrite were largely unaffected. A thin coating of iron carbonate (siderite) on sulfides provided carbonates to promoted thaumasite form of attack in addition to internal sulfate attack from pyrrhotite oxidation</li> </ul> | <ul style="list-style-type: none"> <li>• As low as 0.30% to 2.92% total sulfur by mass of aggregate in pyrrhotite-bearing coarse aggregates that have caused damage, all damaged concrete exceeded the European limit of 0.1% sulfur in aggregate when pyrrhotite is present by 3 times to as high as 30 times.</li> <li>• Less than 5 to 10 percent total sulfide minerals by volume, average 75% of sulfide minerals was pyrrhotite and lesser pyrite and chalcopyrite from a study of 223 house basements containing varying amounts of iron sulfide in gabbro coarse aggregate</li> </ul> | <ul style="list-style-type: none"> <li>• Residential foundations and commercial buildings.</li> <li>• Map cracking (cracks up to 40 mm in width) and yellowish or brownish staining), popouts of oxidized pyrrhotite with white rim of secondary reaction products, and open cracks more pronounced at the corners of the foundation blocks</li> <li>• More than 1000 to as high as estimated 4000 residential and commercial buildings were affected within 3 to 5 years after construction</li> </ul>                                  | <p>Oxidation of sulfide minerals (mainly pyrrhotite) in anorthositic gabbro coarse aggregate in concrete has: (a) formed various “rust” minerals (e.g., ferric oxyhydroxides such as goethite <math>FeO(OH)</math>, limonite, and ferrihydrite) and (b) released sulfuric acid/sulfates, which then reacted with cement hydration products resulting in further expansive formation of gypsum, ettringite, and thaumasite in concrete. Oxidation of pyrrhotite followed by internal sulfate attack of cement paste is the main mechanism of concrete deterioration.</p> |
| <ul style="list-style-type: none"> <li>• <i>Northeastern Connecticut, USA</i> (Wille and Zhong 2016)</li> </ul>  | <ul style="list-style-type: none"> <li>• Foliated schist and gneissic metamorphic rocks, granofels, foliated quartz diorite in a hydrothermally altered vein from a particular quarry in Willington, CT (Becker’s quarry).</li> <li>• Pyrrhotite as the predominant iron sulfide mineral present in metamorphic rocks containing quartz, plagioclase feldspar, micas, and garnet</li> </ul>   | <ul style="list-style-type: none"> <li>• Average 2.54% sulfur in pyrrhotite-bearing quarry aggregate</li> <li>• Pyrrhotite was not detected in XRD analysis of quarry aggregate by Wille and Zhong due to possible presence below the 5% detection limit of XRD</li> </ul>  | <ul style="list-style-type: none"> <li>• Residential foundations.</li> <li>• Map cracking, crumbling, deformation of wall, reddish-brown discoloration, whitish formation of secondary ettringite and thaumasite in the vicinity of surface cracks. Cores from foundation walls of houses showed noticeably lower compressive strengths (some no strength due to complete crumbling) compared to the cores from slabs, indicating possible effect of more oxidation in wall than slab and hence more damage in wall than slab</li> </ul> | <p>Primary expansion due to oxidation of pyrrhotite followed by secondary expansion due to internal sulfate attack by released sulfates</p>   |

| <ul style="list-style-type: none"> <li>• Locality (References)</li> </ul>  | <ul style="list-style-type: none"> <li>• Pyrrhotite containing rocks</li> <li>• Associated sulfide minerals</li> </ul>   | <ul style="list-style-type: none"> <li>• Average sulfur content in aggregate</li> <li>• Pyrrhotite content</li> </ul>   | <ul style="list-style-type: none"> <li>• Structure affected</li> <li>• Type of Damage</li> <li>• Time taken to manifest the damage</li> </ul>   | <p>Proposed Mechanisms of Distress</p>  |
|--|--|---|---|---|
|  |  |   | <ul style="list-style-type: none"> <li>• 10 to 20 years after construction, estimated 34,000 homes are at risk</li> </ul>   |   |
| <ul style="list-style-type: none"> <li>• <i>Catalan Pyrenees, Spain</i> (Araujo et al. 2008)</li> </ul>  | <ul style="list-style-type: none"> <li>• Schist containing quartz, muscovite mica, chlorite and non-expansive illitic clay.</li> <li>• Pyrite and Pyrrhotite</li> </ul>  | <ul style="list-style-type: none"> <li>• 2% sulfur (as SO<sub>3</sub> from XRF) in schist.</li> <li>• Predominantly pyrrhotite (S/Fe ratio 0.62 as opposed to 1.15 of pyrite) but XRD also detected some pyrite</li> </ul>  | <ul style="list-style-type: none"> <li>• Tórán Dam</li> <li>• Map cracking and non-recoverable movements, more dramatic expansion in the downstream face of the dam for upstream displacement of the crest</li> </ul>   | <p>Oxidation of pyrite and pyrrhotite forming surface stains of greyish brown iron hydroxides (goethite) and lighter-green potassium iron sulfates (jarosite), gypsum efflorescence from sulfate attack; and causing expansions, e.g., 6.04 cm<sup>3</sup>/mol from primary expansion from oxidation of iron sulfides followed by 172.19 cm<sup>3</sup>/mol from internal sulfate attack by reaction between released sulfates and cement phases</p>  |
| <ul style="list-style-type: none"> <li>• <i>Central Pyrenees, Spain</i> (Ayora et al. 1998; Oliveira et al. 2014)</li> </ul>   | <ul style="list-style-type: none"> <li>• Schist with bands of pyrrhotite created planes of weakness and cracks that serve as preferential paths for entrance of oxygen thus aggregates containing pyrrhotite bands with cracks have more pronounced oxidation than the aggregates without cracks.</li> <li>• Pyrite</li> </ul>   | <ul style="list-style-type: none"> <li>• Median sulfur (SO<sub>3</sub>) content of 1.42% for rocks from a quarry that have known to cause severe damage when used as aggregate in dam</li> </ul>  | <ul style="list-style-type: none"> <li>• Graus and Tavascan Dams</li> <li>• Map cracking, damage in downstream face and galleries of the Graus Dam due to severe cracking and movement</li> </ul>   | <p>Alteration from acidic solution produced by weathering and oxidation of pyrrhotite in aggregates followed by expansion due to internal sulfate attack and formation of ettringite and gypsum. Characteristic ratios of 2.44 for the Fe/O ratio and of 2.63 for the S/O ratio in pyrrhotite marked critical limits that produced the activation and acceleration of pyrrhotite oxidation leading to an increase of expansive reactions and risk of structural damage.</p>   |
| <ul style="list-style-type: none"> <li>• <i>Ottawa, Quebec City, Matane, and Montreal, Canada</i> (Quigley and Vogan 1970; Berard 1970; Berube et al. 1986; Penner et al. 1972)</li> <li>• <i>Ireland</i></li> <li>• <i>Wales</i> (Hawkins and Pinches 1987)</li> <li>• <i>Marcellus Shale, USA</i> (Hoover and Lehmann 2009)</li> <li>• <i>Chattanooga Shale, Kentucky, USA</i> (Anderson 2008)</li> <li>• <i>SW England in Cornwall and Devon</i></li> </ul> | <ul style="list-style-type: none"> <li>• Black shale containing pyrite (not pyrrhotite). Pyrite is most common in metamorphic and sedimentary rocks as either a primary mineral or a fine, widespread impregnation of subsequent origin.</li> <li>• Pyrite is frequently found in association with coal and shale deposits</li> <li>• Mundic (means mine waste) concrete blocks used in the foundations of thousands of 20<sup>th</sup> century homes in SW England, blocks were prepared using mine waste rocks as aggregates containing pyrite that has caused serious damage (Mundic decay) in foundations</li> </ul> | <p>The minimum amount of pyrite that will cause heaving problems is not known with certainty. Some reports describe difficulties with contents as low as 0.1 per cent by weight. In the Ottawa area heaving problems have been encountered only in rock formations with much higher pyrite contents, although a systematic sampling program has not been carried out. Pyrite weathering is a chemical-microbiological oxidation process; some of the oxidation reactions are solely chemical, others are attributed to autotrophic bacteria of the ferrobacillus-thiobacillus group, and still others are both chemical and micro-biological.</p> | <ul style="list-style-type: none"> <li>• Foundation, basement floor above weathered pyritic substrate. Pyrite weathering was identified as early as 1950 as a major foundation problem in the U.S.A. in buildings dating back to 1920.</li> <li>• Pyrite oxidation in the Chattanooga Shale has caused serious foundation problems in numerous buildings and structures in Estill County, KY.</li> <li>• Heaving of pyritic substrate causes cracking, lifting of concrete floor slabs; differences in levels across floor slabs; cracking, buckling lifting of elements resting on the concrete floor slabs, doors, stairs, fixtures; cracking, bulging, movement of internal or external walls.</li> <li>• Blistering and de-bonding of vinyl tile from concrete floor due to oxidation of pyritic aggregates at the surface of concrete floor (Shayan 1988)</li> </ul> | <p>Oxidation of pyrite in shale or coal causes formation of <i>gypsum</i> from reactions between (a) sulfates or sulfuric acid released from pyrite oxidation and calcium hydroxide component of cement hydration (if pyritic rock is used as aggregate in concrete), and/or (b) between sulfuric acid from oxidation and associated calcite in pyritic rocks cause heaving and associated volume changes. When calcite converts to gypsum, the volume increases by a factor of 2, but of greater importance is the force associated with the growth of gypsum crystals, which can be very high. When gypsum grows in rock under buildings it tends to form needle-like crystals that force the layers apart, resulting in much greater heave than would occur with simple volume expansion during formation. Another oxidation product found in all weathered pyritic materials is jarosite, KFe<sub>3</sub>(SO<sub>4</sub>)<sub>2</sub>(OH)<sub>6</sub>, recognized by its bright yellow-brown color. The calculated volume increase from pyrite to jarosite is 115 per cent, which is another main contributor to volume increase and heaving.</p> |

Table 8: Case studies on concrete deteriorations due to oxidation of iron sulfide minerals in aggregates.



## PYRRHOTITE EPIDEMIC IN EASTERN CONNECTICUT

Figure 37 shows regional spread of the latest reported incident of widespread outbreak of deterioration of concrete due to pyrrhotite oxidation in the aggregate along northeastern Connecticut with many hundreds of homes being affected. Figures 38 through 41 show various manifestations of distress in the affected homes from various sources. Typical visual deterioration was in the form of map cracking, some causing deformation of the wall, extensive longitudinal to random cracking of the wall, reddish-brown discoloration, and whitish formation in the vicinity of surface cracking most of which are shown in Figures 55 to 58. Currently, much of the information available on this problem is limited to newspaper articles but the cause of deterioration has been confirmed by an investigation conducted at the University of Connecticut (Wille and Zhong, 2016, and Jana (2018) as oxidation of pyrrhotite present in the aggregate. In contrast to the problems encountered in Quebec, manifestation of the damage in Connecticut has taken as much as 10 to 20 years.

Most of the damage to date has been linked to one quarry operating in Willington, CT. The geology in the vicinity of the quarry is made up of metamorphic rocks predominately from two to three formations. The formations are comprised predominantly of foliated schists and gneissic rock, granofels, and a foliated quartz diorite. Quartz, plagioclase or oligoclase are primary minerals with micas, and noted are garnet and graphite as common accessory minerals. Iron sulfides are found predominately as pyrrhotite.

Wille and Zhong (2016) did an extensive mechanical, mineralogical, microstructural and chemical tests on the core samples taken from 7 houses and did visual inspection of 14 additional houses, from which the primary findings they found are:

- a) Ubiquitous in all cases of concrete deterioration are the presence of pyrrhotite in aggregates and their oxidation products, such as goethite  $[\text{FeO}(\text{OH})]$ , and ferrihydrite  $[\text{Fe}(\text{OH})_3]$ ;
- b) Sodium sulfate and hydrated forms of sodium sulfate (thenardite and mirabilite) based white efflorescence deposits at the vicinity of surface cracks;
- c) Porous paste and aggregate-paste interfaces, abundance of secondary ettringite crystallization in aggregate-paste interfaces and other open spaces; cracking is often associated with these open spaces and either within the voids or extends into cement paste
- d) Oxidation of pyrrhotite in the presence of water and oxygen is reported to have caused the distress by expansive formation of ferrihydrite, and subsequent release of sulfate to paste, sulfate-aluminate reactions with aluminate phases in paste, and expansive formation of secondary ettringite crystals.
- e) In the presence of carbonate ions secondary thaumasite crystallization is also noted.

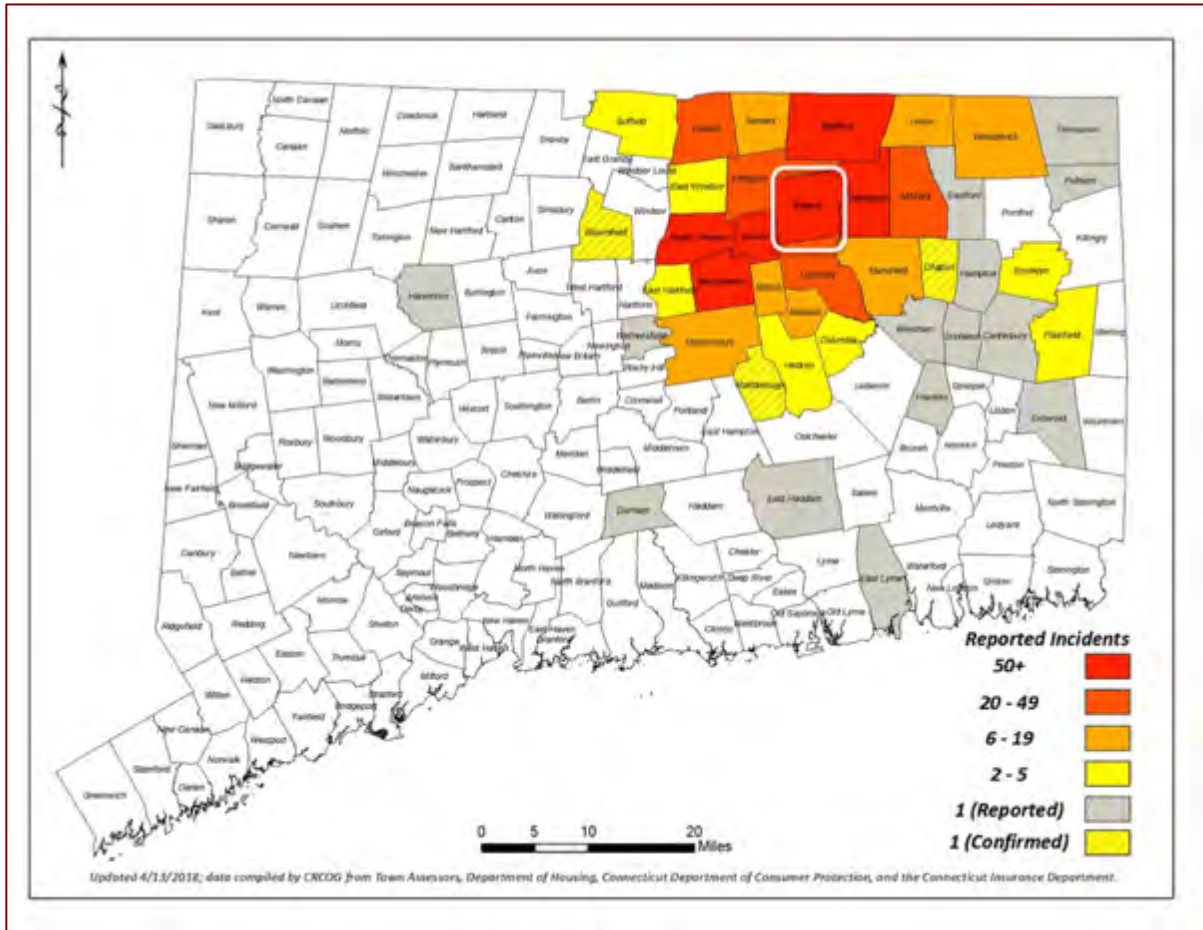


Figure 37: Reported incidences of pyrrhotite-related concrete deterioration in the northeastern Connecticut. Note the present school in Tolland falls right under the high-risk zone for concrete containing aggregates reportedly supplied from the Becker’s quarry that have affected maximum number of foundations.

Along with the findings of Wille and Zhong (2016) and Jana (2018) this study also found formation of poorly crystalline secondary ettringite in the confined areas in paste as ettringite infested paste to be the breeding ground for internal sulfate attack that has caused the expansion and cracking. Relatively well formed secondary ettringite in voids and cracks are the result of exposure to moisture of sulfate-contaminated paste. All these information are primarily obtained from optical microscopy, which is an indispensable tool for this type of investigation. The host rock is garnetiferous quartzo-feldspathic gneiss (again, determined from optical microscopy) containing pyrrhotite having sulfur (as SO<sub>3</sub>) levels from 2 percent in light brown gneiss to as high as 10 percent in predominant dark gray gneiss particles, giving a total bulk sulfate (SO<sub>3</sub>) content of 1.45 percent in the concrete, which is more than 3 times the sulfate in a normal Portland cement concrete without any iron sulfide contaminant. As high as 8 percent pyrrhotite is found from XRD analysis of dark gray gneiss. Pyrrhotite oxidation has readily released sulfates and contaminated the Portland cement paste as detected from high (4 to 6.5%) sulfate contents in paste as opposed to normal less than 1% sulfate found in the paste of a Portland cement concrete containing no iron sulfide contaminants. Ready release of sulfate has promoted internal sulfate attack and subsequent secondary expansion of paste with additional cracking.



Figure 38: Cracking of concrete foundations in Connecticut due to oxidation of pyrrhotite bearing aggregates in concrete. Notice wide cracks in the top row as well as a network of numerous fine cracks in the wall in the bottom right row all from pyrrhotite oxidation and associated expansion of concrete.



Figure 39: Cracking of concrete foundations in Connecticut due to oxidation of pyrrhotite bearing aggregates in concrete. Notice dark reddish brown rust staining on the wall and associated cracking in the top row from pyrrhotite oxidation and formation of ferric oxy-hydroxide oxidation products (goethite, limonite, ferrihydrite rust minerals). Notice wide cracks in the 2<sup>nd</sup> through 4<sup>th</sup> rows from pyrrhotite oxidation and associated expansion of concrete.



Figure 40: Cracking of concrete foundation in Connecticut due to oxidation of pyrrhotite bearing aggregates in concrete. Notice wide cracks in the foundation walls, extensive cracking of walls in the top left photo all reportedly from pyrrhotite oxidation and associated expansion of concrete.

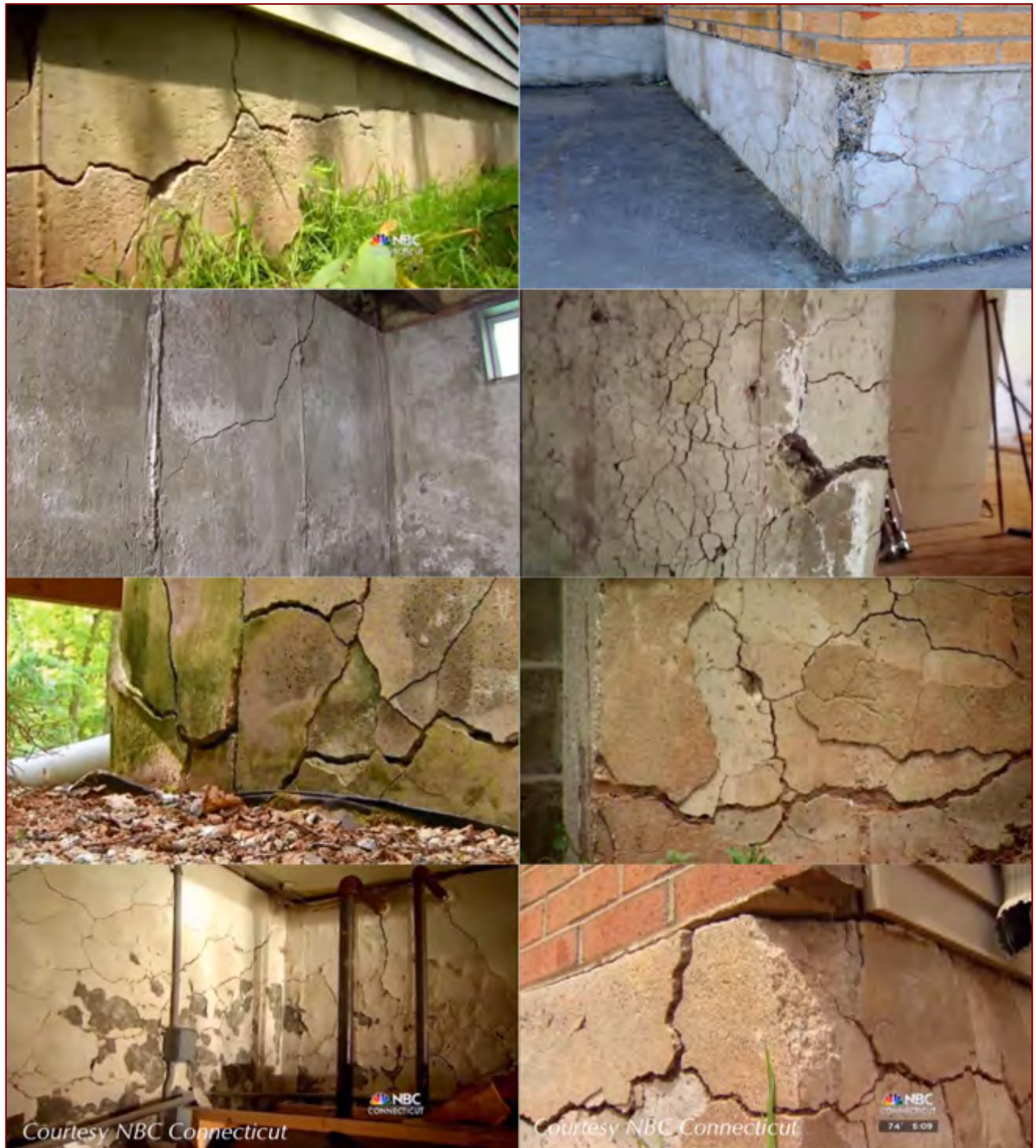


Figure 41: Cracking of concrete foundation in Connecticut due to oxidation of pyrrhotite bearing aggregates in concrete. Notice extensive cracking of foundation in all photos reportedly from pyrrhotite oxidation and associated expansion of concrete.



## CONCLUSIONS

Oxidation of pyrrhotite in concrete aggregates has caused severe damage to concrete foundations in several thousands of residential and commercial buildings in Quebec, Canada, in three concrete dams in Central Pyrenees, Spain, and anticipated to have deteriorated several thousands of residential foundations in eastern Connecticut that have reportedly received concrete containing pyrrhotite-bearing aggregates from the Becker's quarry in Ellington, CT. The amount of pyrrhotite required to cause damage has been found to be as low as 0.3% (total sulfur by mass of aggregate). Recommendations in Europe limit the sulfur content of sulfide-containing aggregates to 1% sulfur by mass unless the presence of pyrrhotite is confirmed in which case the limit is just 0.1% sulfur by mass. Limits on the sulfur contents in aggregates have not yet been imposed in North America.

Based on this comprehensive case study from Tolland, CT, the following conclusions are drawn:

1. Observed cracking of concrete foundation walls around the Birch Grove School in Tolland, CT is determined to be due *oxidation of unsound pyrrhotite grains in crushed garnetiferous quartzo-feldspathic and biotitic gneiss coarse aggregate* particles in the presence of oxygen and moisture during service in concrete.
2. The host rock for pyrrhotite mineralization used as coarse aggregate in concrete is metamorphic crushed stone coarse aggregates, which is a mixture of a predominant dark gray garnetiferous quartzo-feldspathic and micaceous gneiss (having quartz, albite feldspar, biotite mica, and almandine garnet) with a subordinate amount of metamorphosed gabbro (having ortho and/or clino-pyroxenes, oligoclase plagioclase, garnet, and minor biotite), and, a subordinate light brown garnetiferous quartz-feldspar-mica gneiss (having a higher quartz content than the dark gray gneiss) - all having nominal maximum sizes of  $\frac{3}{4}$  in. (19 mm) showing the typical gneissose texture of alternating bands of quartz-albitic feldspar and micaceous (mostly biotite and less muscovite) minerals that often contain almandine garnet poikiloblast, and equigranular granoblastic texture for metamorphosed gabbro. Amount of pyrrhotite grains varied widely amongst different crushed gneiss particles, irrespective of the host rock mineralogy.
3. Sulfur (as  $SO_3$ ) contents in the pyrrhotite-bearing crushed gneiss aggregates are variable amongst various case studies e.g., from Ellington (where  $SO_3$  contents were *2 percent in light brown gneiss to as high as 10 percent in predominant dark gray gneiss particles*, or perhaps even higher, giving a *total bulk sulfate ( $SO_3$ ) content of 1.45 percent in the concrete, which is more than 3 times the sulfate in a normal Portland cement concrete without any iron sulfide contaminant*) to the present study in Tolland where  $SO_3$  content in *unsound crushed gneiss in a core from cracked foundation is 2.43 percent and bulk sulfate contents of concretes across the cores varied from 0.5 to 1.6 percent*. As high as 8 percent pyrrhotite is found from XRD analysis of dark gray gneiss in Ellington, CT indicating significant pyrrhotite mineralization in the dark gray gneiss used as coarse aggregate.
4. Oxidation of pyrrhotite has formed *ferrihydrite* with an expansion of unsound crushed gneiss coarse aggregate causing extensive cracking in many particles having cracks extending from the affected particles to paste. The typical gneissose texture of quarried aggregates has facilitated crack formation during expansion due to the presence of inherent planes of weakness along the micaceous bands in gneiss. Reddish brown rust stain found in many distressed foundations are due to pyrrhotite (and also pyrite) oxidation and formation of iron oxy-hydroxides (e.g., goethite, limonite) and ferrihydrites. The present cores from Tolland, however, do not show any rusty brown discoloration from pyrrhotite oxidation, or popout from expansion of near-surface unsound pyrrhotite.



5. Evidence of pyrrhotite oxidation is confirmed by: (a) detection of ferrihydrite in XRD, and, (b) from SEM-EDS studies of lower than stoichiometric S/Fe ratio of many pyrrhotite grains (mostly <math><0.50</math>) indicating advanced oxidation. Microstructural evidence of oxidation-related expansion of unsound aggregate is found from extensive cracking of many of these crushed gneiss coarse aggregate particles often extending into the paste.
6. Pyrrhotite oxidation has readily released sulfates and either contaminated the Portland cement paste by *in situ* infestation of ettringite as in the case of Ellington, CT, or simple secondary precipitation in voids, cracks, and porous areas, though more than what usually occur in a normal Portland cement paste exposed to moisture, as in the present case of Tolland. Ready release of sulfate and continued exposure to moisture promotes internal sulfate attack and subsequent secondary expansion of paste with additional cracking.
7. To determine the potential for release of sulfate in an oxidizing environment, bulk concretes from multiple cores as well as two unsound crushed gneiss aggregates from a core (D-3) from visibly cracked foundation were pulverized to pass No. 50 sieve, then immersed in distilled water for 24 hours (for concrete) or in a 35% hydrogen peroxide (strong oxidant) solution for several days (for extracted unsound aggregate). Sulfates released from concrete and aggregates to the filtrates were measured (as  $\text{SO}_4^{2-}$ ) in an anion exchange chromatograph. All samples showed noticeable release of sulfates with unsound aggregate showing more than three times more sulfate relative to the bulk concretes, all contrary to no sulfate released from a control gneiss aggregate containing no pyrrhotite.
8. Sulfates released from pyrrhotite oxidation have reacted with cement hydration products (e.g., calcium hydroxide, calcium aluminate hydrate, calcium monosulfaluminate) and formed poorly crystalline or perhaps colloidal form of ettringite within the confined spaces in paste with the resultant secondary expansion of paste and additional cracking within the paste and around aggregate-paste interfaces. Presence of excess sulfates, moisture, and open spaces of air-voids and cracks – all three conditions have facilitated dissolution and precipitation of well-crystallized fibrous secondary ettringite in voids and occasionally in cracks that were visible in optical microscopy and SEM analyses.
9. Evidence of internal sulfate attack in paste came first from the paste chemistry i.e. (a) very high sulfate ( $\text{SO}_3$ ) content of paste from SEM-EDS studies as in the case of Ellington, CT, and/or from various microstructural evidences in optical and scanning electron microscopy, e.g., (b) ettringite-infested paste containing poorly crystalline (perhaps some colloidal) form of ettringite, (c) well-formed secondary ettringite crystallization in aggregate-paste interfaces, microcracks, and air-voids, often due to moisture-induced dissolution of ettringite from ettringite-infested confined areas of paste and precipitation of relatively well-formed ettringite in voids and cracks, and (d) gaps between aggregates due to expansion of paste (more common in many other concrete distresses due to internal sulfate attack than the present one).
10. Relative roles of primary expansion of unsound aggregates due to pyrrhotite oxidation and secondary expansion of paste due to internal sulfate attack in the overall distress of foundation depend on various factors, e.g., proportion of pyrrhotite (and total available sulfate), moisture condition during service, consolidation and degree of impermeability of concrete to moisture ingress, etc. In the case of Ellington both mechanism were prominent where in the present case of Tolland former is more evident than latter.
11. In light of the observed cracking of foundation walls, particularly in some cores where cracks are seen extended all throughout their recovered lengths (e.g., A-1, A-2, C-1, C-2, D-1, D-2, D-3), and its anticipated progress with potential worsening of condition with time especially in continued presence of moisture at the ground level, repair of the walls showing visible cracks are necessary along with similar precautions for walls where visible cracking has not developed yet even though concrete inside shows cracking (e.g., Cores A-2, A-3, C-2).
12. If the pyrrhotite-bearing crushed gneiss coarse aggregate found in this concrete was indeed from the Becker's quarry in Ellington, CT (as reported for other foundations undergoing similar pyrrhotite-oxidation-related distress including the ones in Ellington), then due to the known geology of pyrrhotite mineralization



in the hydrothermal vein in which this quarry is situated, and its known devastating effects when used in concrete from case studies of multiple homes (Wille and Zhong 2016, Jana 2018) including the present one, use of crushed stone from this quarry for concrete aggregate should be abandoned, or should only be used after extensive evaluation of aggregates for the presence of pyrrhotite (e.g., from magnetic test, total sulfur test from XRF, XRD detection of pyrrhotite amount) and its potential release of sulfate in an accelerated oxidation test of aggregates.

13. Aggregate to be used in a new foundation from other quarries must be evaluated for the possible presence of any unsound constituents, including iron sulfide minerals, e.g., (a) from XRD analysis of quarried stones to detect the amount and speciation of iron sulfide minerals present, (b) from XRF analysis to detect the total sulfur (as  $\text{SO}_3$ ) content of quarried stones, (d) from accelerated oxidation test to detect the rate and level of sulfates that can be released from aggregates, and (e) even from a magnetic test to separate weakly magnetic pyrrhotite grains from other non-magnetic iron sulfide minerals.
14. Since there is no industry specification on the threshold pyrrhotite limit above which potential for oxidation-related distress can occur, and, in fact as low as 0.3% pyrrhotite by mass of aggregate in the host rock has reportedly shown severe distress in concrete (e.g., in Quebec Canada), the best solution is to avoid aggregates containing pyrrhotite for its known damaging affects without further laboratory verification of its potential unsoundness in concrete (e.g., from expansion of mortar bar or concrete prism tests similar to those used for ASR-expansion).

## REFERENCES

- ACI Committee Report 201.2R, Guide to Durable Concrete, ACI Manual of Concrete Practice, Vol. 1, American Concrete Institute, 2008.
- Anderson, W.H., Foundation Problems and Pyrite Oxidation in the Chattanooga Shale, Estill County, Kentucky, Kentucky Geological Survey Report of Investigation, 2008.
- Araujo, G.S., Chinchon, S., and Aguado, A., Evaluation of the behavior of concrete gravity dams suffering from internal sulfate attack, *Revista Ibracon de Estruturas e Materiais* (Ibracon Structures and Materials Journal), Vol. 1, No. 1, pp 84-112, 2008.
- ASTM C 856 "Standard Practice for Petrographic Examination of Hardened Concrete," Vol. 4.02, ASTM International, West Conshohocken, PA, 2014.
- Ayora, C., Chinchon, S., Aguado, A. and Guirado, F. (1998). Weathering of iron sulfides and concrete alteration: thermodynamic model and observation in dams from Central Pyrenees, Spain. *Cement and Concrete Research*, Vol. 28, Issue 4, pp. 1223–1235.
- Belzile, N., Y.W. Chen, M.F.Cai, and Y. Li. (2004). A review on pyrrhotite oxidation. *J., Geochem. Explor.*, Vol. 84, pp. 65–76.
- Bérard, J., Black shale heaving at Ottawa, Canada: Discussion. *Canadian Geotechnical Journal* 1970. 7(2): 113-114.
- Bérubé, M.A., Locat, J., Gélinas, P., Chagon, J.Y., and Lefrancois, P., Heaving of black shale in Québec City. *Canadian Journal of Earth Sciences* 1986. 23: 1774-1781.
- Capitol Region Council of Governments (CRCOG) Meeting on July 2016
- Casanova, I; Agulló, L.; Aguado, A. Aggregate Expansivity Due To Sulfide Oxidation - I. Reaction System And Rate Model, *Cement And Concrete Research*, Vol. 26, No. 7, 1996, P. 993-998.
- Casanova, I.; Aguado, A.; Agulló, L. Aggregate Expansivity due to Sulfide Oxidation - II Physico-Chemical Modeling of Sulfate Attack, *Cement and Concrete Research*, vol. 27, no. 11, 1997, p. 1627-1632



Chinchón-Payá, S.; Aguado, A.; Chinchón, S., A comparative investigation of the degradation of pyrite and pyrrhotite under simulated laboratory conditions. *Engineering Geology*, v. 127, p. 75-80, 2012

Chinchón, J. S., Ayora, C., Aguado, A. and Guirado, F. (1995). Influence of weathering of iron sulfides contained in aggregates on concrete durability, *Cement and Concrete Research*, Vol. 25, No. 6, pp. 1264–1272.

Connecticut Geological and Natural History Survey, DEP, in cooperation with the U.S. Geological Survey, 2000, Bedrock Geology of Connecticut, data format: shape file, file name: bedrock, downloaded from: [http://magic.lib.uconn.edu/cgi-bin/MAGIC\\_DBsearch2.pl? Geography=37800&Loc=0000](http://magic.lib.uconn.edu/cgi-bin/MAGIC_DBsearch2.pl? Geography=37800&Loc=0000) on 9/18/2003, scale 1:50,000.

Côté, F., Bérard, J., Roux, R. Cas de réactivité et de gonflement de remblais granulaires riches en shale pyriteux. *Collection Environment et Géologie*, APGGQ 1991. 12: 225-246. 93

Côté, F., Expansion de shales pyriteux. M.Sc. thesis, Département de genie mineral, École Polytechnique de Montréal, Montréal, Qué, 1990.

CSA A23.1-14/A23.2-14, Appendix P. “Concrete Materials and Methods of Concrete Construction/Test Methods and Standard Practices for Concrete,” Canadian Standards Association, Mississauga, ON, Canada, 2014, pp.668.

Deer, W., Howie, R. and Zussman, J. (1992). An introduction to the rock-forming minerals. 2nd Edition. Pearson education limited, England, 696p.

Duchesne, J. and Fournier, B. (2011). Petrography of concrete deteriorated by weathering of sulphide minerals. *International Cement Microscopy Association Conference*, San Francisco, USA, April 2011. EN-12620 (2003) Aggregates for concrete.

Duchesne, J., Benoît, F., Deterioration of concrete by the oxidation of sulphide minerals in the aggregate. *Journal of Civil Engineering and Architecture* 2013. 7(8): 922-931. EN-12620 (2003) Aggregates for concrete.

Grattan-Bellew, P.E. and W.J. Eden. (1975). Concrete Deterioration and Floor Heave Due to Biogeochemical Weathering of Underlying Shale, *Canadian Geotechnical Journal*, Vol. 12, pp. 372–378.

Hawkins, A.B., and Pinches, G.M., Cause and significance of heave at Llandough Hospital, Cardiff—a case history of ground floor heave due to gypsum growth, *Quarterly Journal of Engineering Geology and Hydrogeology*, 20, 41-57, 1, 1987.

Hoover, S.E., and Lehmann, D., The expansive effects of concentrated pyritic zones within the Devonian Marcellus Shale Formation of North America, *Quarterly Journal of Engineering Geology and Hydrogeology* (2009) 42 (2): 157-164.

Jana, D., “Sample Preparation Techniques in Petrographic Examinations of Construction Materials: A State-of-the-art Review”, *Proceedings of the 28<sup>th</sup> Conference on Cement Microscopy*, International Cement Microscopy Association, Denver, Colorado, pp. 23-70, 2006.

Jana, D., Concrete deterioration from pyrite staining, sewer gases, and chimney flue gases – Case studies showing microstructural similarities, *Proc. of the 30<sup>th</sup> Conference on Cement Microscopy*, International Cement Microscopy Association, Reno, Nevada, 2008.

Jana, D., DEF and ASR in Concrete – A Systematic Approach from Petrography, *Proc. of the 30<sup>th</sup> Conference on Cement Microscopy*, International Cement Microscopy Association, Reno, Nevada, 2008.

Jana, D., Pyrrhotite Epidemic in Eastern Connecticut – A Case Study From Ellington, CT, CMC Interim Report 2018, <https://www.cmc-concrete.com/case-studies>.

Lee, H., Cody, R.D., Cody, A.M., Spry, P.G., The formation and role of ettringite in Iowa highway concrete deterioration. *Cement and Concrete Research* 2005. 35: 332-343.

Mahoney, J., Aggregates Containing Pyrrhotite, Executive Director, Connecticut Transportation Institute, PowerPoint Presentation.



- Marcelino, A.P., Calixto, J.M., Gumieri, A.G., Ferreira, M.C., Caldeira C.L., Silva, M.V., and Costa A.L., Evaluation of pyrite and pyrrhotite in concretes, *Revista ibracon de estruturas e materiais* (Ibracon Structures and Materials Journal), Vol. 9, No. 3, 2016.
- Moum, J., Rosenqvist, I.Th.. 1959. Sulfate Attack on Concrete in the Oslo Region, *Journal of the American Concrete Institute*, 56-18, pp. 257-264.
- Oliveira, I., Cavalaro, S.H.P., Aguado, A. (2014). Evolution of pyrrhotite oxidation in aggregates for concrete, *Materiales De Construccion*, Vo. 64, Issue 316, e038.
- Penner, E., Eden, W.J., Grattan-Bellew, Expansion of pyritic shales, NRC Publication archive, Canadian Building Digest, CBD 152, 1972.
- Quigley, R.M., Vogan, R.W., Black shale heaving at Ottawa, Canada. *Canadian Geotechnical Journal* 1970. 7(2): 106-112.
- Rodgers, John, compiler, 1985. *Bedrock Geological Map of Connecticut: Connecticut Geological and Natural History Survey*. Hartford, Connecticut. 2 sheets, scale 125,000.
- Rodrigues, A., Duchesne, J., Fournier, B. 2015. A new accelerated mortar bar test to assess the potential deleterious effect of sulfide-bearing aggregate in concrete. *Cement and Concrete Research*, 73: 96-110.
- Rodrigues, A., Duchesne, J., Fournier, B. 2016 : Quantitative assessment of the oxidation potential of sulfide-bearing aggregates in concrete using an oxygen consumption test. *Cement and Concrete Composites*, 67: 93-100.
- Rodrigues, A., Duchesne, J., Fournier, B. et al. 2012. Mineralogical and chemical assessment of concrete damaged by oxidation of sulphide-bearing aggregates. *Cement and Concrete Research*, 42: 1336-47.
- Rodrigues, A., Duchesne, J., Fournier, B., Durand, B., Shehata, M., Rivard, P. 2016. Evaluation protocol for concrete aggregates containing iron sulfide minerals. *ACI Materials Journal*, 113 (3): 349-359.
- Shayan, A., Deterioration of a concrete surface due to the oxidation of pyrite contained in pyritic aggregate. *Cement and Concrete Research* 1988. 18: 723-730.
- Tagnit-Hamou, A., M. Saric-Coric and P. Rivard. (2005). Internal deterioration of concrete by oxidation of pyrrhotitic aggregates, *Cement and Concrete Research*, Vol. 35, p. 99–107.
- Uytenbogaardt. W., Burke, E.A.J. *Tables for Microscopic Identification of Ore Minerals*. Amsterdam, Netherlands: Elsevier Publishing Company. Pp. 139, 1971.
- Wille, K. and Zhong, R. 2016. "Investigating the deterioration of basement walls made of concrete in CT." University of Connecticut, Storrs, CT 06269. 93 p.

★ ★ ★ END OF TEXT ★ ★ ★

The above conclusions are based solely on the information and samples provided at the time of this investigation. The conclusion may expand or modify upon receipt of further information, field evidence, or samples. Samples will be returned after submission of the report as requested. All reports are the confidential property of clients, and information contained herein may not be published or reproduced pending our written approval. Neither CMC nor its employees assume any obligation or liability for damages, including, but not limited to, consequential damages arising out of, or, in conjunction with the use, or inability to use this resulting information.



# APPENDIX A

## Field Photos, Core Locations, and Cores As Received

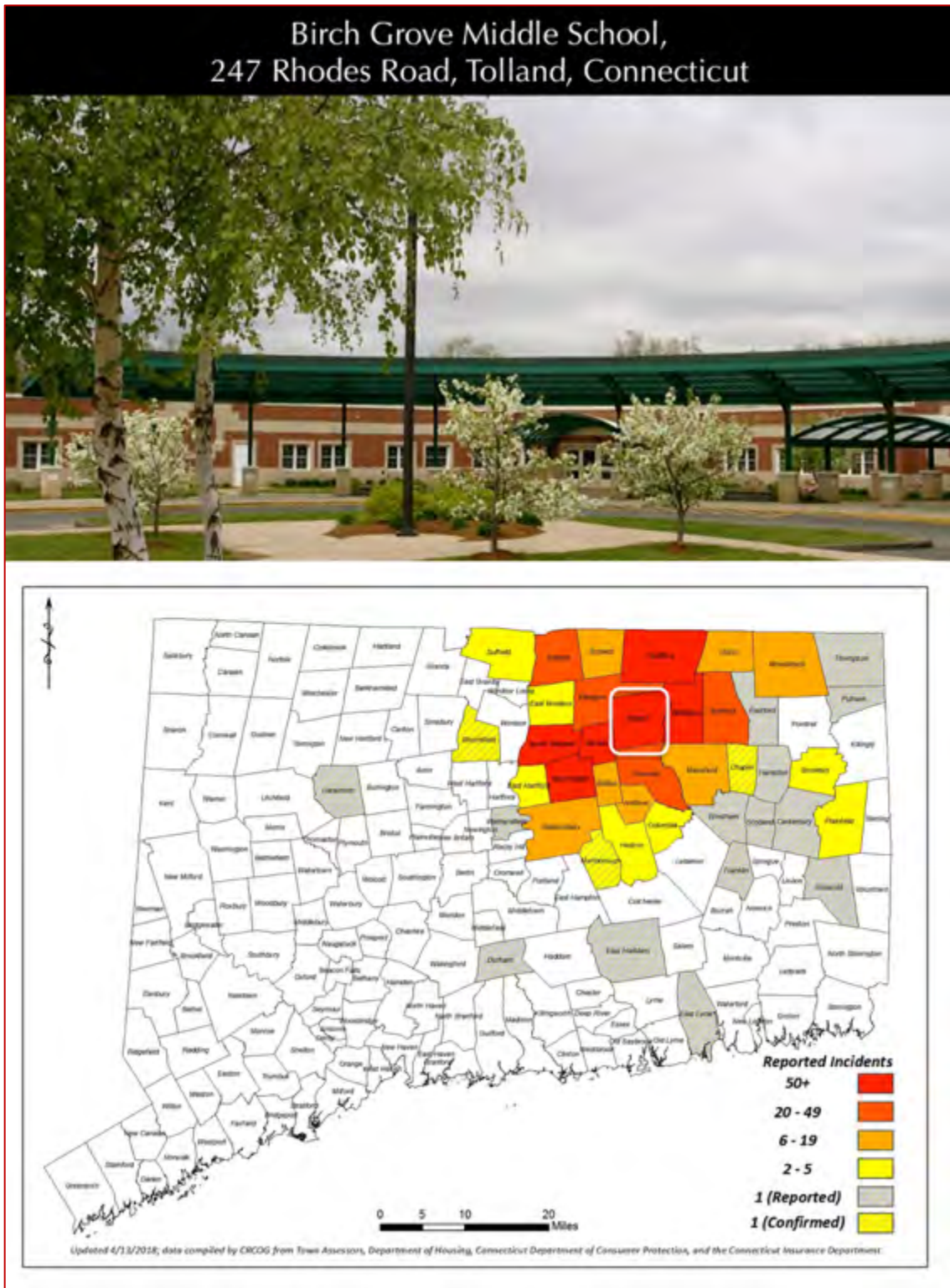


Figure A 1: Birch Grove Middle School at 247 Rhodes Road, Tolland, Connecticut from where concrete core samples for this study were retrieved. Bottom map of eastern Connecticut shows locations where pyrrhotite-related cracking of concrete foundations are reported. Tolland is located in a zone (boxed) that has the maximum occurrence of pyrrhotite-related distress where more than 50 buildings as of April of 2018 are reported to have cracked from pyrrhotite in crushed stone coarse aggregates used in concrete.

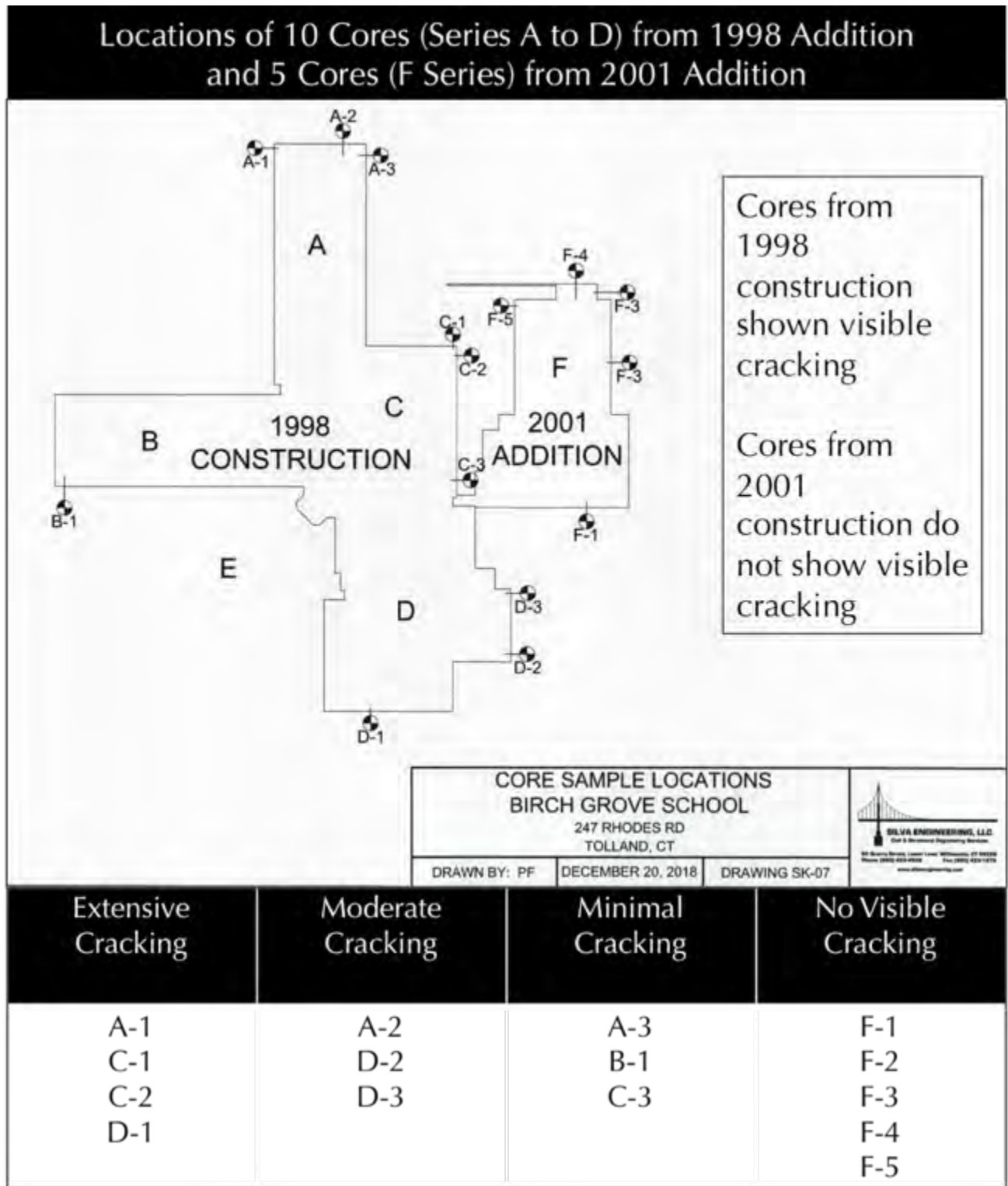


Figure A 2: Schematic drawing showing locations of cores collected from around the buildings from 1998 and 2001 constructions. Different degree of cracking visible on the cylindrical and exposed surfaces of cores from 1998 construction related to availability of moisture into concrete during service to trigger pyrrhotite-related deteriorations to cause cracking.



Figure A 3: Conditions of concrete foundations at the locations of cores from A-series, and B-1. Some visible map cracks are seen in the foundation from where Core A-1 was retrieved.



Figure A 4: Conditions of concrete foundations at the locations of cores from C-series. Some visible map cracks are seen in the foundation from where Core C-1 was retrieved.



Figure A 5: Conditions of concrete foundations at the locations of cores from D-series. Some visible map cracks are seen in the foundation from all three core locations.



Figure A 6: Conditions of concrete foundations at the locations of cores from F-series. Some visible map cracks are seen in the foundation from where Core F-4 was retrieved.



Figure A 7: Shown are the formed exposed wall surface with coarse voids and no visible cracking (top left), the fresh fractured inside surface (top right), and cylindrical side views of Core A-1 (middle and bottom), as received. Notice extensive cracking of concrete throughout the depth of the core in the cylindrical side surfaces many of which are marked with arrows.



Figure A 8: Shown are the formed exposed wall surface with a few coarse voids and Y-shaped visible cracking (top left), the fresh fractured inside surface (top right), and cylindrical side views of Core A-2 (middle and bottom), as received. Notice moderate cracking of concrete, mostly at the exposed surface end of the core at the left edge of cylindrical side surfaces which are marked with arrows. Core was received in two unequal pieces probably cracked during coring operation and/or during transportation to our laboratory, probably broke along a pre-existing crack.

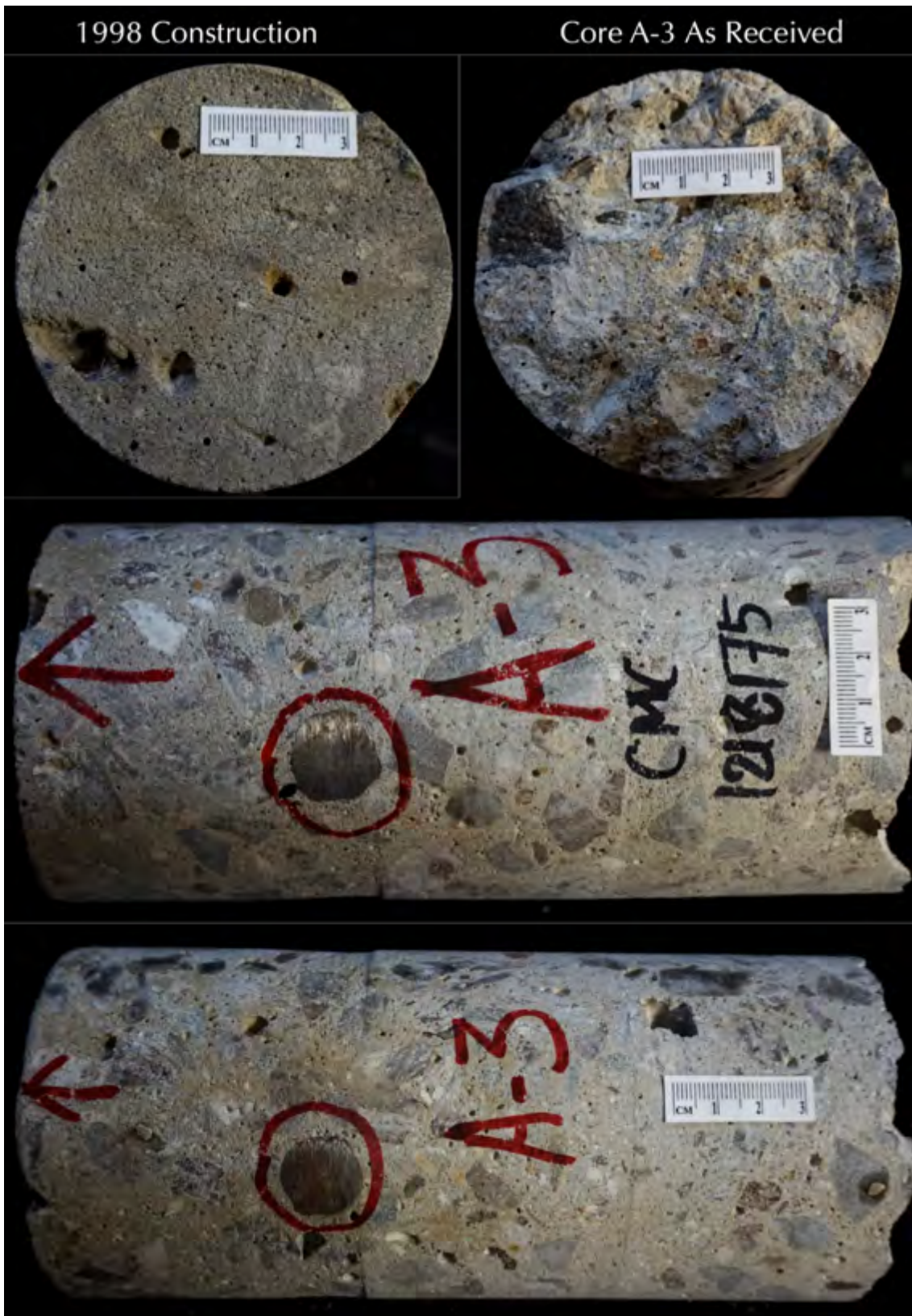


Figure A 9: Shown are the formed exposed wall surface with coarse voids and no visible cracking (top left), the fresh fractured inside surface (top right), and cylindrical side views of Core A-3 (middle and bottom), as received. Notice no visible cracking of concrete throughout the depth of the core in the cylindrical side surfaces.



Figure A 10: Shown are the formed exposed wall surface with coarse voids and no visible cracking (top left), the fresh fractured inside surface (top right), and cylindrical side views of Core B-1 (middle and bottom), as received. Notice no visible cracking of concrete throughout the depth of the core in the cylindrical side surfaces.



Figure A 11: Shown are the formed exposed wall surface with coarse voids and a visible crack marked in red line (top left), the fresh fractured inside surface (top right), and cylindrical side views of Core C-1 (middle and bottom), as received. Notice extensive cracking of concrete throughout the depth of the core in the cylindrical side surfaces many of which are marked with arrows. A No. 6 reinforcing steel at a depth of  $1\frac{3}{4}$  in. from the exposed surface is marked.



Figure A 12: Shown are the formed exposed wall surface with coarse voids and a visible crack marked in red line (top left), the fresh fractured inside surface (top right), and cylindrical side views of Core C-2 (middle and bottom), as received. Notice extensive cracking of concrete throughout the depth of the core in the cylindrical side surfaces many of which are marked with arrows. A No. 6 reinforcing steel at a depth of 2 in. from the exposed surface is marked.



Figure A 13: Shown are the formed exposed wall surface with coarse voids and a visible crack marked in red line (top left), the fresh fractured inside surface (top right), and cylindrical side views of Core C-3 (middle and bottom), as received. Notice no visible cracking of concrete throughout the depth of the core in the cylindrical side surfaces. A No. 6 reinforcing steel at a depth of 1<sup>1</sup>/<sub>4</sub> in. from the exposed surface is marked.



Figure A 14: Shown are the formed exposed wall surface with coarse voids and two perpendicular visible cracks on the exposed surface marked with arrows (top left), the fresh fractured inside surface (top right), and cylindrical side views of Core D-1 (middle and bottom), as received. Notice extensive cracking of concrete throughout the depth of the core in the cylindrical side surfaces many of which are marked with arrows. A No. 6 reinforcing steel at a depth of 1½ in. from the exposed surface is marked.



Figure A 15: Shown are the formed exposed wall surface with a visible crack marked in red line (top left), the fresh fractured inside surface (top right), and cylindrical side views of Core D-2 (middle and bottom), as received. Notice moderate cracking of concrete mostly at the exposed surface end of the core.



Figure A 16: Shown are the formed exposed wall surface (top left), the fresh fractured inside surface (top right), and cylindrical side views of Core D-3 (middle and bottom), as received. Notice moderate cracking of concrete mostly at the exposed surface end of the core.



Figure A 17: Shown are the exposed surface with a thin (~1 mm) protective skim coat (top left), the fresh fractured inside surface (top right), and cylindrical side views of Core F-1 (middle and bottom), as received in two portions with a possible construction joint between the two (marked with arrows in the middle photo). Notice the visibly crack free nature of the concrete throughout the depths of the core. A No. 6 reinforcing steel at a depth of 2 in. from the exposed surface is marked.



Figure A 18: Shown are the exposed surface with a thin (~1 mm) protective skim coat (top left), the fresh fractured inside surface (top right), and cylindrical side views of Core F-2 (middle and bottom), as received. Notice the relatively crack free nature of the concrete throughout the depths of the core.



Figure A 19: Shown are the exposed surface with a thin (~1 mm) protective skim coat (top left), the fresh fractured inside surface (top right), and cylindrical side views of Core F-3 (middle and bottom), as received. Notice the visibly crack free nature of the concrete throughout the depths of the core. A No. 6 reinforcing steel at a depth of 4 in. from the exposed surface is marked.



Figure A 20: Shown are the exposed surface with a thin (~1 mm) protective skim coat (top left), the fresh fractured inside surface (top right), and cylindrical side views of Core F-4 (middle and bottom), as received. Notice the visibly crack free nature of the concrete throughout the depths of the core. A No. 6 reinforcing steel at a depth of 3 1/4 in. from the exposed surface is marked.



Figure A 21: Shown are the exposed surface with a thin (~1 mm) skim coat (top left), the fresh fractured inside surface (top right), and cylindrical side views of Core F-5 (middle and bottom), as received. Notice the relatively crack free nature of the concrete throughout the depths of the core, except along the fresh fractured inside surface (middle photos). A No. 6 reinforcing steel at a depth of 1 1/4 in. from the exposed surface is marked.



# APPENDIX B

## Lapped Cross Sections, Cracks, and Carbonation

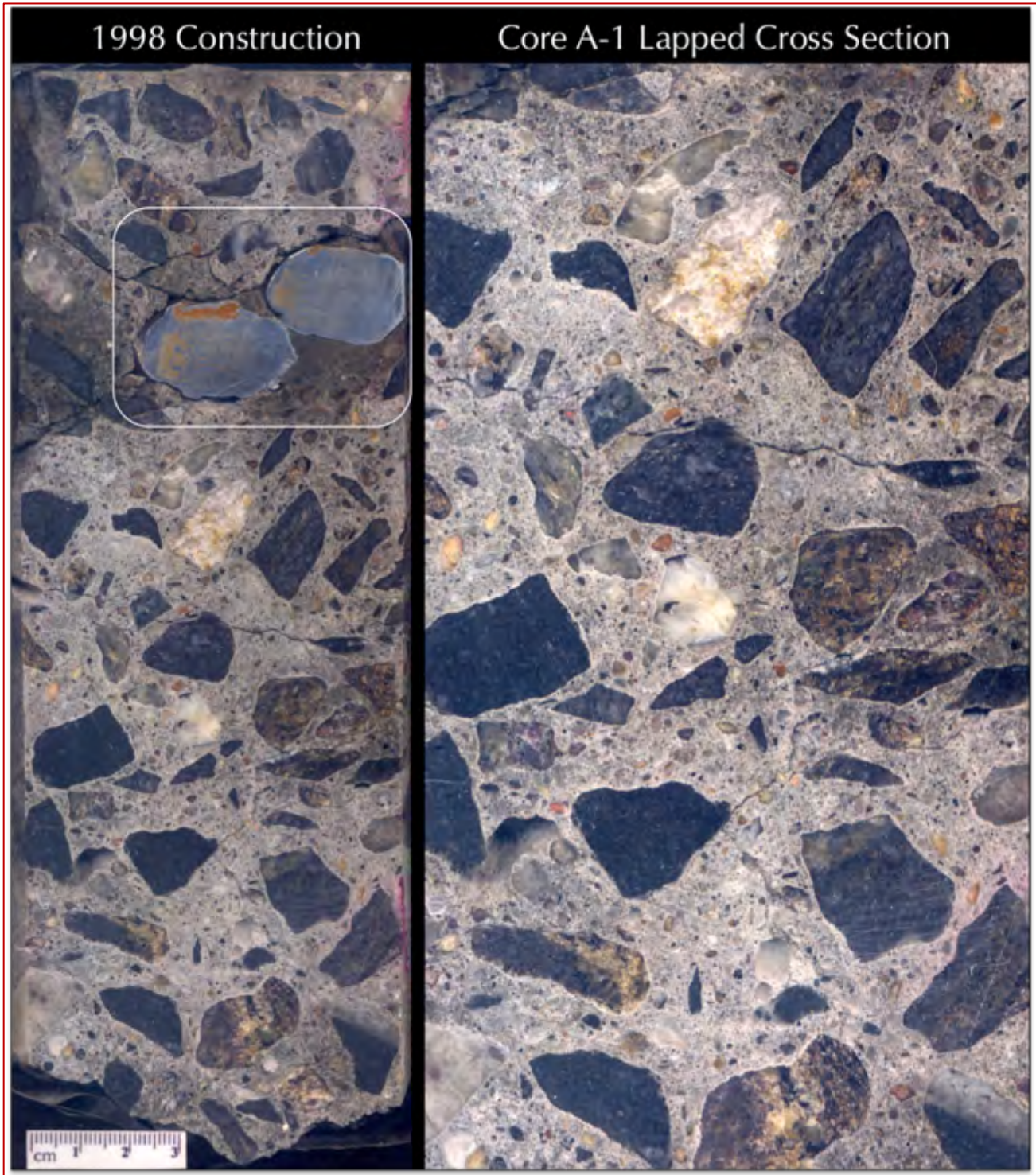


Figure B 1: Lapped cross sections of Core A-1 (right one is enlarged from the left full-depth section) showing: (a) size, shape, angularity, gradation, and distribution of crushed stone coarse aggregate consisting of mixture of a dark gray stone and a lighter pinkish-brown stone, which are found to be metamorphosed gabbro (pyroxene granulite) and garnetiferous quartz-feldspar-biotite gneiss, respectively; (b) natural siliceous sand fine aggregate, (c) reinforcing steels (boxed) that show some surface corrosion; (d) overall dense and well-consolidated nature of concrete across the wall from the exposed end at the top to the opposite fractured end at the bottom; and, most importantly, (e) extensive visible cracking all throughout the depth of the core, which are marked in the next Figure.

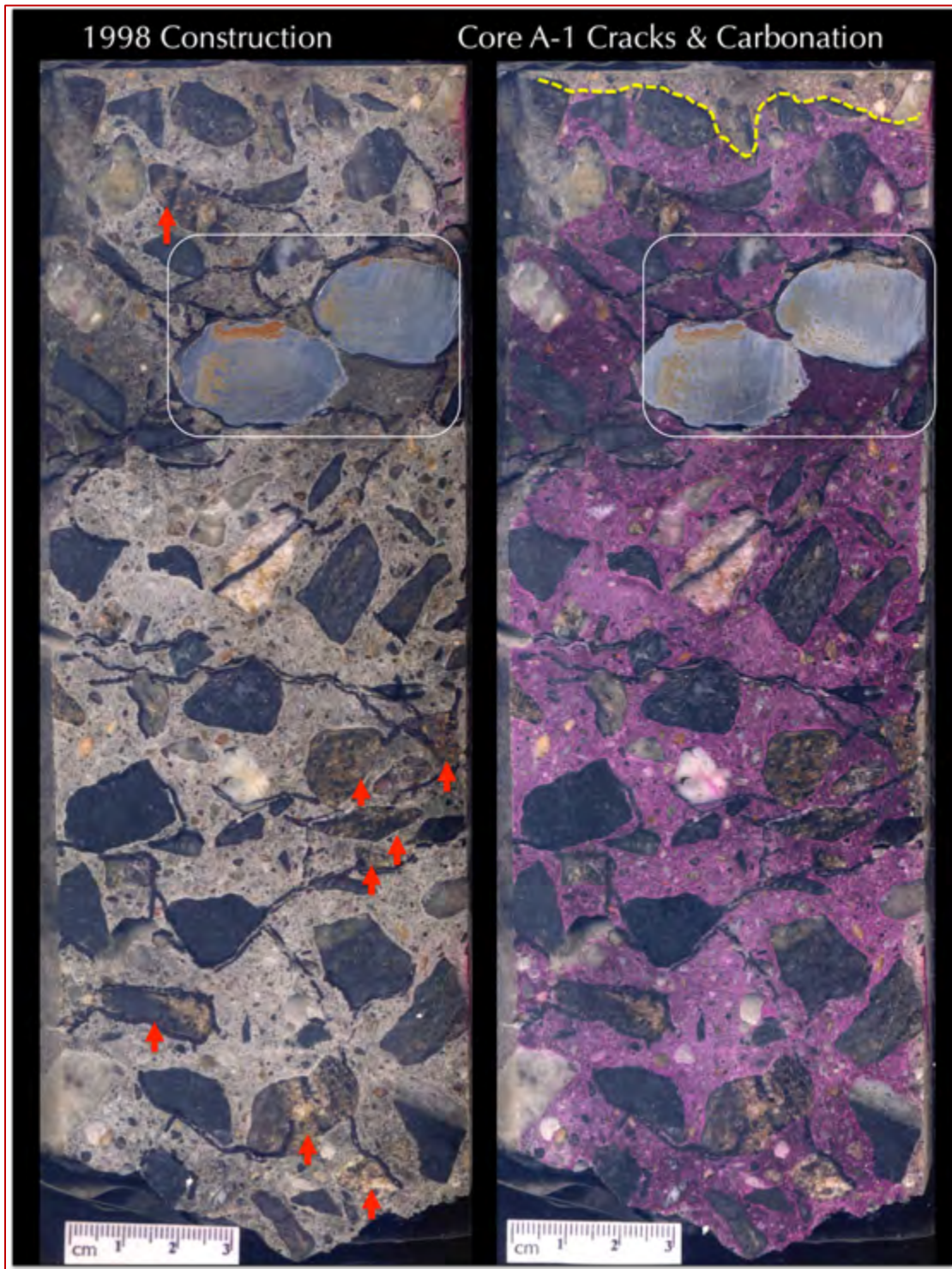


Figure B 2: Lapped cross sections of Core A-1 showing: (a) extensive cracking all throughout the depth of the core, where all visible cracks revealed during stereo-microscopical examination of the lapped cross section are marked with a black marker pen, along with a few unsound light pinkish-brown crushed stone coarse aggregate (garnetiferous quartz-feldspar biotite gneiss) marked in red arrows in the left; and (b) minimal (less than 10 mm deep) carbonation from the formed exposed end of concrete (carbonation front is marked in dashed yellow line on right) after 20 years of service since 1998, a testament of dense, well-consolidated nature of concrete.

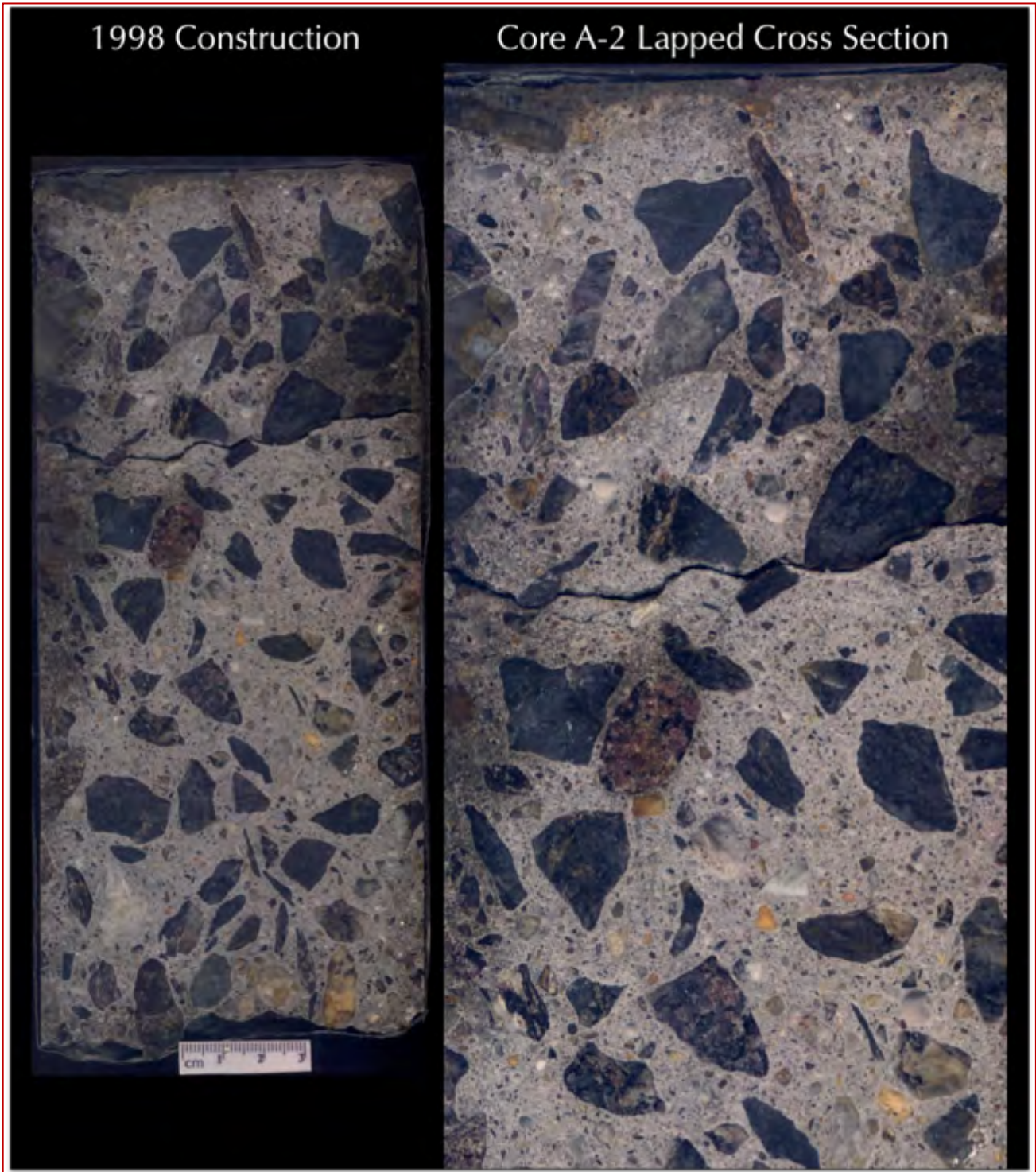


Figure B 3: Lapped cross sections of Core A-2 (right one is enlarged from the left full-depth section) showing: (a) size, shape, angularity, gradation, and distribution of crushed stone coarse aggregate consisting of mixture of a dark gray stone and a lighter pinkish-brown stone, which are found to be metamorphosed gabbro (pyroxene granulite) and garnetiferous quartz-feldspar-biotite gneiss, respectively; (b) natural siliceous sand fine aggregate, (c) overall dense and well-consolidated nature of concrete across the wall from the exposed end at the top to the opposite fractured end at the bottom; and, most importantly, (d) moderate visible cracking all throughout the depth of the core, which are marked in the next Figure.

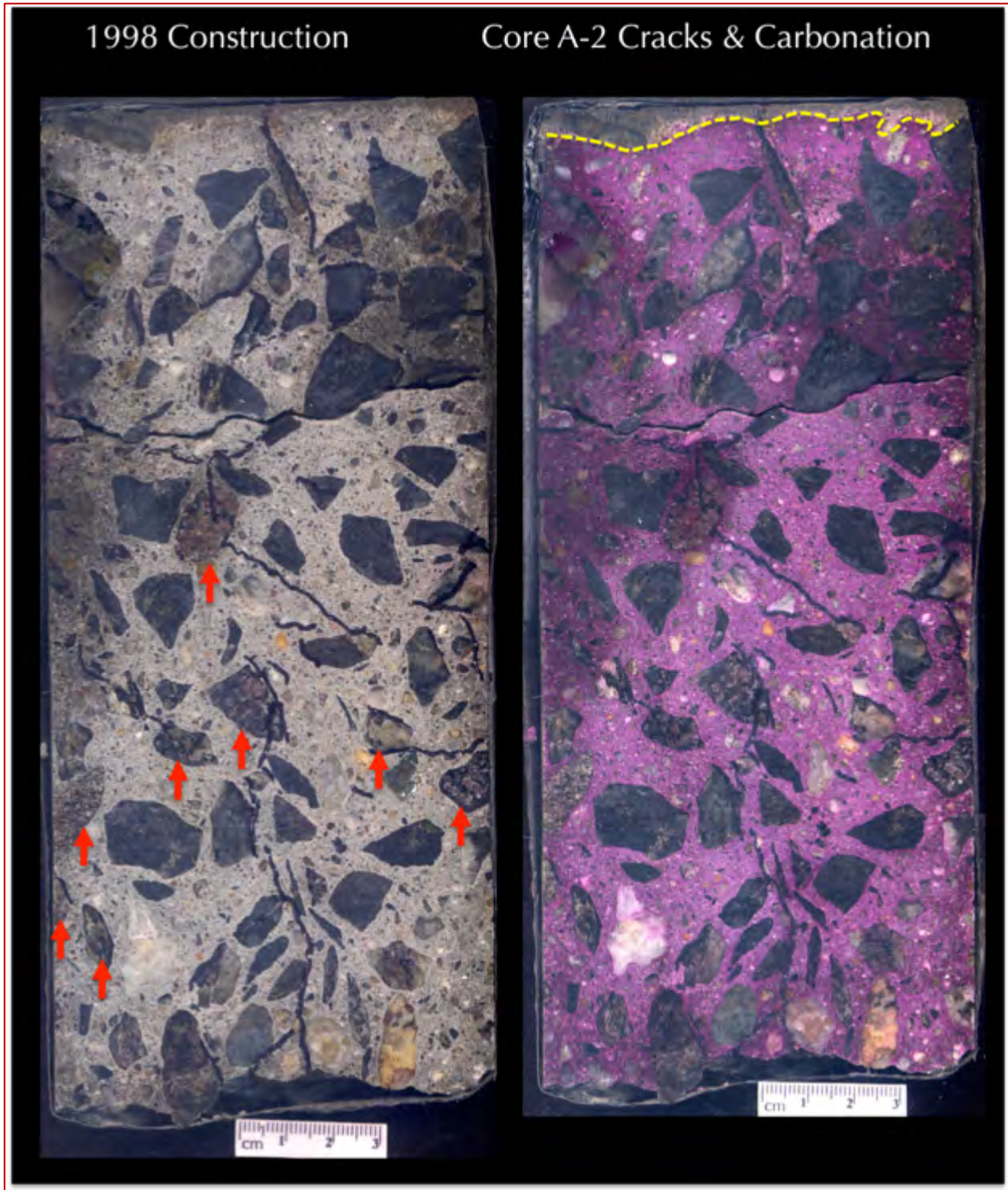


Figure B 4: Lapped cross sections of Core A-2 showing: (a) moderate cracking all throughout the depth of the core, where all visible cracks revealed during stereo-microscopical examination of the lapped cross section are marked with a black marker pen, along with a few unsound light pinkish-brown crushed stone coarse aggregate (garnetiferous quartz-feldspar biotite gneiss) marked in red arrows in the left; and (b) minimal (less than 5 mm deep) carbonation from the formed exposed end of concrete (carbonation front is marked in dashed yellow line on right) after 20 years of service since 1998, a testament of dense, well-consolidated nature of concrete.

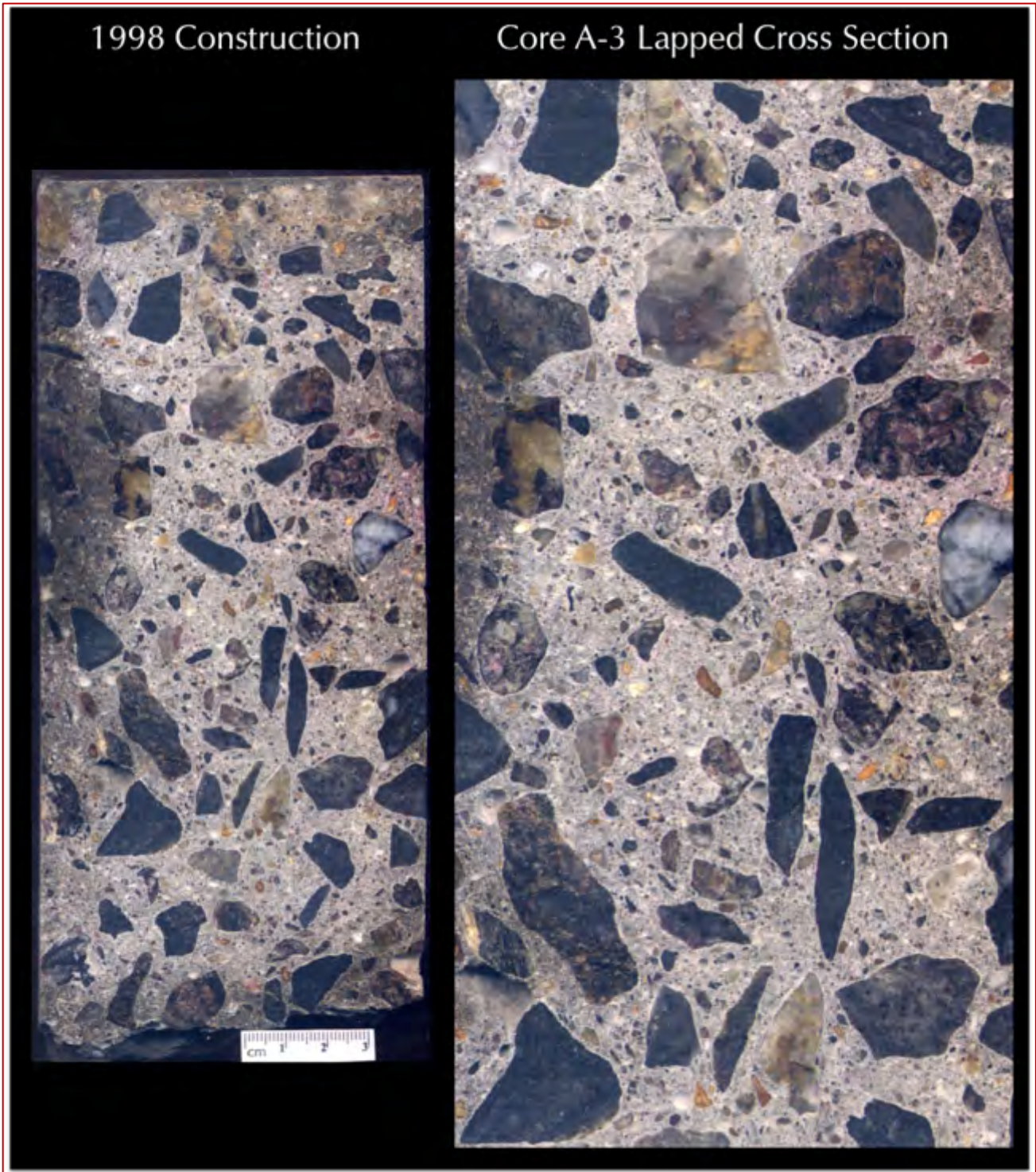


Figure B 5: Lapped cross sections of Core A-3 (right one is enlarged from the left full-depth section) showing: (a) size, shape, angularity, gradation, and distribution of crushed stone coarse aggregate consisting of mixture of a dark gray stone and a lighter pinkish-brown stone, which are found to be metamorphosed gabbro (pyroxene granulite) and garnetiferous quartz-feldspar-biotite gneiss, respectively; (b) natural siliceous sand fine aggregate, (c) overall dense and well-consolidated nature of concrete across the wall from the exposed end at the top to the opposite fractured end at the bottom; and, most importantly, (d) minimal localized visible cracking confined mostly within some crushed stone aggregates.

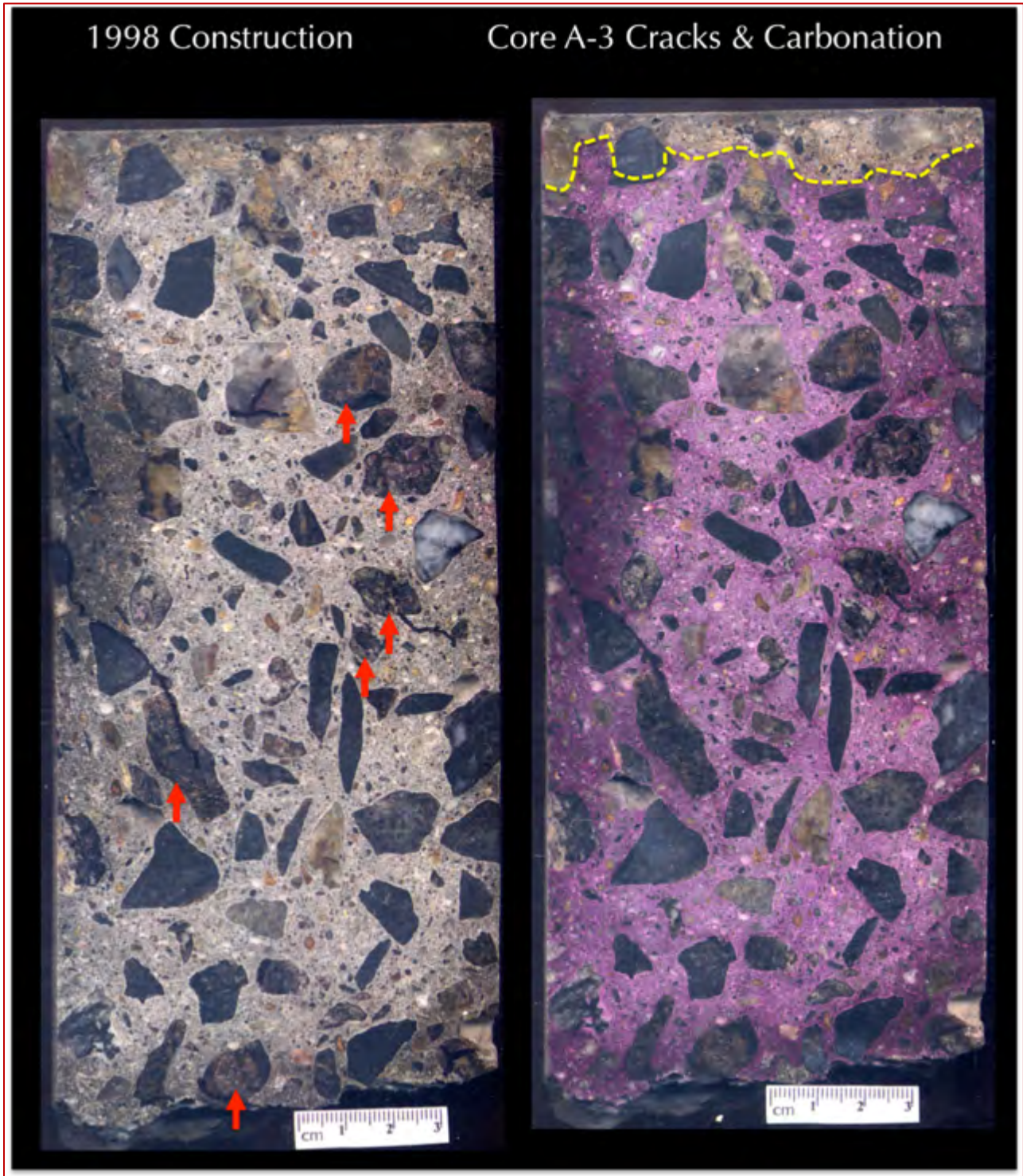


Figure B 6: Lapped cross sections of Core A-3 showing: (a) minimal localized visible cracking confined mostly within some crushed stone aggregates, where visible cracks revealed during stereo-microscopical examination of the lapped cross section are marked with a black marker pen, along with a few unsound light pinkish-brown crushed stone coarse aggregate (garnetiferous quartz-feldspar biotite gneiss) marked in red arrows in the left; and (b) minimal (less than 15 mm deep) carbonation from the formed exposed end of concrete (carbonation front is marked in dashed yellow line on right) after 20 years of service since 1998, a testament of dense, well-consolidated nature of concrete.

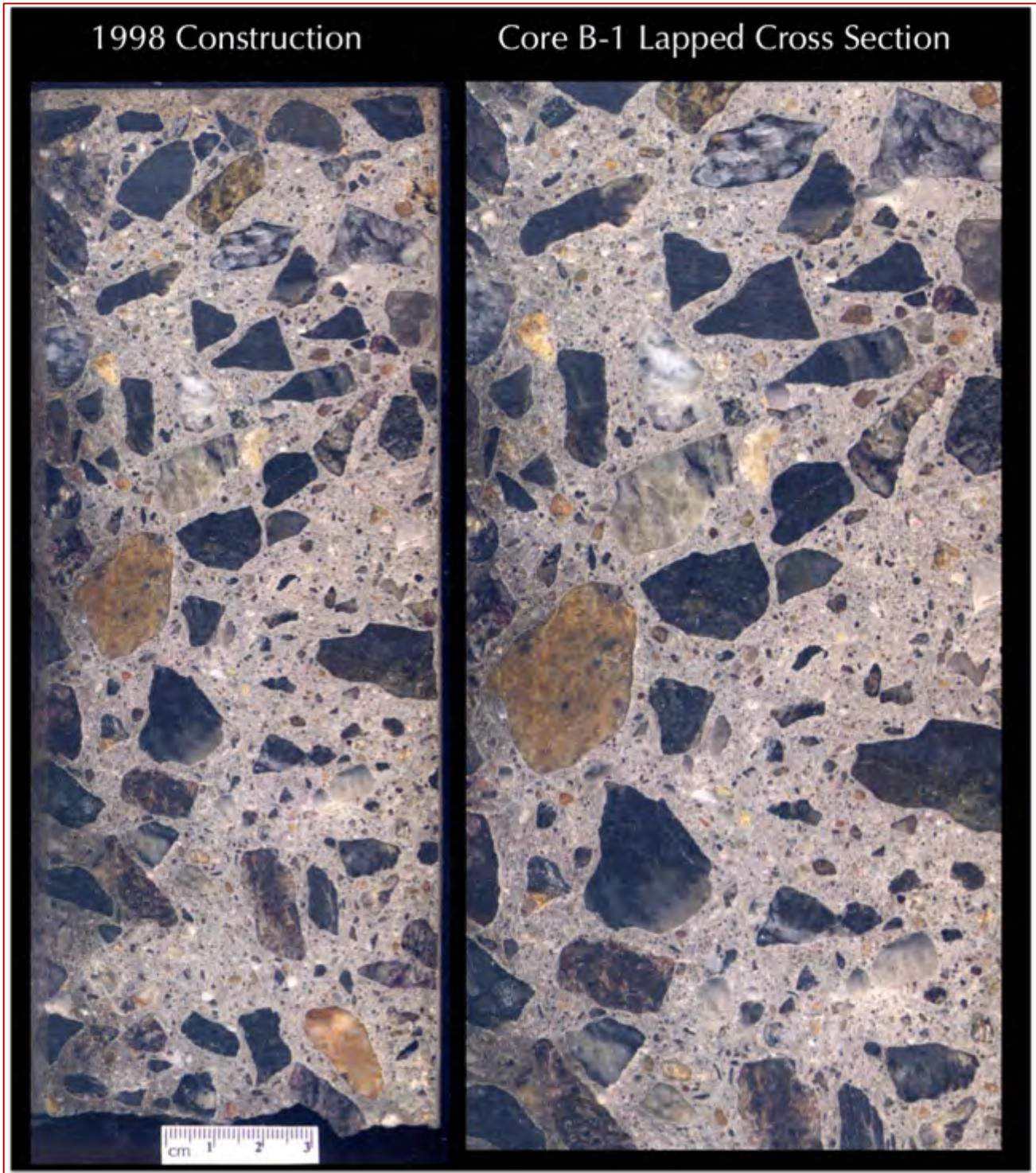


Figure B 7: Lapped cross sections of Core B-1 (right one is enlarged from the left full-depth section) showing: (a) size, shape, angularity, gradation, and distribution of crushed stone coarse aggregate consisting of mixture of a dark gray stone and a lighter pinkish-brown stone, which are found to be metamorphosed gabbro (pyroxene granulite) and garnetiferous quartz-feldspar-biotite gneiss, respectively; (b) natural siliceous sand fine aggregate, (c) overall dense and well-consolidated nature of concrete across the wall from the exposed end at the top to the opposite fractured end at the bottom; and, most importantly, (d) minimal localized visible cracking confined mostly within some crushed stone aggregates.

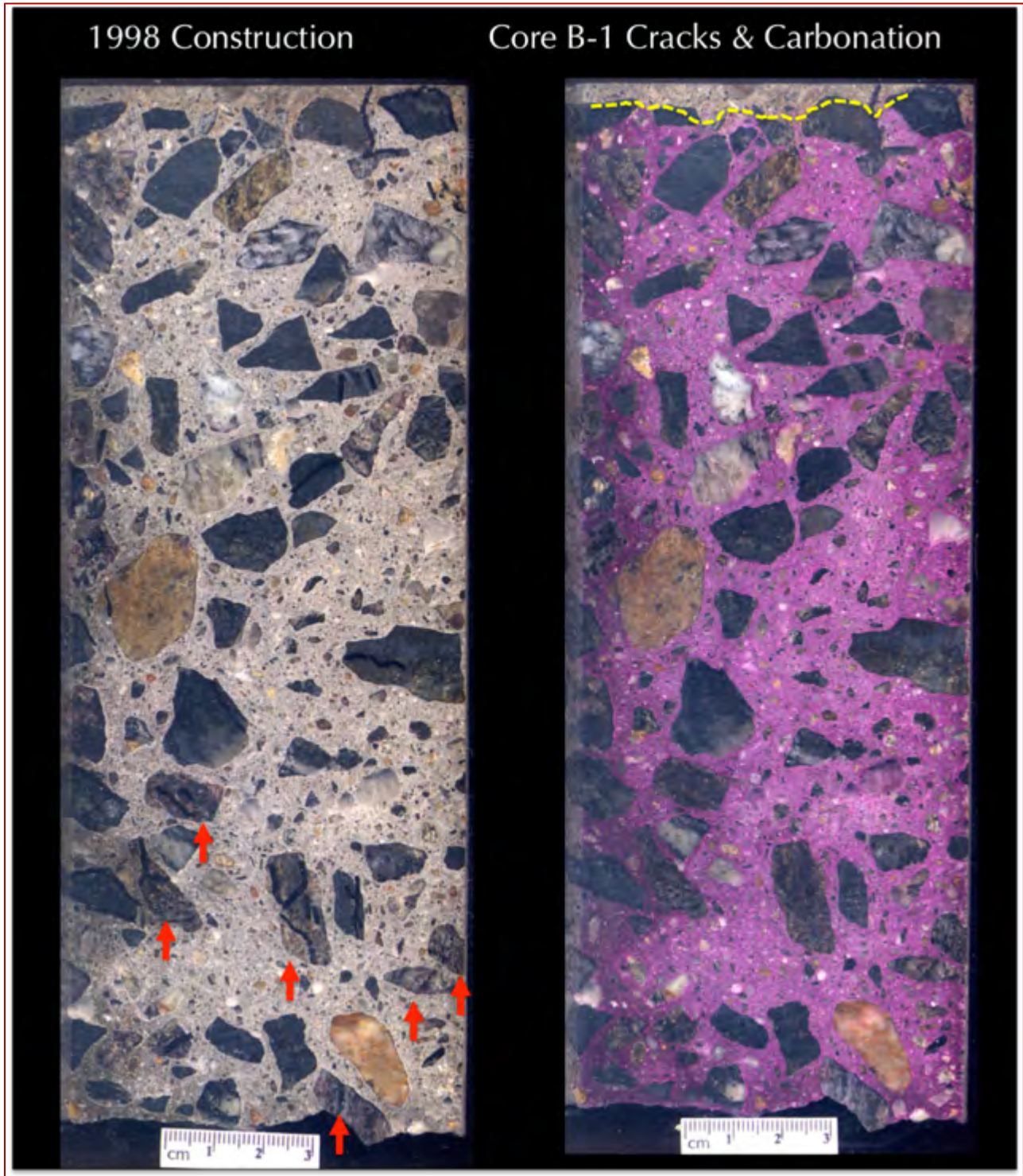


Figure B 8: Lapped cross sections of Core B-1 showing: (a) minimal localized visible cracking confined mostly within some crushed stone aggregates, where visible cracks revealed during stereo-microscopical examination of the lapped cross section are marked with a black marker pen, along with a few unsound light pinkish-brown crushed stone coarse aggregate (garnetiferous quartz-feldspar biotite gneiss) marked in red arrows in the left; and (b) minimal (less than 5 mm deep) carbonation from the formed exposed end of concrete (carbonation front is marked in dashed yellow line on right) after 20 years of service since 1998, a testament of dense, well-consolidated nature of concrete.

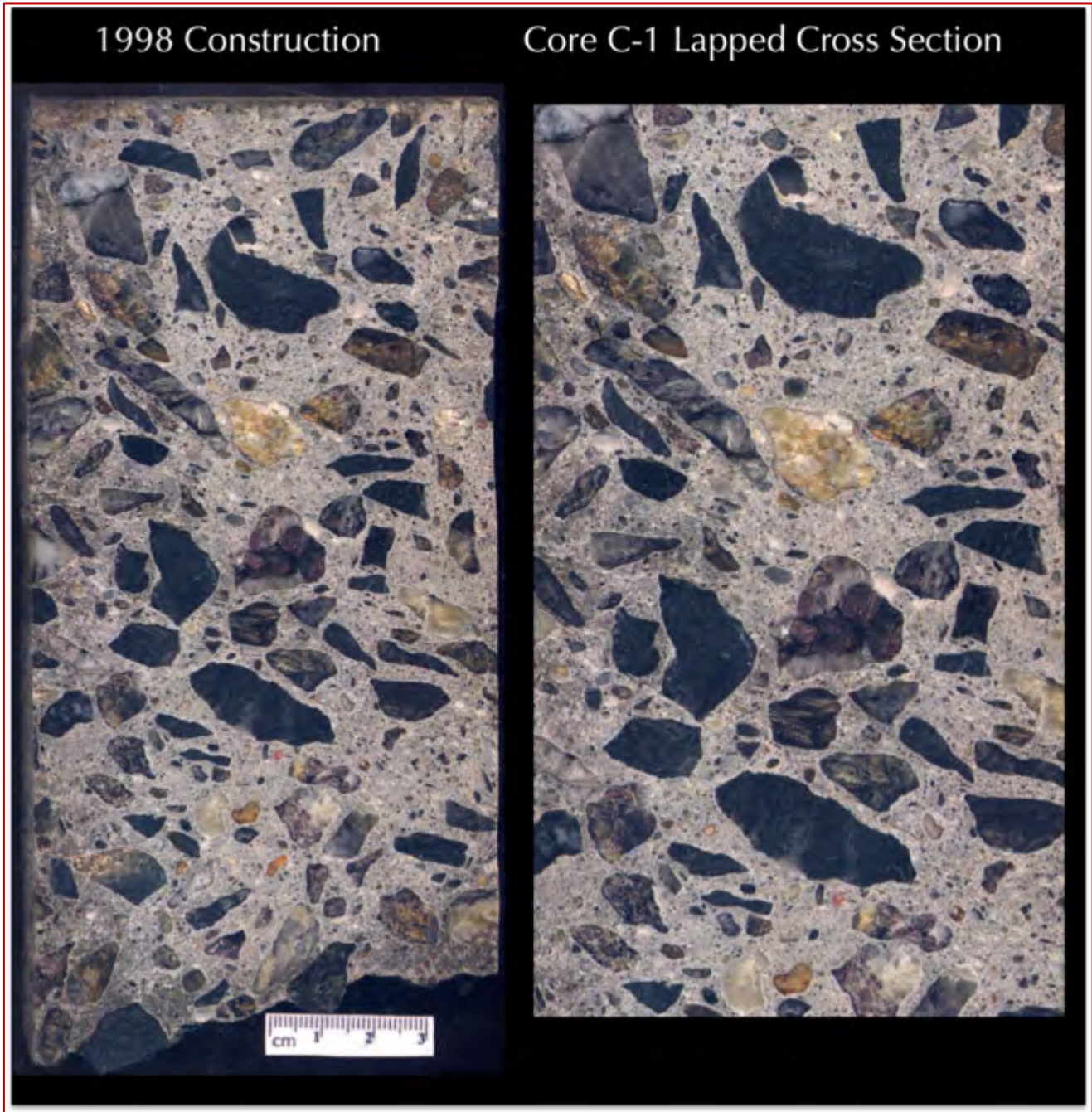


Figure B 9: Lapped cross sections of Core C-1 (right one is enlarged from the left full-depth section) showing: (a) size, shape, angularity, gradation, and distribution of crushed stone coarse aggregate consisting of mixture of a dark gray stone and a lighter pinkish-brown stone, which are found to be metamorphosed gabbro (pyroxene granulite) and garnetiferous quartz-feldspar-biotite gneiss, respectively; (b) natural siliceous sand fine aggregate, (c) overall dense and well-consolidated nature of concrete across the wall from the exposed end at the top to the opposite fractured end at the bottom; and, most importantly, (d) extensive visible cracking all throughout the depth of the core, which are marked in the next Figure.

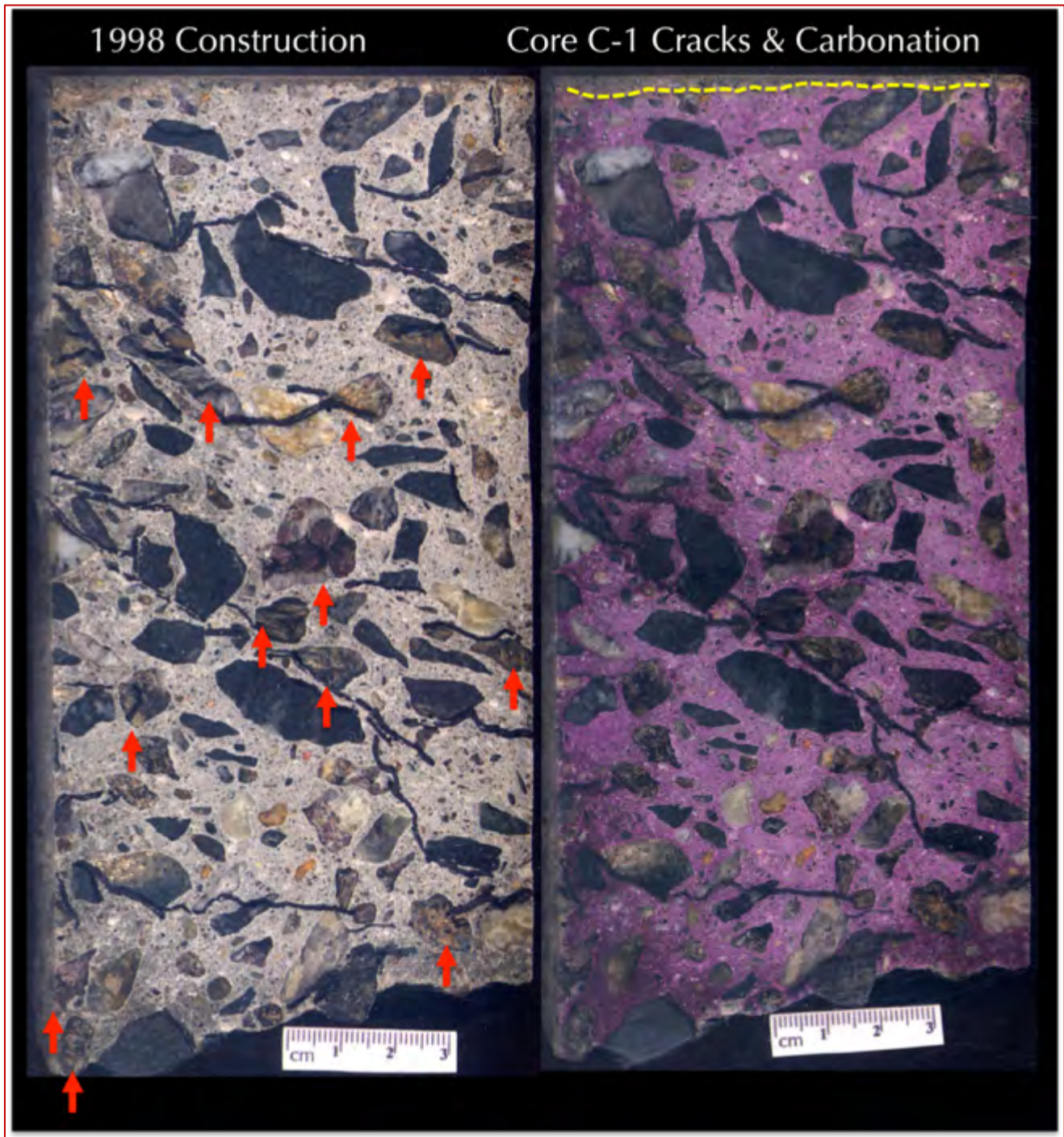


Figure B 10: Lapped cross sections of Core C-1 showing: (a) extensive cracking all throughout the depth of the core, where all visible cracks revealed during stereo-microscopical examination of the lapped cross section are marked with a black marker pen, along with a few unsound light pinkish-brown crushed stone coarse aggregate (garnetiferous quartz-feldspar biotite gneiss) marked in red arrows in the left; and (b) minimal (less than 5 mm deep) carbonation from the formed exposed end of concrete (carbonation front is marked in dashed yellow line on right) after 20 years of service since 1998, a testament of dense, well-consolidated nature of concrete.

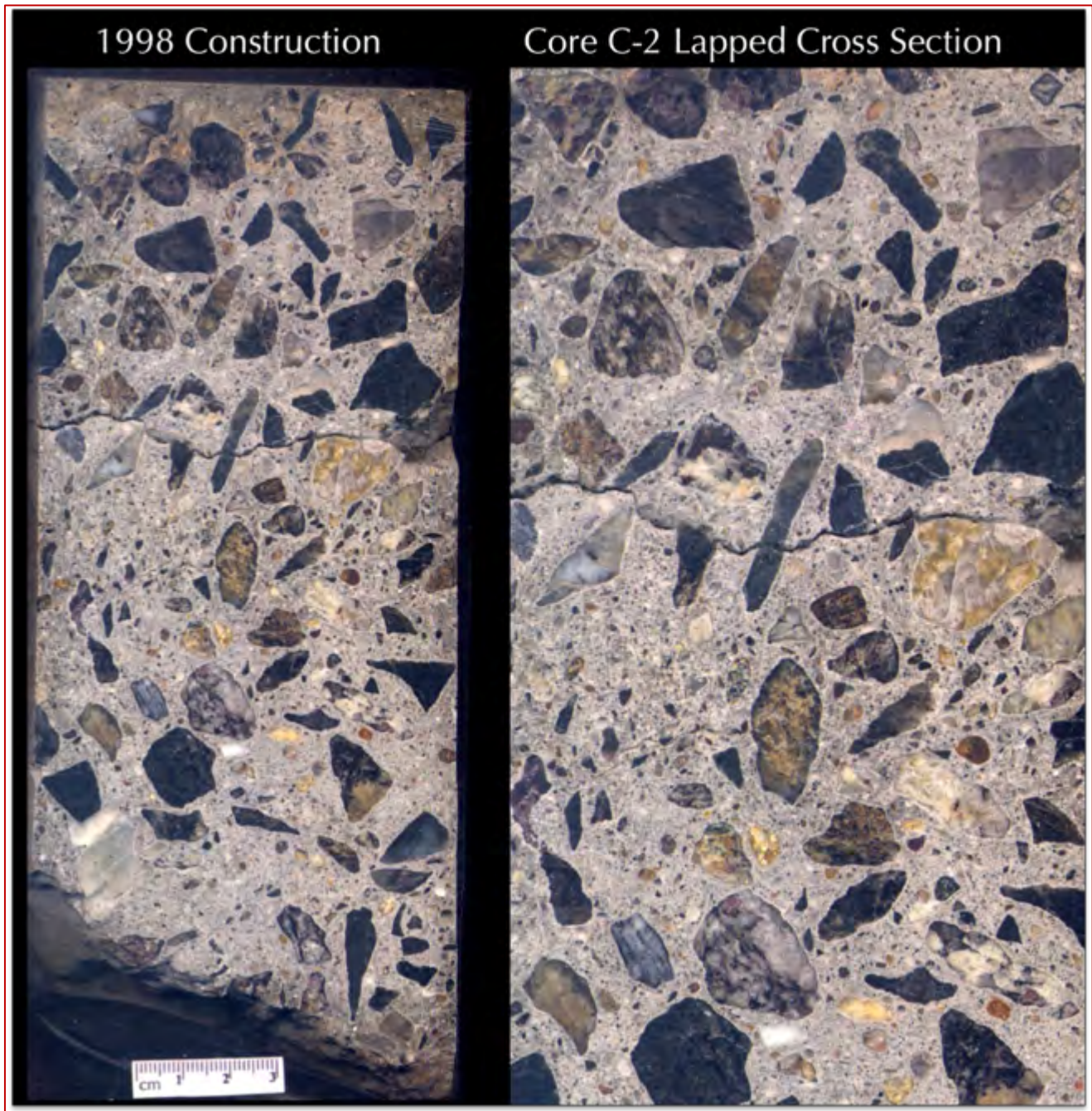


Figure B 11: Lapped cross sections of Core C-2 (right one is enlarged from the left full-depth section) showing: (a) size, shape, angularity, gradation, and distribution of crushed stone coarse aggregate consisting of mixture of a dark gray stone and a lighter pinkish-brown stone, which are found to be metamorphosed gabbro (pyroxene granulite) and garnetiferous quartz-feldspar-biotite gneiss, respectively; (b) natural siliceous sand fine aggregate, (c) overall dense and well-consolidated nature of concrete across the wall from the exposed end at the top to the opposite fractured end at the bottom; and, most importantly, (d) extensive visible cracking all throughout the depth of the core, which are marked in the next Figure.

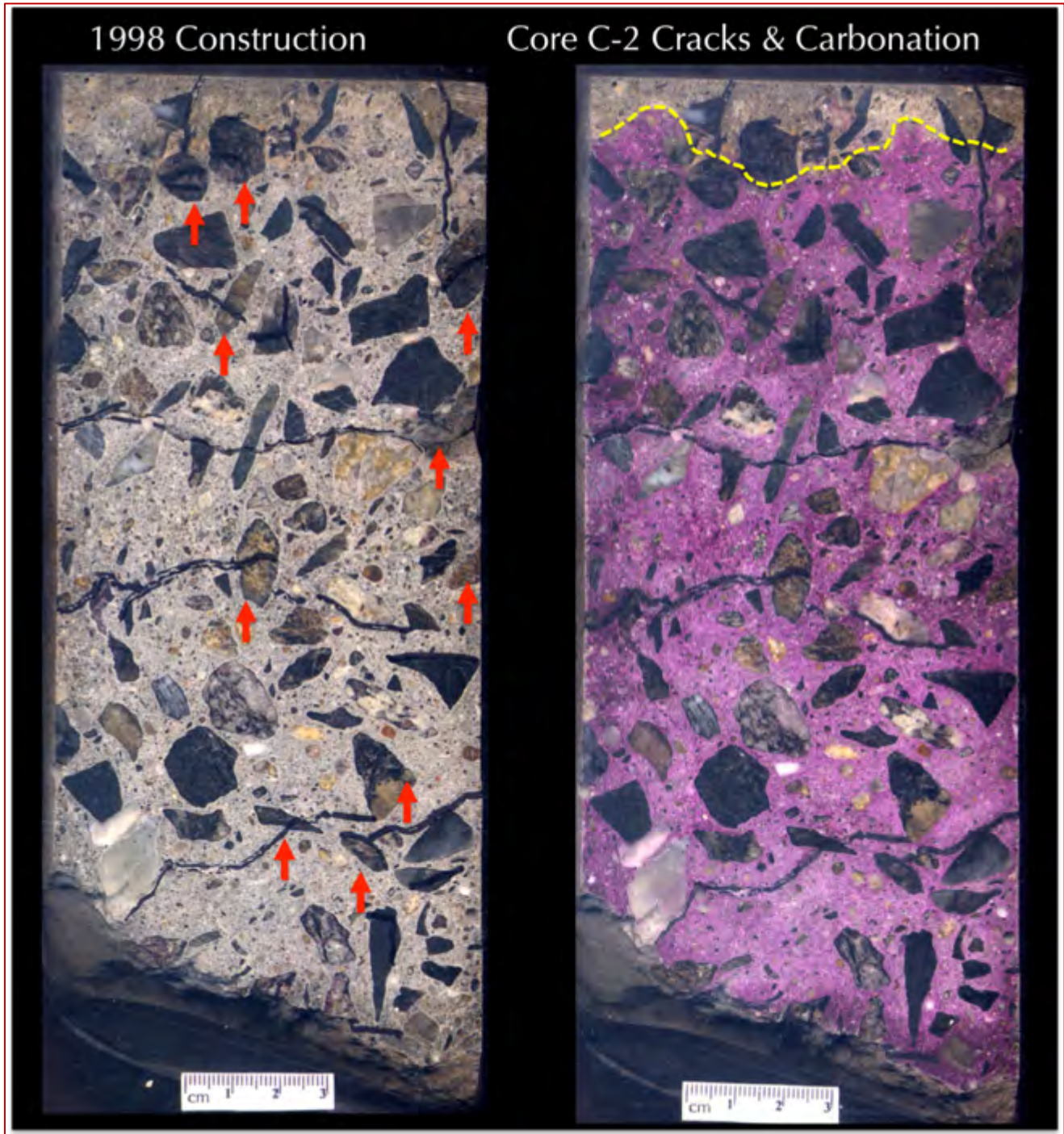


Figure B 12: Lapped cross sections of Core C-2 showing: (a) extensive cracking all throughout the depth of the core, where all visible cracks revealed during stereo-microscopical examination of the lapped cross section are marked with a black marker pen, along with a few unsound light pinkish-brown crushed stone coarse aggregate (garnetiferous quartz-feldspar biotite gneiss) marked in red arrows in the left; and (b) minimal (less than 20 mm deep) carbonation from the formed exposed end of concrete (carbonation front is marked in dashed yellow line on right) after 20 years of service since 1998, a testament of dense, well-consolidated nature of concrete.

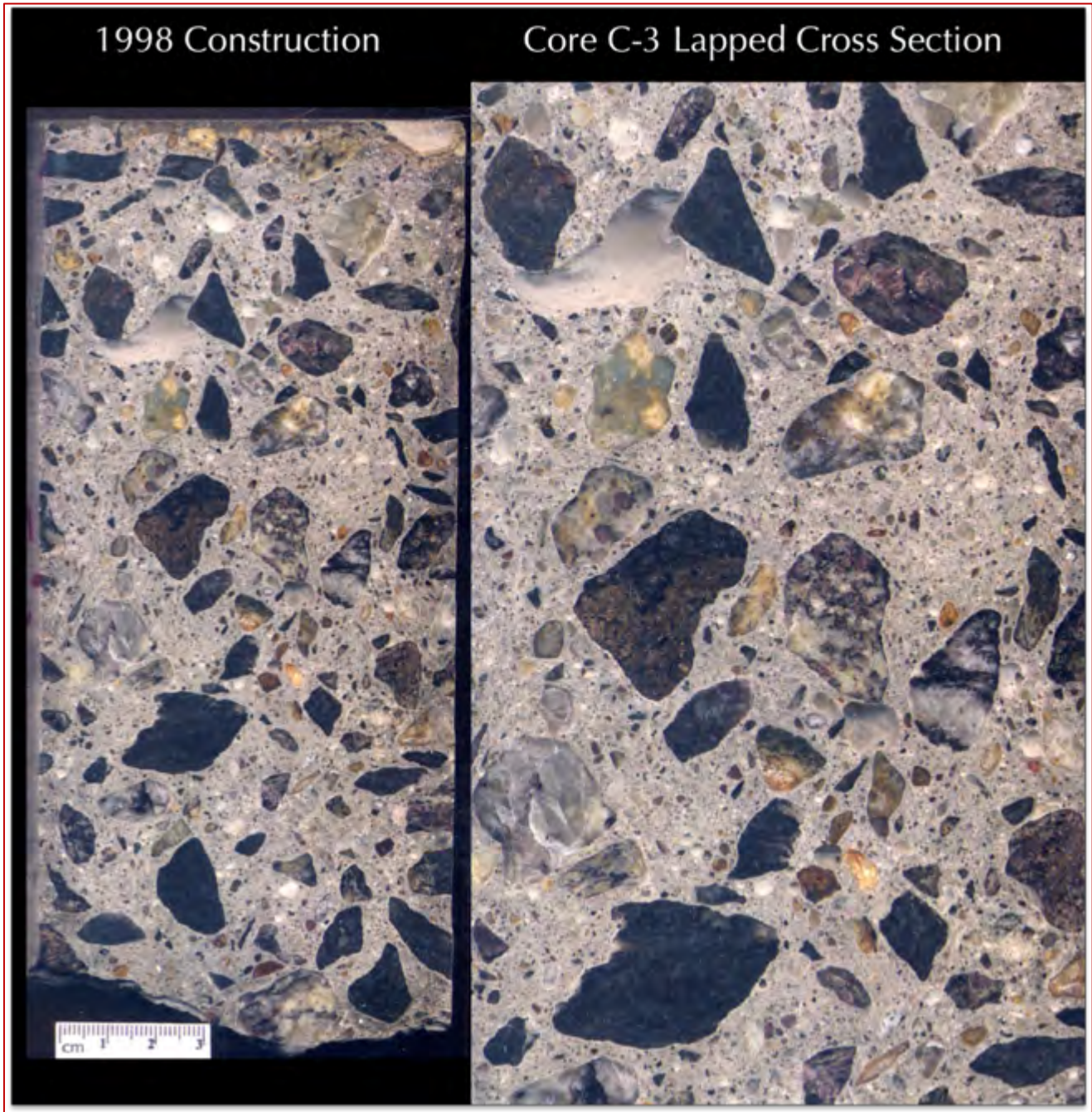


Figure B 13: Lapped cross sections of Core C-3 (right one is enlarged from the left full-depth section) showing: (a) size, shape, angularity, gradation, and distribution of crushed stone coarse aggregate consisting of mixture of a dark gray stone and a lighter pinkish-brown stone, which are found to be metamorphosed gabbro (pyroxene granulite) and garnetiferous quartz-feldspar-biotite gneiss, respectively; (b) natural siliceous sand fine aggregate, (c) overall dense and well-consolidated nature of concrete across the wall from the exposed end at the top to the opposite fractured end at the bottom; and, most importantly, (d) minimal localized visible cracking confined mostly within some crushed stone aggregates.

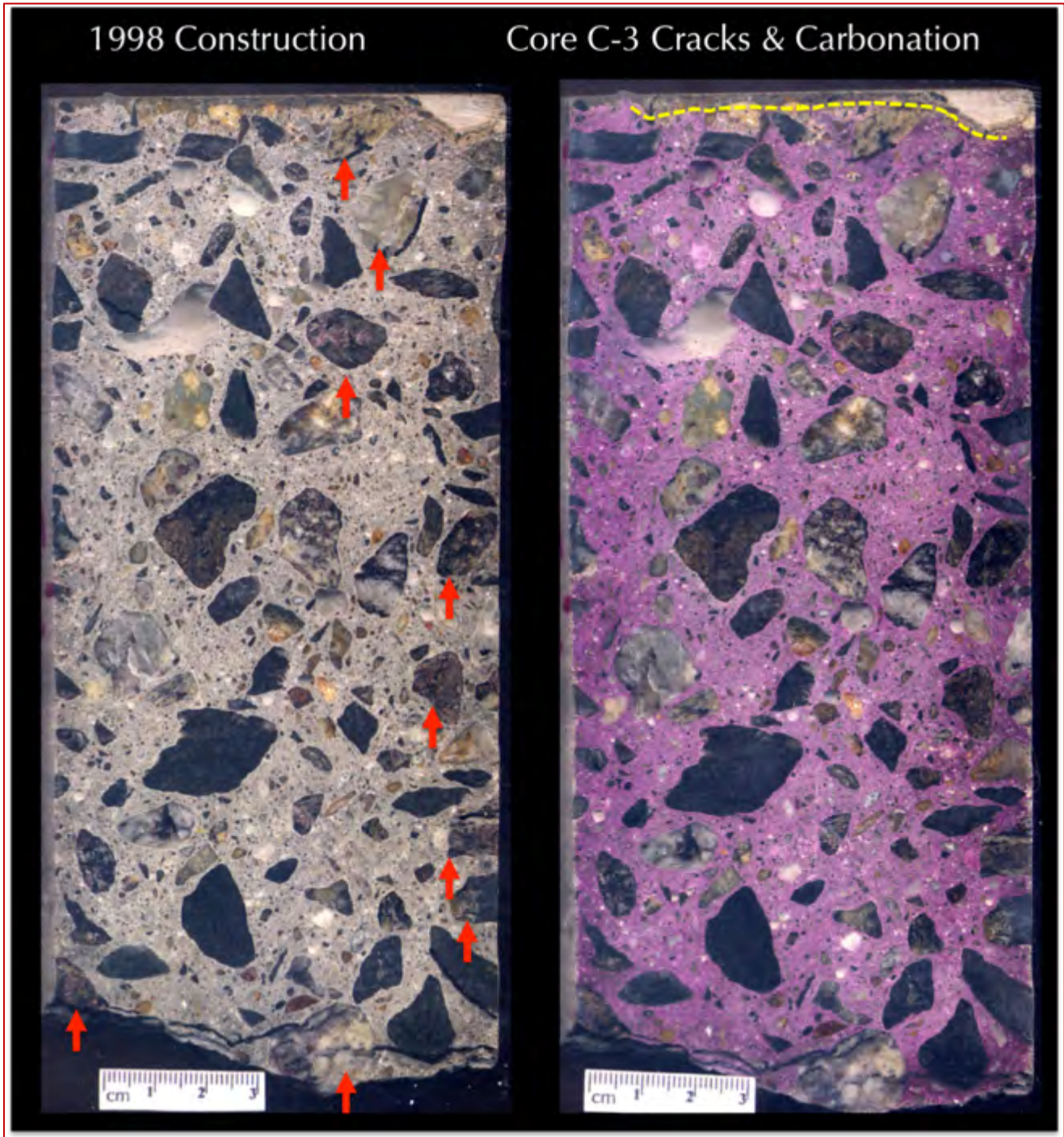


Figure B 14: Lapped cross sections of Core C-3 showing: (a) minimal localized visible cracking confined mostly within some crushed stone aggregates, where visible cracks revealed during stereo-microscopical examination of the lapped cross section are marked with a black marker pen, along with a few unsound light pinkish-brown crushed stone coarse aggregate (garnetiferous quartz-feldspar biotite gneiss) marked in red arrows in the left; and (b) minimal (less than 5 mm deep) carbonation from the formed exposed end of concrete (carbonation front is marked in dashed yellow line on right) after 20 years of service since 1998, a testament of dense, well-consolidated nature of concrete.

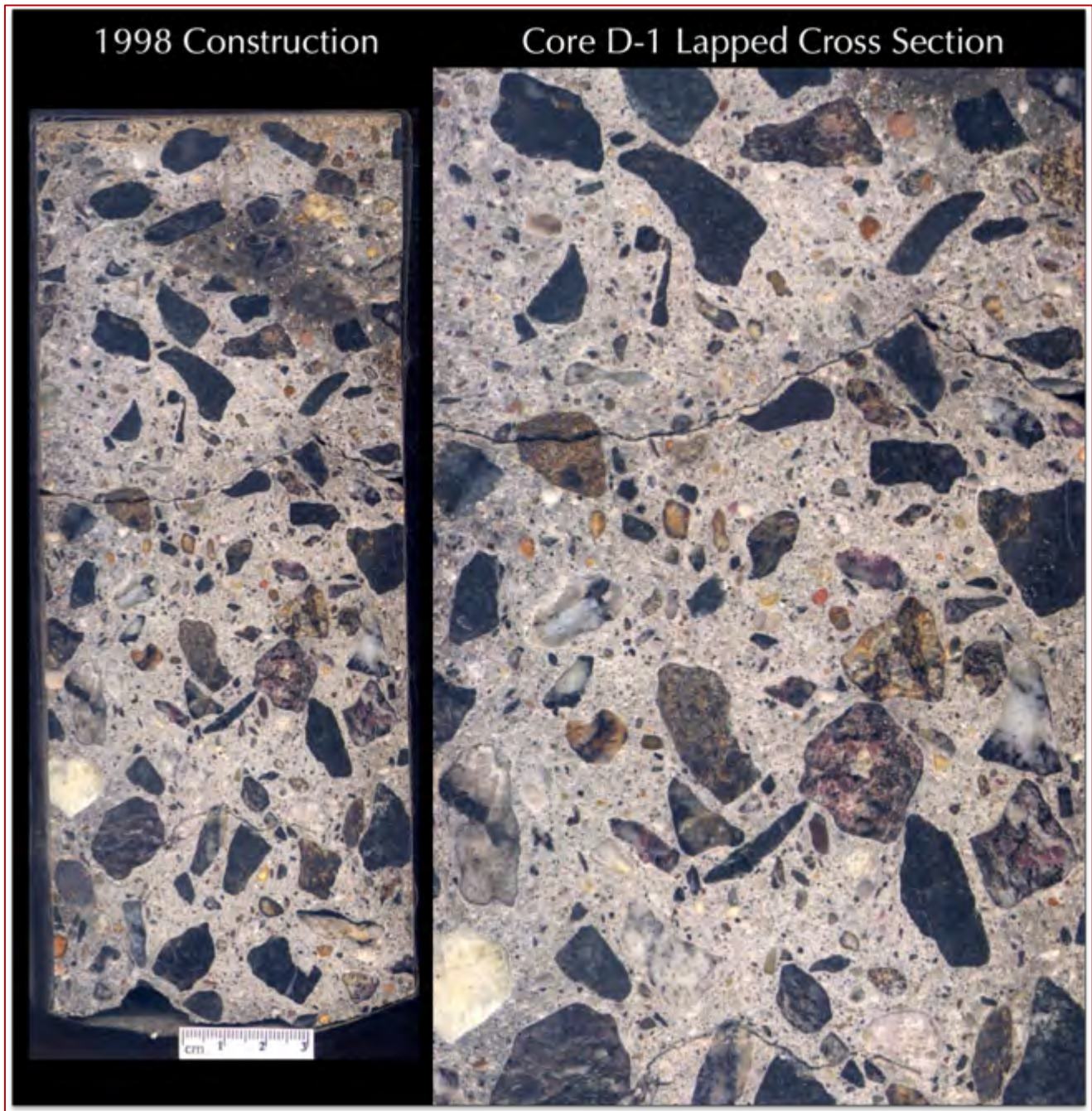


Figure B 15: Lapped cross sections of Core D-1 (right one is enlarged from the left full-depth section) showing: (a) size, shape, angularity, gradation, and distribution of crushed stone coarse aggregate consisting of mixture of a dark gray stone and a lighter pinkish-brown stone, which are found to be metamorphosed gabbro (pyroxene granulite) and garnetiferous quartz-feldspar-biotite gneiss, respectively; (b) natural siliceous sand fine aggregate, (c) overall dense and well-consolidated nature of concrete across the wall from the exposed end at the top to the opposite fractured end at the bottom; and, most importantly, (d) extensive visible cracking all throughout the depth of the core, which are marked in the next Figure.

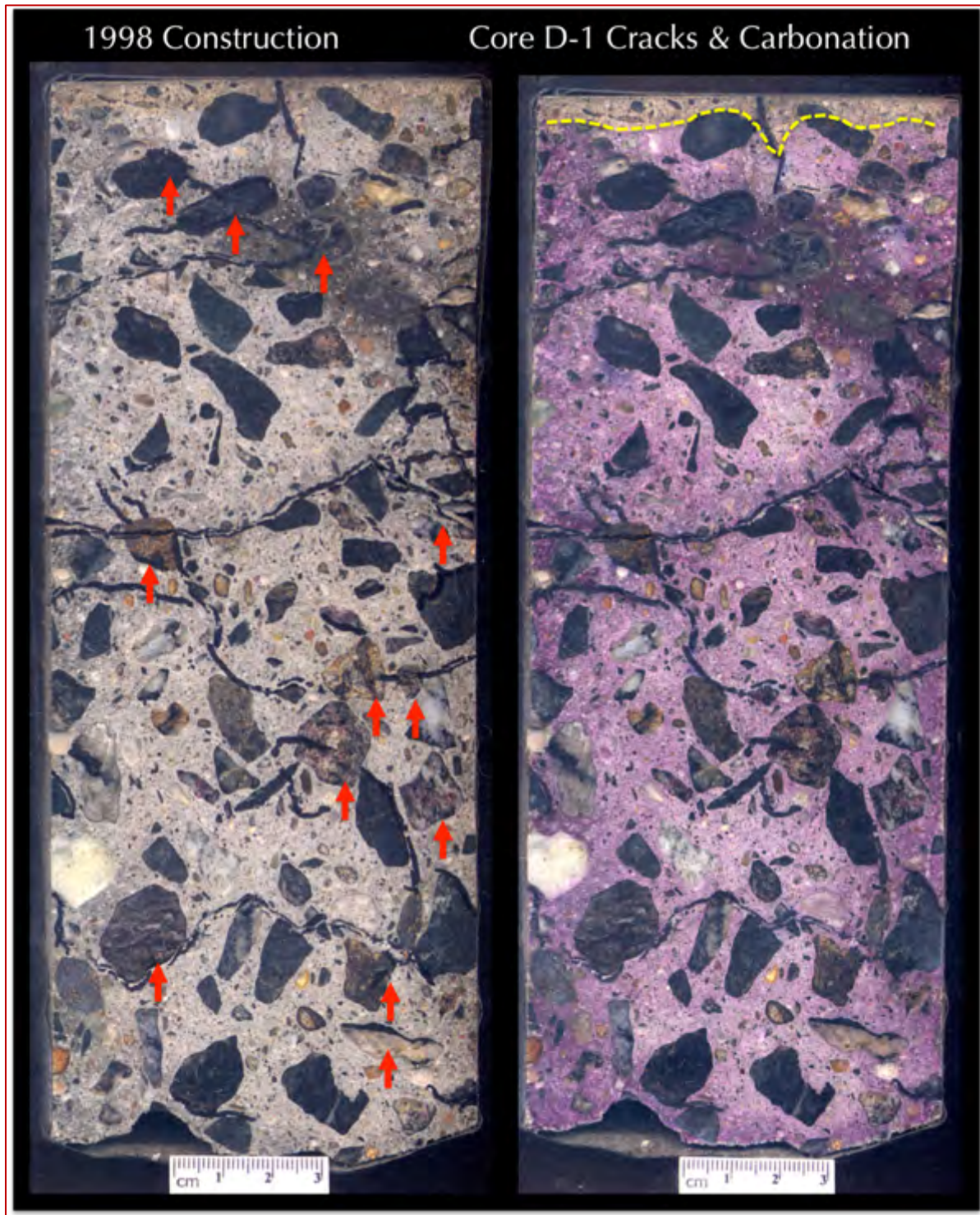


Figure B 16: Lapped cross sections of Core D-1 showing: (a) extensive cracking all throughout the depth of the core, where all visible cracks revealed during stereo-microscopical examination of the lapped cross section are marked with a black marker pen, along with a few unsound light pinkish-brown crushed stone coarse aggregate (garnetiferous quartz-feldspar biotite gneiss) marked in red arrows in the left; and (b) minimal (less than 5 mm deep) carbonation from the formed exposed end of concrete (carbonation front is marked in dashed yellow line on right) after 20 years of service since 1998, a testament of dense, well-consolidated nature of concrete.

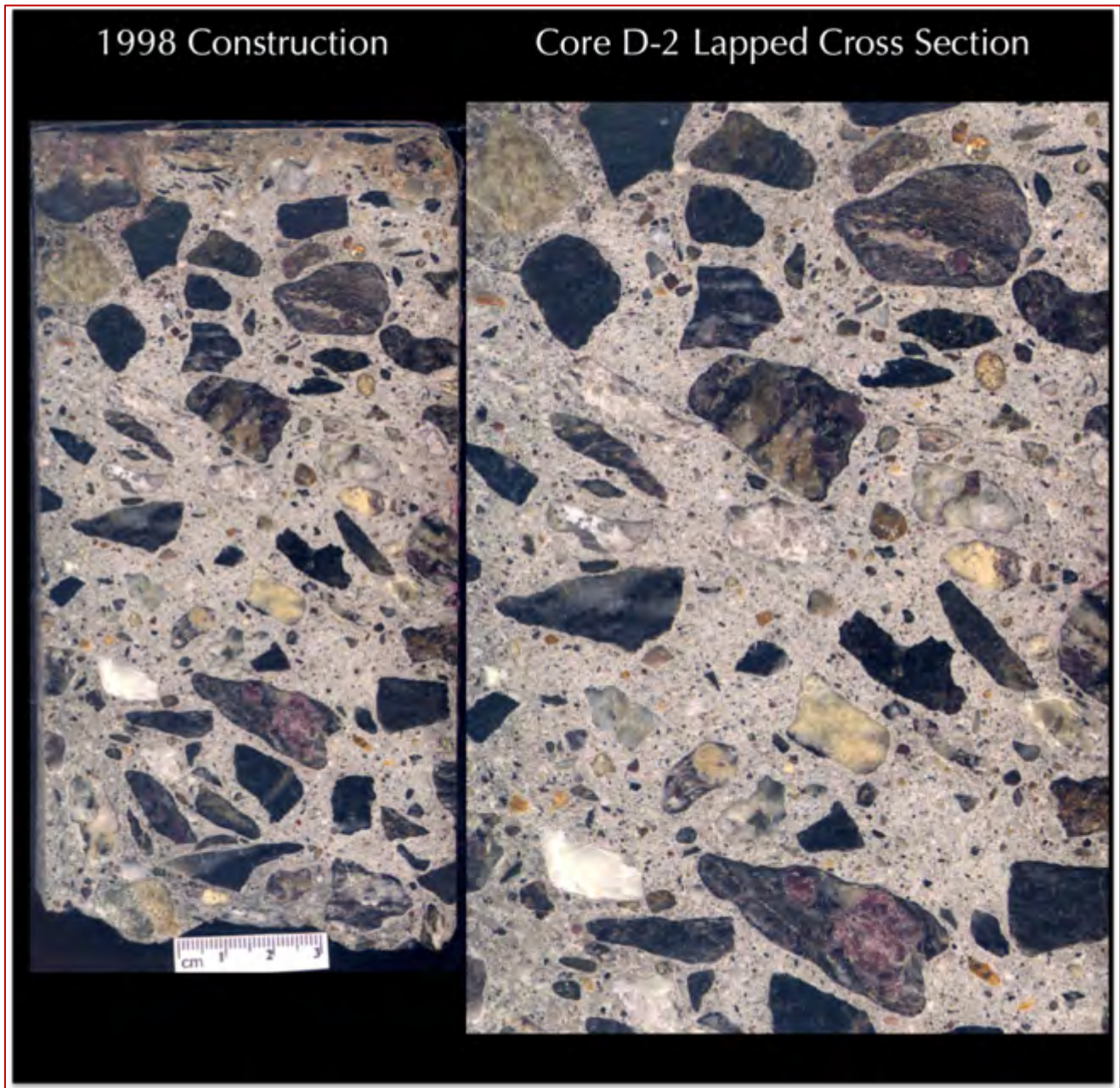


Figure B 17: Lapped cross sections of Core D-2 (right one is enlarged from the left full-depth section) showing: (a) size, shape, angularity, gradation, and distribution of crushed stone coarse aggregate consisting of mixture of a dark gray stone and a lighter pinkish-brown stone, which are found to be metamorphosed gabbro (pyroxene granulite) and garnetiferous quartz-feldspar-biotite gneiss, respectively; (b) natural siliceous sand fine aggregate, (c) overall dense and well-consolidated nature of concrete across the wall from the exposed end at the top to the opposite fractured end at the bottom; and, most importantly, (d) moderate to extensive visible cracking all throughout the depth of the core, which are marked in the next Figure.

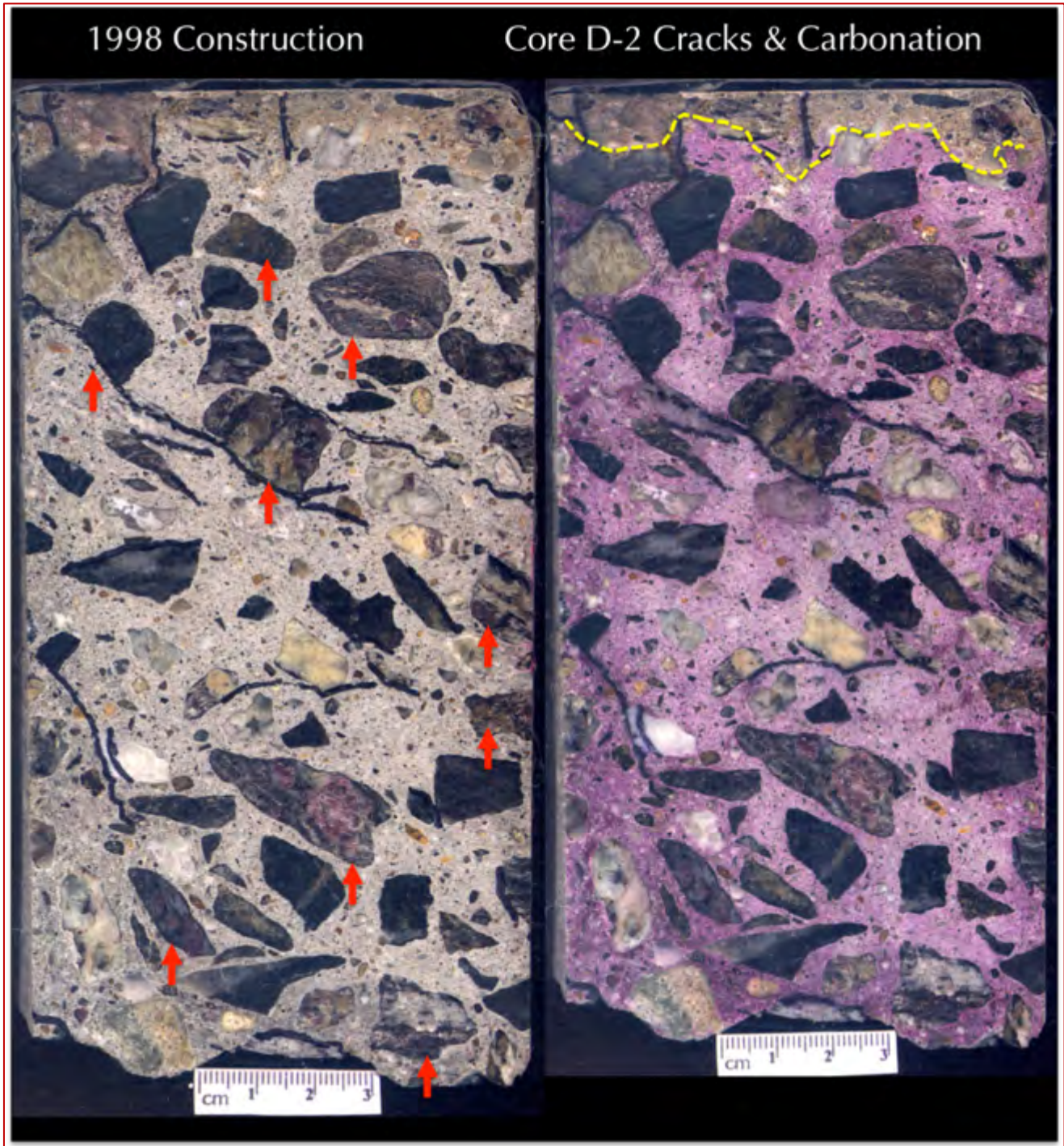


Figure B 18: Lapped cross sections of Core D-2 showing: (a) moderate to extensive cracking all throughout the depth of the core, where all visible cracks revealed during stereo-microscopical examination of the lapped cross section are marked with a black marker pen, along with a few unsound light pinkish-brown crushed stone coarse aggregate (garnetiferous quartz-feldspar biotite gneiss) marked in red arrows in the left; and (b) minimal (less than 20 mm deep) carbonation from the formed exposed end of concrete (carbonation front is marked in dashed yellow line on right) after 20 years of service since 1998, a testament of dense, well-consolidated nature of concrete.

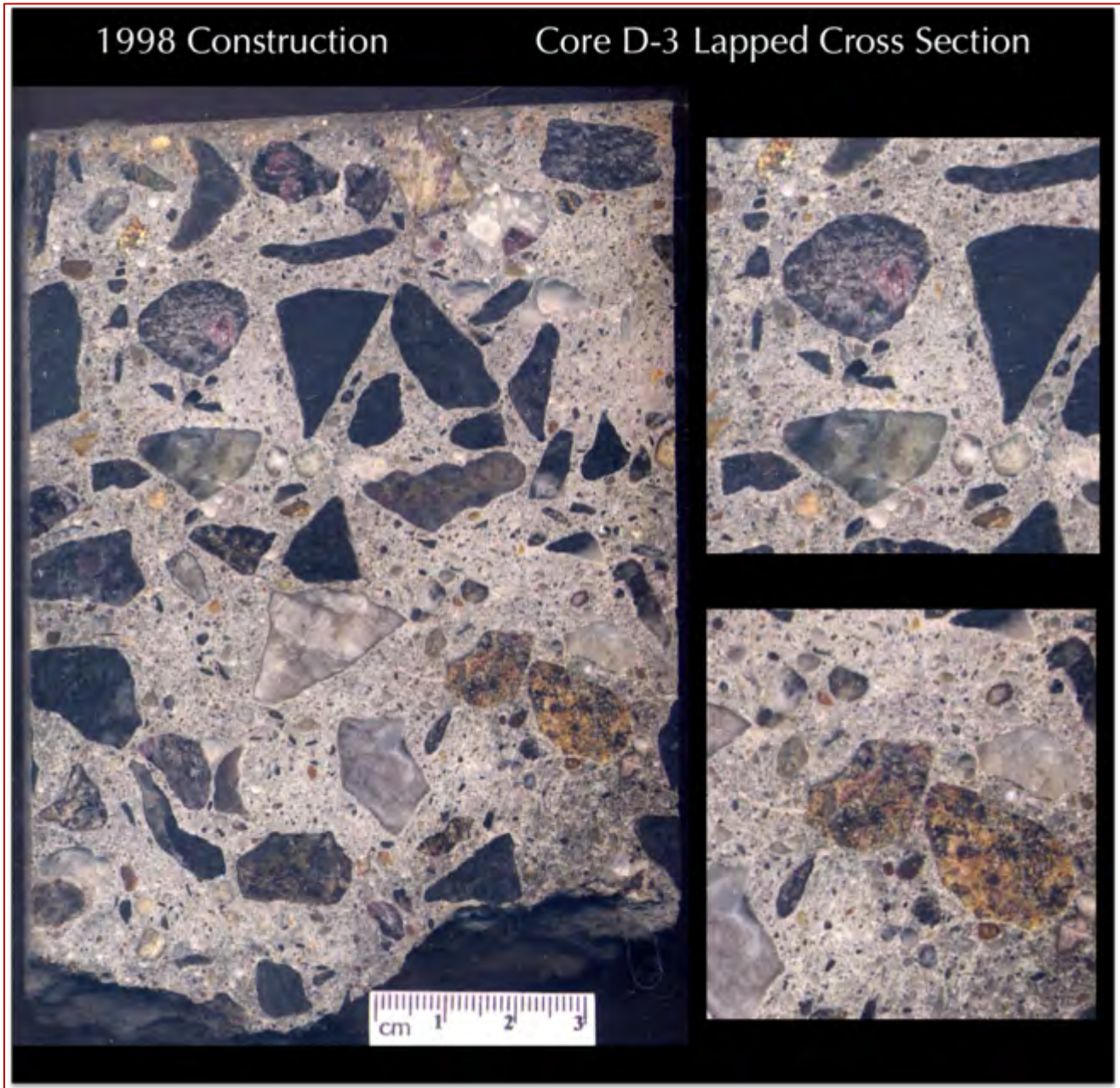


Figure B 19: Lapped cross sections of Core D-3 (right two photos are enlarged from the left full-depth section) showing: (a) size, shape, angularity, gradation, and distribution of crushed stone coarse aggregate consisting of mixture of a dark gray stone and a lighter pinkish-brown stone, which are found to be metamorphosed gabbro (pyroxene granulite) and garnetiferous quartz-feldspar-biotite gneiss, respectively; (b) natural siliceous sand fine aggregate, (c) overall dense and well-consolidated nature of concrete across the wall from the exposed end at the top to the opposite fractured end at the bottom; and, most importantly, (d) moderate to extensive visible cracking all throughout the depth of the core, which are marked in the next Figure.

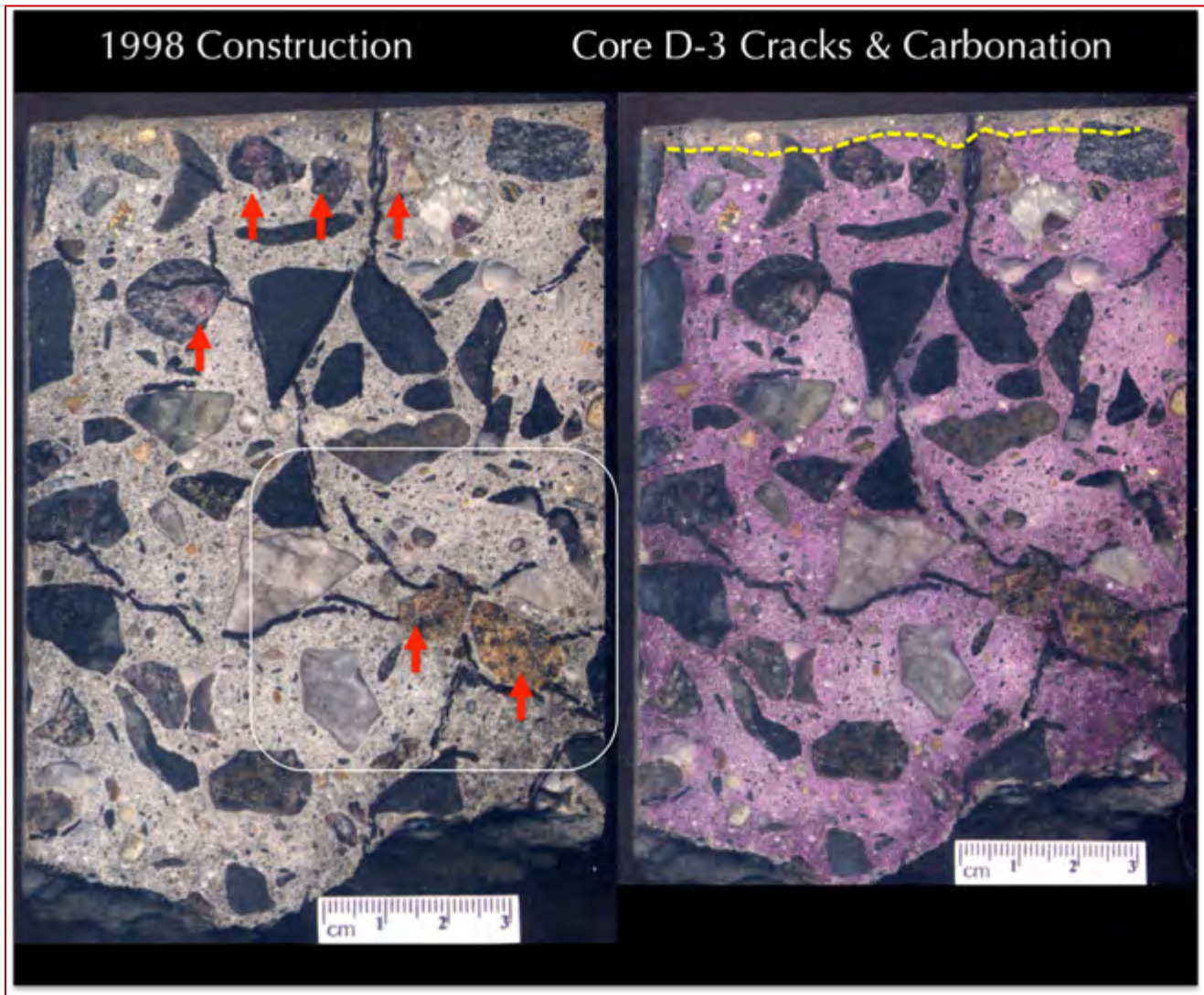


Figure B 20: Lapped cross sections of Core D-3 showing: (a) moderate to extensive cracking all throughout the depth of the core, where all visible cracks revealed during stereo-microscopical examination of the lapped cross section are marked with a black marker pen, along with a few unsound light pinkish-brown crushed stone coarse aggregate (garnetiferous quartz-feldspar biotite gneiss) marked in red arrows in the left; and (b) minimal (less than 5 mm deep) carbonation from the formed exposed end of concrete (carbonation front is marked in dashed yellow line on right) after 20 years of service since 1998, a testament of dense, well-consolidated nature of concrete.

Within the boxed area in the left photo are two unsound light pinkish-brown garnetiferous quartz-feldspar-biotite gneiss particles (also shown in the bottom right photo in Figure B19) and associated radial cracks from those two particles marked with black lines along the cracks. This is a classic microstructure of pyrrhotite-related deterioration where expansion from oxidation of pyrrhotite in aggregate has caused radial cracking.

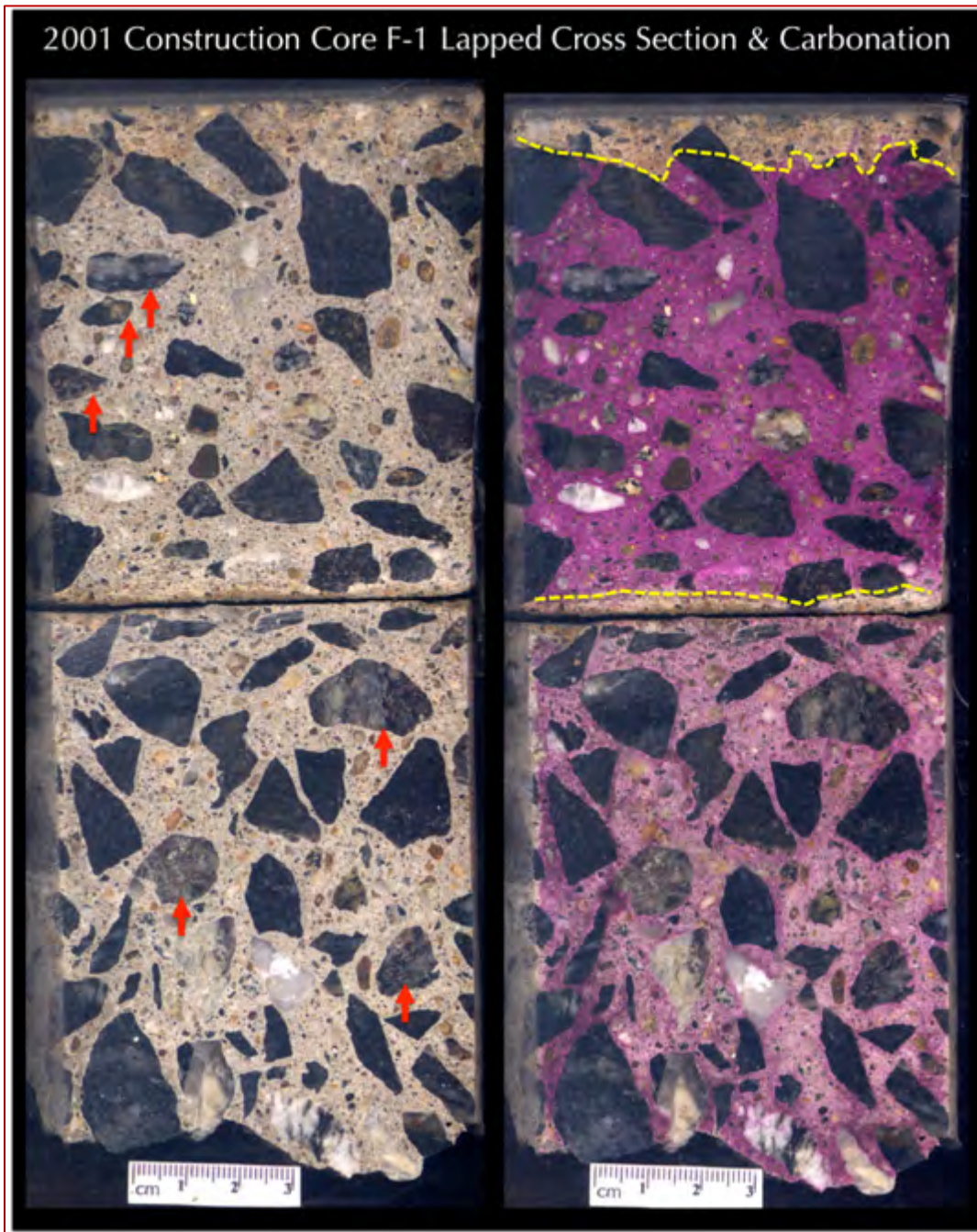


Figure B 21: Lapped cross sections of Core F-1 from 2001 construction (right one is after treating the left section with phenolphthalein alcoholic solution to determine the depth of carbonation) showing: (a) size, shape, angularity, gradation, and distribution of crushed stone coarse aggregate consisting of mixture of a dark gray stone and a lighter speckled gray/brown stone, which are found to be metamorphosed gabbro (pyroxene granulite) and garnetiferous quartz-feldspar-biotite gneiss, respectively, which are compositionally similar to the stone used during 1998 construction; (b) natural siliceous sand fine aggregate, (c) overall dense and well-consolidated nature of concrete across the wall from the exposed end at the top to the opposite fractured end at the bottom; (d) absence of any visible cracking despite some unsound crushed stone marked in red arrows; and (e) minimal (less than 10 mm deep) carbonation from the formed exposed end of concrete (carbonation front is marked in dashed yellow line on right) after 18 years of service since 2001, a testament of dense, well-consolidated nature of concrete.

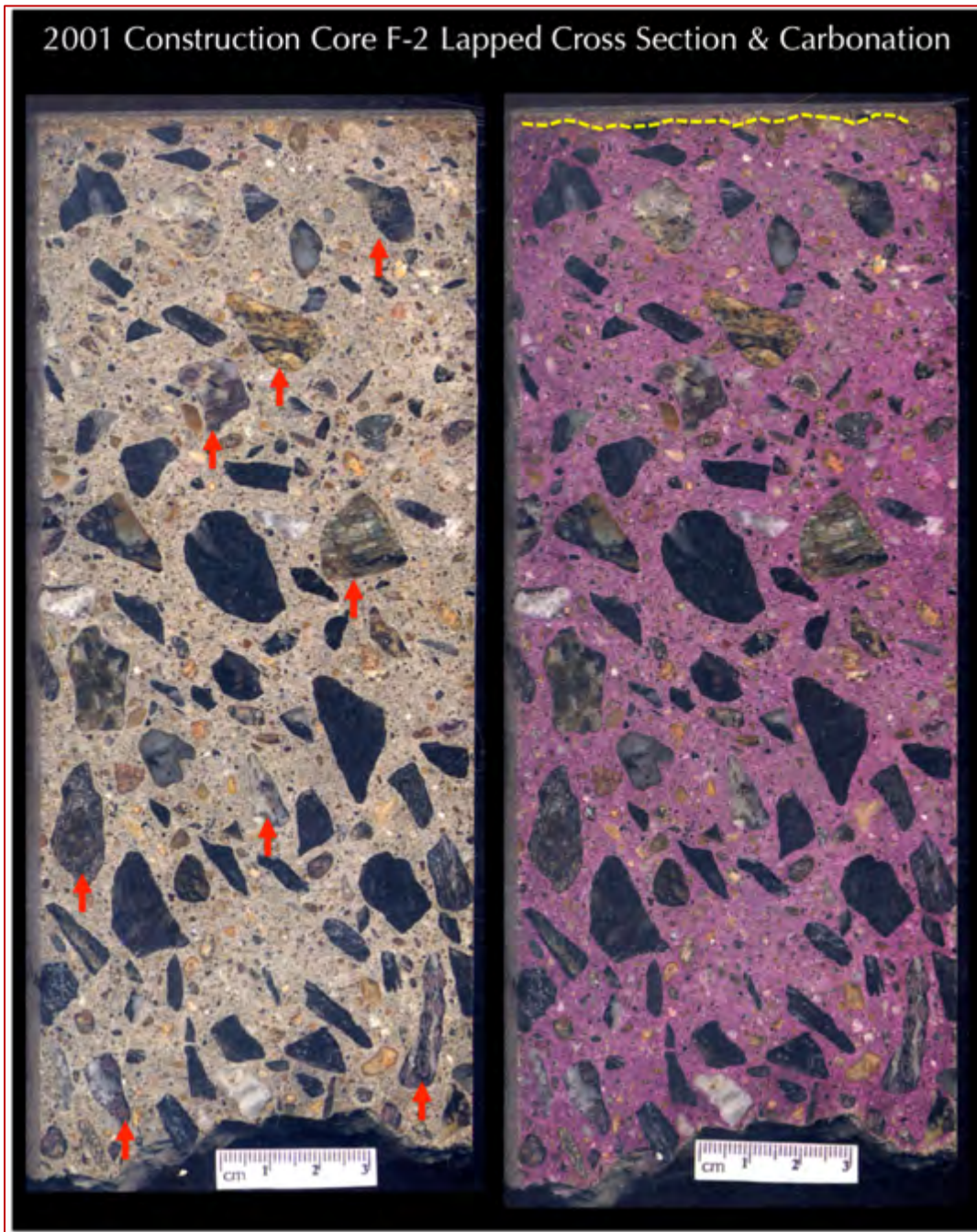


Figure B 22: Lapped cross sections of Core F-2 from 2001 construction (right one is after treating the left section with phenolphthalein alcoholic solution to determine the depth of carbonation) showing: (a) size, shape, angularity, gradation, and distribution of crushed stone coarse aggregate consisting of mixture of a dark gray stone and a lighter speckled gray/brown stone, which are found to be metamorphosed gabbro (pyroxene granulite) and garnetiferous quartz-feldspar-biotite gneiss, respectively, which are compositionally similar to the stone used during 1998 construction; (b) natural siliceous sand fine aggregate, (c) overall dense and well-consolidated nature of concrete across the wall from the exposed end at the top to the opposite fractured end at the bottom; (d) absence of any visible cracking despite some unsound crushed stone marked in red arrows; and (e) minimal (less than 5 mm deep) carbonation from the formed exposed end of concrete (carbonation front is marked in dashed yellow line on right) after 18 years of service since 2001, a testament of dense, well-consolidated nature of concrete.

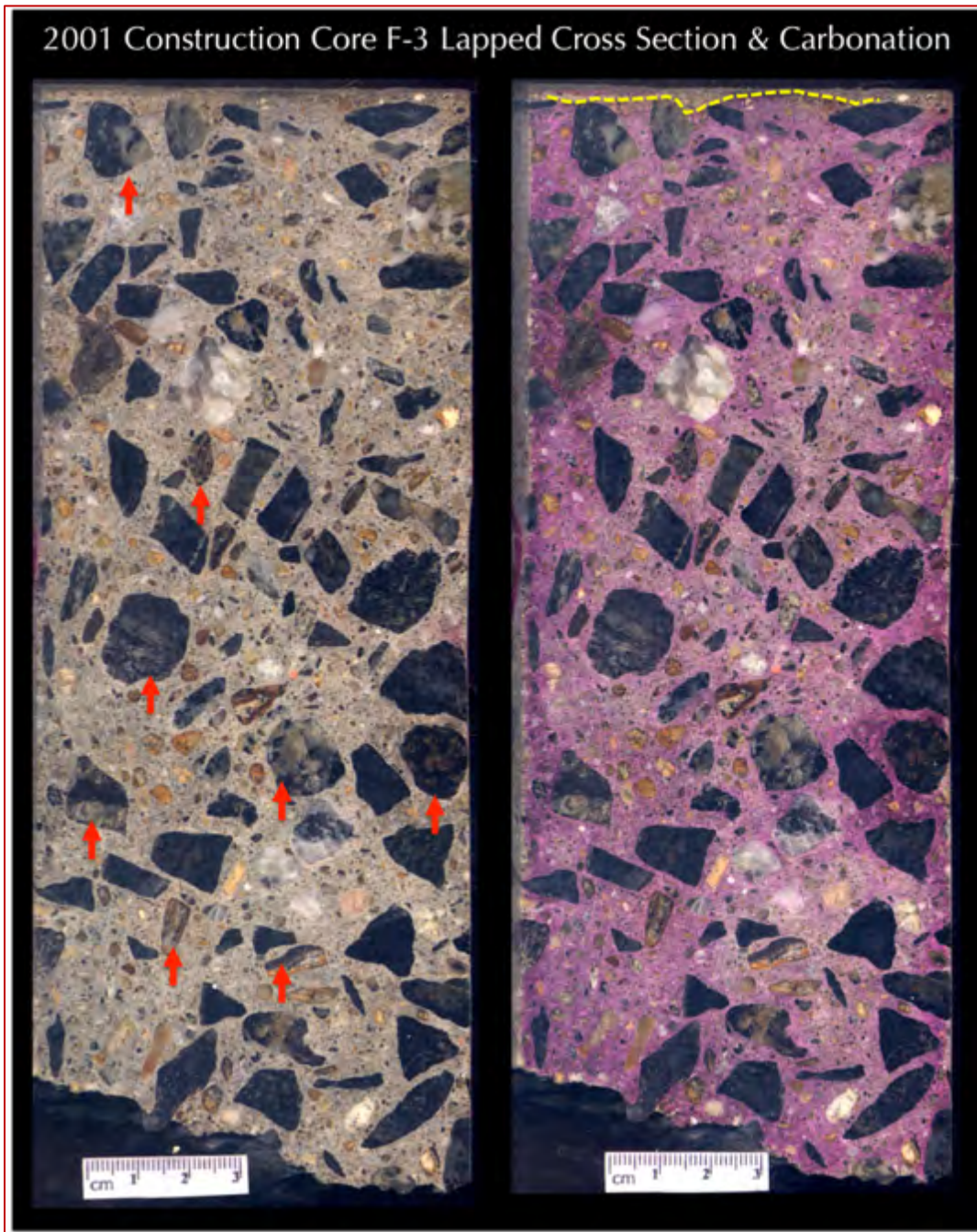


Figure B 23: Lapped cross sections of Core F-3 from 2001 construction (right one is after treating the left section with phenolphthalein alcoholic solution to determine the depth of carbonation) showing: (a) size, shape, angularity, gradation, and distribution of crushed stone coarse aggregate consisting of mixture of a dark gray stone and a lighter speckled gray/brown stone, which are found to be metamorphosed gabbro (pyroxene granulite) and garnetiferous quartz-feldspar-biotite gneiss, respectively, which are compositionally similar to the stone used during 1998 construction; (b) natural siliceous sand fine aggregate, (c) overall dense and well-consolidated nature of concrete across the wall from the exposed end at the top to the opposite fractured end at the bottom; (d) absence of any visible cracking despite some unsound crushed stone marked in red arrows; and (e) minimal (less than 5 mm deep) carbonation from the formed exposed end of concrete (carbonation front is marked in dashed yellow line on right) after 18 years of service since 2001, a testament of dense, well-consolidated nature of concrete.

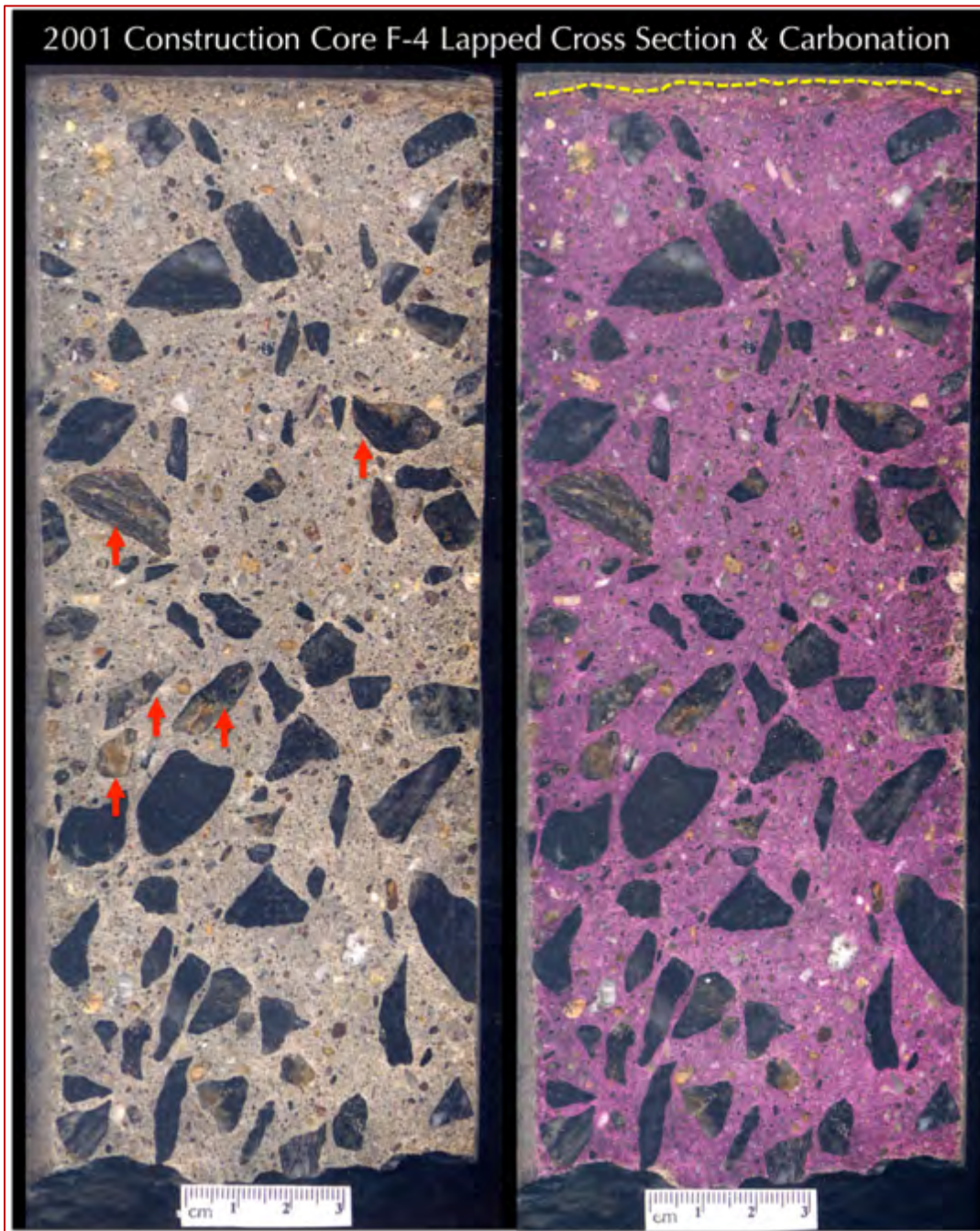


Figure B 24: Lapped cross sections of Core F-4 from 2001 construction (right one is after treating the left section with phenolphthalein alcoholic solution to determine the depth of carbonation) showing: (a) size, shape, angularity, gradation, and distribution of crushed stone coarse aggregate consisting of mixture of a dark gray stone and a lighter speckled gray/brown stone, which are found to be metamorphosed gabbro (pyroxene granulite) and garnetiferous quartz-feldspar-biotite gneiss, respectively, which are compositionally similar to the stone used during 1998 construction; (b) natural siliceous sand fine aggregate, (c) overall dense and well-consolidated nature of concrete across the wall from the exposed end at the top to the opposite fractured end at the bottom; (d) absence of any visible cracking despite some unsound crushed stone marked in red arrows; and (e) minimal (less than 5 mm deep) carbonation from the formed exposed end of concrete (carbonation front is marked in dashed yellow line on right) after 18 years of service since 2001, a testament of dense, well-consolidated nature of concrete.

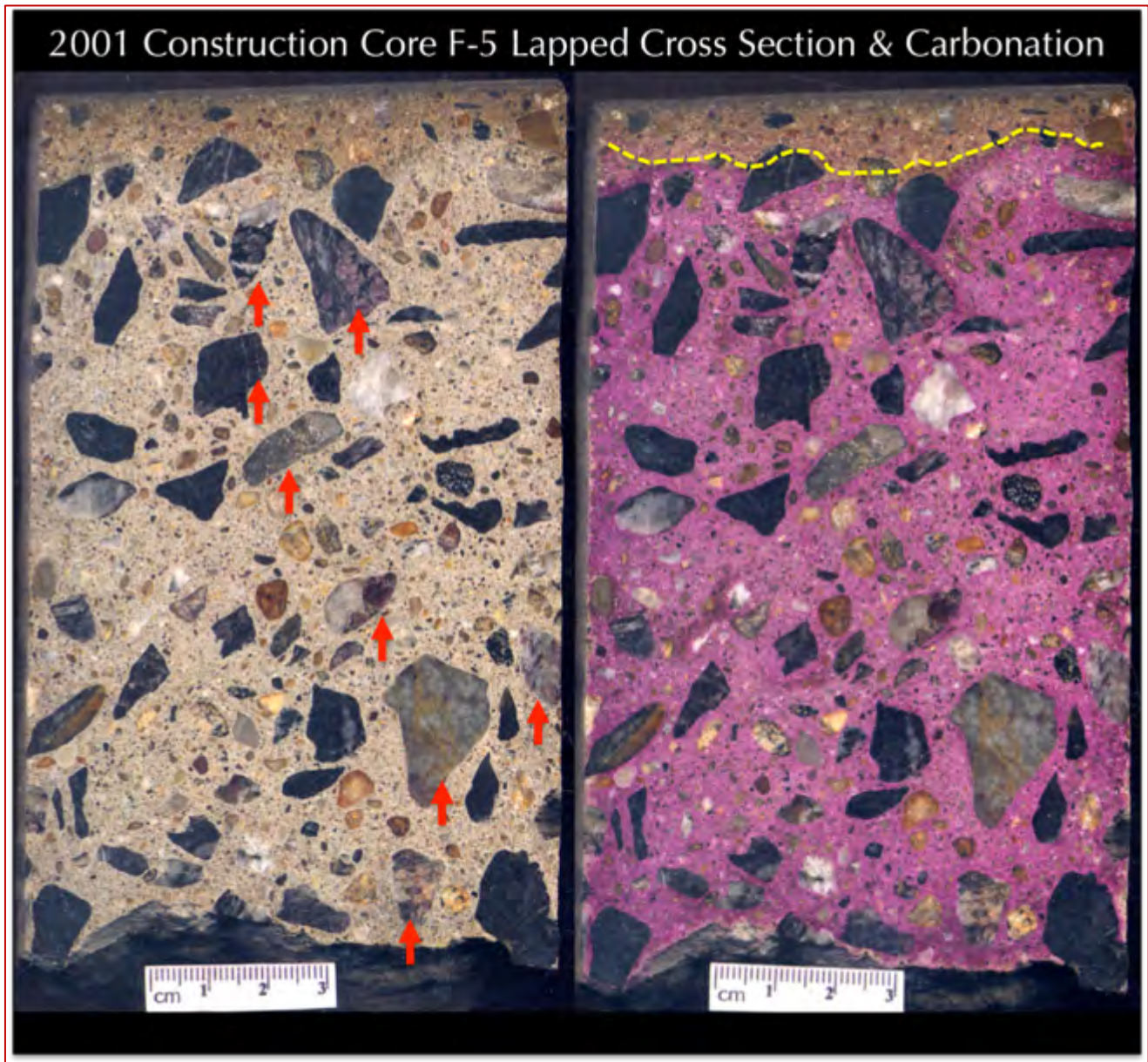


Figure B 25: Lapped cross sections of Core F-5 from 2001 construction (right one is after treating the left section with phenolphthalein alcoholic solution to determine the depth of carbonation) showing: (a) size, shape, angularity, gradation, and distribution of crushed stone coarse aggregate consisting of mixture of a dark gray stone and a lighter speckled gray/brown stone, which are found to be metamorphosed gabbro (pyroxene granulite) and garnetiferous quartz-feldspar-biotite gneiss, respectively, which are compositionally similar to the stone used during 1998 construction; (b) natural siliceous sand fine aggregate, (c) overall dense and well-consolidated nature of concrete across the wall from the exposed end at the top to the opposite fractured end at the bottom; (d) absence of any visible cracking despite some unsound crushed stone marked in red arrows; and (e) minimal (less than 15 mm deep) carbonation from the formed exposed end of concrete (carbonation front is marked in dashed yellow line on right) after 18 years of service since 2001, a testament of dense, well-consolidated nature of concrete.

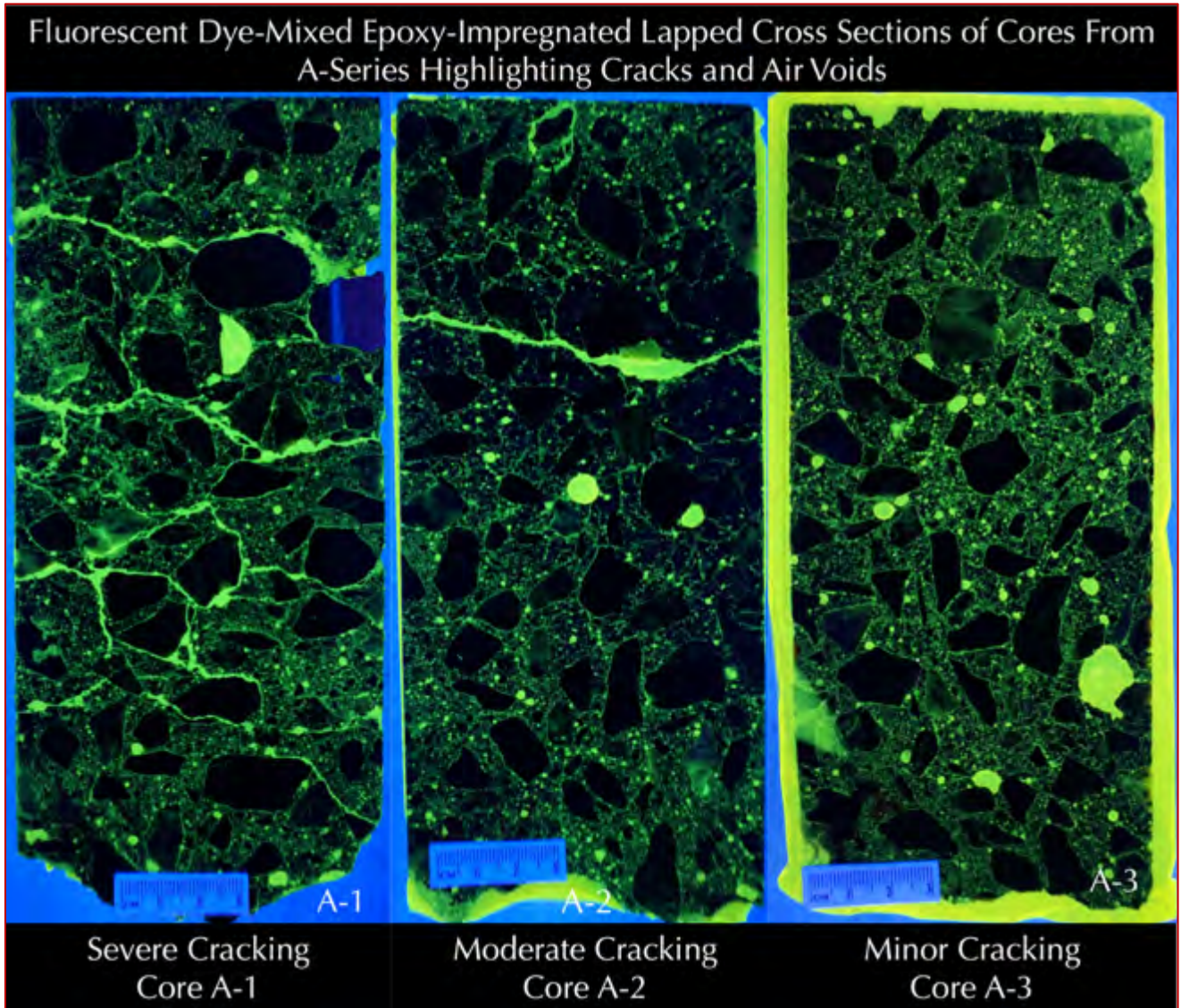


Figure B 26: Fluorescent dye-mixed epoxy-impregnated lapped cross sections of three cores from A-series showing extensive cracking in Core A-1 where cracks are highlighted by the fluorescent dye (when viewed in ultraviolet light), moderate cracking in Core A-2, and minor cracking in Core A-3.

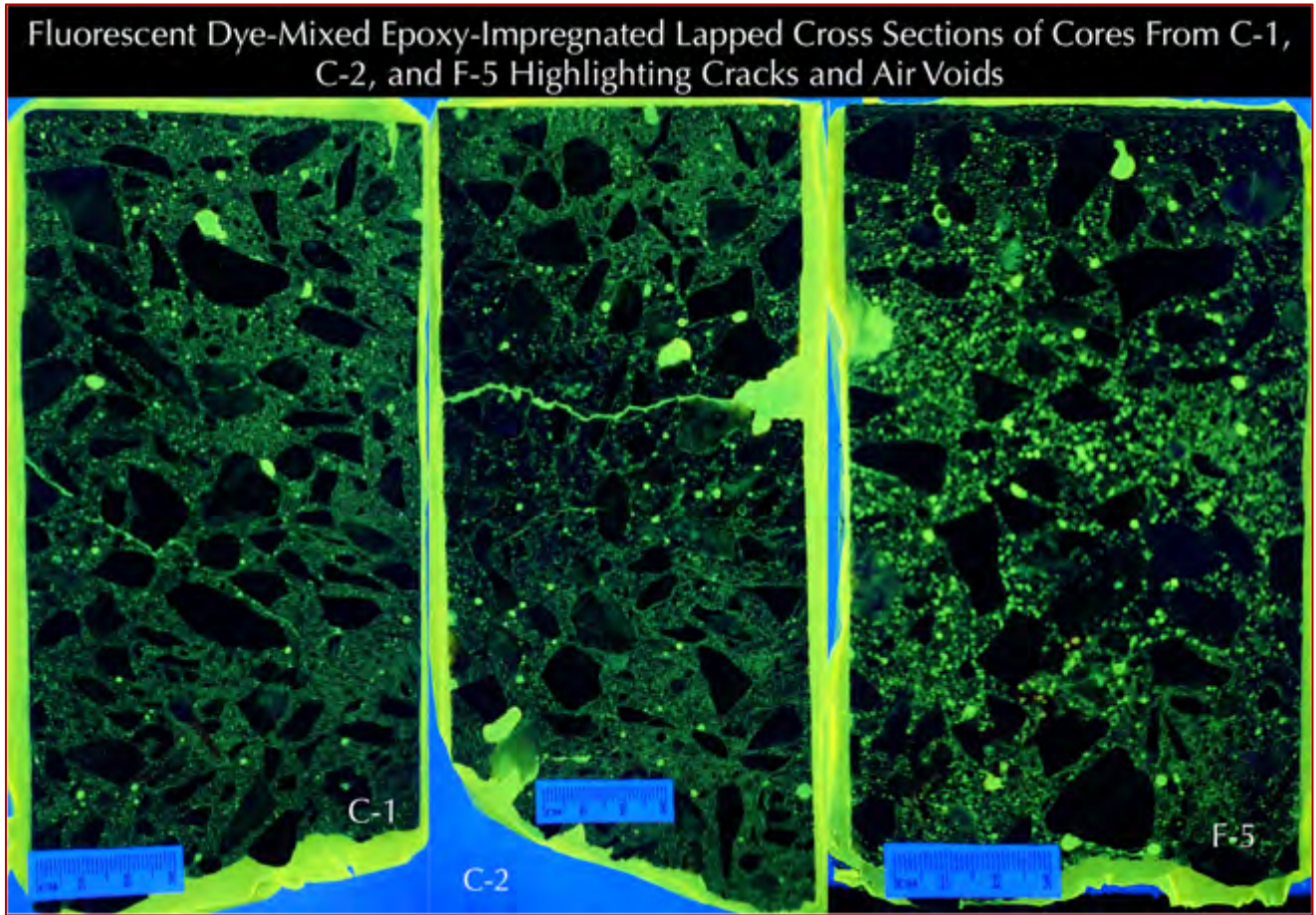


Figure B 27: Fluorescent dye-mixed epoxy-impregnated lapped cross sections of three cores C-1, C-2, and F-5 showing extensive cracking in Core C-1 where cracks are highlighted by the fluorescent dye (when viewed in ultraviolet light), moderate cracking in Core C-2, and no cracking only air voids in Core F-5.

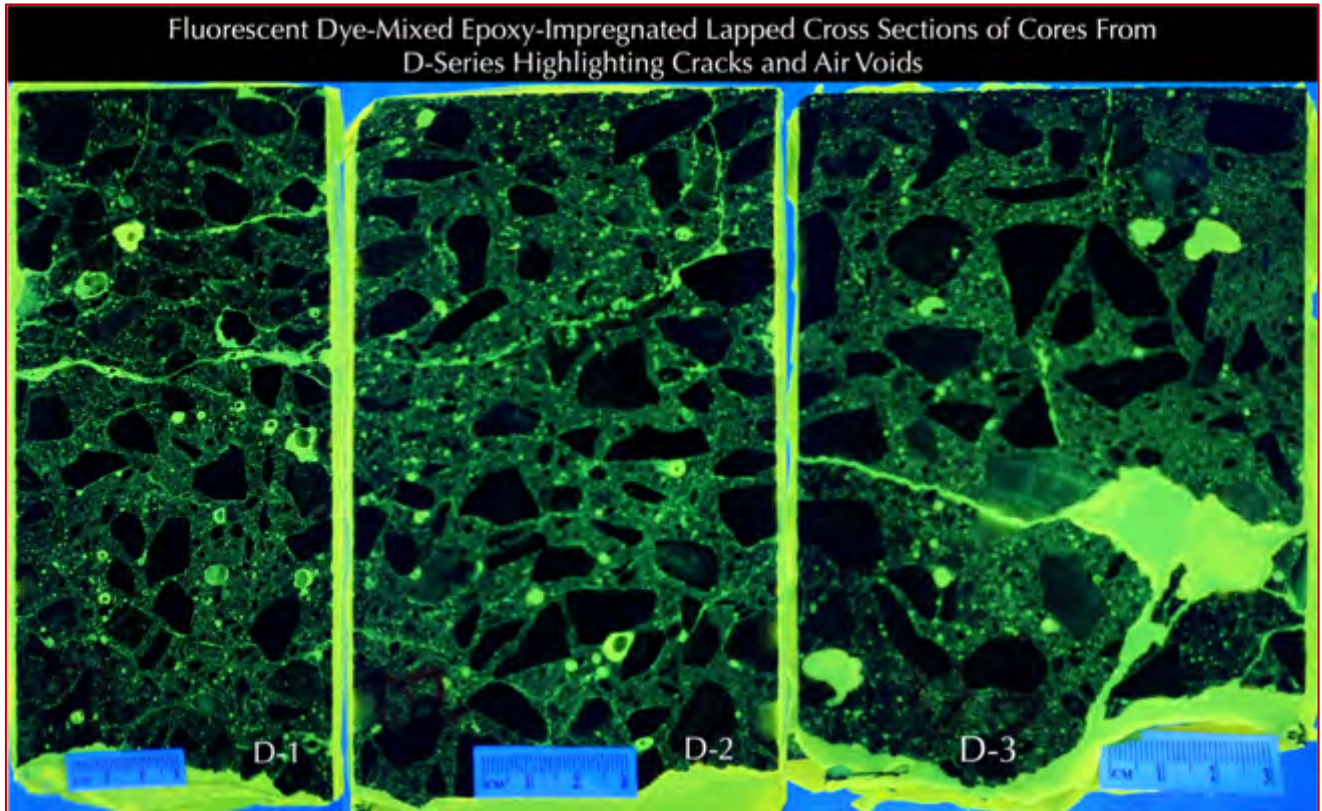


Figure B 28: Fluorescent dye-mixed epoxy-impregnated lapped cross sections of three cores from D-series showing extensive cracking in Core D-1 where cracks are highlighted by the fluorescent dye (when viewed in ultraviolet light), moderate cracking in Cores D-2 and D-3.



# APPENDIX C

## Photomicrographs of Lapped Cross Sections



Figure C 1: Photomicrographs of lapped cross section of Core A-1 showing: (a) air-entrained nature of concrete having numerous fine (< 1 mm size), discrete spherical entrained air-voids; and (b) cracking in many unsound crushed gneiss coarse aggregate particles.



Figure C 2: Photomicrographs of lapped cross section of Core A-1 showing: (a) air-entrained nature of concrete having numerous fine (< 1 mm size), discrete spherical entrained air-voids; and (b) cracking in many unsound crushed gneiss coarse aggregate particles.



Figure C 3: Photomicrographs of lapped cross section of Core A-2 showing: (a) air-entrained nature of concrete having numerous fine (< 1 mm size), discrete spherical entrained air-voids; and (b) cracking in many unsound crushed gneiss coarse aggregate particles.



Figure C 4: Photomicrographs of lapped cross section of Core A-2 showing: (a) air-entrained nature of concrete having numerous fine (< 1 mm size), discrete spherical entrained air-voids; and (b) cracking in many unsound crushed gneiss coarse aggregate particles. Notice some large red almandine garnet crystals in gneiss.



Figure C 5: Photomicrographs of lapped cross section of Core A-3 showing: (a) air-entrained nature of concrete having numerous fine (< 1 mm size), discrete spherical entrained air-voids; and (b) cracking in many unsound crushed gneiss coarse aggregate particles. Notice some large red almandine garnet crystals in gneiss.

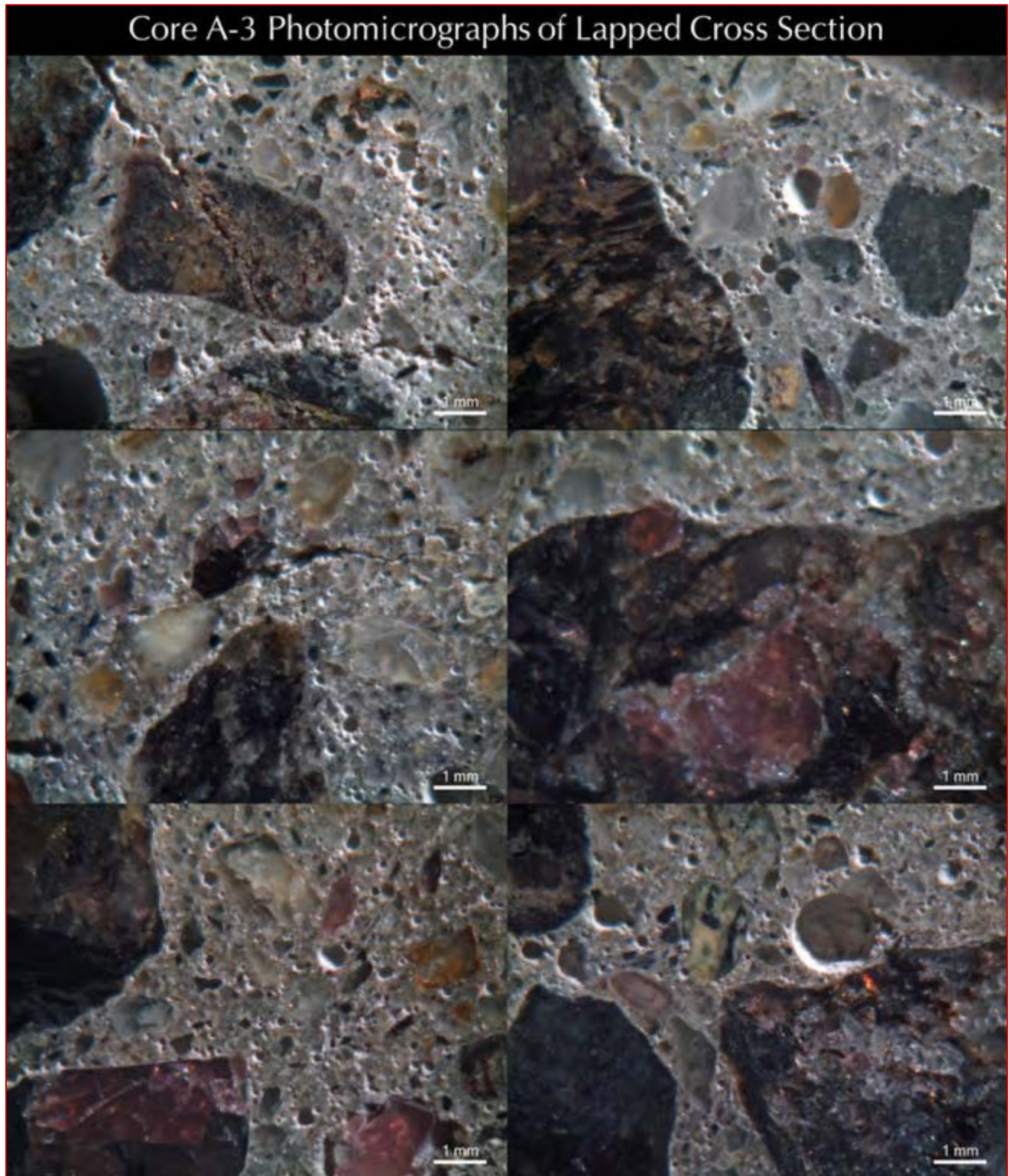


Figure C 6: Photomicrographs of lapped cross section of Core A-3 showing: (a) air-entrained nature of concrete having numerous fine (< 1 mm size), discrete spherical entrained air-voids; and (b) cracking in many unsound crushed gneiss coarse aggregate particles. Notice some large red almandine garnet crystals in gneiss.



Figure C 7: Photomicrographs of lapped cross section of Core B-1 showing: (a) air-entrained nature of concrete having numerous fine (< 1 mm size), discrete spherical entrained air-voids; and (b) many unsound crushed gneiss coarse aggregate particles.

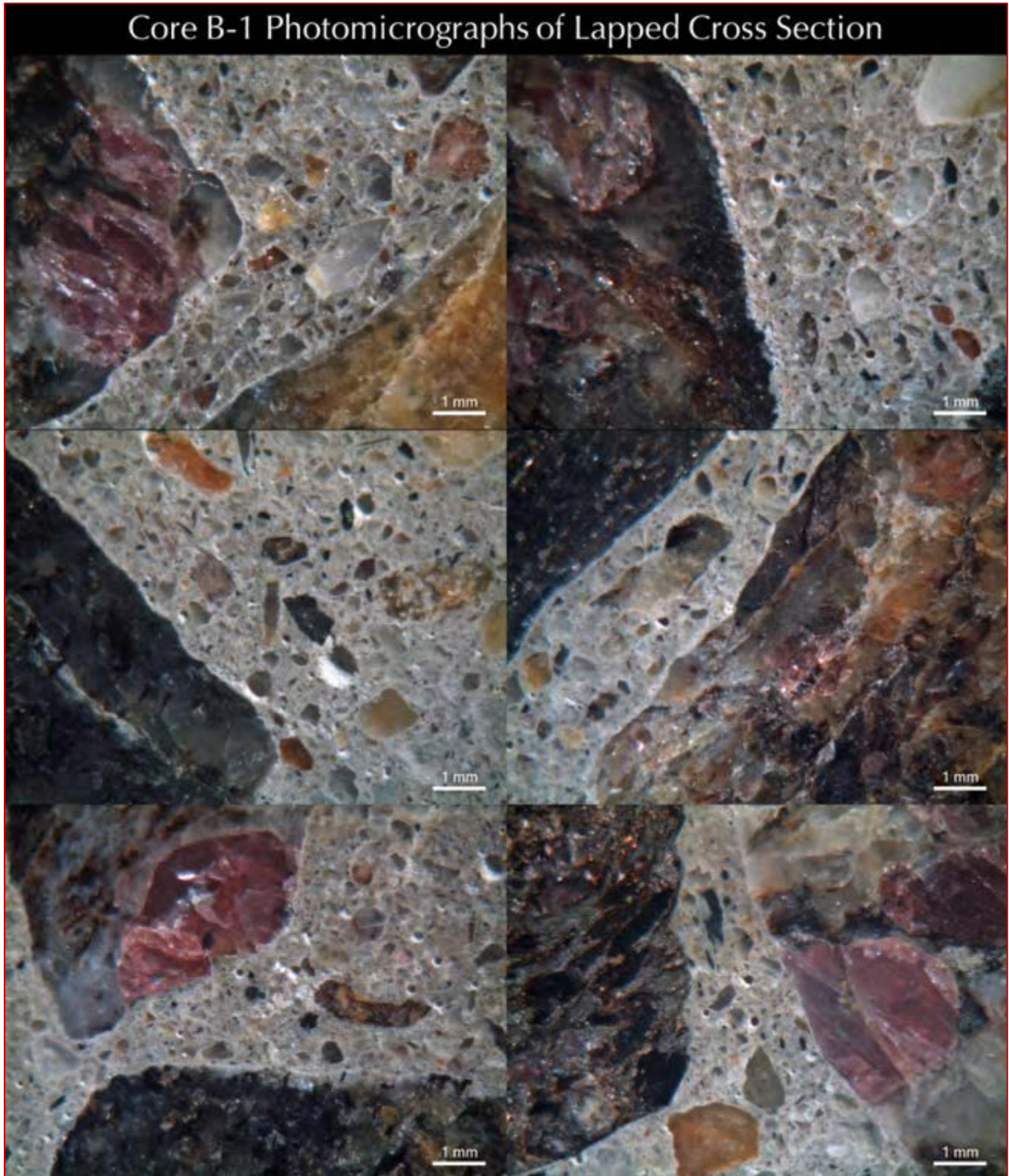


Figure C 8: Photomicrographs of lapped cross section of Core B-1 showing: (a) air-entrained nature of concrete having numerous fine (< 1 mm size), discrete spherical entrained air-voids; and (b) many unsound crushed gneiss coarse aggregate particles. Notice some large red almandine garnet crystals in gneiss.



Figure C 9: Photomicrographs of lapped cross section of Core C-1 showing: (a) air-entrained nature of concrete having numerous fine (< 1 mm size), discrete spherical entrained air-voids; and (b) cracking in many unsound crushed gneiss coarse aggregate particles. Notice some large red almandine garnet crystals in gneiss.



Figure C 10: Photomicrographs of lapped cross section of Core C-1 showing: (a) air-entrained nature of concrete having numerous fine (< 1 mm size), discrete spherical entrained air-voids; and (b) cracking in many unsound crushed gneiss coarse aggregate particles. Notice some large red almandine garnet crystals in gneiss.



Figure C 11: Photomicrographs of lapped cross section of Core C-1 showing: (a) air-entrained nature of concrete having numerous fine (< 1 mm size), discrete spherical entrained air-voids; and (b) cracking in many unsound crushed gneiss coarse aggregate particles.



Figure C 12: Photomicrographs of lapped cross section of Core C-1 showing: (a) air-entrained nature of concrete having numerous fine (< 1 mm size), discrete spherical entrained air-voids; and (b) cracking in many unsound crushed gneiss coarse aggregate particles. Notice some large red almandine garnet crystals in gneiss.

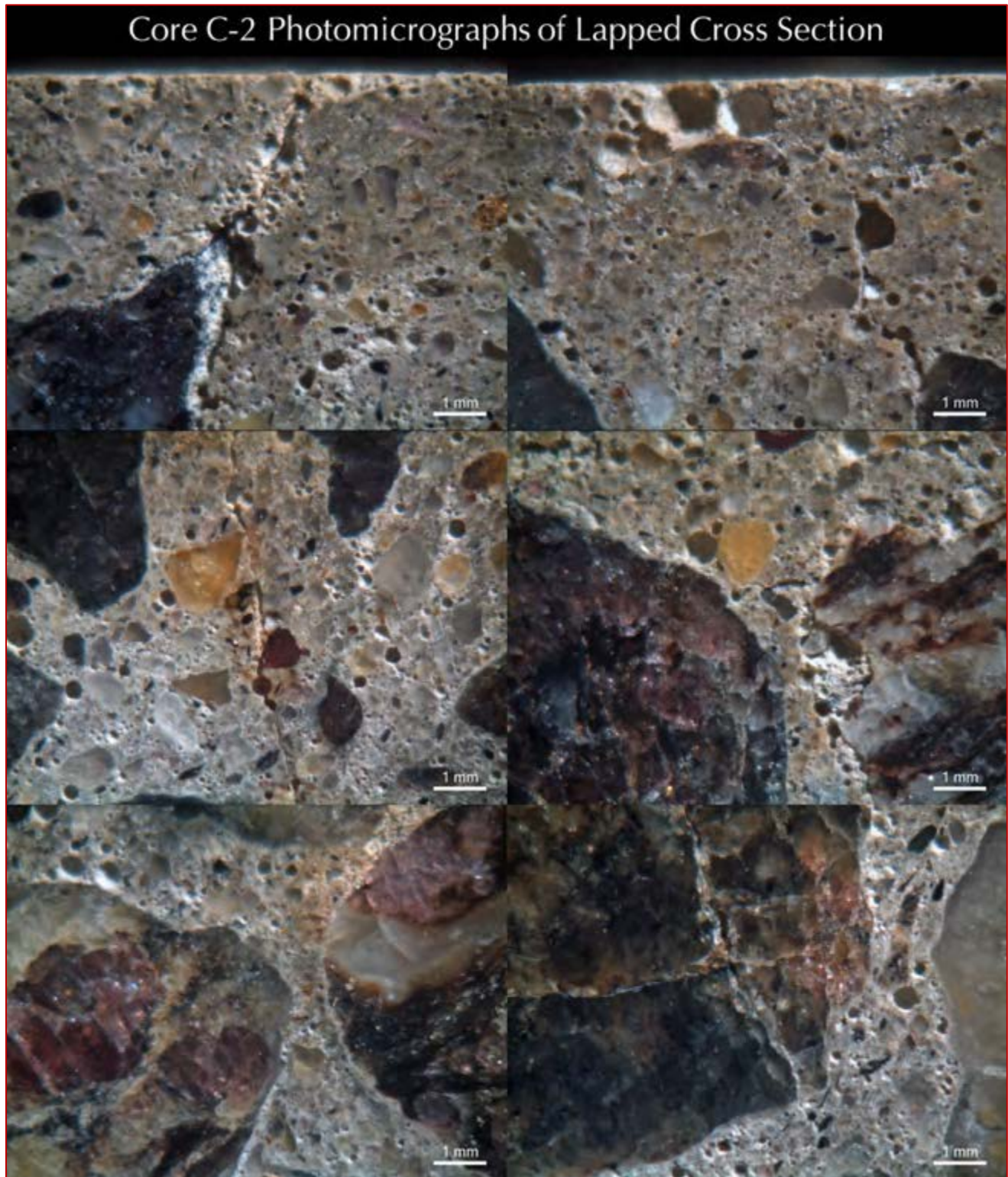


Figure C 13: Photomicrographs of lapped cross section of Core C-2 showing: (a) air-entrained nature of concrete having numerous fine (< 1 mm size), discrete spherical entrained air-voids; and (b) cracking in many unsound crushed gneiss coarse aggregate particles. Notice some large red almandine garnet crystals in gneiss.



Figure C 14: Photomicrographs of lapped cross section of Core C-2 showing: (a) air-entrained nature of concrete having numerous fine (< 1 mm size), discrete spherical entrained air-voids; and (b) cracking in many unsound crushed gneiss coarse aggregate particles.



Figure C 15: Photomicrographs of lapped cross section of Core C-2 showing: (a) air-entrained nature of concrete having numerous fine (< 1 mm size), discrete spherical entrained air-voids; and (b) cracking in many unsound crushed gneiss coarse aggregate particles. Notice some large red almandine garnet crystals in gneiss.

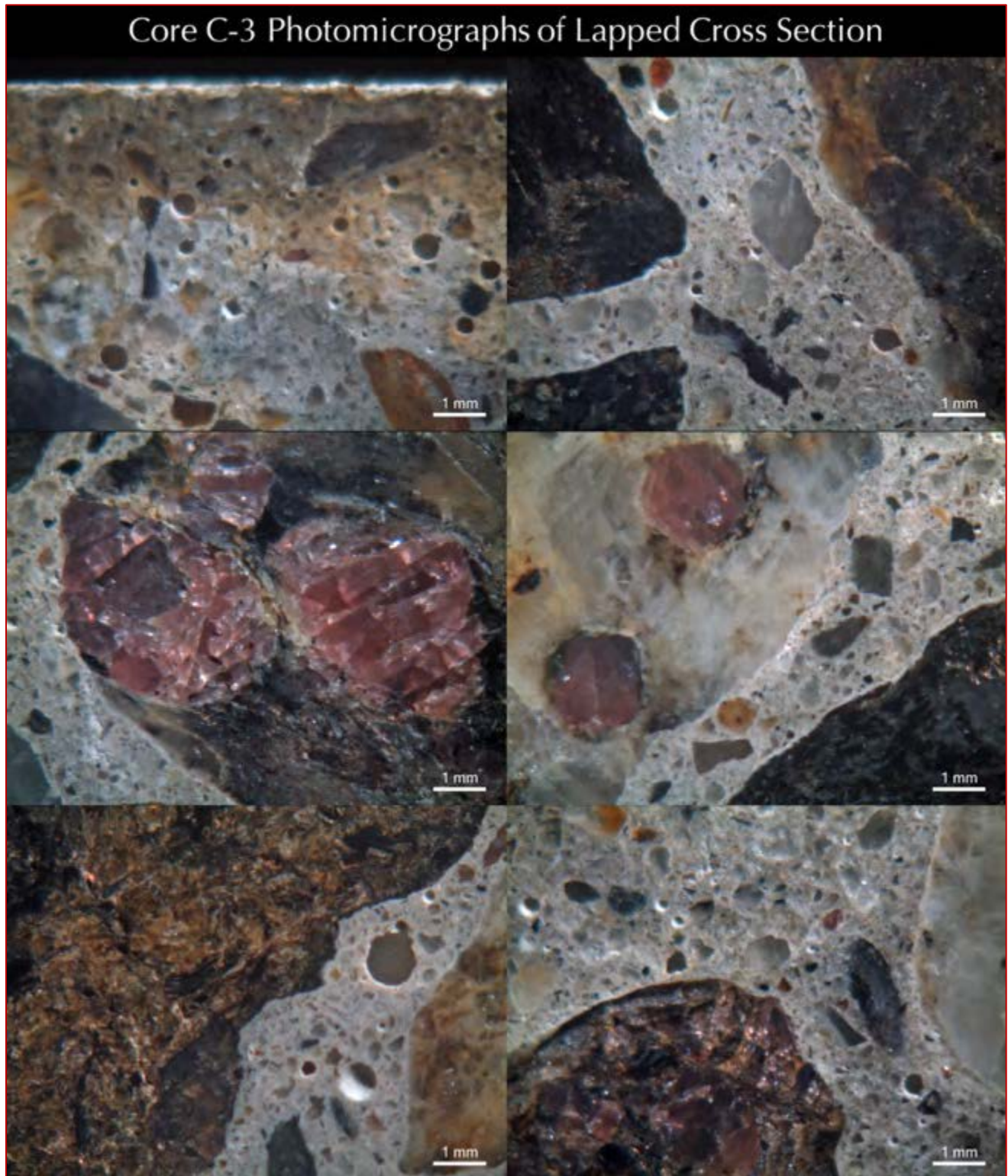


Figure C 16: Photomicrographs of lapped cross section of Core C-3 showing: (a) air-entrained nature of concrete having numerous fine (< 1 mm size), discrete spherical entrained air-voids; and (b) many unsound crushed gneiss coarse aggregate particles. Notice some large red almandine garnet crystals in gneiss.

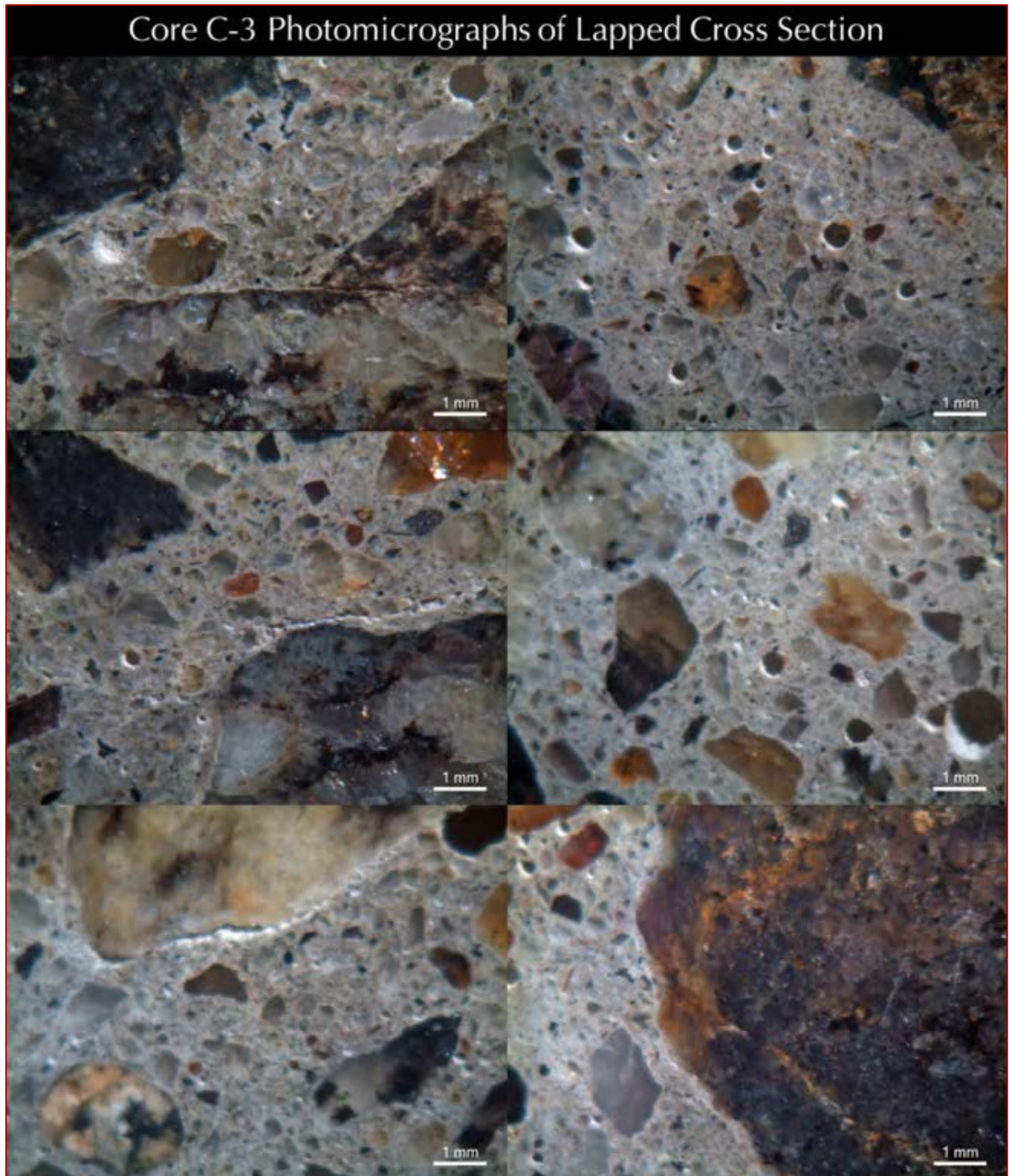


Figure C 17: Photomicrographs of lapped cross section of Core C-3 showing: (a) air-entrained nature of concrete having numerous fine (< 1 mm size), discrete spherical entrained air-voids; and (b) many unsound crushed gneiss coarse aggregate particles.

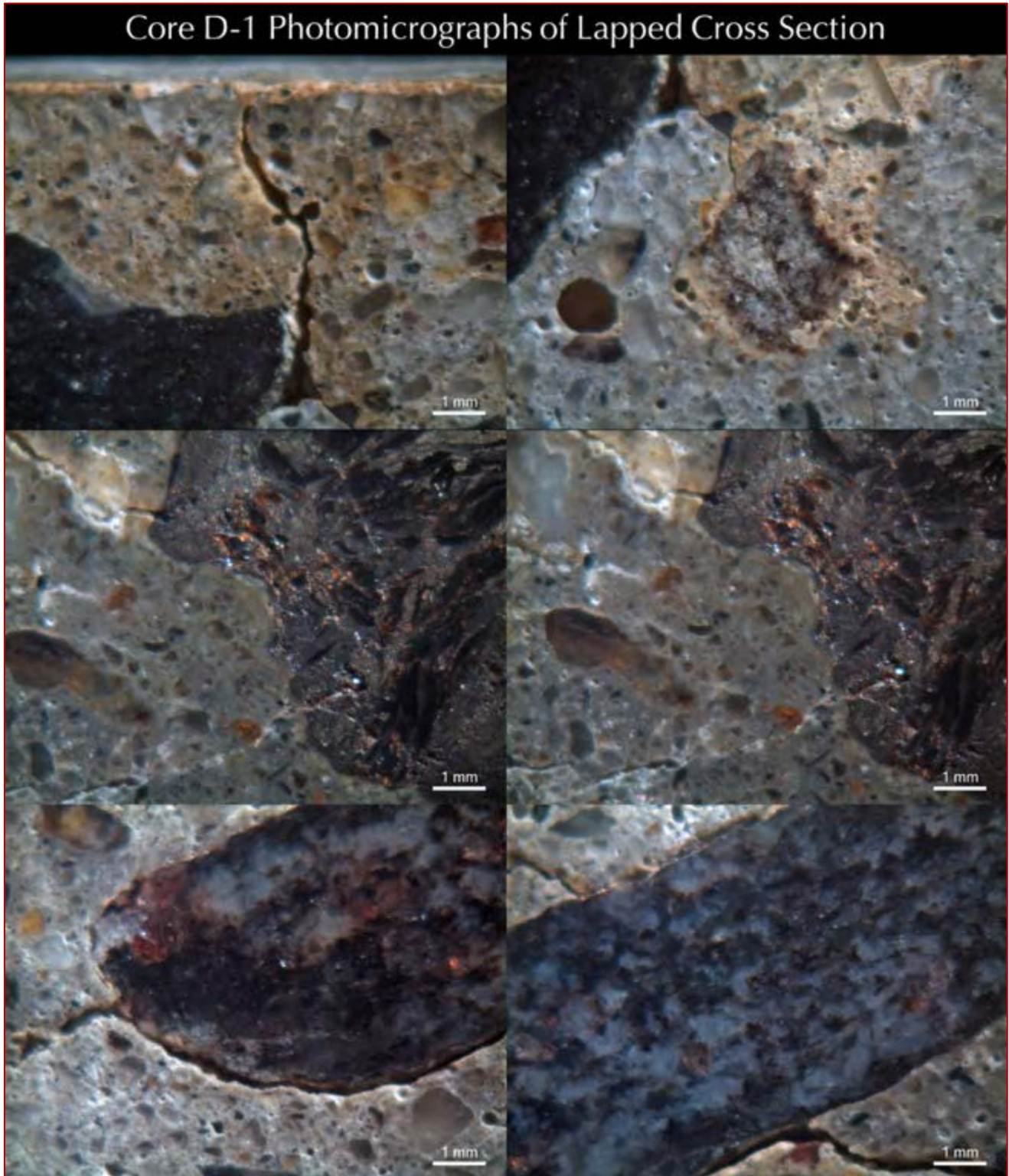


Figure C 18: Photomicrographs of lapped cross section of Core D-1 showing: (a) air-entrained nature of concrete having numerous fine (< 1 mm size), discrete spherical entrained air-voids; and (b) cracking in many unsound crushed gneiss coarse aggregate particles. Notice some large red almandine garnet crystals in gneiss.



Figure C 19: Photomicrographs of lapped cross section of Core D-1 showing: (a) air-entrained nature of concrete having numerous fine (< 1 mm size), discrete spherical entrained air-voids; and (b) cracking in many unsound crushed gneiss coarse aggregate particles. Notice some large red almandine garnet crystals in gneiss.



Figure C 20: Photomicrographs of lapped cross section of Core D-1 showing: (a) air-entrained nature of concrete having numerous fine (< 1 mm size), discrete spherical entrained air-voids; and (b) cracking in many unsound crushed gneiss coarse aggregate particles. Notice some large red almandine garnet crystals in gneiss.



Figure C 21: Photomicrographs of lapped cross section of Core D-2 showing: (a) air-entrained nature of concrete having numerous fine (< 1 mm size), discrete spherical entrained air-voids; and (b) cracking in many unsound crushed gneiss coarse aggregate particles. Notice some large red almandine garnet crystals in gneiss.



Figure C 22: Photomicrographs of lapped cross section of Core D-2 showing: (a) air-entrained nature of concrete having numerous fine (< 1 mm size), discrete spherical entrained air-voids; and (b) cracking in many unsound crushed gneiss coarse aggregate particles. Notice some large red almandine garnet crystals in gneiss.



Figure C 23: Photomicrographs of lapped cross section of Core D-2 showing: (a) air-entrained nature of concrete having numerous fine (< 1 mm size), discrete spherical entrained air-voids; and (b) cracking in many unsound crushed gneiss coarse aggregate particles. Notice some large red almandine garnet crystals in gneiss.

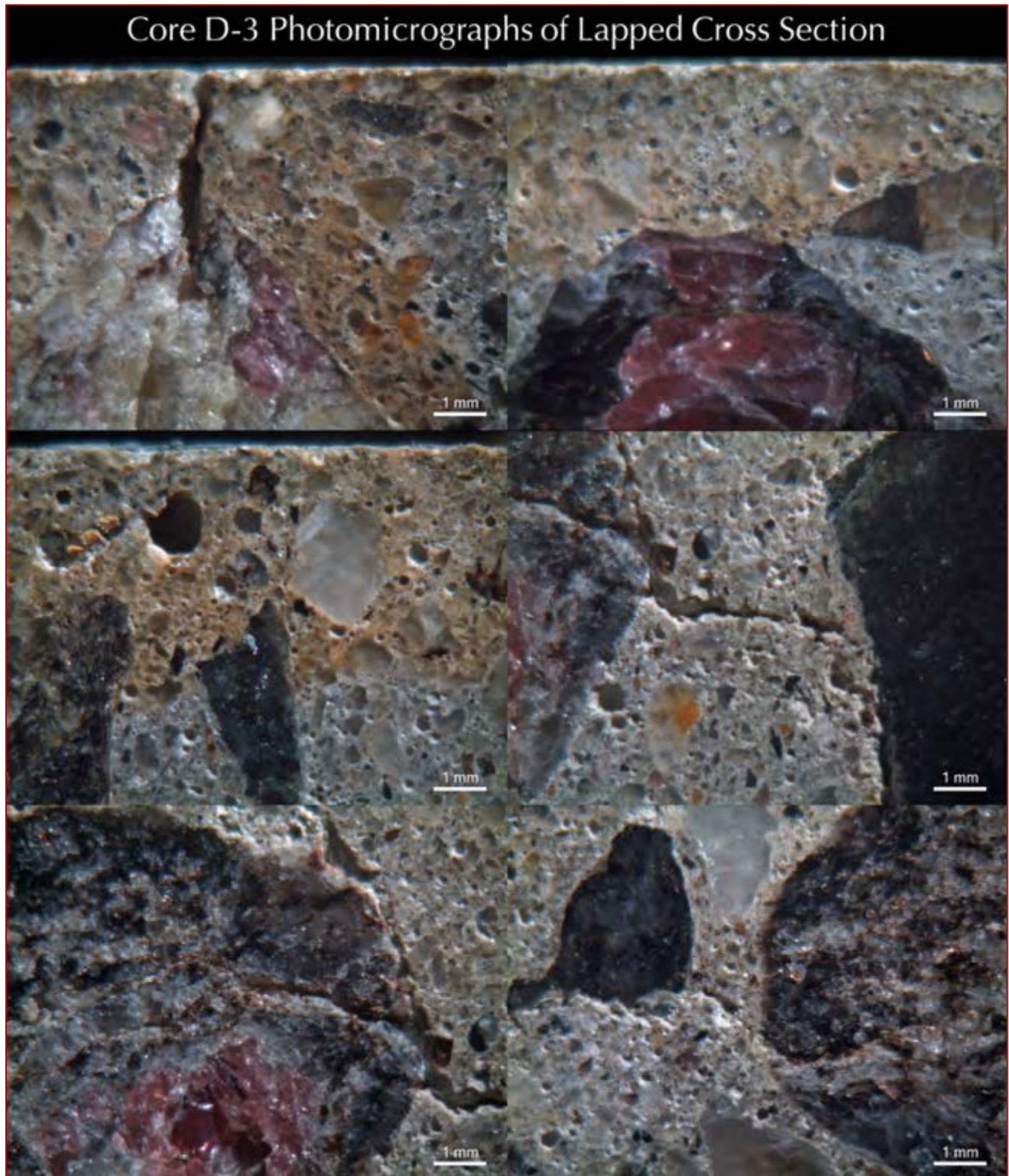


Figure C 24: Photomicrographs of lapped cross section of Core D-3 showing: (a) air-entrained nature of concrete having numerous fine (< 1 mm size), discrete spherical entrained air-voids; and (b) cracking in many unsound crushed gneiss coarse aggregate particles. Notice some large red almandine garnet crystals in gneiss.

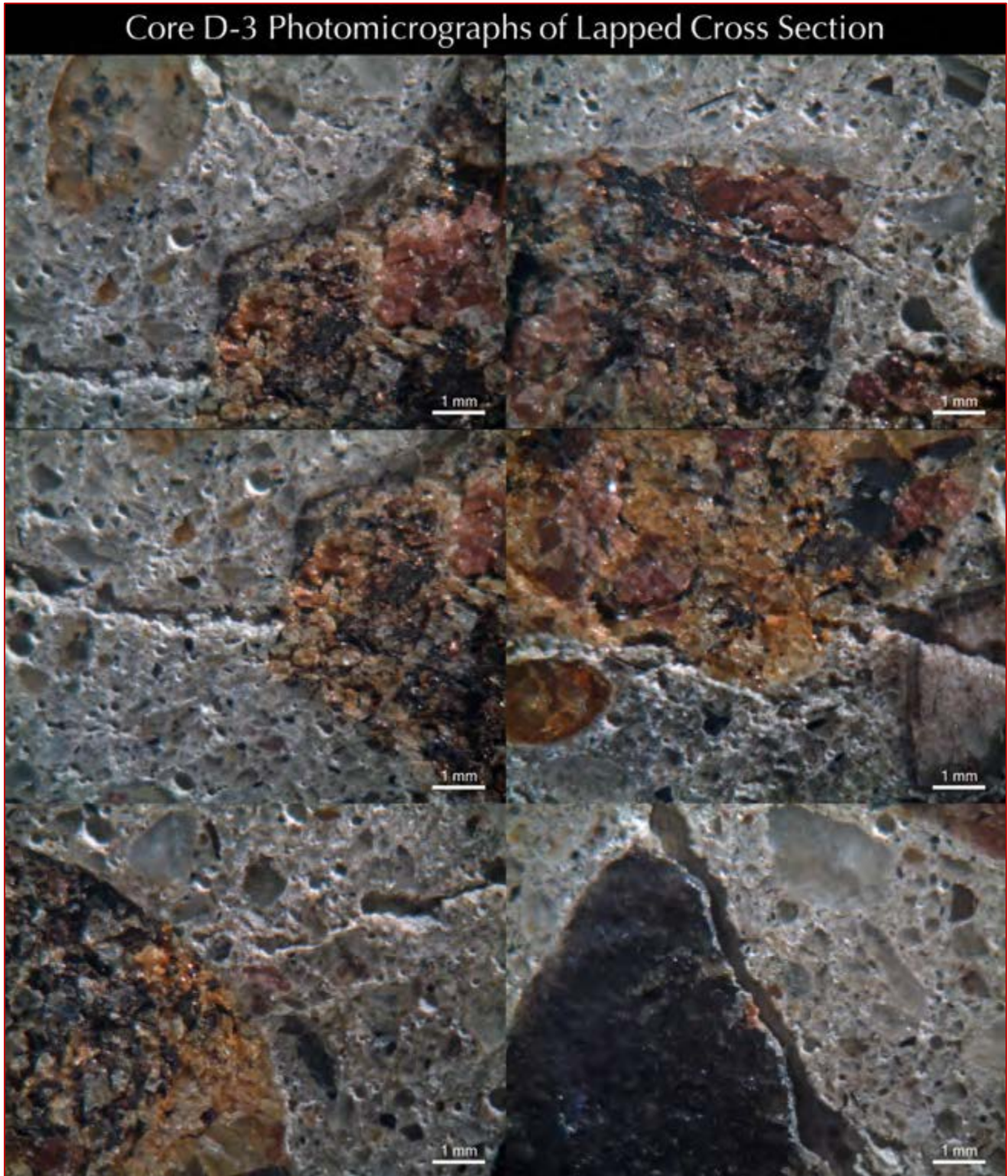


Figure C 25: Photomicrographs of lapped cross section of Core D-3 showing: (a) air-entrained nature of concrete having numerous fine (< 1 mm size), discrete spherical entrained air-voids; and (b) cracking in many unsound crushed gneiss coarse aggregate particles. Notice some large red almandine garnet crystals in gneiss.



Figure C 26: Photomicrographs of lapped cross section of Core D-3 showing: (a) air-entrained nature of concrete having numerous fine (< 1 mm size), discrete spherical entrained air-voids; and (b) cracking in many unsound crushed gneiss coarse aggregate particles. Notice some large red almandine garnet crystals in gneiss.



Figure C 27: Photomicrographs of lapped cross section of Core F-1 showing: (a) a thin (< 1 mm thick) air-entrained dark gray cementitious protective skim coat well-bonded to the wall concrete beneath; (b) air-entrained nature of concrete having numerous fine (< 1 mm size), discrete spherical entrained air -oids; and (c) some localized cracking in some potentially unsound crushed gneiss coarse aggregate particles. Notice some large red almandine garnet crystals in gneiss.

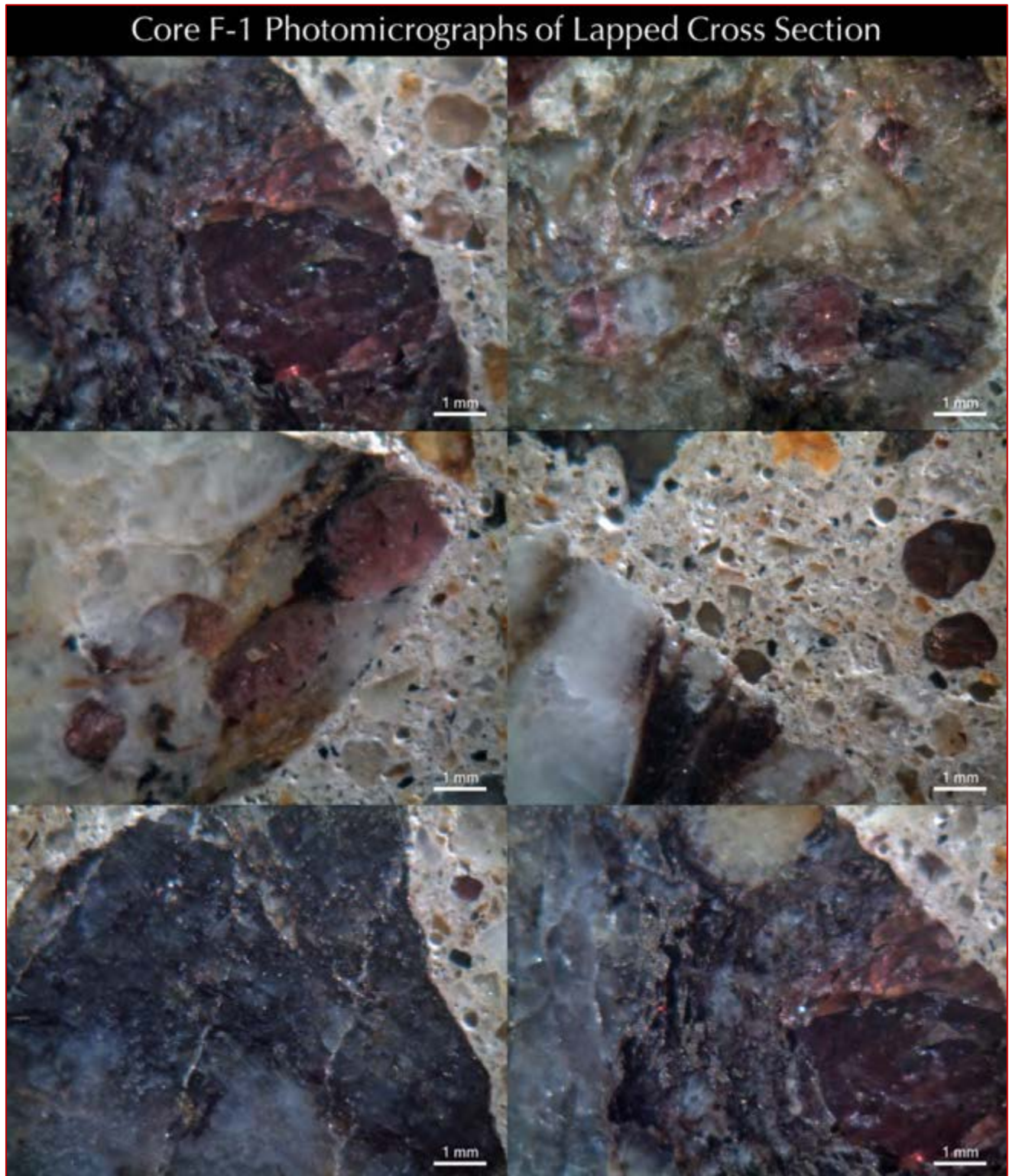


Figure C 28: Photomicrographs of lapped cross section of Core F-1 showing: (a) air-entrained nature of concrete having numerous fine (< 1 mm size), discrete spherical entrained air-voids; and (b) many unsound crushed gneiss coarse aggregate particles that are compositionally similar to the ones found in aggregate used in 1998 construction, apparently from the same concrete supplier. Notice some large red almandine garnet crystals in gneiss.



Figure C 29: Photomicrographs of lapped cross section of Core F-2 showing: (a) a thin (< 1 mm thick) air-entrained dark gray cementitious protective skim coat well-bonded to the wall concrete beneath; (b) air-entrained nature of concrete having numerous fine (< 1 mm size), discrete spherical entrained air-voids; and (c) some localized cracking in some potentially unsound crushed gneiss coarse aggregate particles. Notice some large red almandine garnet crystals in gneiss.

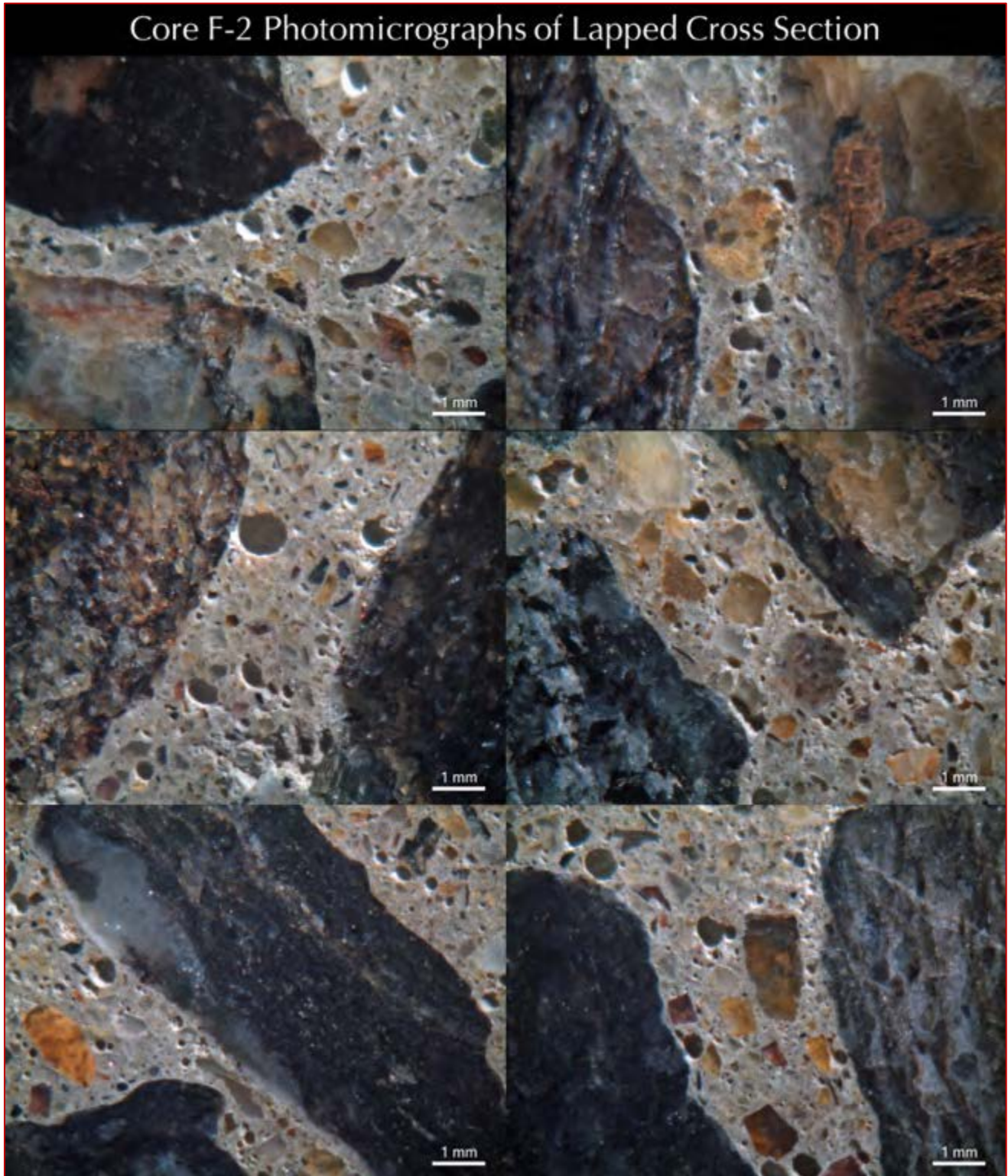


Figure C 30: Photomicrographs of lapped cross section of Core F-2 showing: (a) air-entrained nature of concrete having numerous fine (< 1 mm size), discrete spherical entrained air-voids; and (b) many unsound crushed gneiss coarse aggregate particles that are compositionally similar to the ones found in aggregate used in 1998 construction, apparently from the same concrete supplier.



Figure C 31: Photomicrographs of lapped cross section of Core F-3 showing: (a) a thin (< 1 mm thick) air-entrained dark gray cementitious protective skim coat well-bonded to the wall concrete beneath; (b) air-entrained nature of concrete having numerous fine (< 1 mm size), discrete spherical entrained air-voids; and (c) some localized cracking in some potentially unsound crushed gneiss coarse aggregate particles.

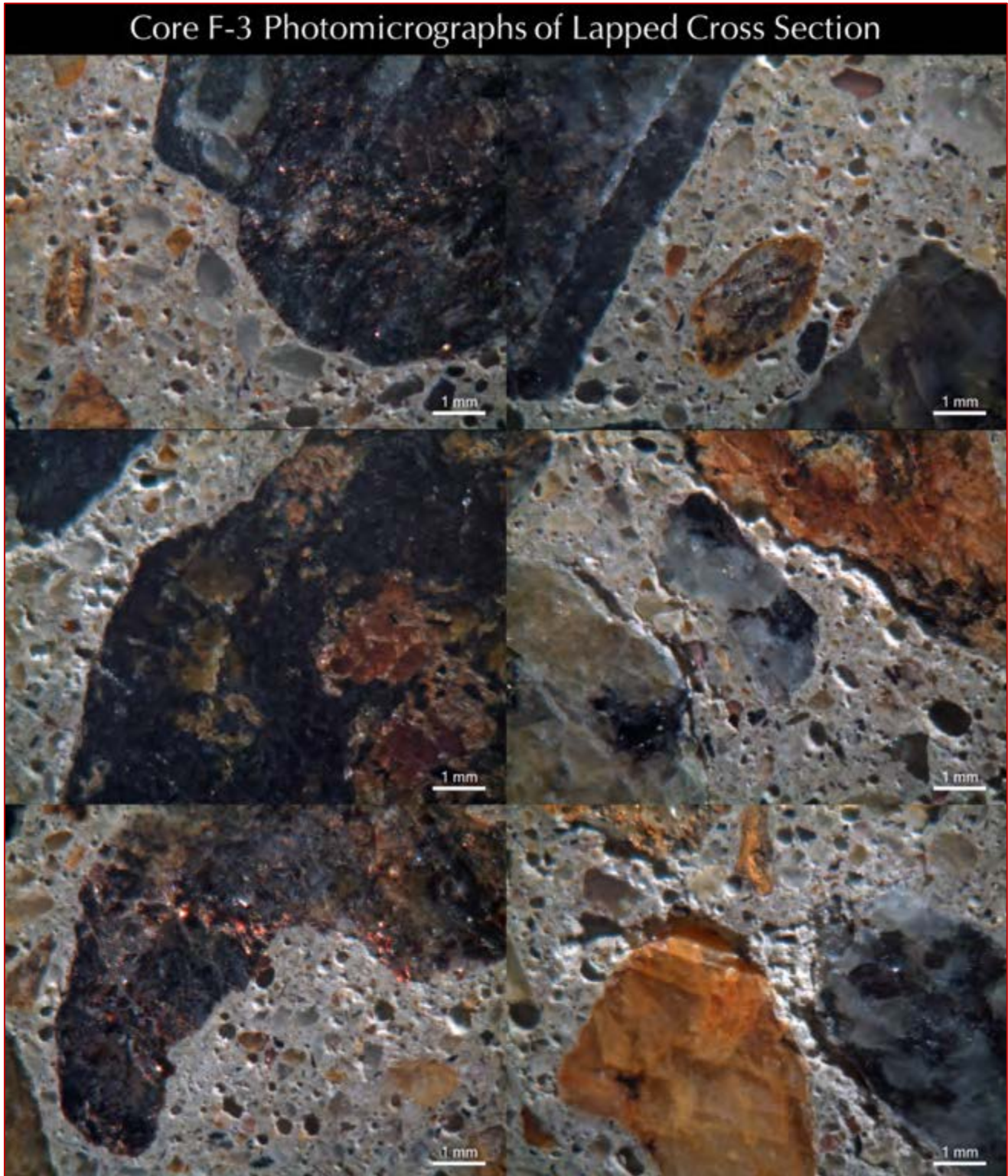


Figure C 32: Photomicrographs of lapped cross section of Core F-2 showing: (a) air-entrained nature of concrete having numerous fine (< 1 mm size), discrete spherical entrained air-voids; and (b) many unsound crushed gneiss coarse aggregate particles that are compositionally similar to the ones found in aggregate used in 1998 construction, apparently from the same concrete supplier. Notice some large red almandine garnet crystals in gneiss.

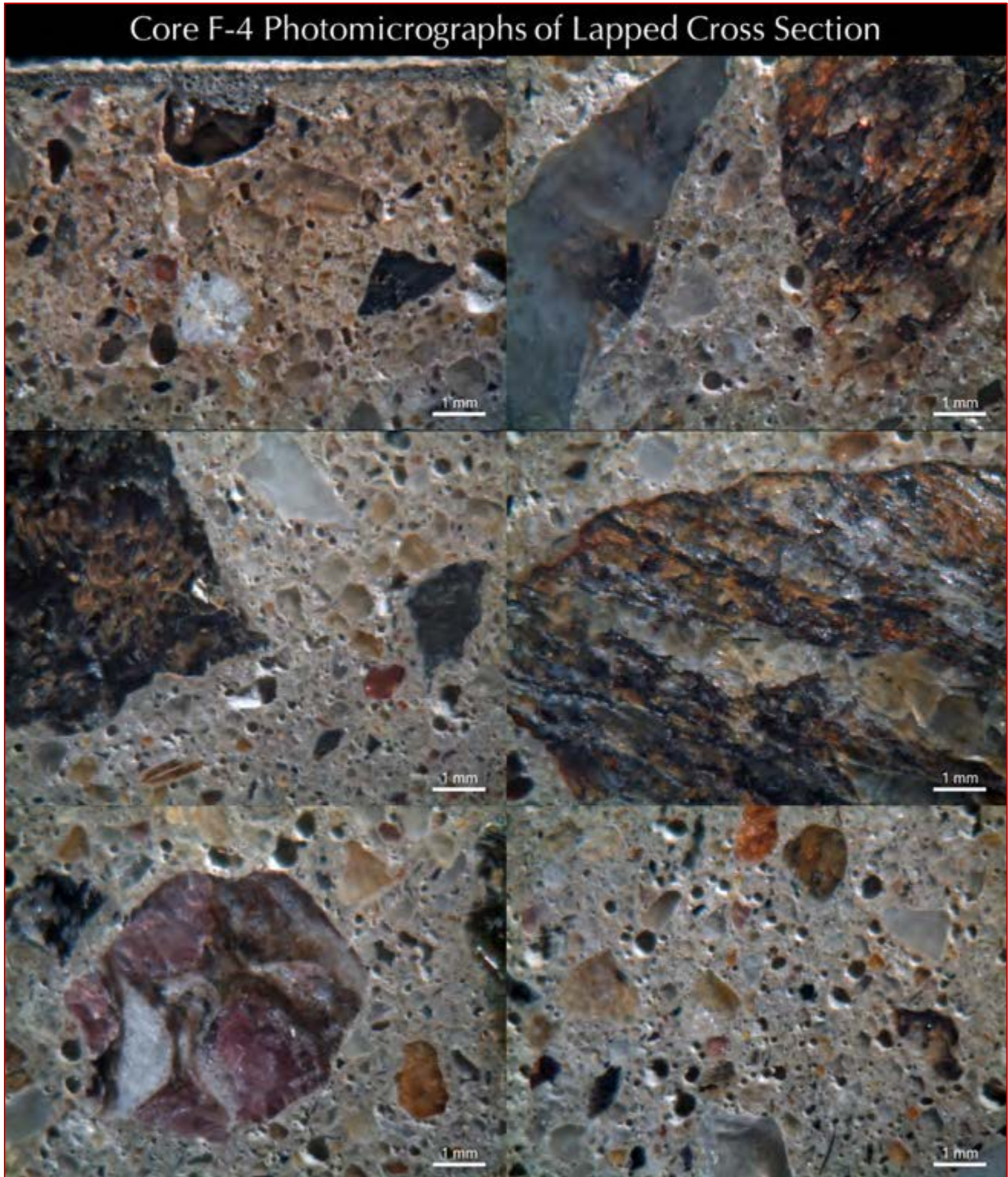


Figure C 33: Photomicrographs of lapped cross section of Core F-4 showing: (a) a thin (< 1 mm thick) air-entrained dark gray cementitious protective skim coat well-bonded to the wall concrete beneath; (b) air-entrained nature of concrete having numerous fine (< 1 mm size), discrete spherical entrained air-voids; and (c) some localized cracking in some potentially unsound crushed gneiss coarse aggregate particles. Notice some large red almandine garnet crystals in gneiss.



Figure C 34: Photomicrographs of lapped cross section of Core F-4 showing: (a) air-entrained nature of concrete having numerous fine (< 1 mm size), discrete spherical entrained air-voids; and (b) many unsound crushed gneiss coarse aggregate particles that are compositionally similar to the ones found in aggregate used in 1998 construction, apparently from the same concrete supplier.



Figure C 35: Photomicrographs of lapped cross section of Core F-5 showing: (a) a thin (< 1 mm thick) air-entrained dark gray cementitious protective skim coat well-bonded to the wall concrete beneath; (b) air-entrained nature of concrete having numerous fine (< 1 mm size), discrete spherical entrained air-voids; and (c) some localized cracking in some potentially unsound crushed gneiss coarse aggregate particles. Notice some large red almandine garnet crystals in gneiss.

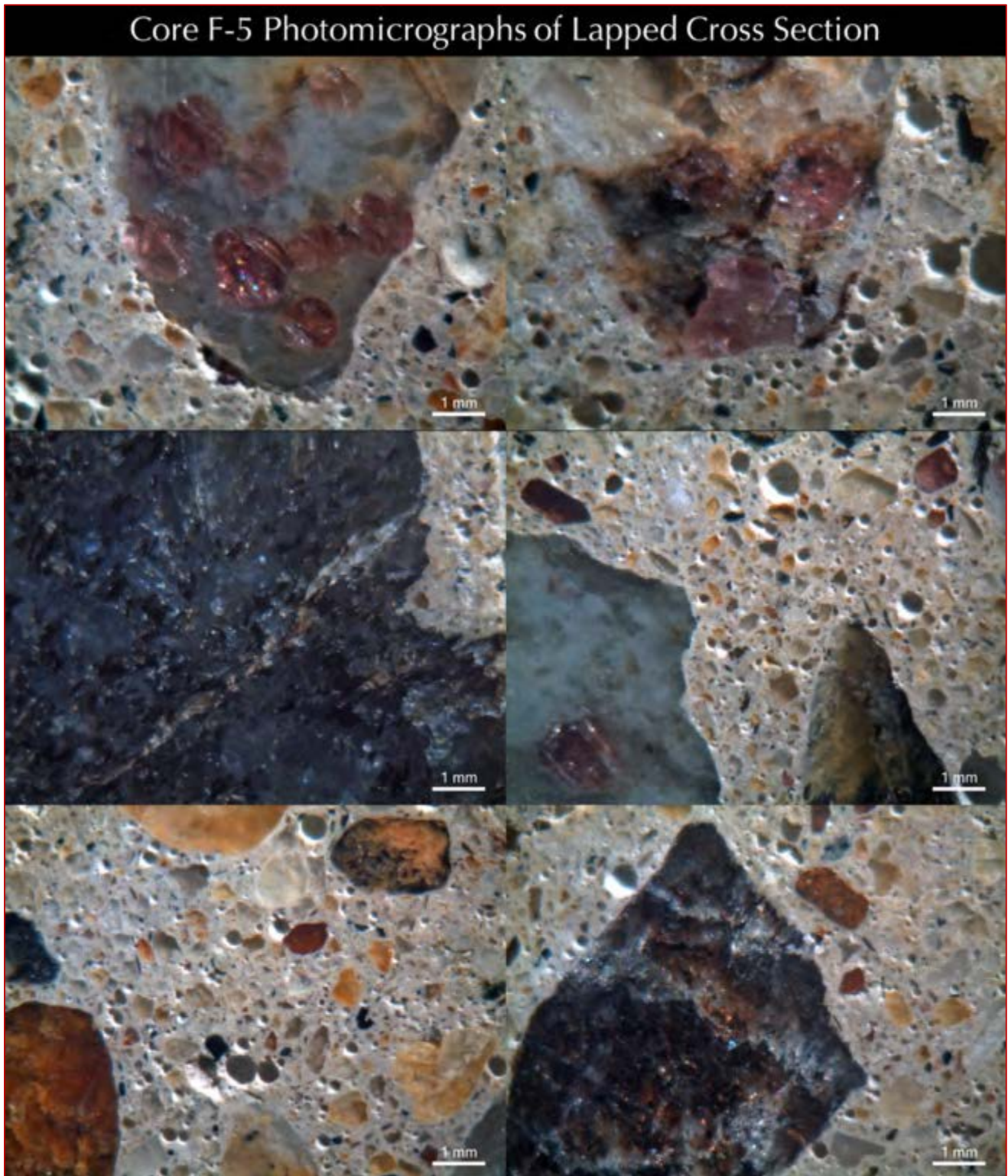


Figure C 36: Photomicrographs of lapped cross section of Core F-5 showing: (a) air-entrained nature of concrete having numerous fine (< 1 mm size), discrete spherical entrained air-voids; and (b) many unsound crushed gneiss coarse aggregate particles that are compositionally similar to the ones found in aggregate used in 1998 construction, apparently from the same concrete supplier. Notice some large red almandine garnet crystals in gneiss.



# APPENDIX D

## Photomicrographs of Thin Sections

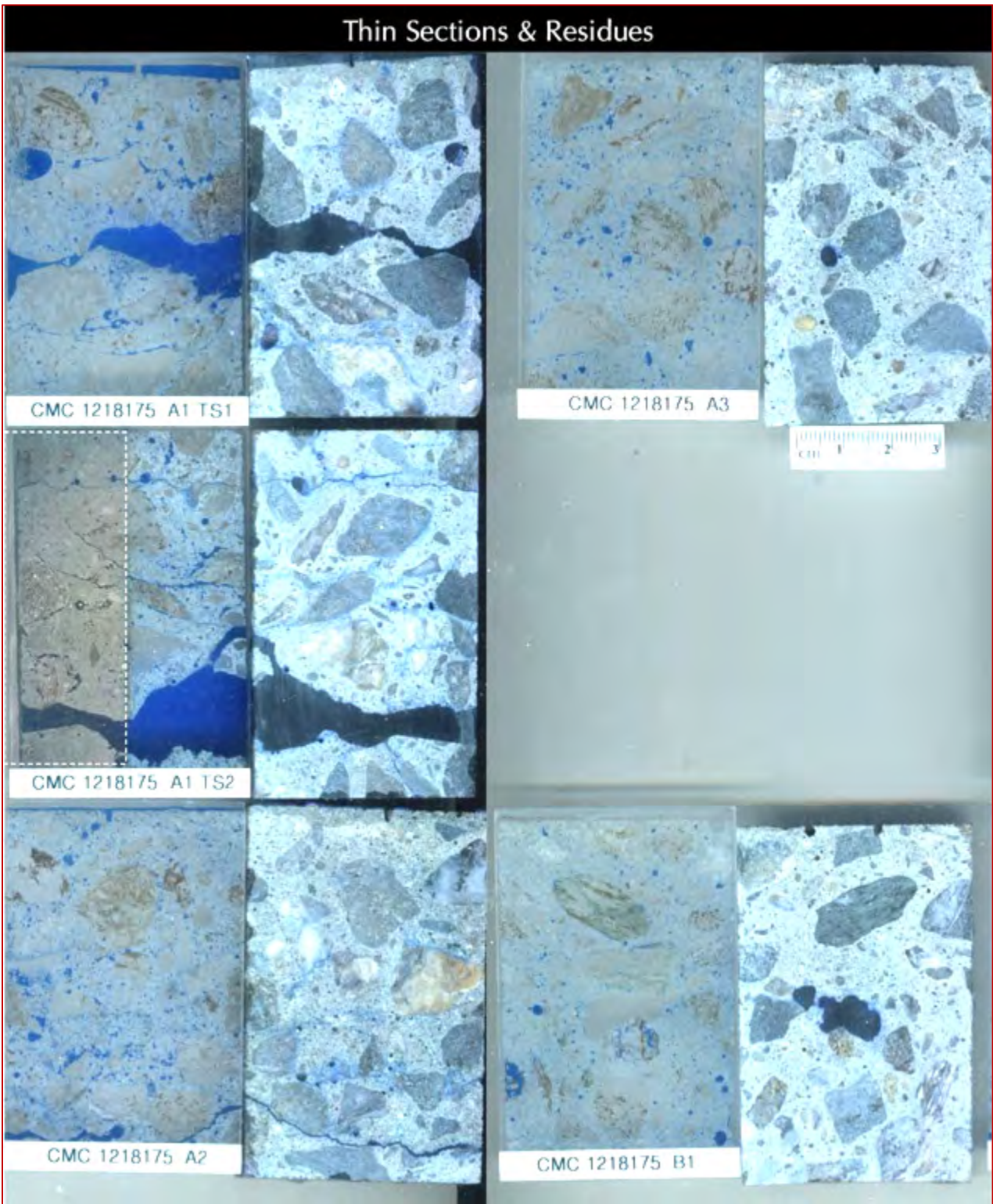


Figure D 1: Blue dye-mixed epoxy-impregnated thin sections and residues left after thin sectioning of Cores from A-series, and B-1 (1998 construction) where blue dye-mixed epoxy was impregnated into the concrete under vacuum to highlight porous areas of paste, voids, and cracks. Boxed areas on thin sections were coated with a thin film of gold for SEM-EDS analyses.

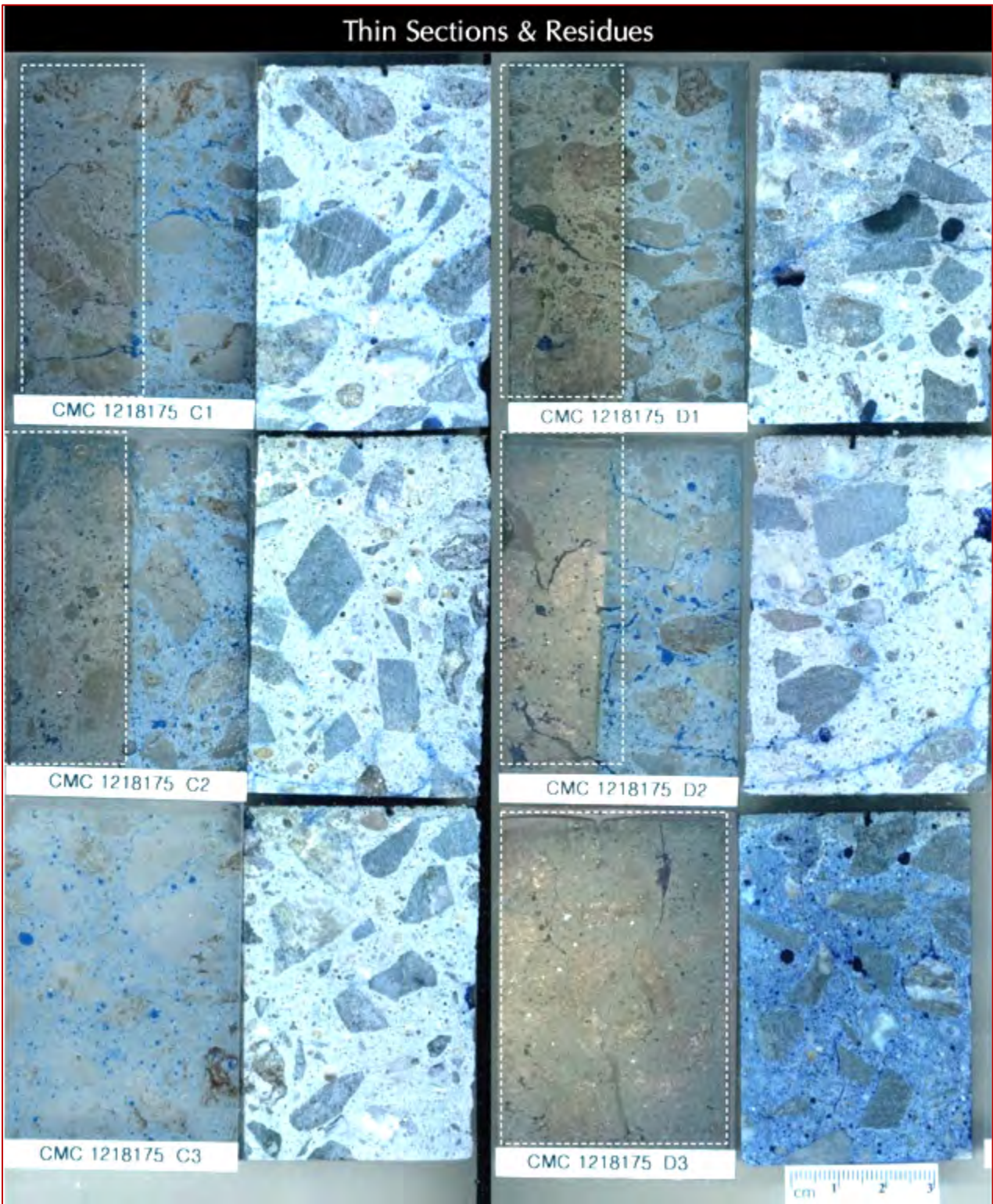


Figure D 2: Blue dye-mixed epoxy-impregnated thin sections and residues left after thin sectioning of Cores from C-series, and D-series (1998 construction) where blue dye-mixed epoxy was impregnated into the concrete under vacuum to highlight porous areas of paste, voids, and cracks. Boxed areas on thin sections were coated with a thin film of gold for SEM-EDS analyses.

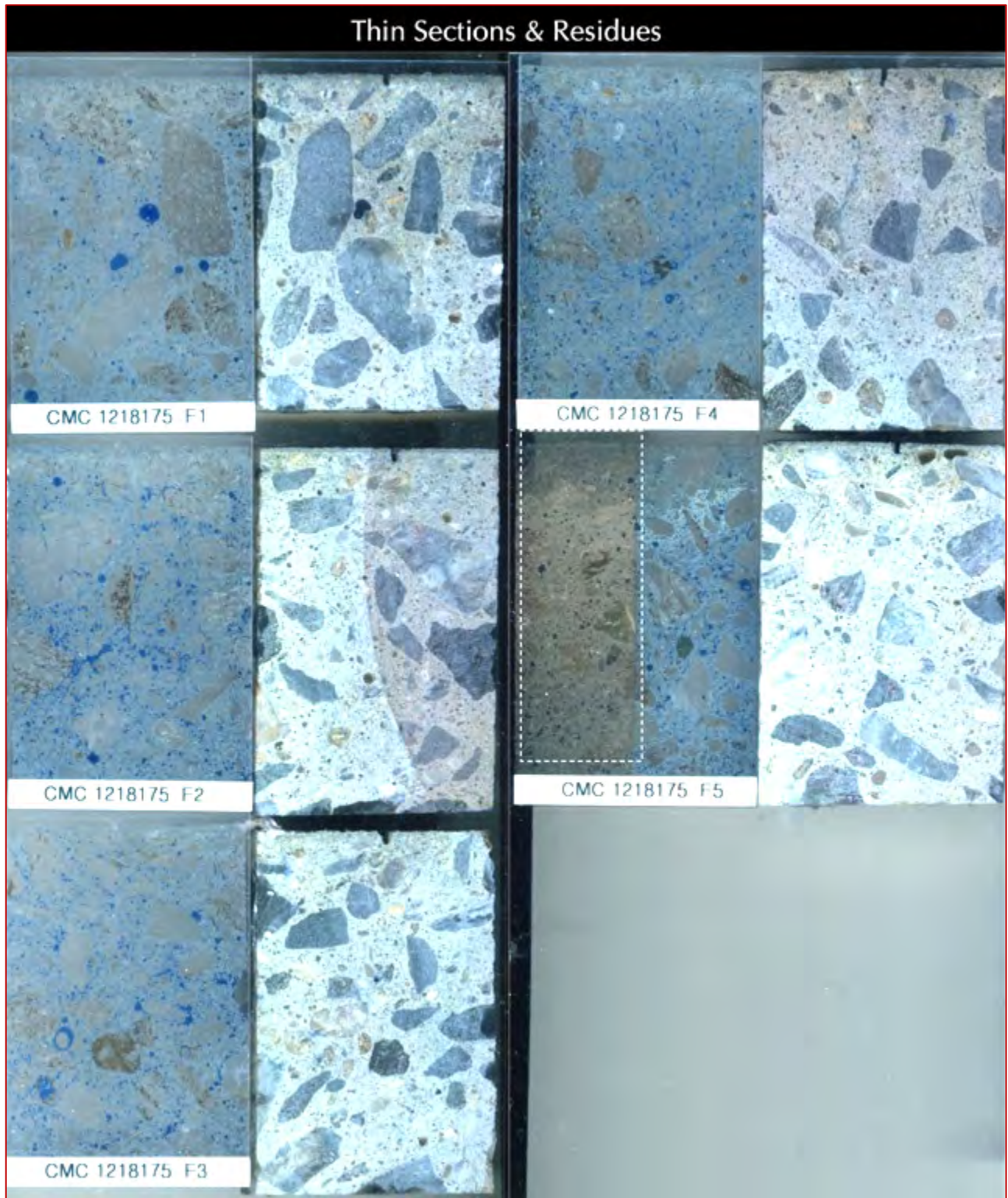


Figure D 3: Blue dye-mixed epoxy-impregnated thin sections and residues left after thin sectioning of Cores from F-series (2001 construction) where blue dye-mixed epoxy was impregnated into the concrete under vacuum to highlight porous areas of paste, voids, and cracks. Boxed areas on thin sections were coated with a thin film of gold for SEM-EDS analyses.

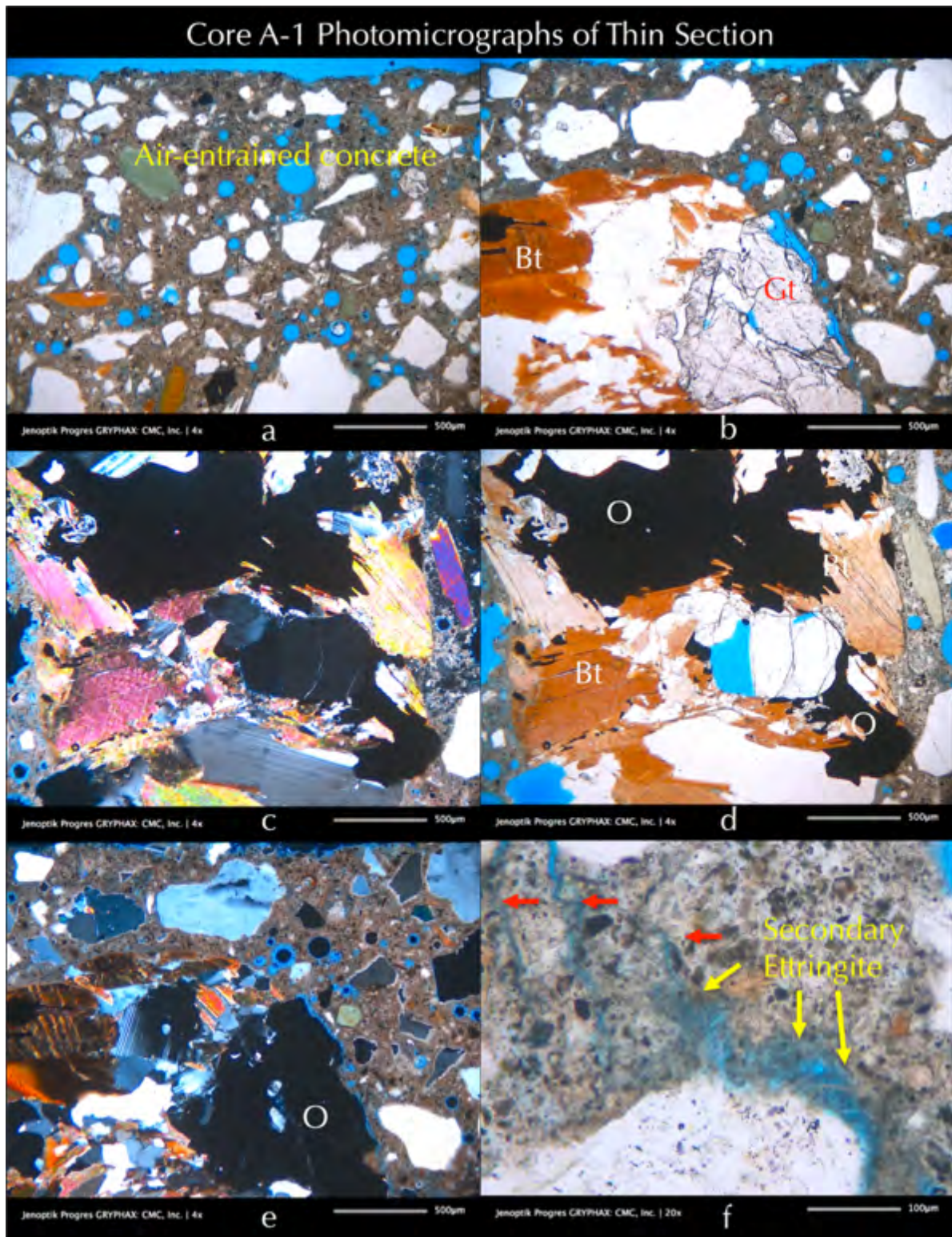


Figure D 4: Photomicrographs of thin section of Core A-1 showing mineralogies, textures, and microstructures of concrete and aggregates. Photos: a – air-entrained concrete where air bubbles are highlighted in blue epoxy; b to e – garnetiferous (Gt) quartz (Q) -feldspar (albitic plagioclase, Pl) -biotite (Bt) gneiss where opaque (O) grains in dark are of iron sulfide (pyrrhotite) and iron-titanium oxide (ilmenite); f – microcracks filled with fibrous ettringite deposits, a telltale feature of concrete deterioration by oxidation of pyrrhotite where sulfates released from oxidation form ettringite, which eventually precipitate by moisture from the paste to the open spaces of voids and cracks.

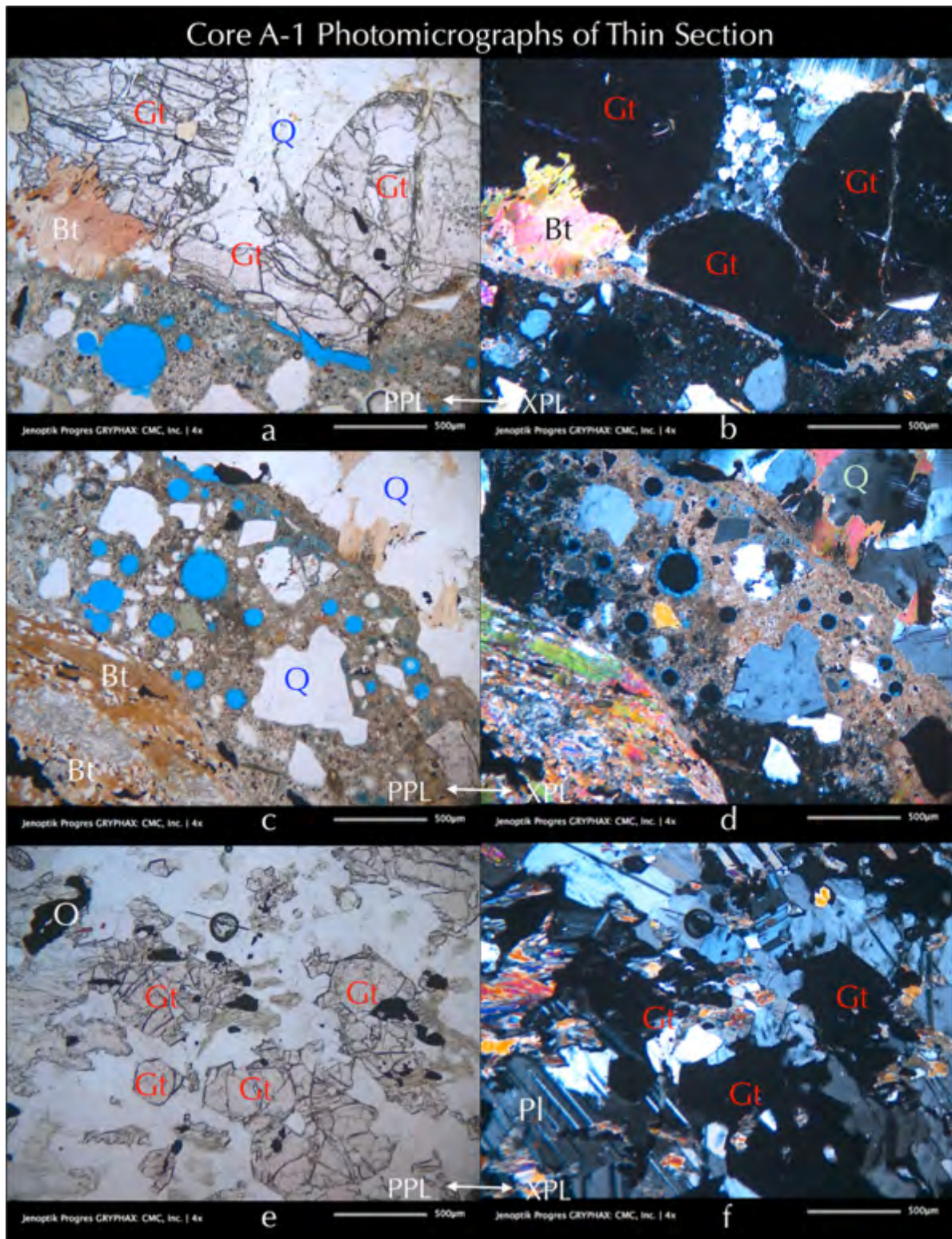


Figure D 5: Photomicrographs of thin section of Core A-1 showing mineralogies, textures, and microstructures of concrete and aggregates. Photos: a to f – garnetiferous (Gt) quartz (Q)-feldspar (albitic plagioclase, Pl)-biotite (Bt) gneiss where disseminated opaque (O) grains in dark are of iron sulfide (pyrrhotite) and iron-titanium oxide (ilmenite). PPL-XPL photos of same microstructure taken in plane and crossed polarized-light modes with a petrographic microscope.

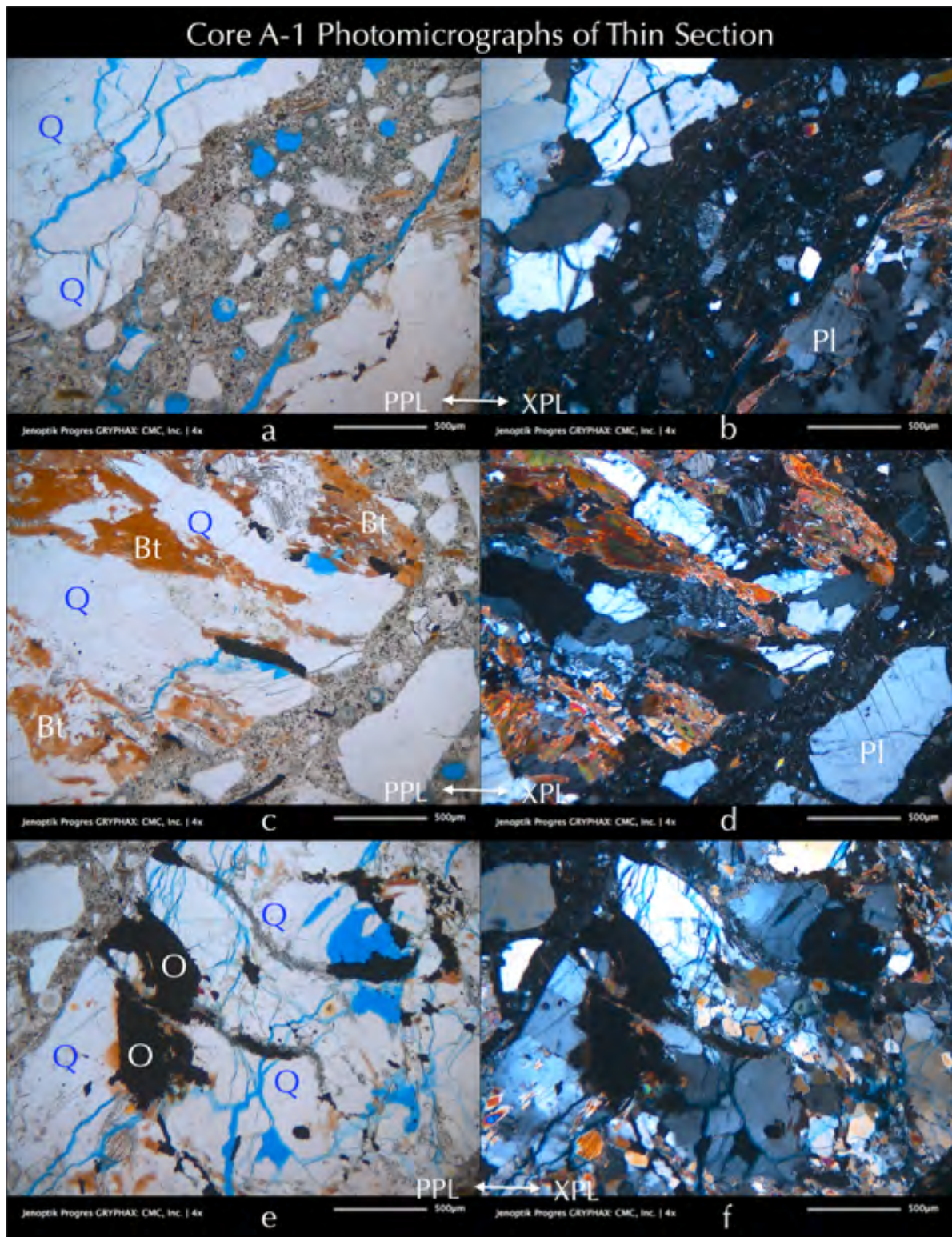


Figure D 6: Photomicrographs of thin section of Core A-1 showing mineralogies, textures, and microstructures of concrete and aggregates. Photos: a to f – garnetiferous (Gt) quartz (Q) -feldspar (albitic plagioclase, Pl) -biotite (Bt) gneiss where disseminated opaque (O) grains in dark are of iron sulfide (pyrrhotite) and iron-titanium oxide (ilmenite). PPL-XPL photos of same microstructure taken in plane and crossed polarized-light modes with a petrographic microscope.

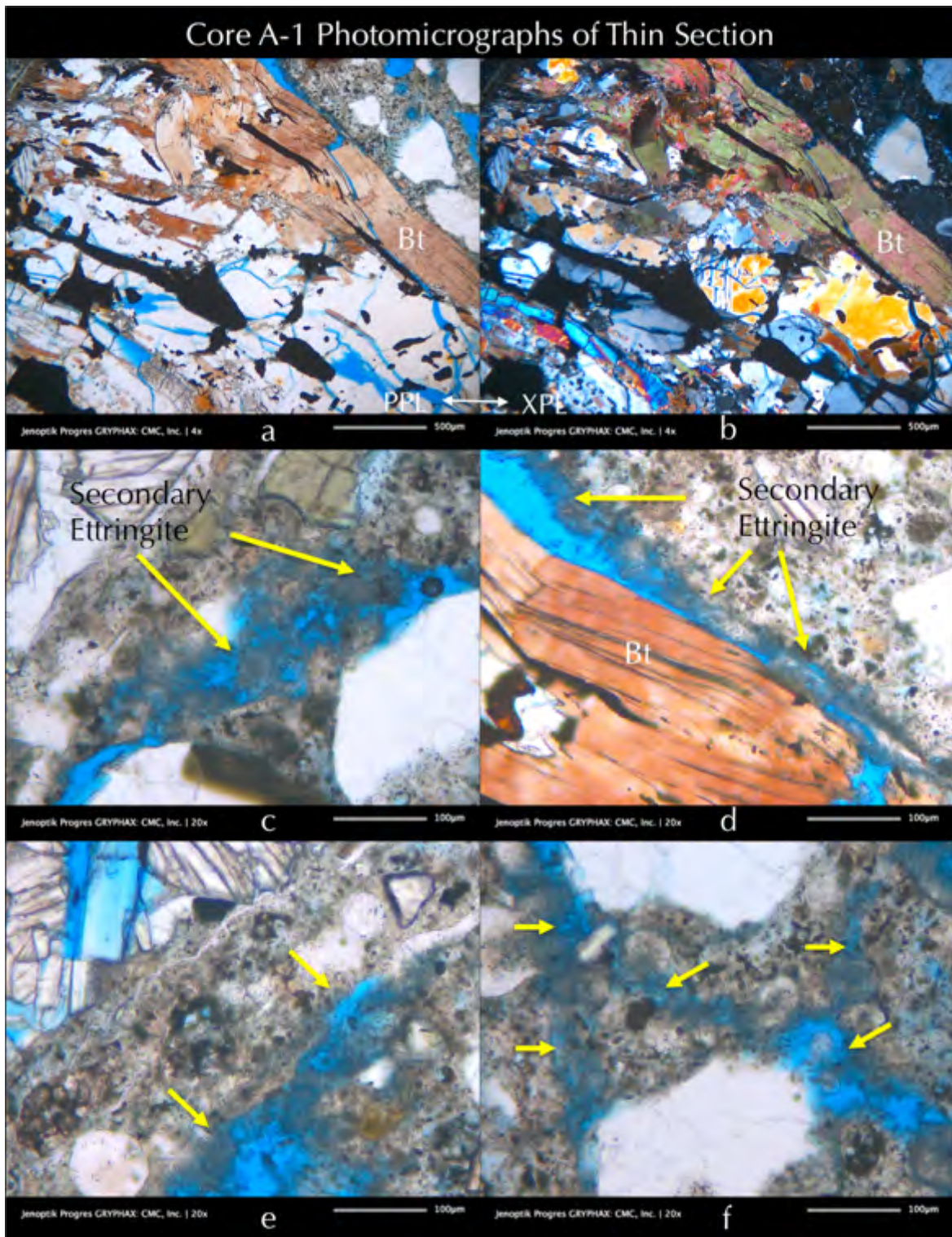


Figure D 7: Photomicrographs of thin section of Core A-1 showing mineralogies, textures, and microstructures of concrete and aggregates. Photos: a, b – garnetiferous (Gt) quartz (Q) -feldspar (albitic plagioclase, Pl) -biotite (Bt) gneiss where disseminated opaque (O) grains in dark are of iron sulfide (pyrrhotite) and iron-titanium oxide (ilmenite). PPL-XPL photos of same microstructure taken in plane and crossed polarized-light modes with a petrographic microscope. Photos c to f – microcracks filled with fibrous ettringite deposits, a telltale feature of concrete deterioration by oxidation of pyrrhotite where sulfates released from oxidation form ettringite, which eventually precipitate by moisture from the paste to the open spaces of voids and cracks.

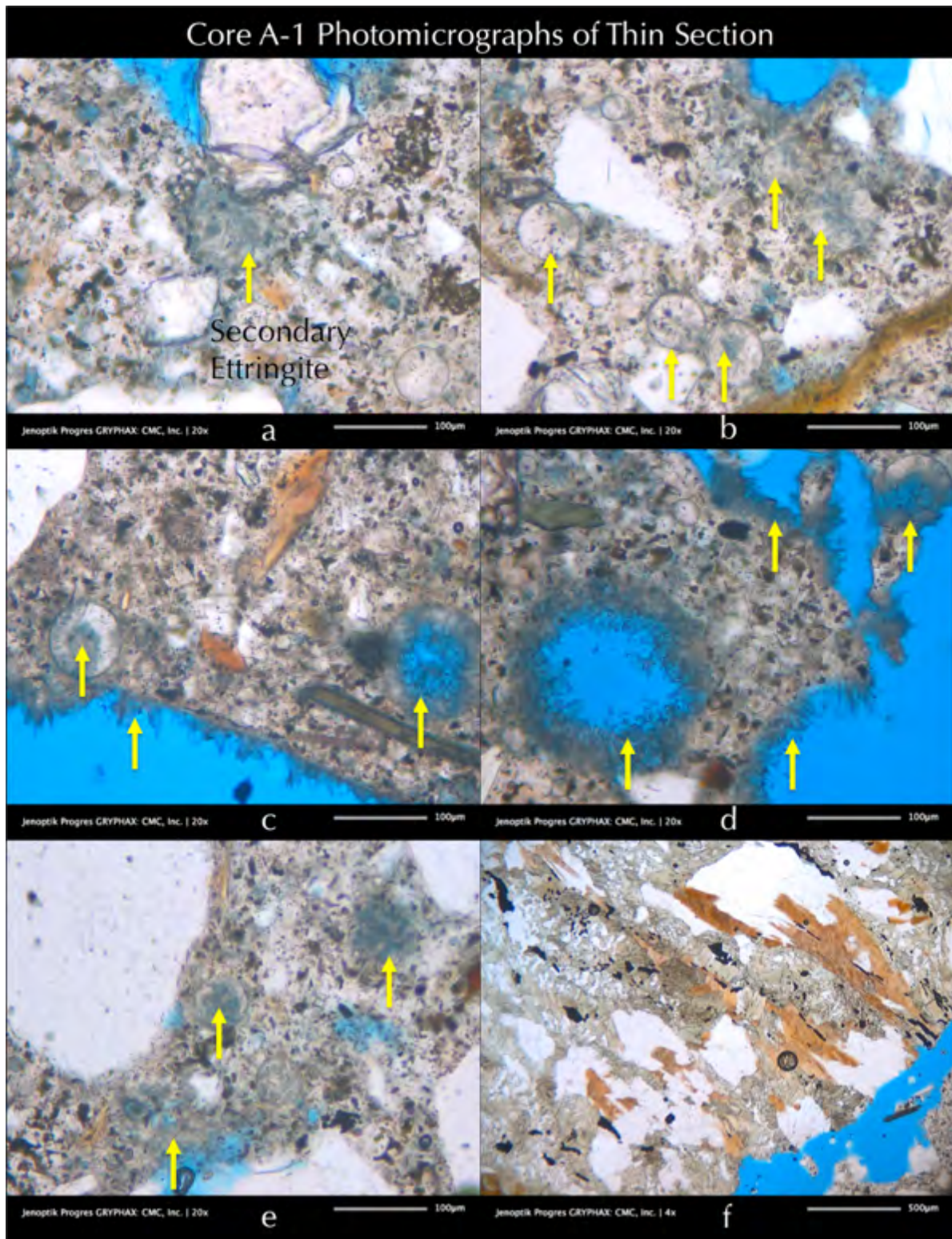


Figure D 8: Photomicrographs of thin section of Core A-1 showing porous areas, voids, and microcracks filled with fibrous ettringite deposits, a telltale feature of concrete deterioration by oxidation of pyrrhotite where sulfates released from oxidation form ettringite, which eventually precipitate by moisture from the paste to the open spaces of voids and cracks.

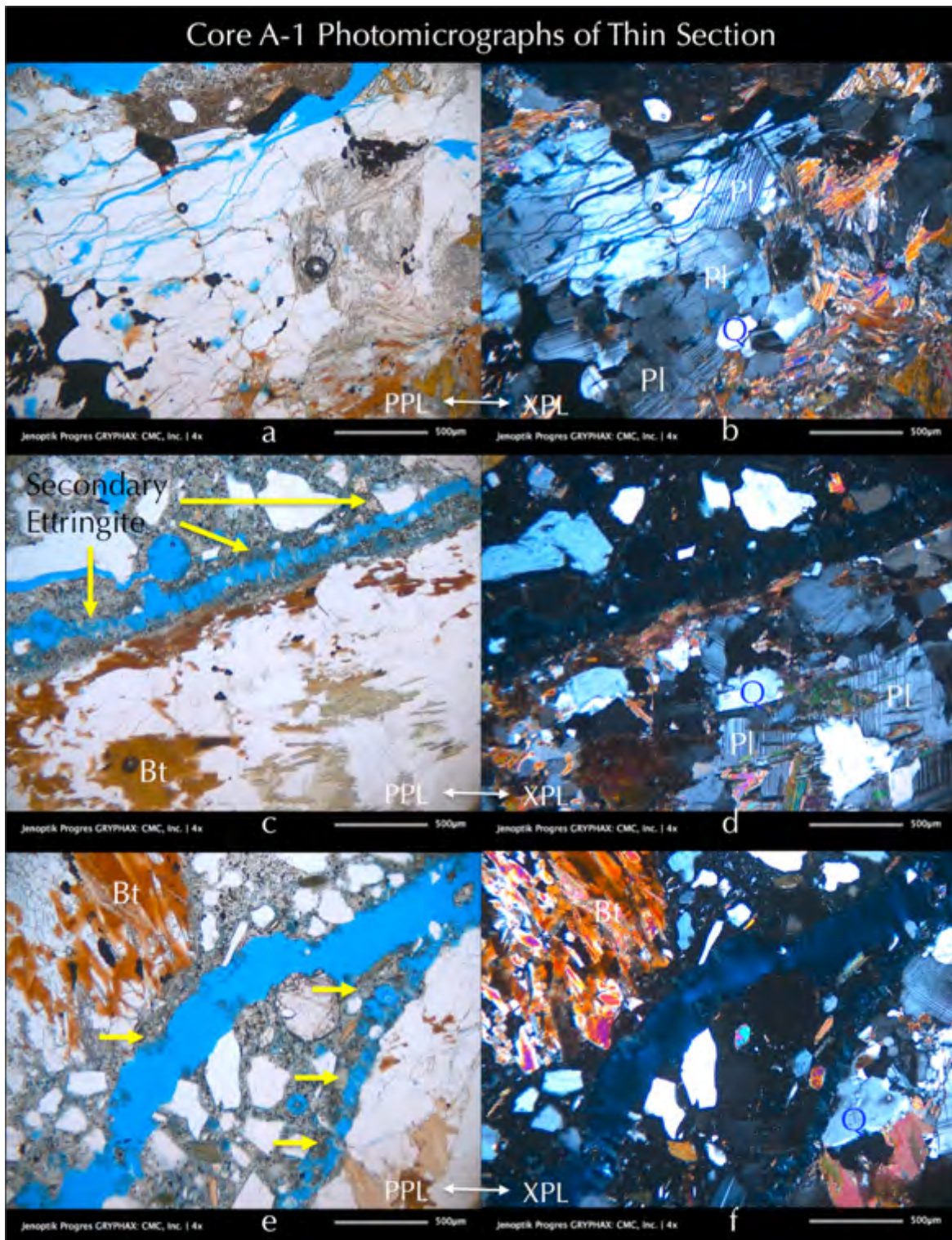


Figure D 9: Photomicrographs of thin section of Core A-1 showing mineralogies, textures, and microstructures of concrete and aggregates. Photos: a to f – garnetiferous (Gt) quartz (Q) -feldspar (albitic plagioclase, Pl) -biotite (Bt) gneiss where disseminated opaque (O) grains in dark are of iron sulfide (pyrrhotite) and iron-titanium oxide (ilmenite). PPL-XPL photos of same microstructure taken in plane and crossed polarized-light modes with a petrographic microscope. Photos: c to f show secondary ettringite deposits along aggregate-paste interfaces and in cracks - a telltale feature of concrete deterioration by oxidation of pyrrhotite where sulfates released for oxidation forms ettringite, which eventually precipitate by moisture from the paste to the open spaces of voids and cracks.

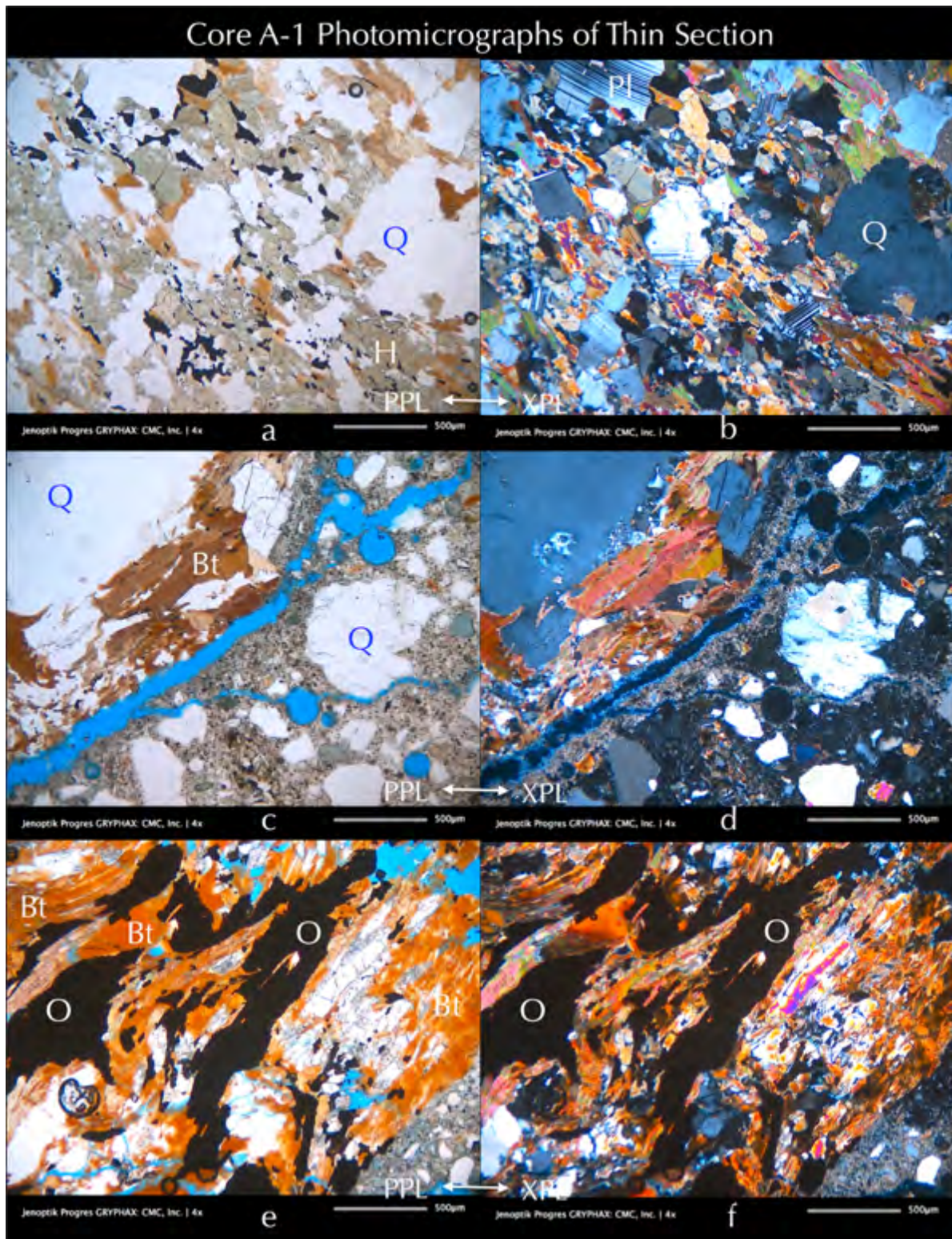


Figure D 10: Photomicrographs of thin section of Core A-1 showing mineralogies, textures, and microstructures of concrete and aggregates. Photos: a to f – garnetiferous (Gt) quartz (Q) -feldspar (albitic plagioclase, Pl) -biotite (Bt) gneiss where disseminated opaque (O) grains in dark are of iron sulfide (pyrrhotite) and iron-titanium oxide (ilmenite). PPL-XPL photos of same microstructure taken in plane and crossed polarized-light modes with a petrographic microscope.

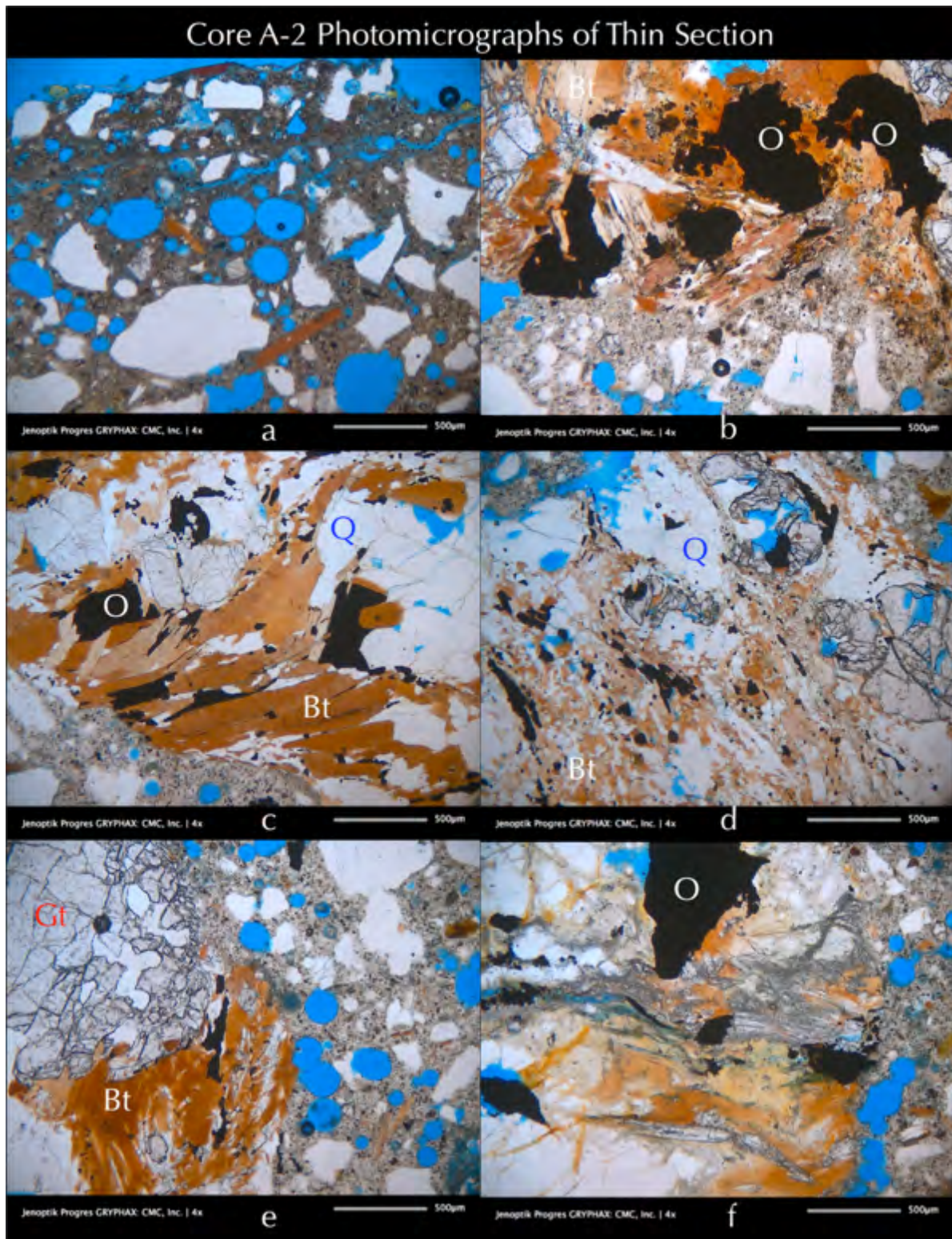


Figure D 11: Photomicrographs of thin section of Core A-2 showing mineralogies, textures, and microstructures of concrete and aggregates. Photos: a – air-entrained concrete where air voids are highlighted in blue epoxy; b to f – garnetiferous (Gt) quartz (Q) -feldspar (albitic plagioclase, Pl) -biotite (Bt) gneiss where disseminated opaque (O) grains in dark are of iron sulfide (pyrrhotite) and iron-titanium oxide (ilmenite).

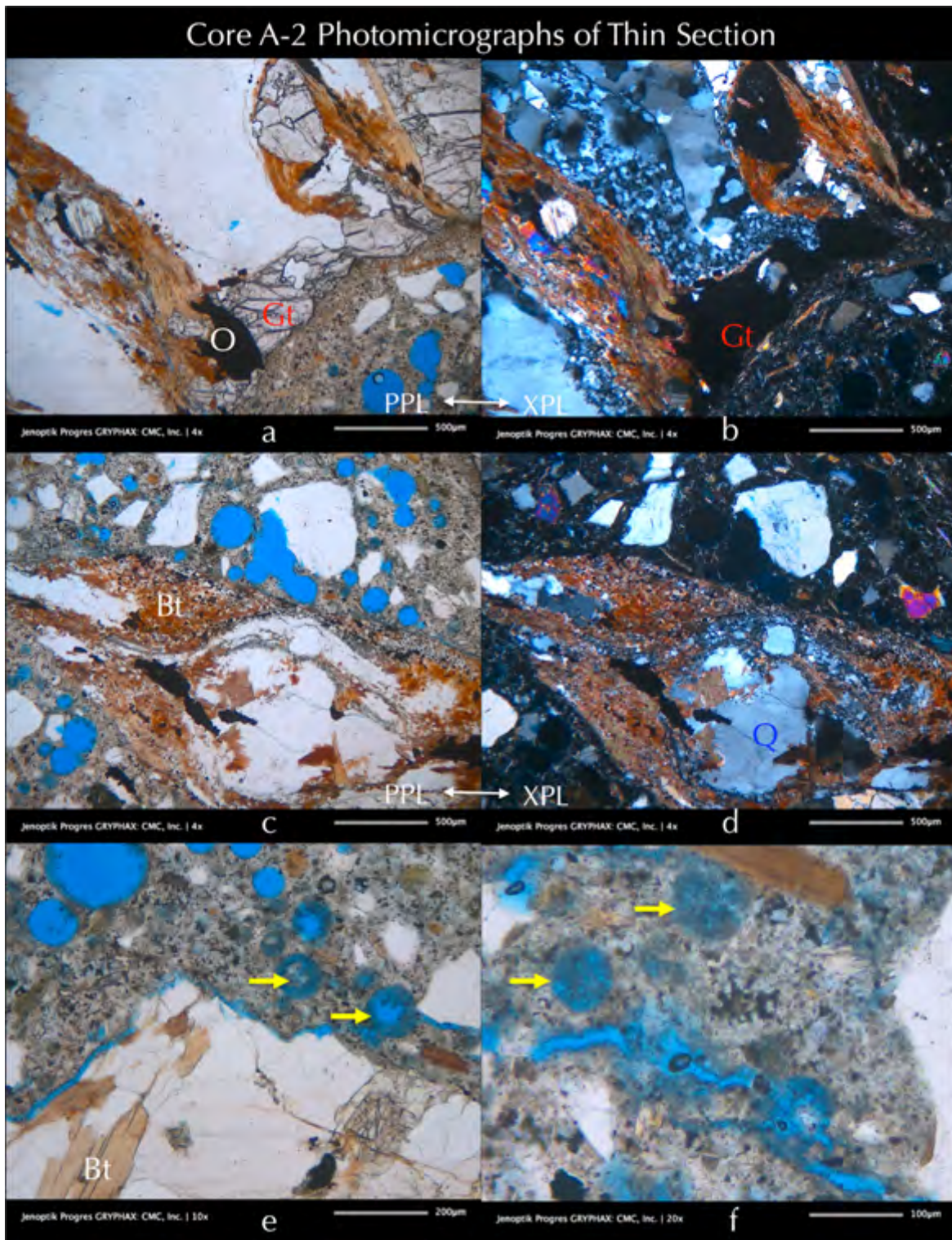


Figure D 12: Photomicrographs of thin section of Core A-2 showing mineralogies, textures, and microstructures of concrete and aggregates. Photos: a to d – garnetiferous (Gt) quartz (Q)-feldspar (albitic plagioclase, Pl)-biotite (Bt) gneiss where disseminated opaque (O) grains in dark are of iron sulfide (pyrrhotite) and iron-titanium oxide (ilmenite). PPL-XPL photos of same microstructure taken in plane and crossed polarized-light modes with a petrographic microscope. Photos: e and f - secondary ettringite deposits along aggregate-paste interfaces and in cracks - a telltale feature of concrete deterioration by oxidation of pyrrhotite where sulfates released from oxidation form ettringite, which eventually precipitate by moisture from the paste to the open spaces of voids and cracks.

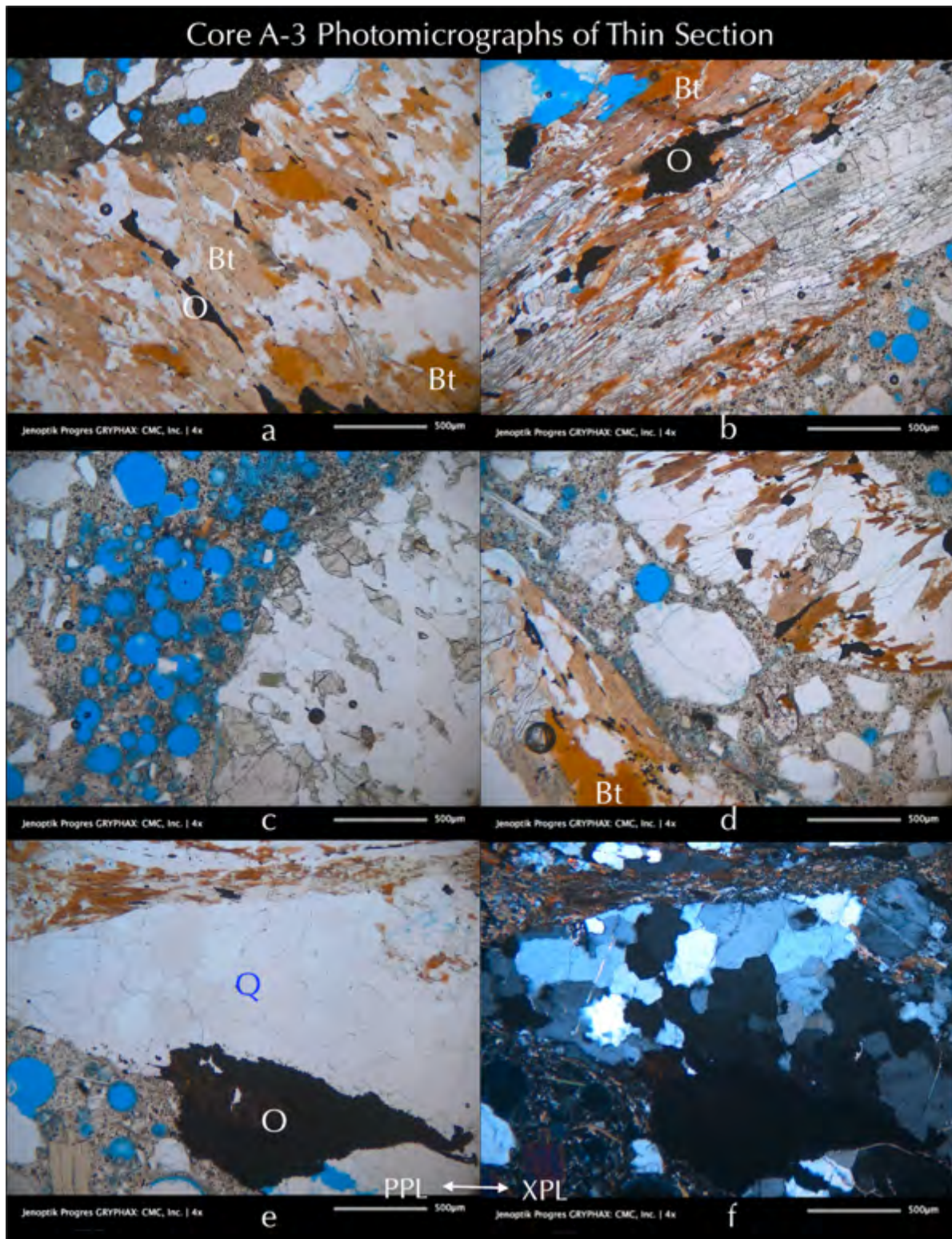


Figure D 13: Photomicrographs of thin section of Core A-3 showing mineralogies, textures, and microstructures of concrete and aggregates. Photos: a, b, d to f – garnetiferous (Gt) quartz (Q) -feldspar (albitic plagioclase, Pl) -biotite (Bt) gneiss where disseminated opaque (O) grains in dark are of iron sulfide (pyrrhotite) and iron-titanium oxide (ilmenite). PPL-XPL photos of same microstructure taken in plane and crossed polarized-light modes with a petrographic microscope. Photo: c - air-entrained concrete where air-voids are highlighted in blue epoxy.

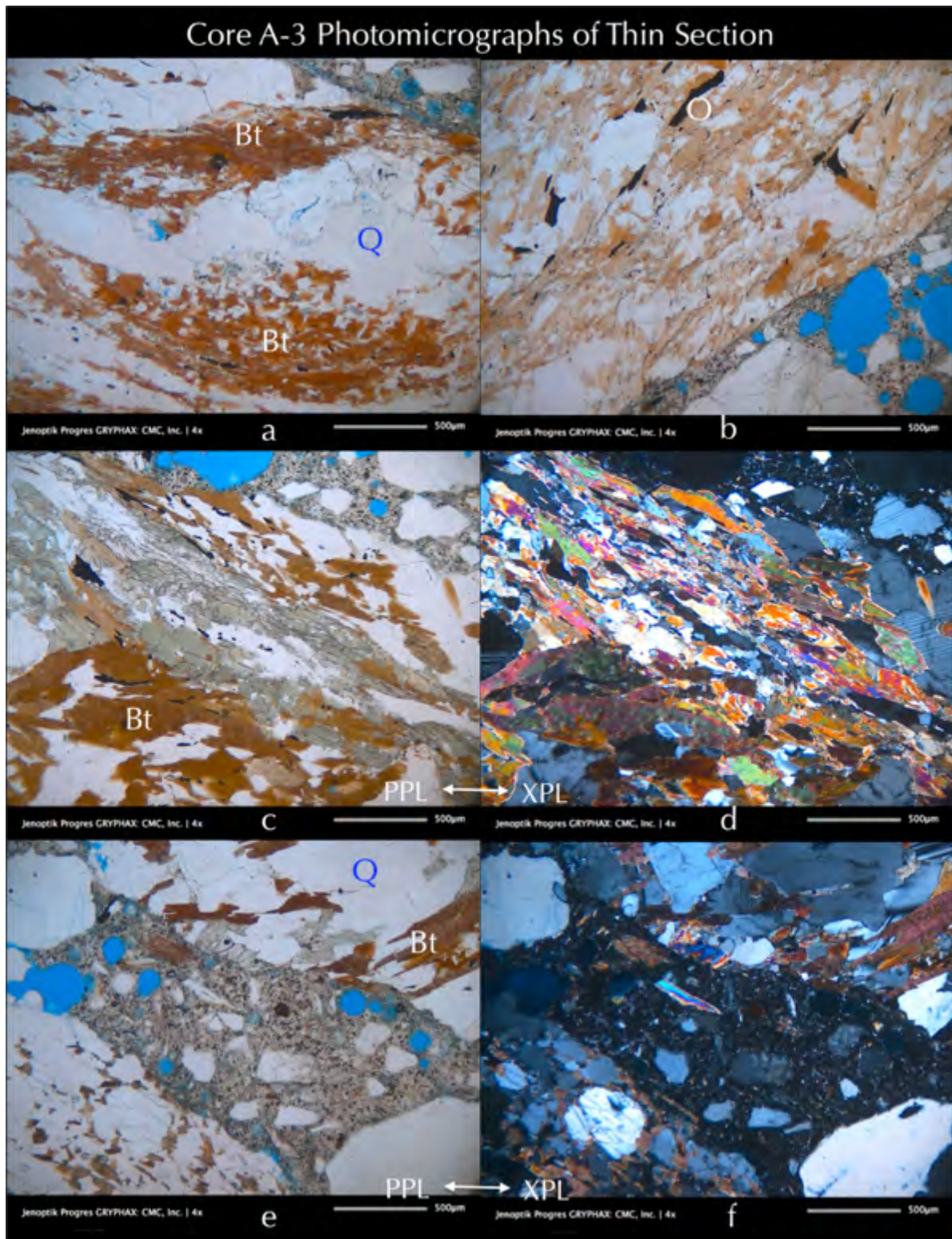


Figure D 14: Photomicrographs of thin section of Core A-3 showing mineralogies, textures, and microstructures of concrete and aggregates. Photos: a, b, d to f – garnetiferous (Gt) quartz (Q) -feldspar (albitic plagioclase, Pl) -biotite (Bt) gneiss where disseminated opaque (O) grains in dark are of iron sulfide (pyrrhotite) and iron-titanium oxide (ilmenite). PPL-XPL photos of same microstructure taken in plane and crossed polarized-light modes with a petrographic microscope.

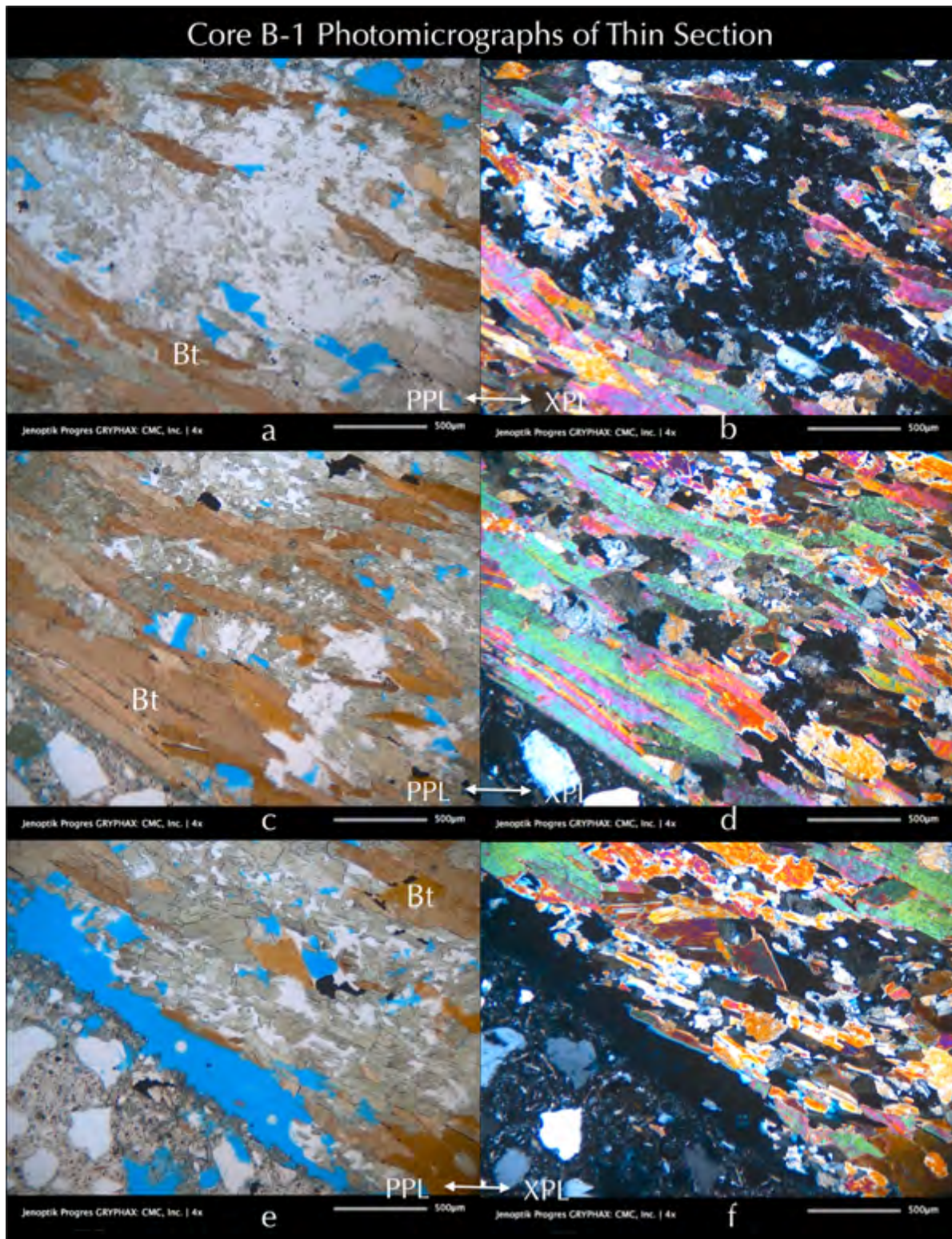


Figure D 15: Photomicrographs of thin section of Core B-1 showing mineralogies, textures, and microstructures of concrete and aggregates. Photos: a to f – garnetiferous (Gt) quartz (Q) -feldspar (albitic plagioclase, Pl) -biotite (Bt) gneiss where disseminated opaque (O) grains in dark are of iron sulfide (pyrrhotite) and iron-titanium oxide (ilmenite). PPL-XPL photos of same microstructure taken in plane and crossed polarized-light modes with a petrographic microscope.

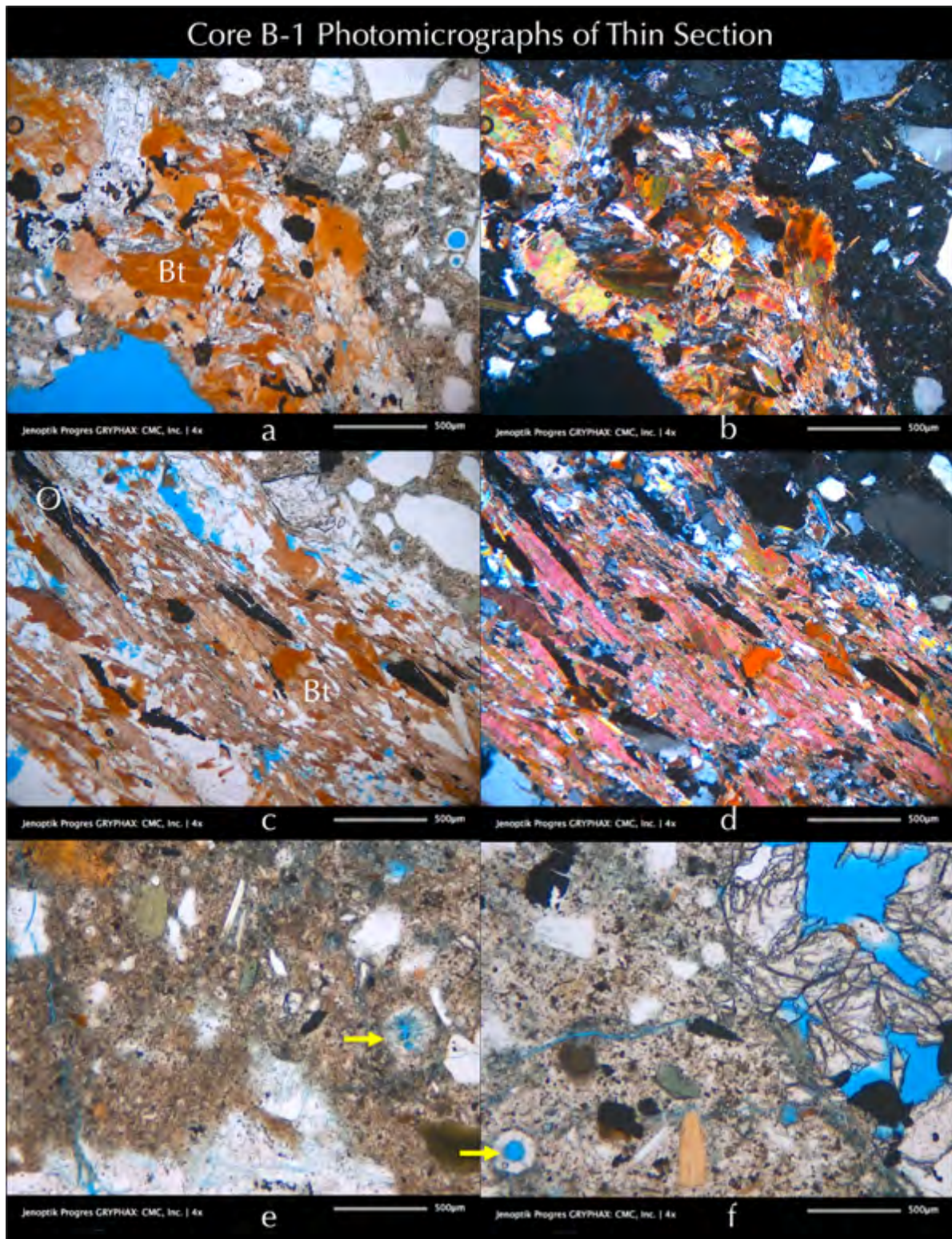


Figure D 16: Photomicrographs of thin section of Core B-1 showing mineralogies, textures, and microstructures of concrete and aggregates. Photos: a to f – garnetiferous (Gt) quartz (Q) -feldspar (albitic plagioclase, Pl) -biotite (Bt) gneiss where opaque (O) grains in dark are of iron sulfide (pyrrhotite) and iron-titanium oxide (ilmenite). Photos: e and f - secondary ettringite deposits along aggregate-paste interfaces, voids, and in cracks - a telltale feature of concrete deterioration by oxidation of pyrrhotite where sulfates released from oxidation form ettringite, which eventually precipitate by moisture from the paste to the open spaces of voids and cracks.

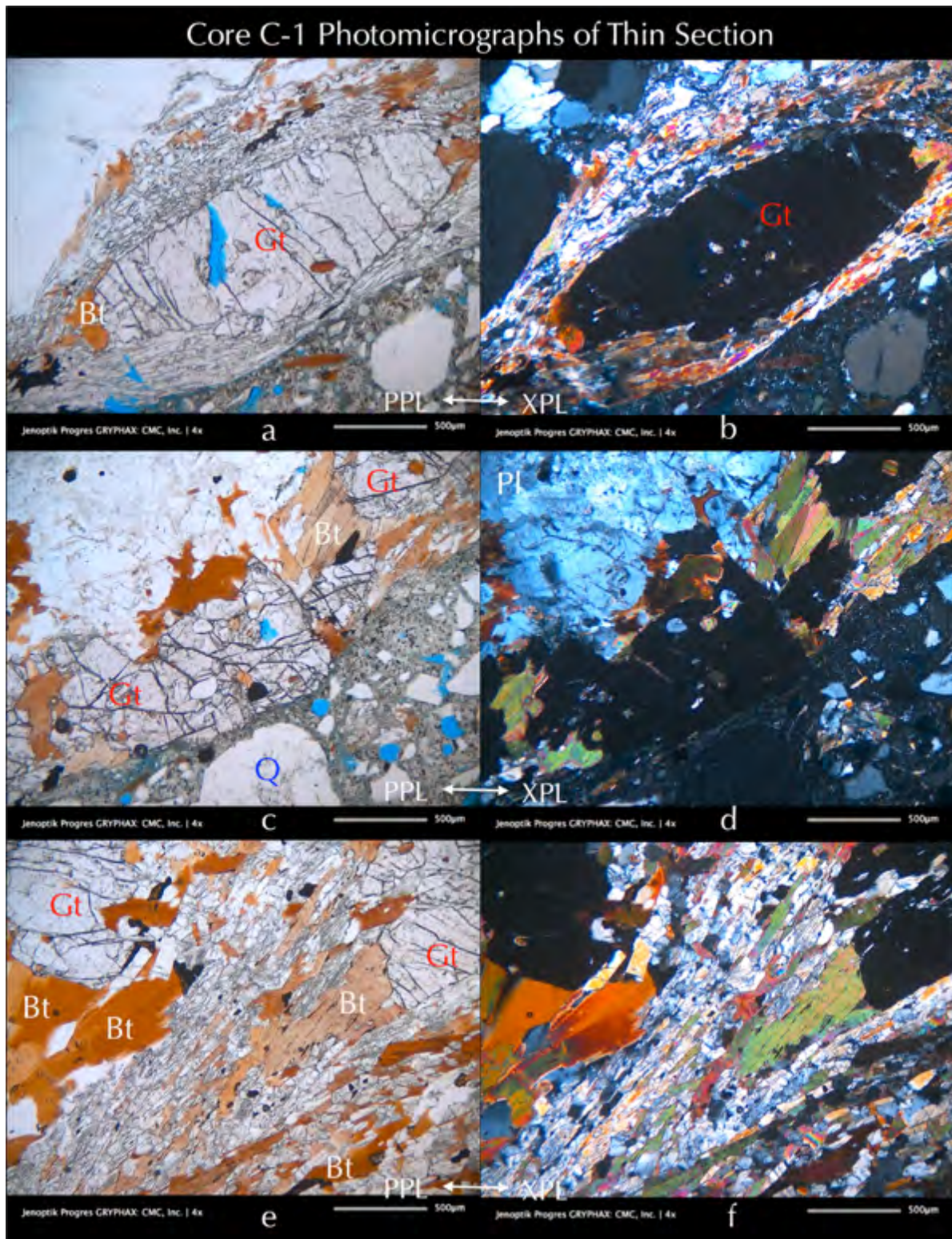


Figure D 17: Photomicrographs of thin section of Core C-1 showing mineralogies, textures, and microstructures of concrete and aggregates. Photos: a to f – garnetiferous (Gt) quartz (Q)-feldspar (albitic plagioclase, Pl)-biotite (Bt) gneiss where disseminated opaque (O) grains in dark are of iron sulfide (pyrrhotite) and iron-titanium oxide (ilmenite). PPL-XPL photos of same microstructure taken in plane and crossed polarized-light modes with a petrographic microscope.

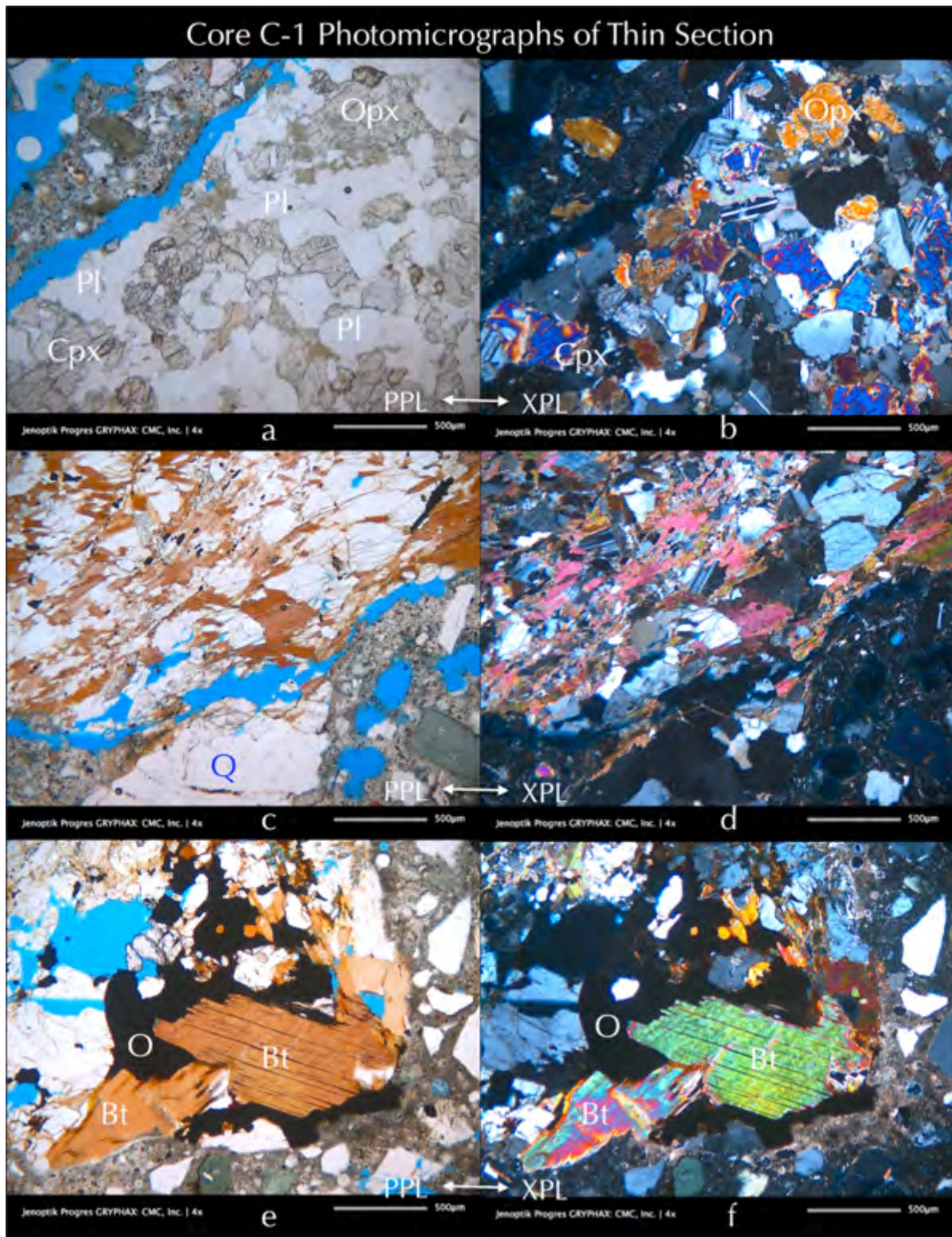


Figure D 18: Photomicrographs of thin section of Core C-1 showing mineralogies, textures, and microstructures of concrete and aggregates. Photos: a, b – metamorphosed gabbro (pyroxene granulite) consisting of pyroxene (Opx and Cpx) and plagioclase (Pl). Photos: c to f – garnetiferous (Gt) quartz (Q) -feldspar (albitic plagioclase, Pl) -biotite (Bt) gneiss where disseminated opaque (O) grains in dark are of iron sulfide (pyrrhotite) and iron-titanium oxide (ilmenite). PPL-XPL photos of same microstructure taken in plane and crossed polarized-light modes with a petrographic microscope.

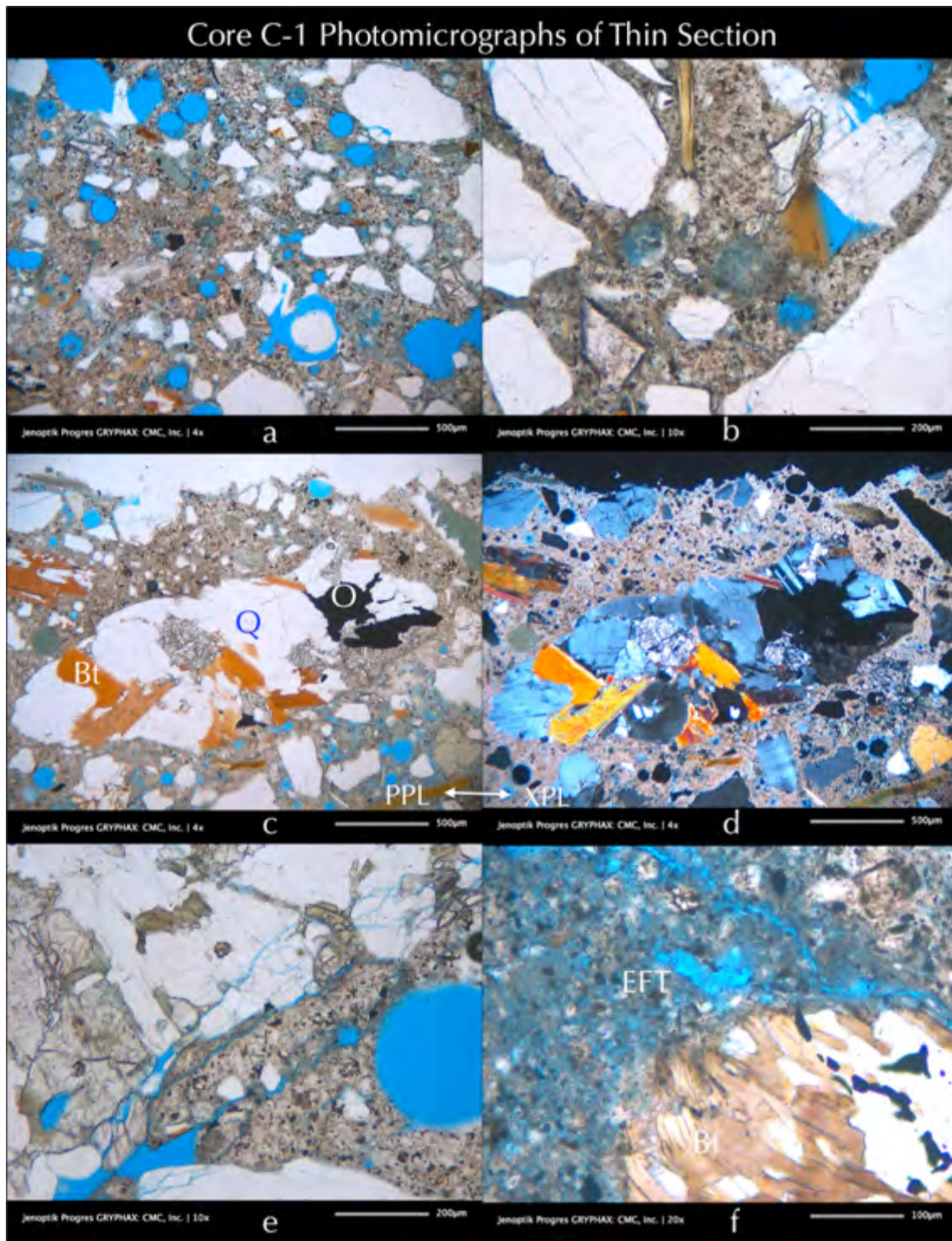


Figure D 19: Photomicrographs of thin section of Core C-1 showing mineralogies, textures, and microstructures of concrete and aggregates. Photo: a – air-entrained concrete where air-voids are highlighted in blue epoxy. Photos: c and d - garnetiferous (Gt) quartz (Q) -feldspar (albitic plagioclase, Pl) -biotite (Bt) gneiss where disseminated opaque (O) grains in dark are of iron sulfide (pyrrhotite) and iron-titanium oxide (ilmenite). PPL-XPL photos of same microstructure taken in plane and crossed polarized-light modes with a petrographic microscope. Photos: e and f - secondary ettringite deposits in porous areas of paste, voids, and in cracks - a telltale feature of concrete deterioration by oxidation of pyrrhotite where sulfates released from oxidation form ettringite, which eventually precipitate by moisture from the paste to the open spaces of voids and cracks.

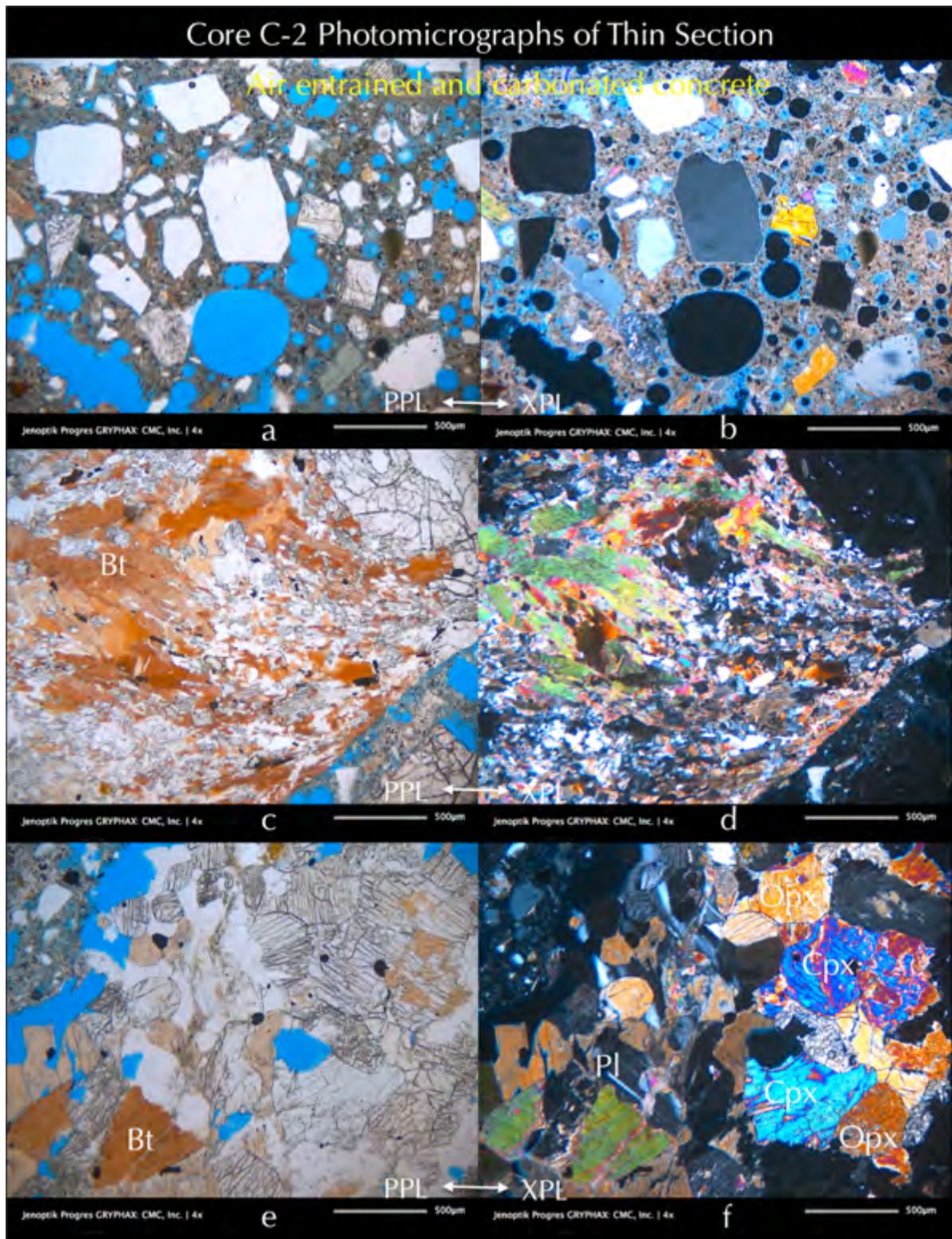


Figure D 20: Photomicrographs of thin section of Core C-2 showing mineralogies, textures, and microstructures of concrete and aggregates. Photos: a – air-entrained concrete where air-voids are highlighted in blue epoxy; b to f – garnetiferous (Gt) quartz (Q) -feldspar (albitic plagioclase, Pl) -biotite (Bt) gneiss where disseminated opaque (O) grains in dark are of iron sulfide (pyrrhotite) and iron-titanium oxide (ilmenite).

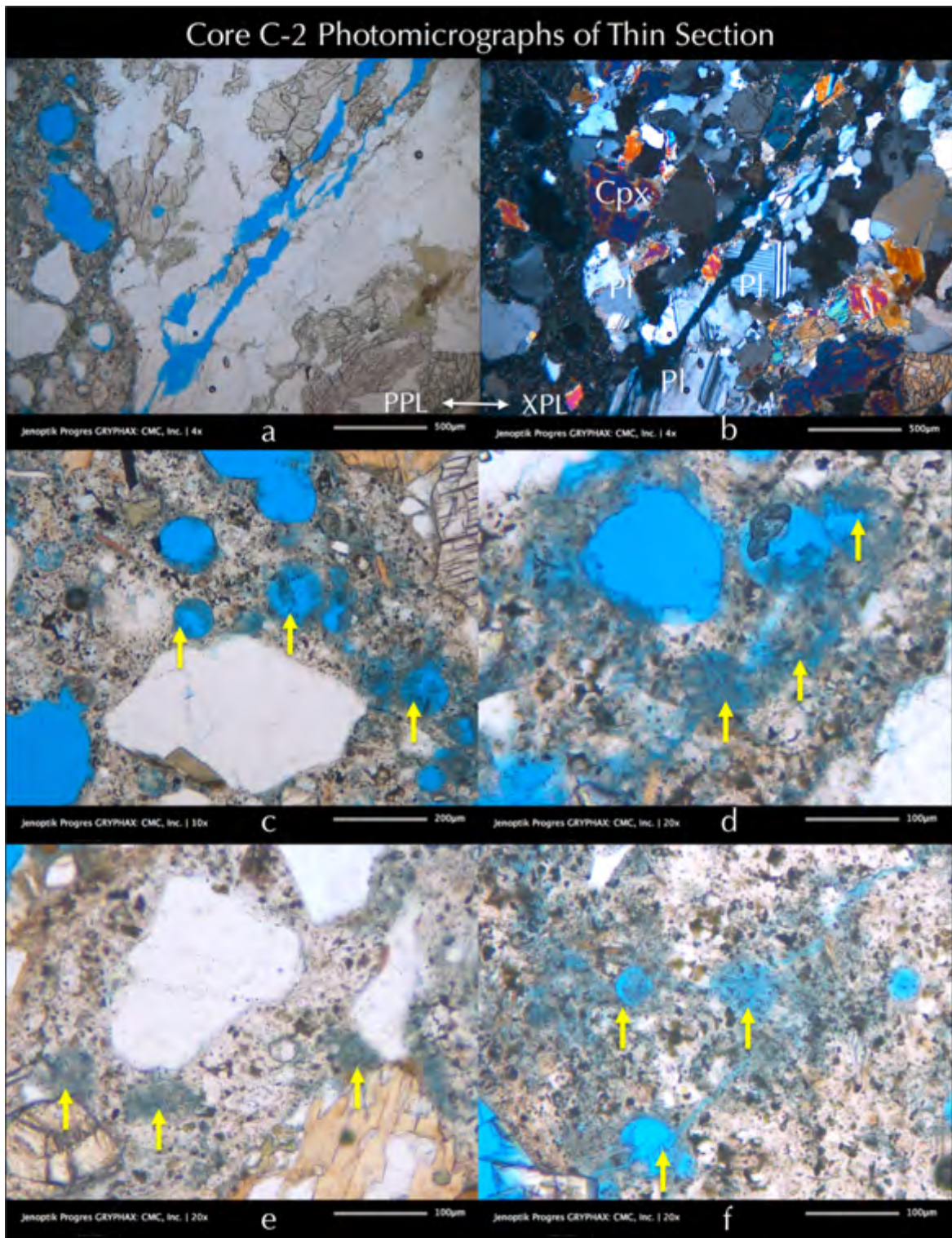


Figure D 21: Photomicrographs of thin section of Core C-2 showing mineralogies, textures, and microstructures of concrete and aggregates. Photos: a, b – metamorphosed gabbro (pyroxene granulite) consisting of pyroxene (Cpx - augite) and plagioclase (oligoclase, Pl). PPL-XPL photos of same microstructure taken in plane and crossed polarized-light modes with a petrographic microscope. Photos: c to f - secondary ettringite deposits in porous areas of paste, voids, and cracks - a telltale feature of concrete deterioration by oxidation of pyrrhotite where sulfates released from oxidation form ettringite, which eventually precipitate by moisture from the paste to the open spaces of voids and cracks.

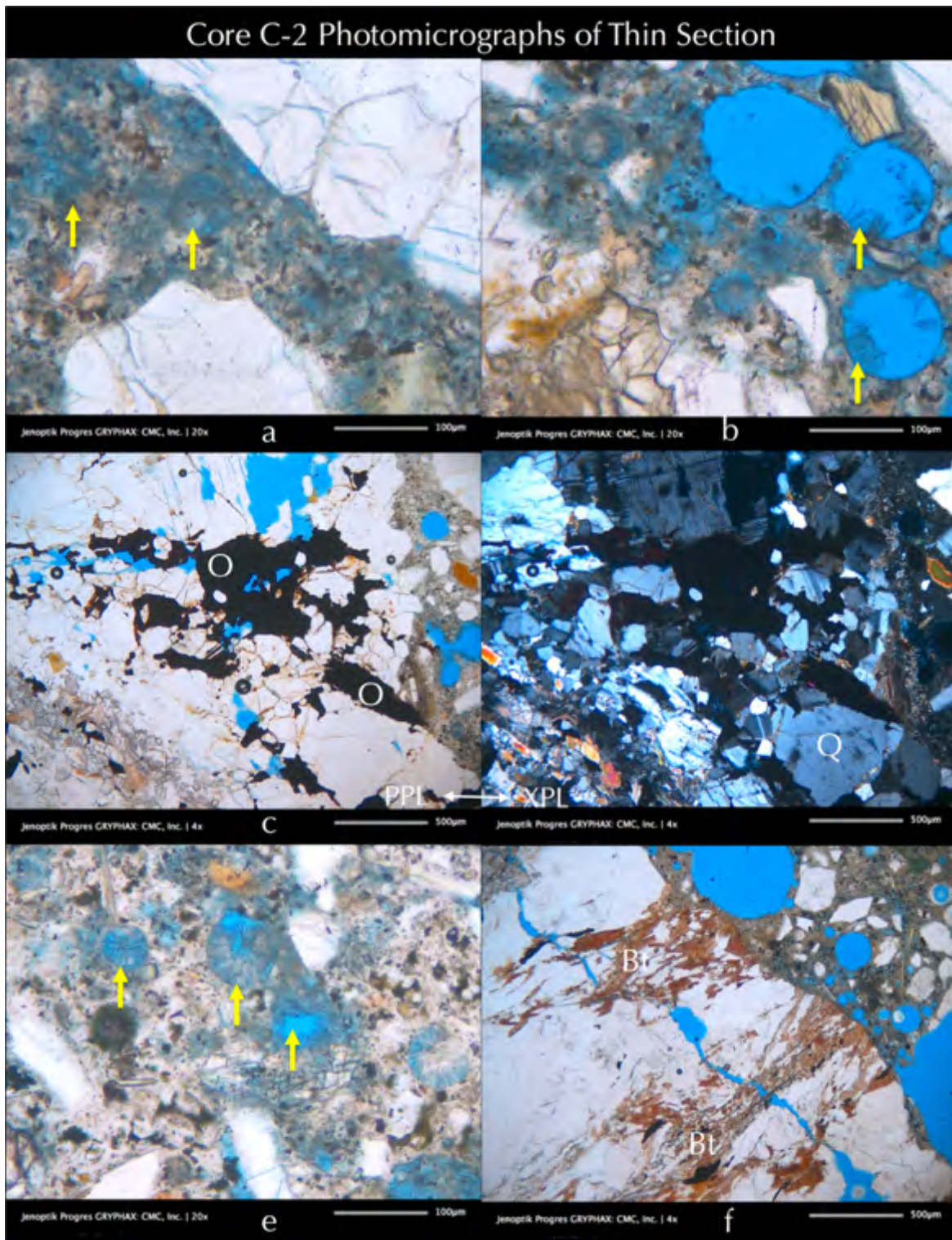


Figure D 22: Photomicrographs of thin section of Core C-2 showing mineralogies, textures, and microstructures of concrete and aggregates. Photos a, b, and e – secondary ettringite deposits in porous areas of paste, voids, and in cracks - a telltale feature of concrete deterioration by oxidation of pyrrhotite where sulfates released from oxidation form ettringite, which eventually precipitate by moisture from the paste to the open spaces of voids and cracks. Photos: c, d, and f - garnetiferous (Gt) quartz (Q) -feldspar (albitic plagioclase, Pl) -biotite (Bt) gneiss where disseminated opaque (O) grains in dark are of iron sulfide (pyrrhotite) and iron-titanium oxide (ilmenite). PPL-XPL photos of same microstructure taken in plane and crossed polarized-light modes with a petrographic microscope.

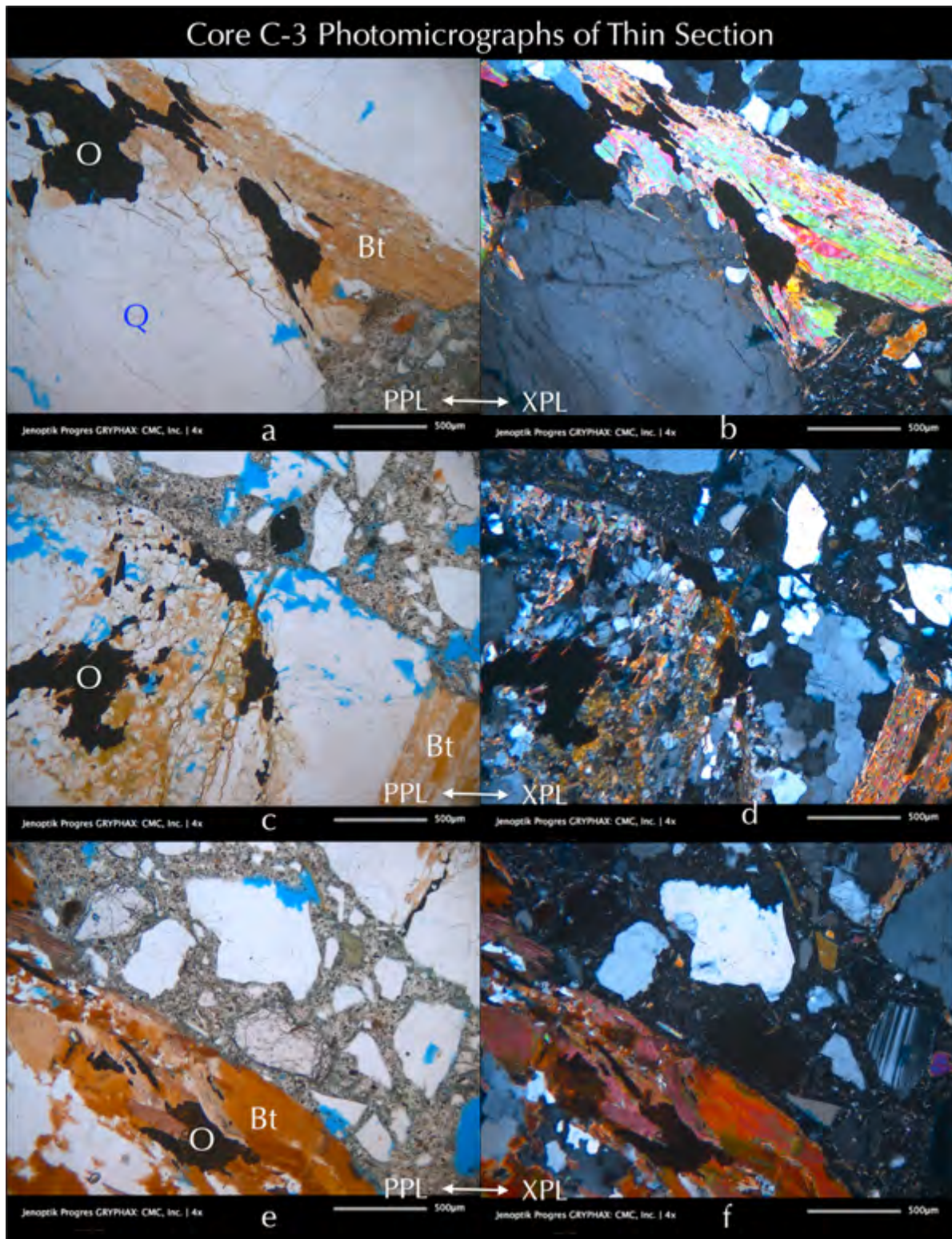


Figure D 23: Photomicrographs of thin section of Core C-3 showing mineralogies, textures, and microstructures of concrete and aggregates. Photos: a to f – garnetiferous (Gt) quartz (Q) -feldspar (albitic plagioclase, Pl) -biotite (Bt) gneiss where disseminated opaque (O) grains in dark are of iron sulfide (pyrrhotite) and iron-titanium oxide (ilmenite). PPL-XPL photos of same microstructure taken in plane and crossed polarized-light modes with a petrographic microscope.

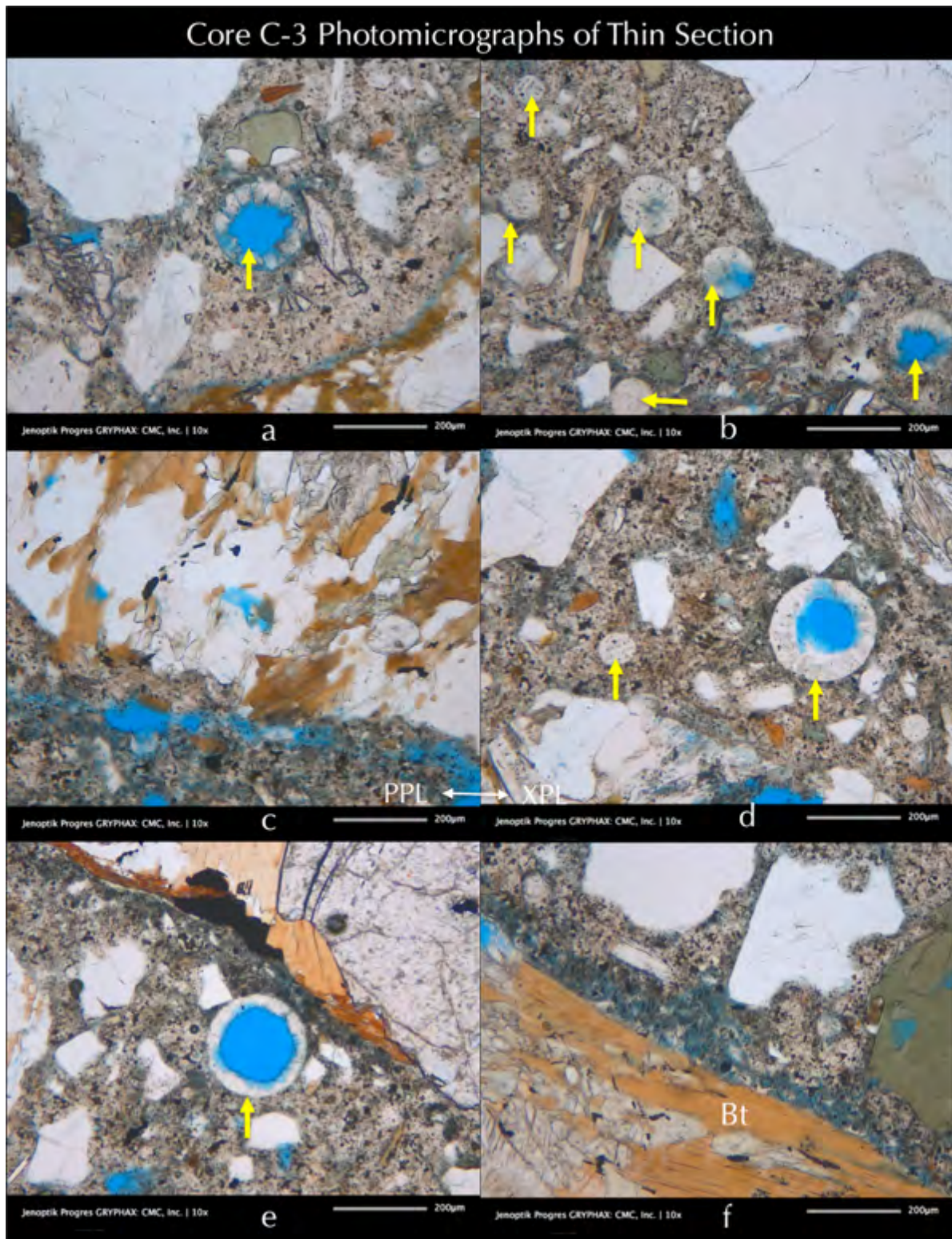


Figure D 24: Photomicrographs of thin section of Core C-3 showing porous areas of paste, voids, and microcracks filled or lined with fibrous ettringite deposits, a telltale feature of concrete deterioration by oxidation of pyrrhotite where sulfates released from oxidation form ettringite, which eventually precipitate by moisture from the paste to the open spaces of voids and cracks.

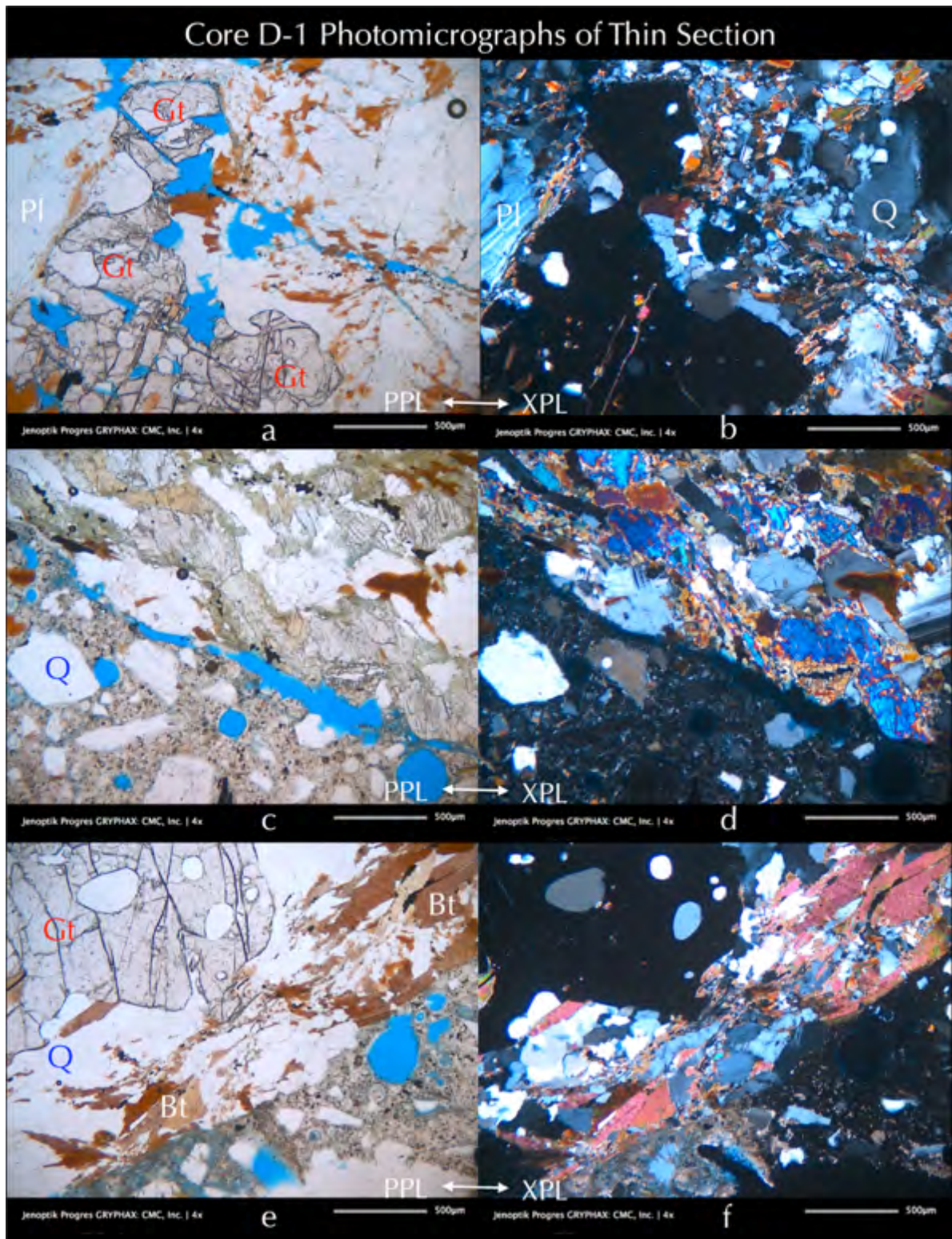


Figure D 25: Photomicrographs of thin section of Core D-1 showing mineralogies, textures, and microstructures of concrete and aggregates. Photos: a to f – garnetiferous (Gt) quartz (Q)-feldspar (albitic plagioclase, Pl) -biotite (Bt) gneiss where disseminated opaque (O) grains in dark are of iron sulfide (pyrrhotite) and iron-titanium oxide (ilmenite). PPL-XPL photos of same microstructure taken in plane and crossed polarized-light modes with a petrographic microscope.

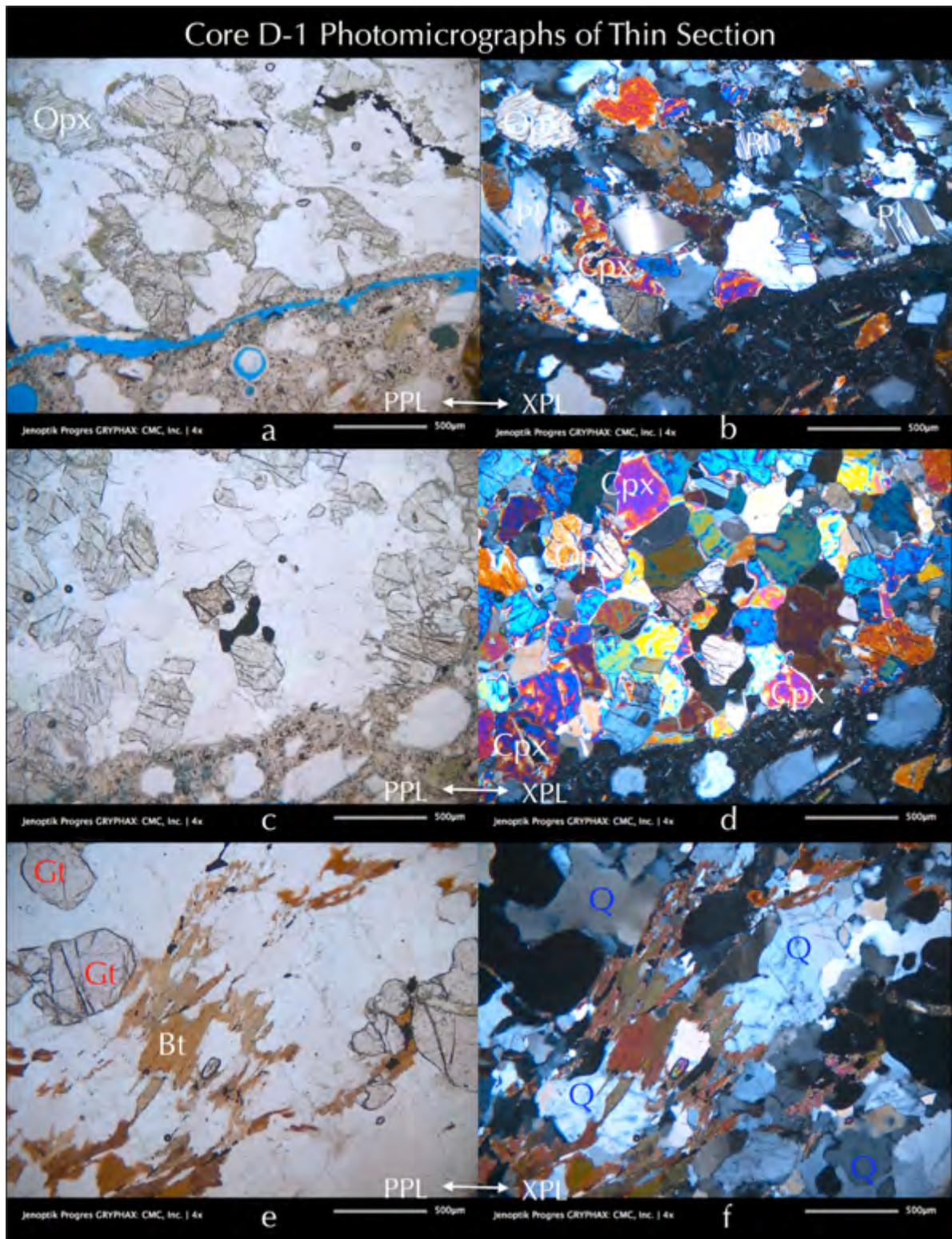


Figure D 26: Photomicrographs of thin section of Core D-1 showing mineralogies, textures, and microstructures of concrete and aggregates. Photos: a to d – metamorphosed gabbro (pyroxene granulite) consisting of pyroxene (Opx – enstatite, Cpx -augite) and plagioclase (oligoclase, Pl). Photos: e and f - garnetiferous (Gt) quartz (Q) -feldspar (albitic plagioclase, Pl) -biotite (Bt) gneiss where disseminated opaque (O) grains in dark are of iron sulfide (pyrrhotite) and iron-titanium oxide (ilmenite). PPL-XPL photos of same microstructure taken in plane and crossed polarized-light modes with a petrographic microscope.

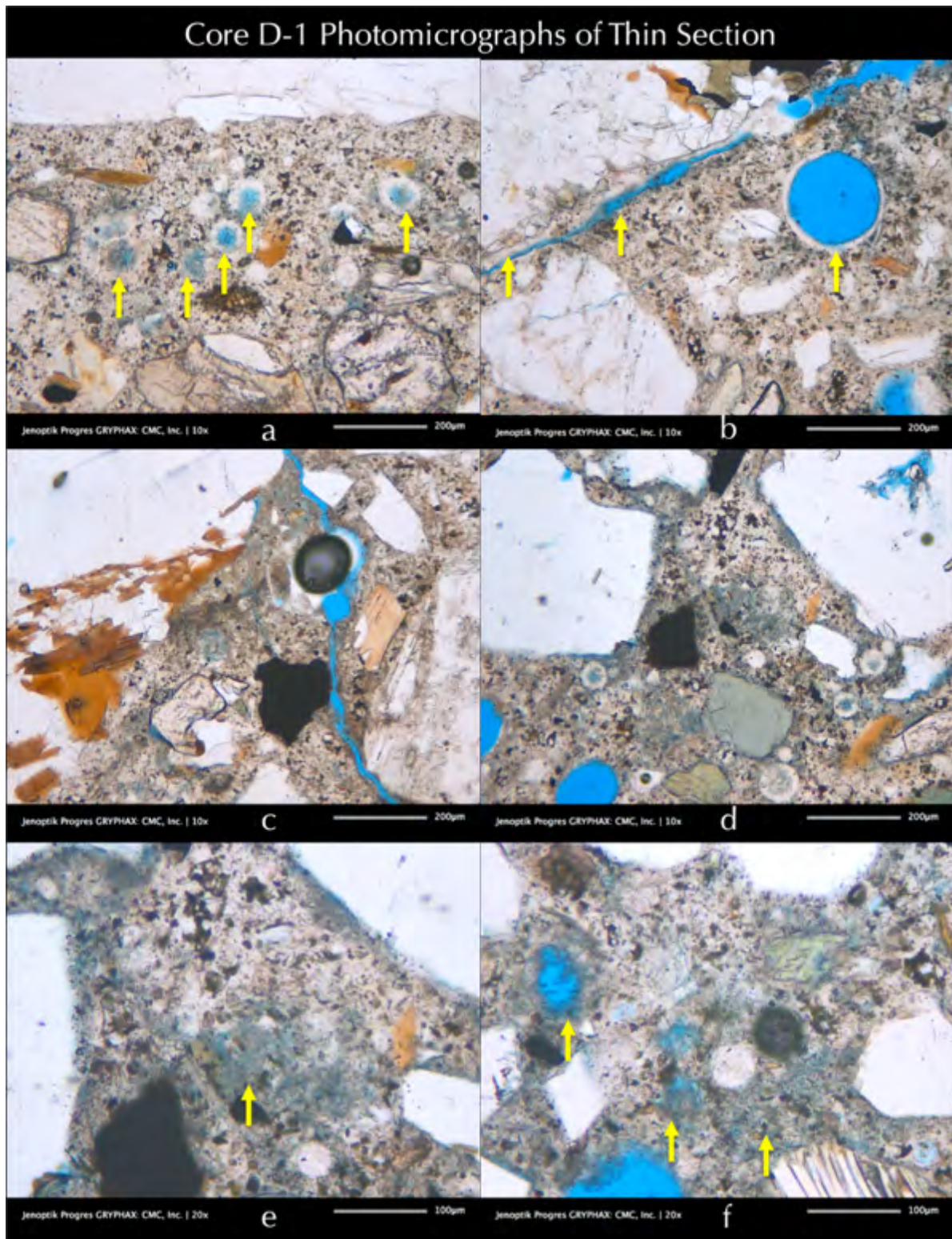


Figure D 27: Photomicrographs of thin section of Core D-1 showing porous areas of paste, voids, and microcracks filled or lined with fibrous ettringite deposits, a telltale feature of concrete deterioration by oxidation of pyrrhotite where sulfates released from oxidation form ettringite, which eventually precipitate by moisture from the paste to the open spaces of voids and cracks.

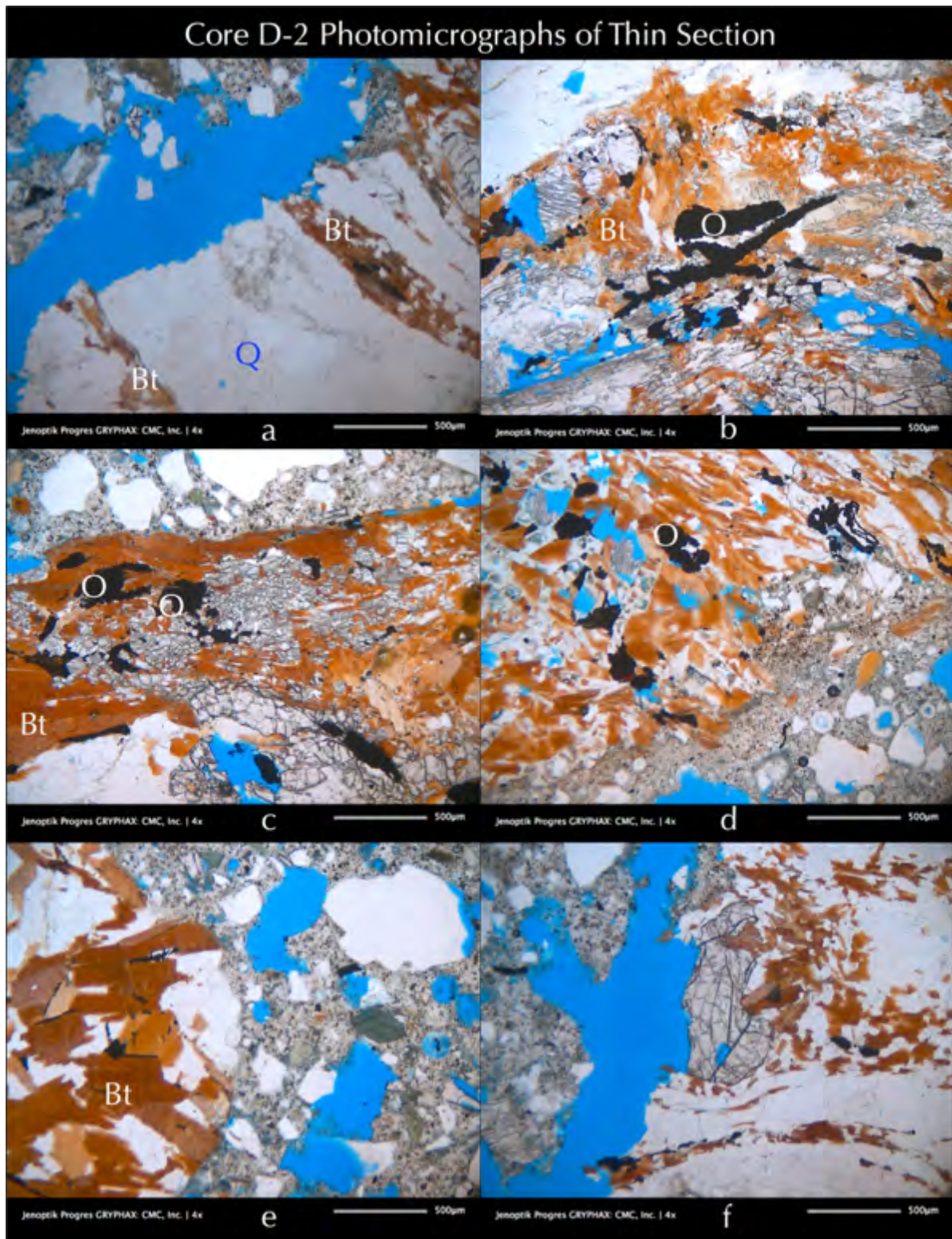


Figure D 28: Photomicrographs of thin section of Core D-2 showing mineralogies, textures, and microstructures of concrete and aggregates. Photos: a to f – garnetiferous (Gt) quartz (Q) -feldspar (albitic plagioclase, Pl) -biotite (Bt) gneiss where disseminated opaque (O) grains in dark are of iron sulfide (pyrrhotite) and iron-titanium oxide (ilmenite).

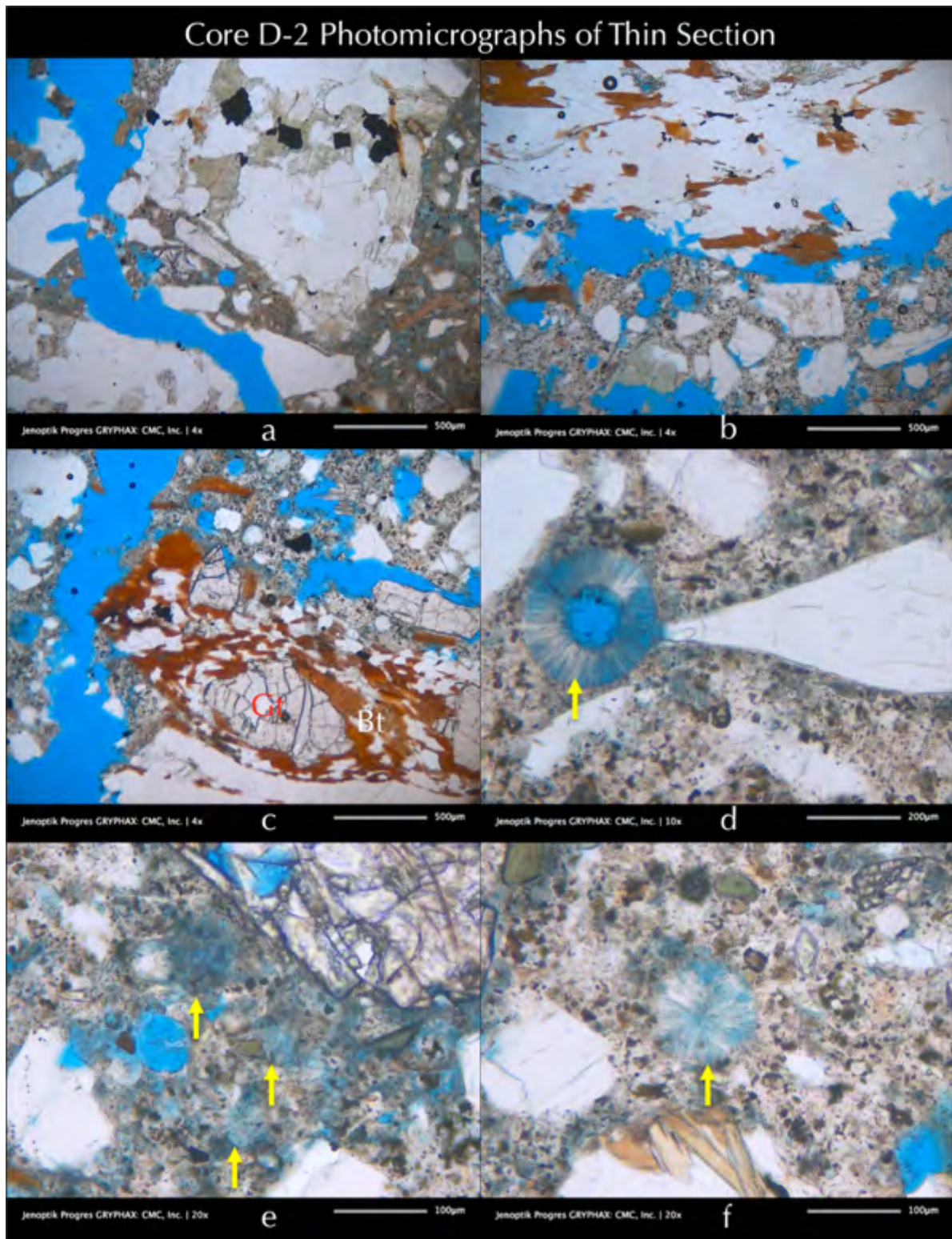


Figure D 29: Photomicrographs of thin section of Core D-2 showing mineralogies, textures, and microstructures of concrete and aggregates. Photos: a to c – garnetiferous (Gt) quartz (Q) -feldspar (albitic plagioclase, Pl) -biotite (Bt) gneiss where disseminated opaque (O) grains in dark are of iron sulfide (pyrrhotite) and iron-titanium oxide (ilmenite). Photos: d to f - porous areas of paste, voids, and microcracks filled or lined with fibrous ettringite deposits, a telltale feature of concrete deterioration by oxidation of pyrrhotite where sulfates released from oxidation form ettringite, which eventually precipitate by moisture from the paste to the open spaces of voids and cracks.

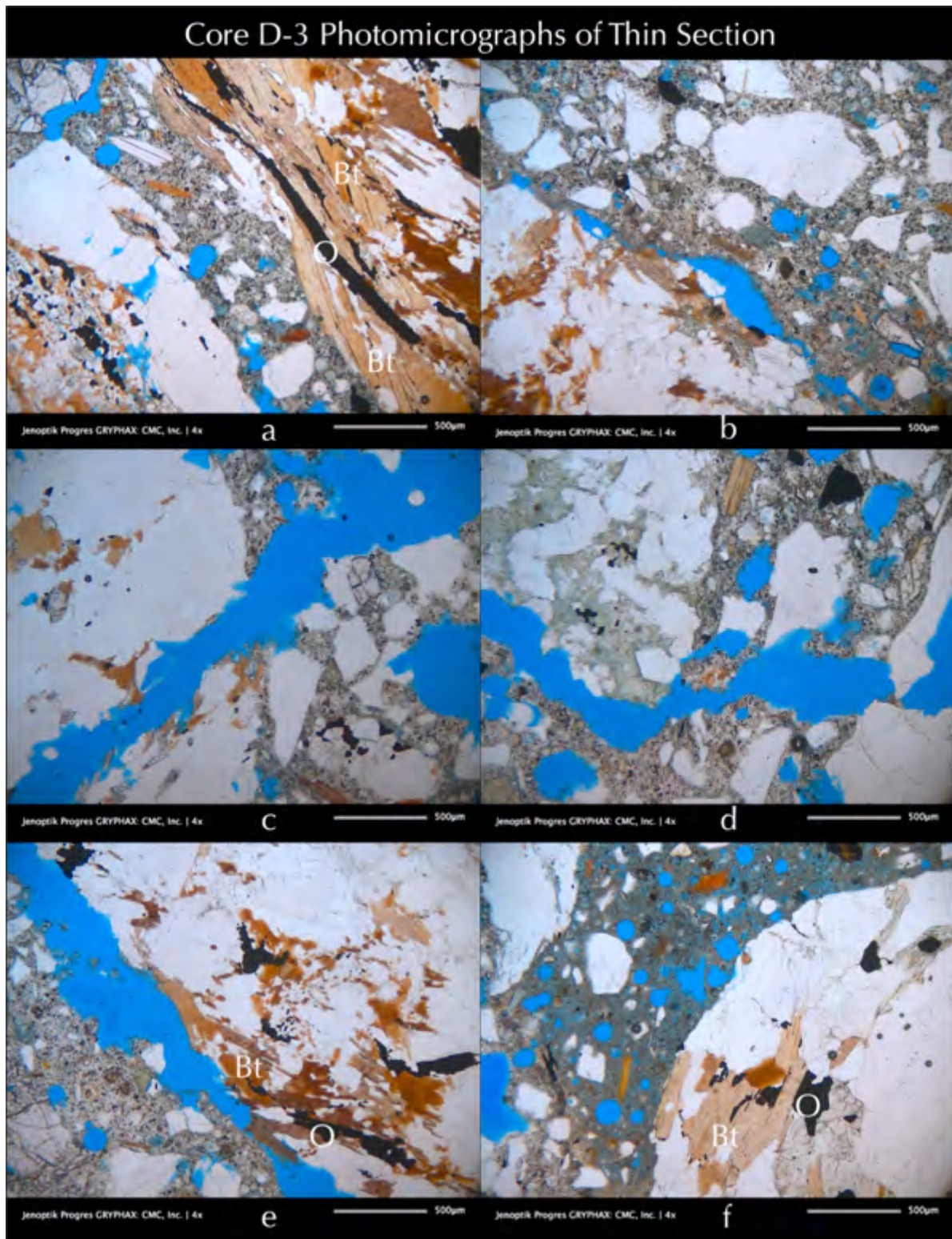


Figure D 30: Photomicrographs of thin section of Core D-3 showing mineralogies, textures, and microstructures of concrete and aggregates. Photos: a, b, e, and f – garnetiferous (Gt) quartz (Q) -feldspar (albitic plagioclase, Pl) - biotite (Bt) gneiss where disseminated opaque (O) grains in dark are of iron sulfide (pyrrhotite) and iron-titanium oxide (ilmenite). Photos: c, d – cracks highlighted in epoxy. Photo: f – air-entrained concrete where air-voids are highlighted in blue epoxy.

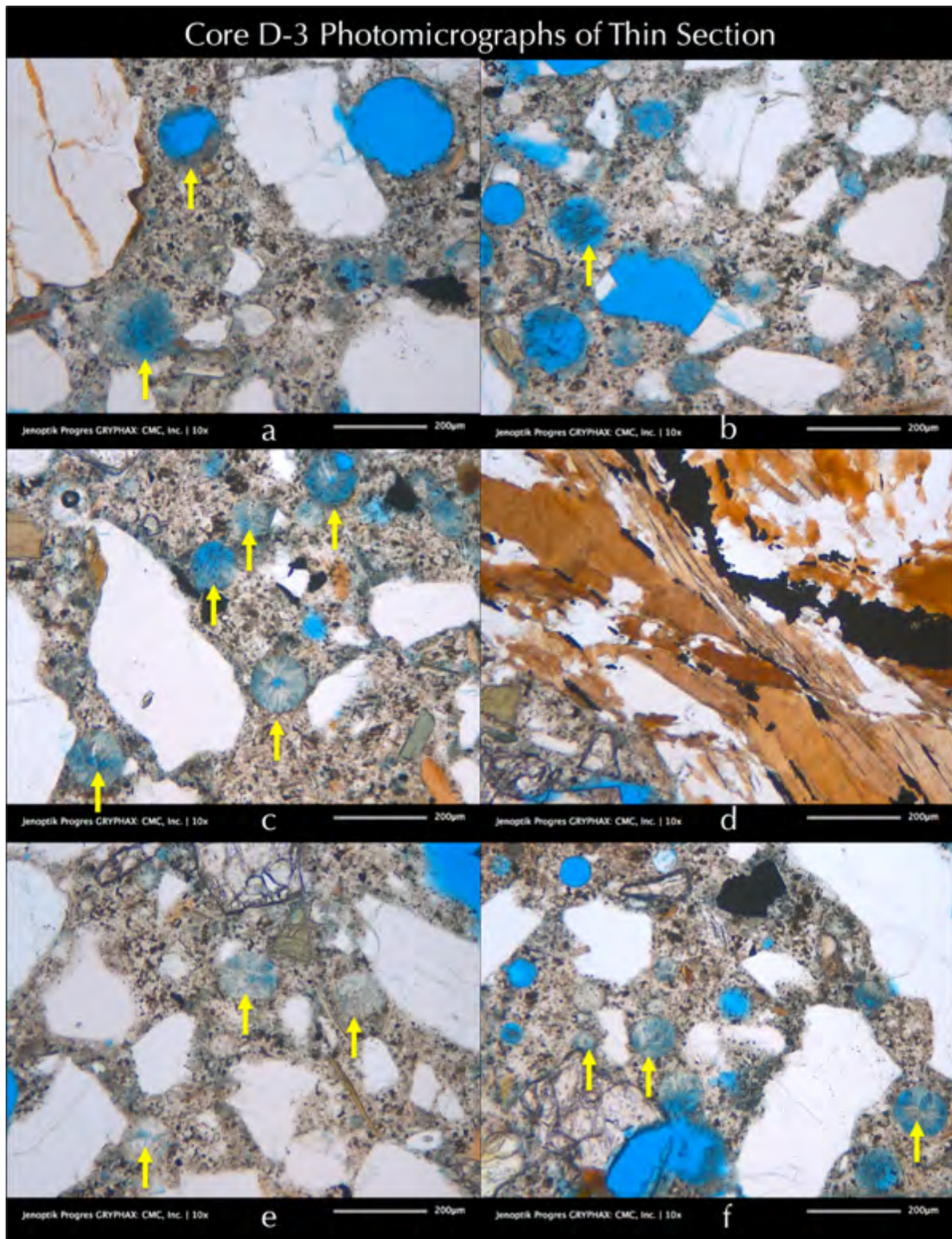


Figure D 31: Photomicrographs of thin section of Core D-3 showing porous areas of paste, voids, and microcracks filled or lined with fibrous ettringite deposits, a telltale feature of concrete deterioration by oxidation of pyrrhotite where sulfates released from oxidation form ettringite, which eventually precipitate by moisture from the paste to the open spaces of voids and cracks.

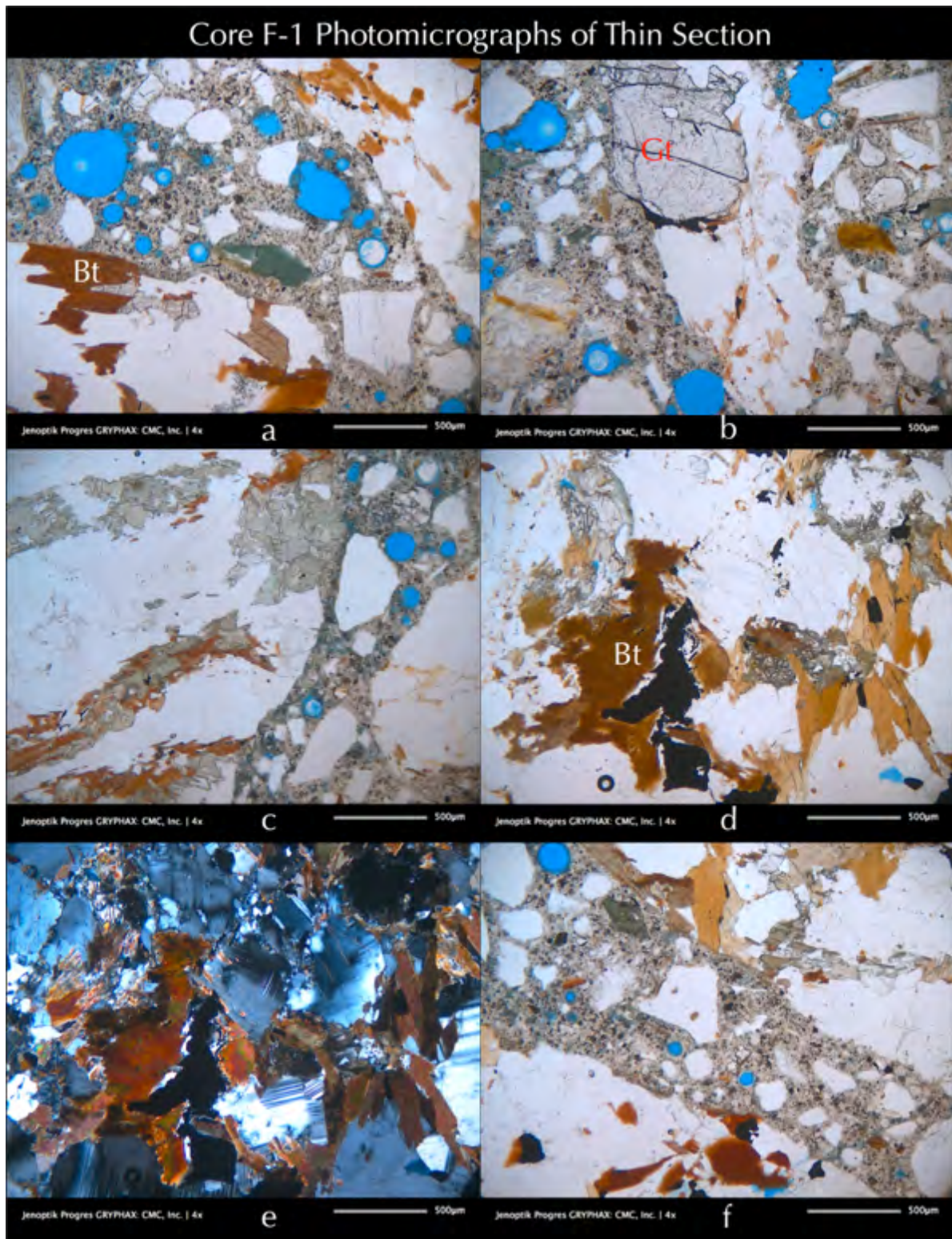


Figure D 32: Photomicrographs of thin section of Core F-1 showing mineralogies, textures, and microstructures of concrete and aggregates. Photos: a to f – garnetiferous (Gt) quartz (Q) -feldspar (albitic plagioclase, Pl) -biotite (Bt) gneiss where disseminated opaque (O) grains in dark are of iron sulfide (pyrrhotite) and iron-titanium oxide (ilmenite).

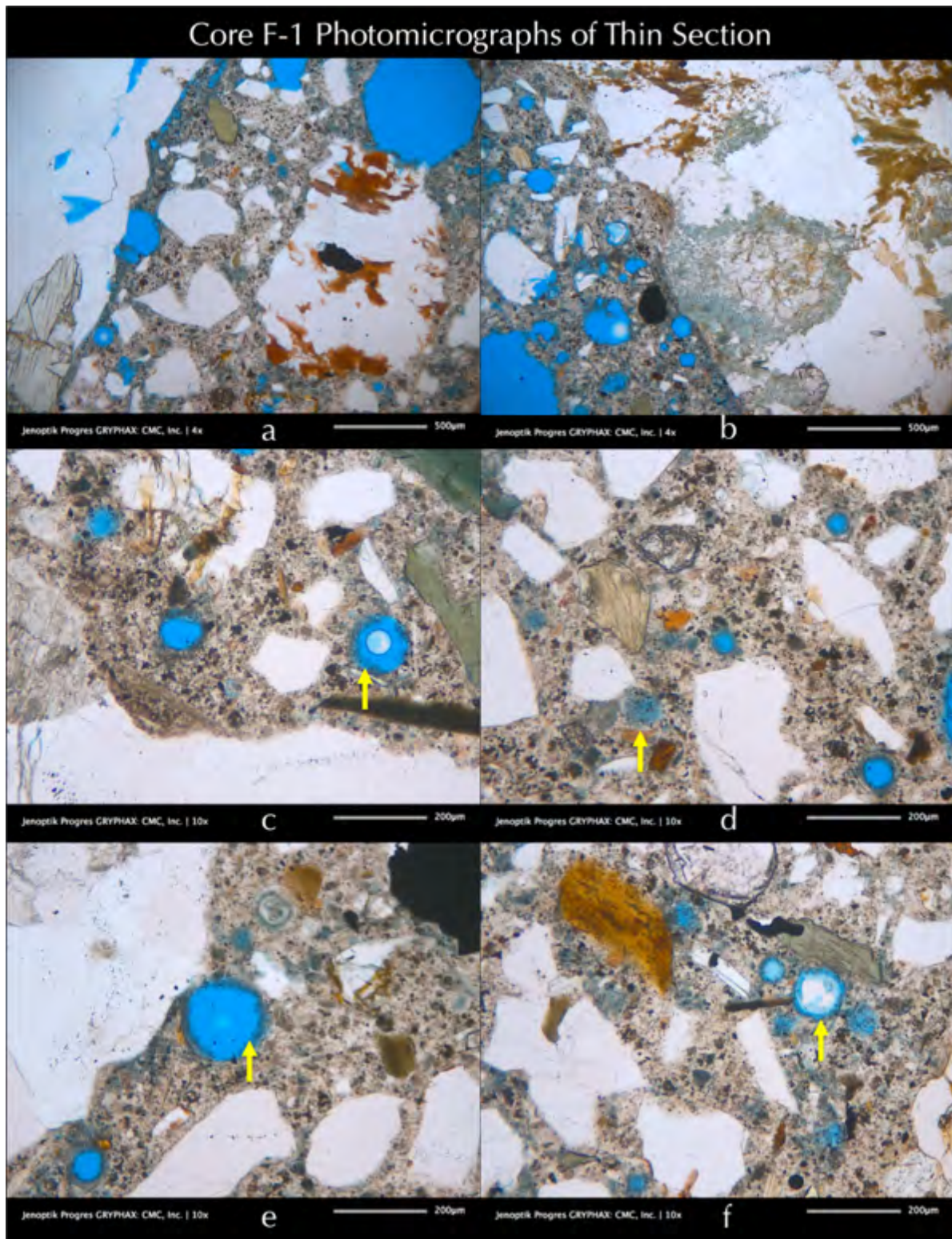


Figure D 33: Photomicrographs of thin section of Core F-1 showing porous areas of paste, voids, and microcracks filled or lined with fibrous ettringite deposits, a telltale feature of pyrrhotite oxidation, where sulfates released from oxidation form ettringite, which eventually precipitate by moisture from the paste to the open spaces of voids and cracks.

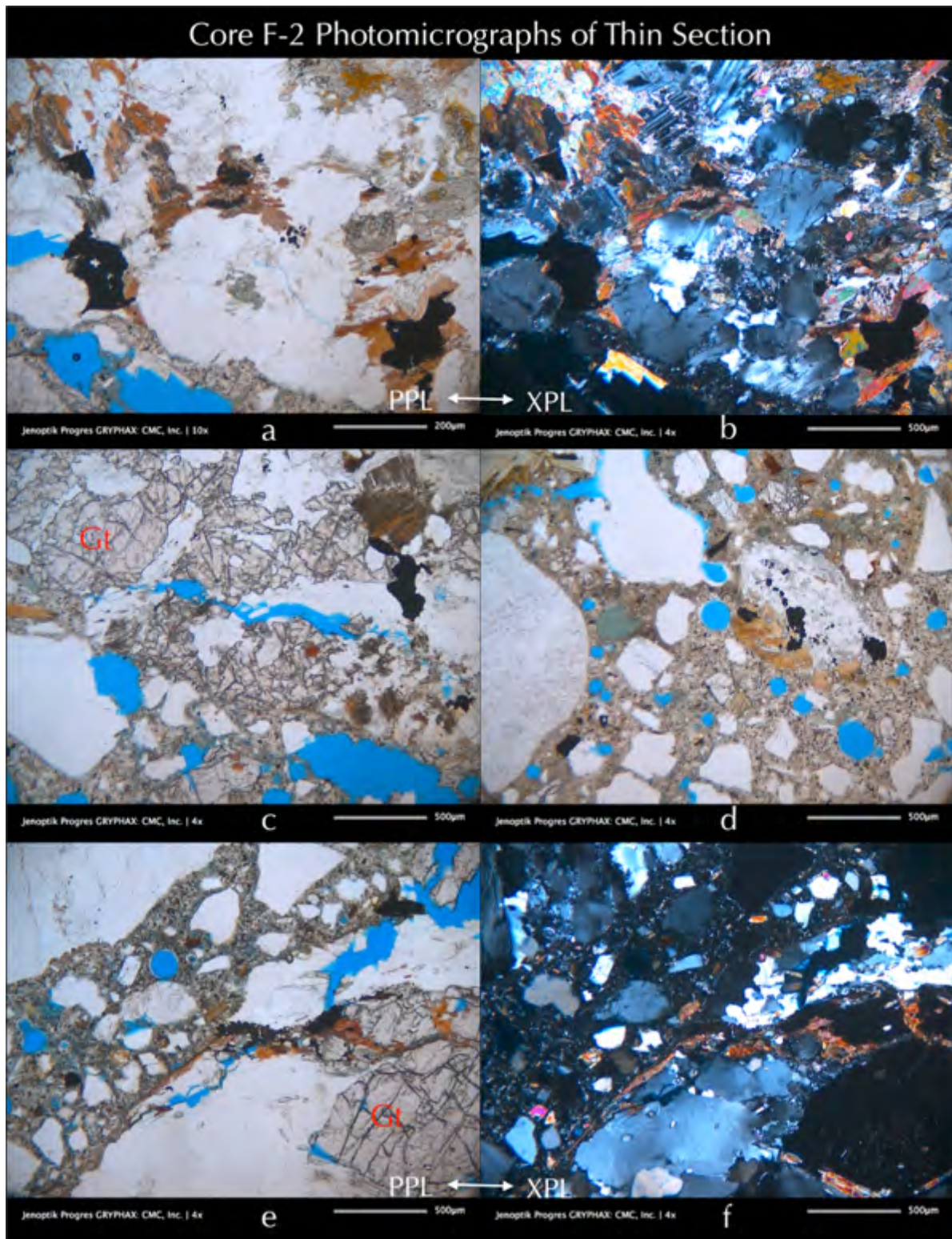


Figure D 34: Photomicrographs of thin section of Core F-2 showing mineralogies, textures, and microstructures of concrete and aggregates. Photos: a to f – garnetiferous (Gt) quartz (Q) -feldspar (albitic plagioclase, Pl) -biotite (Bt) gneiss where disseminated opaque (O) grains in dark are of iron sulfide (pyrrhotite) and iron-titanium oxide (ilmenite).

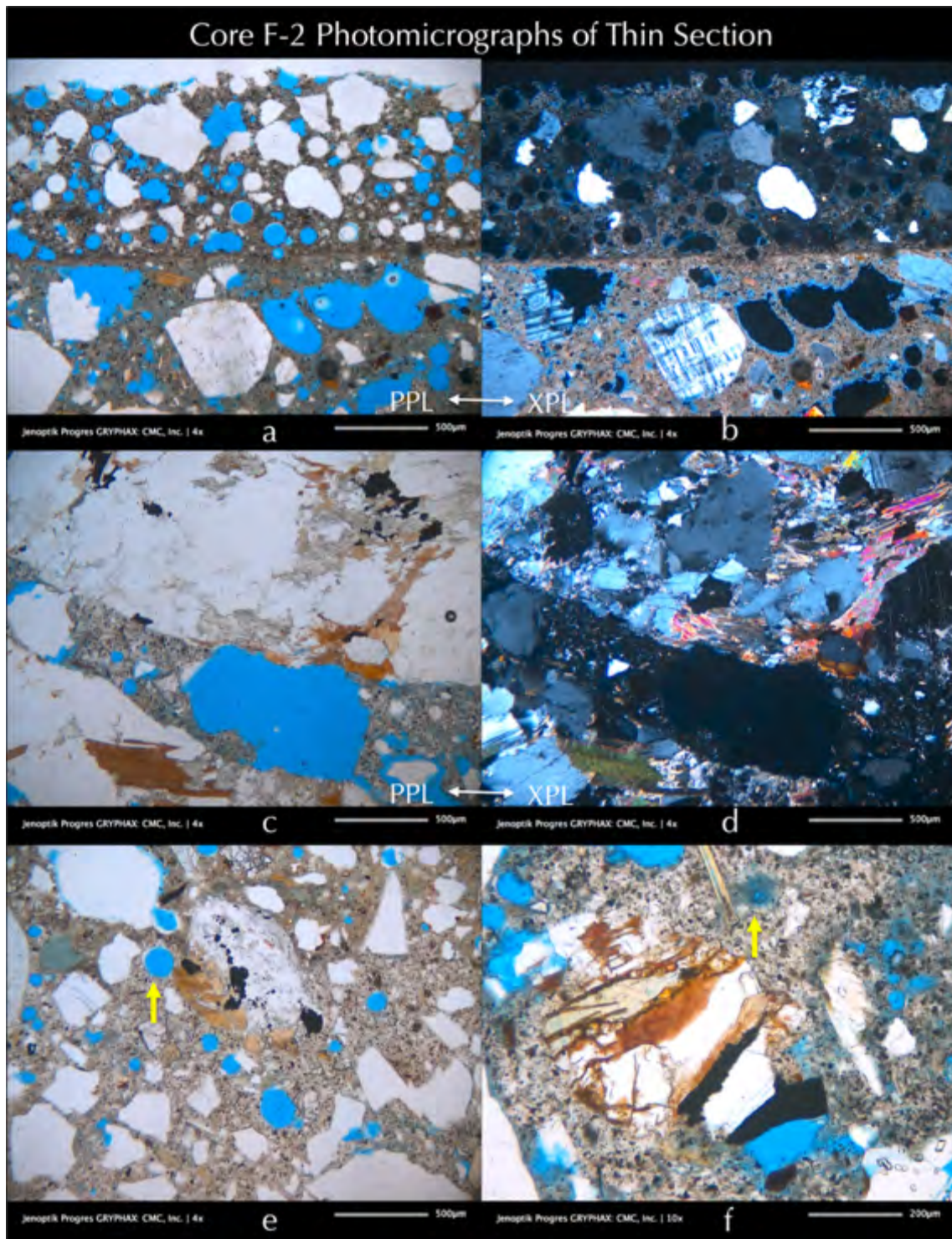


Figure D 35: Photomicrographs of thin section of Core F-2 showing mineralogies, textures, and microstructures of concrete and aggregates. Photos: a and b – thin air-entrained cementitious protective coating well-bonded to concrete beneath. Photos: c and d – garnetiferous (Gt) quartz (Q) -feldspar (albitic plagioclase, Pl) -biotite (Bt) gneiss where disseminated opaque (O) grains in dark are of iron sulfide (pyrrhotite) and iron-titanium oxide (ilmenite). PPL-XPL photos of same microstructure taken in plane and crossed polarized-light modes with a petrographic microscope. Photos: e and f - porous areas of paste, voids, and microcracks filled or lined with fibrous ettringite deposits, a telltale feature of pyrrhotite oxidation, where sulfates released from oxidation form ettringite, which eventually precipitate by moisture from the paste to the open spaces of voids and cracks.

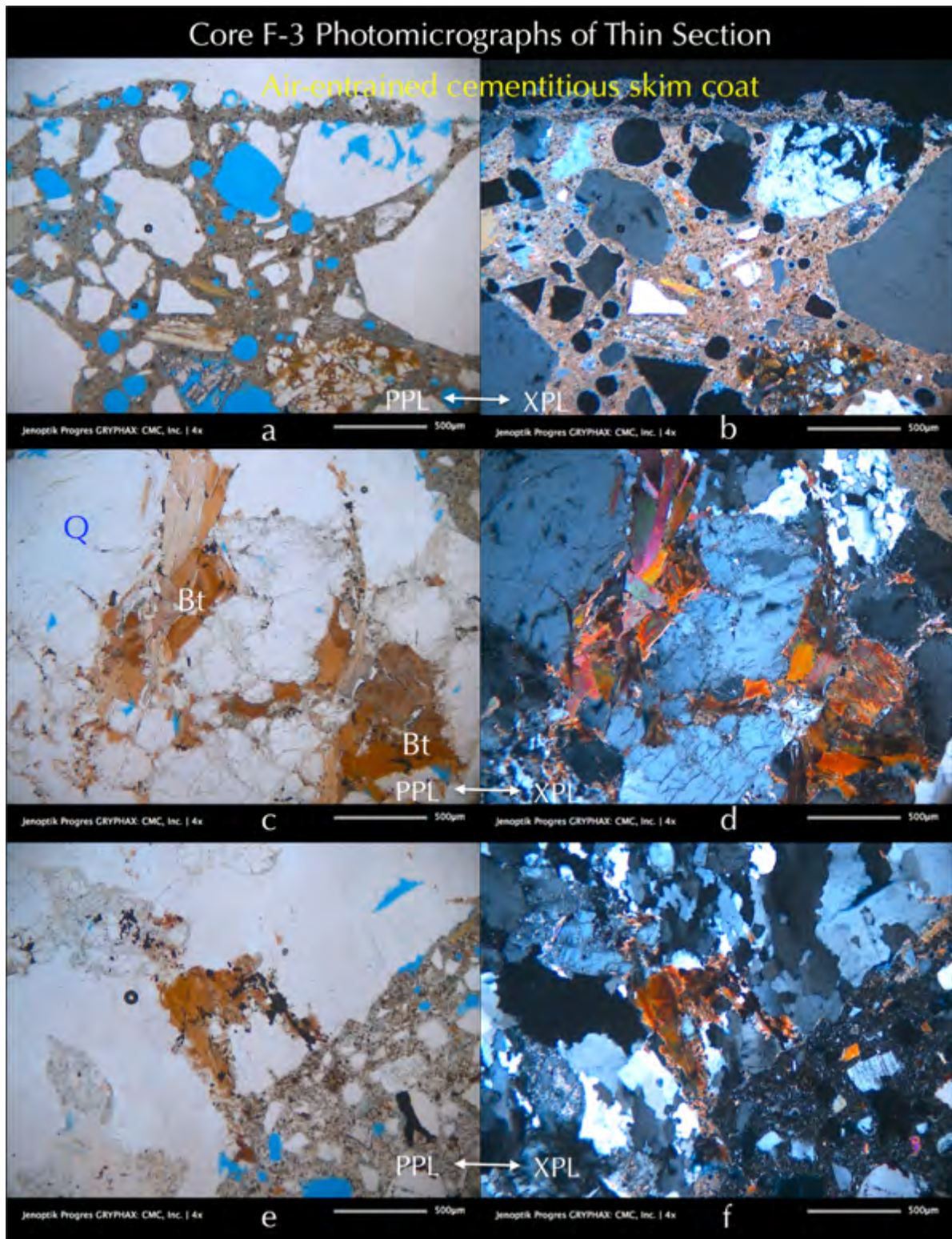


Figure D 36: Photomicrographs of thin section of Core F-3 showing mineralogies, textures, and microstructures of concrete and aggregates. Photos: a and b – thin air-entrained cementitious protective coating well-bonded to concrete beneath. Photos: c to f – garnetiferous (Gt) quartz (Q) -feldspar (albitic plagioclase, Pl) -biotite (Bt) gneiss where disseminated opaque (O) grains in dark are of iron sulfide (pyrrhotite) and iron-titanium oxide (ilmenite). PPL-XPL photos of same microstructure taken at plane and crossed polarized-light modes in a petrographic microscope.

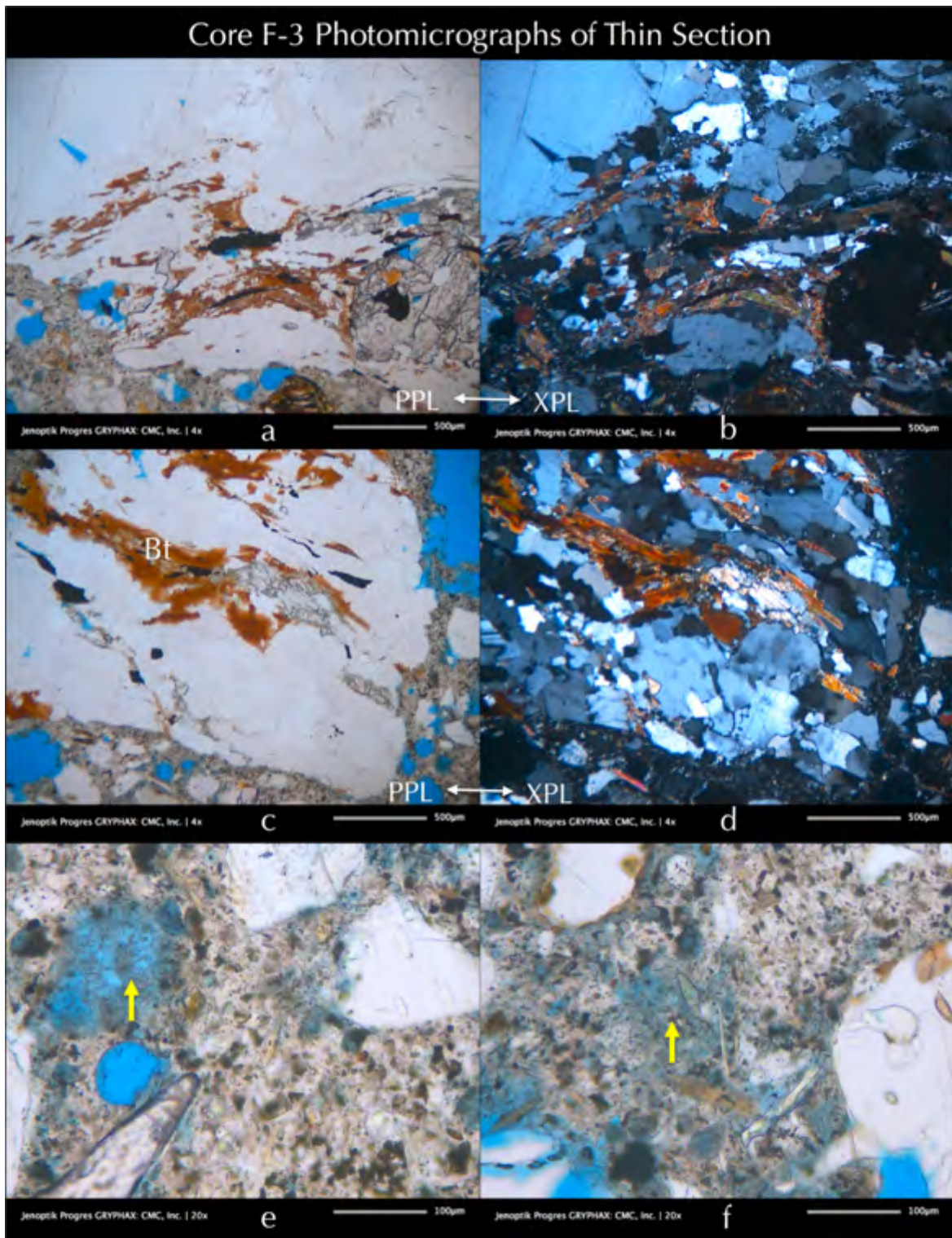


Figure D 37: Photomicrographs of thin section of Core F-3 showing mineralogies, textures, and microstructures of concrete and aggregates. Photos: a to d – garnetiferous (Gt) quartz (Q) -feldspar (albitic plagioclase, Pl) -biotite (Bt) gneiss where disseminated opaque (O) grains in dark are of iron sulfide (pyrrhotite) and iron-titanium oxide (ilmenite). PPL-XPL photos of same microstructure taken in plane and crossed polarized-light modes with a petrographic microscope. Photos: e and f - porous areas of paste, voids, and microcracks filled or lined with fibrous ettringite deposits, a telltale feature of pyrrhotite oxidation, where sulfates released from oxidation form ettringite, which eventually precipitate by moisture from the paste to the open spaces of voids and cracks.

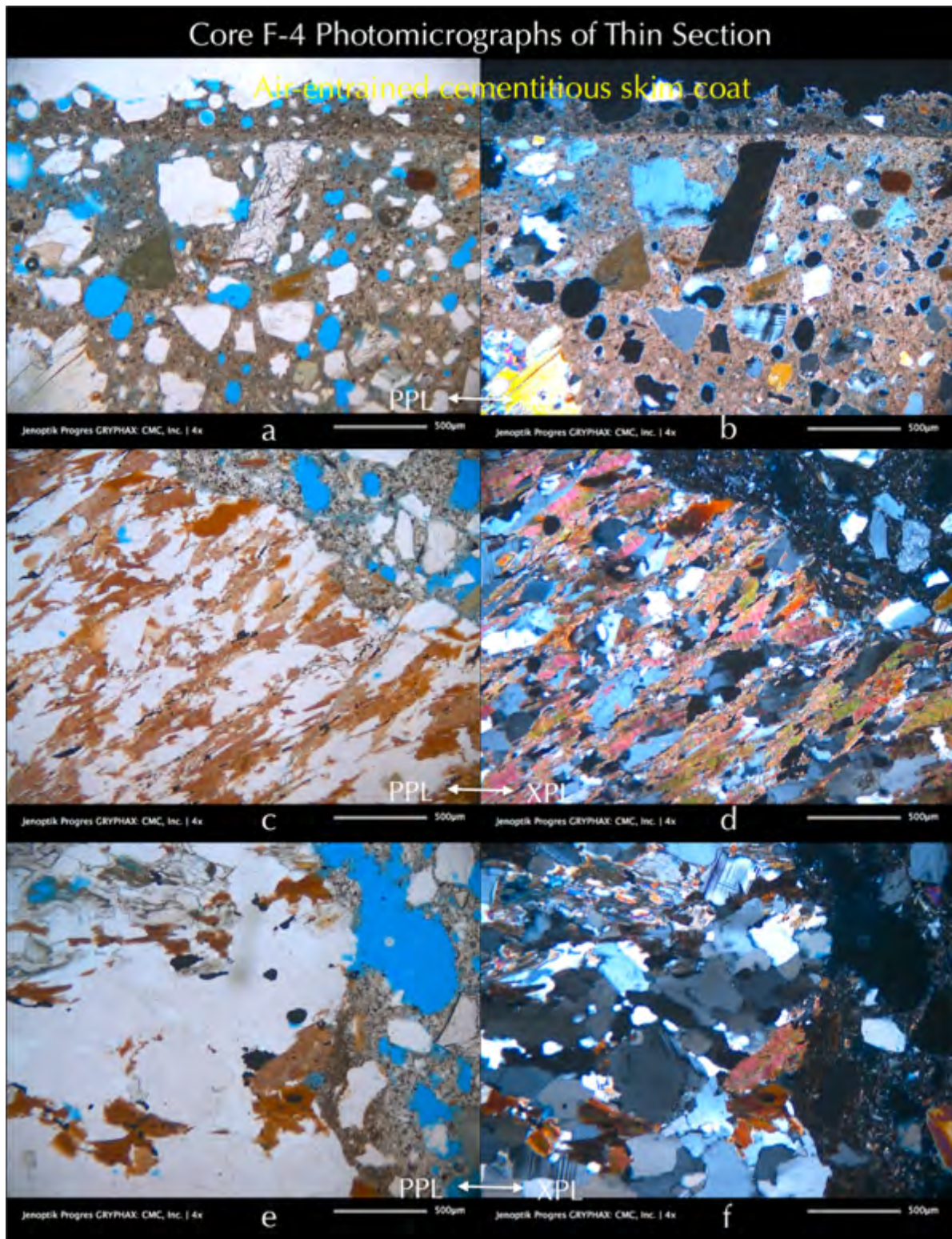


Figure D 38: Photomicrographs of thin section of Core F-4 showing mineralogies, textures, and microstructures of concrete and aggregates. Photos: a and b – thin air-entrained cementitious protective coating well-bonded to concrete beneath. Photos: c to f – garnetiferous (Gt) quartz (Q) -feldspar (albitic plagioclase, Pl) -biotite (Bt) gneiss where disseminated opaque (O) grains in dark are of iron sulfide (pyrrhotite) and iron-titanium oxide (ilmenite). PPL-XPL photos of same microstructure taken in plane and crossed polarized-light modes with a petrographic microscope.

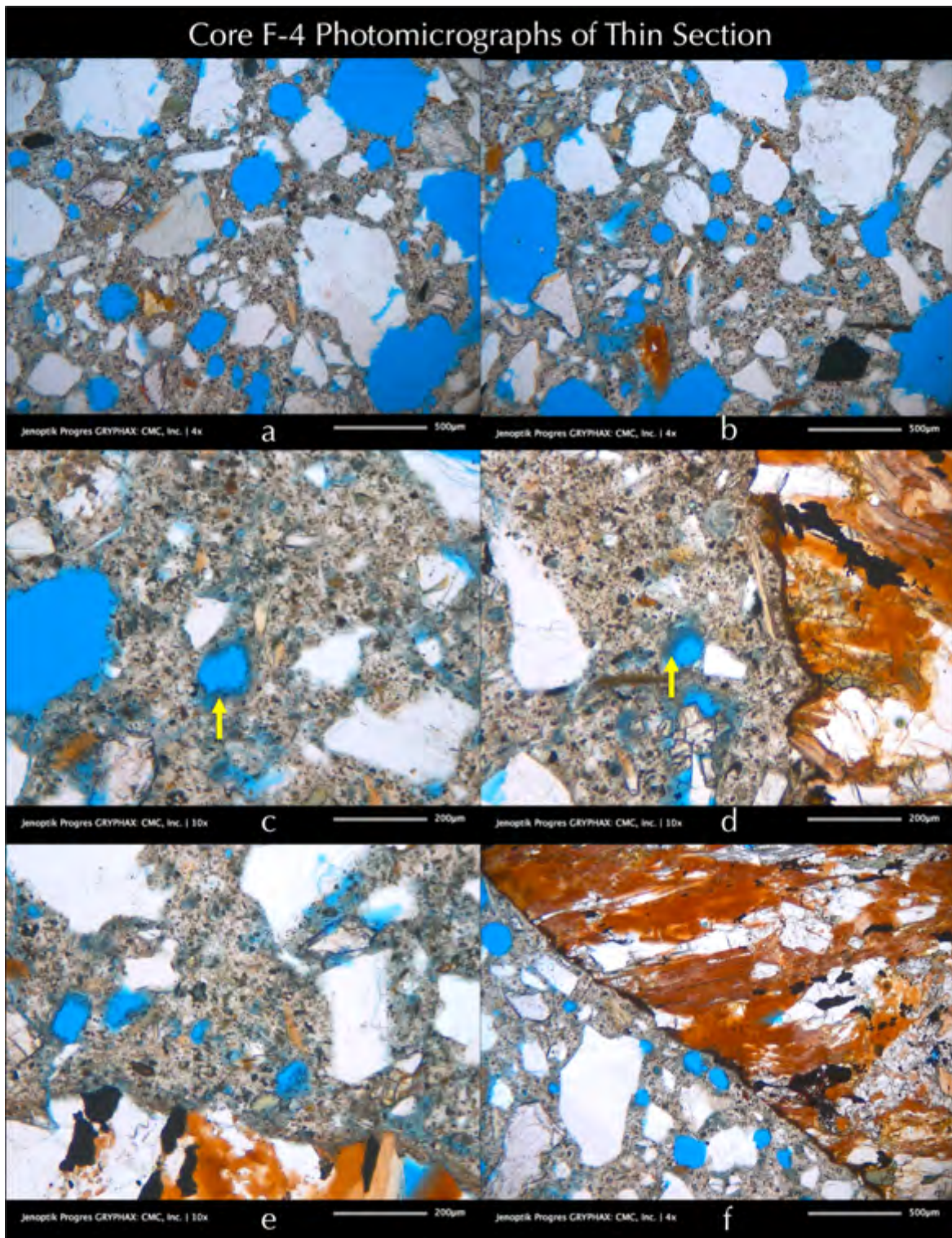


Figure D 39: Photomicrographs of thin section of Core F-4 showing mineralogies, textures, and microstructures of concrete and aggregates. Photos: a and b – air-entrained concrete where air-voids are highlighted in blue epoxy. Photos: c to f – garnetiferous (Gt) quartz (Q)-feldspar (albitic plagioclase, Pl)-biotite (Bt) gneiss where disseminated opaque (O) grains in dark are of iron sulfide (pyrrhotite) and iron-titanium oxide (ilmenite). Also shown are porous areas of paste, voids, and microcracks filled or lined with fibrous ettringite deposits, a telltale feature of pyrrhotite oxidation, where sulfates released from oxidation form ettringite, which eventually precipitate by moisture from the paste to the open spaces of voids and cracks.

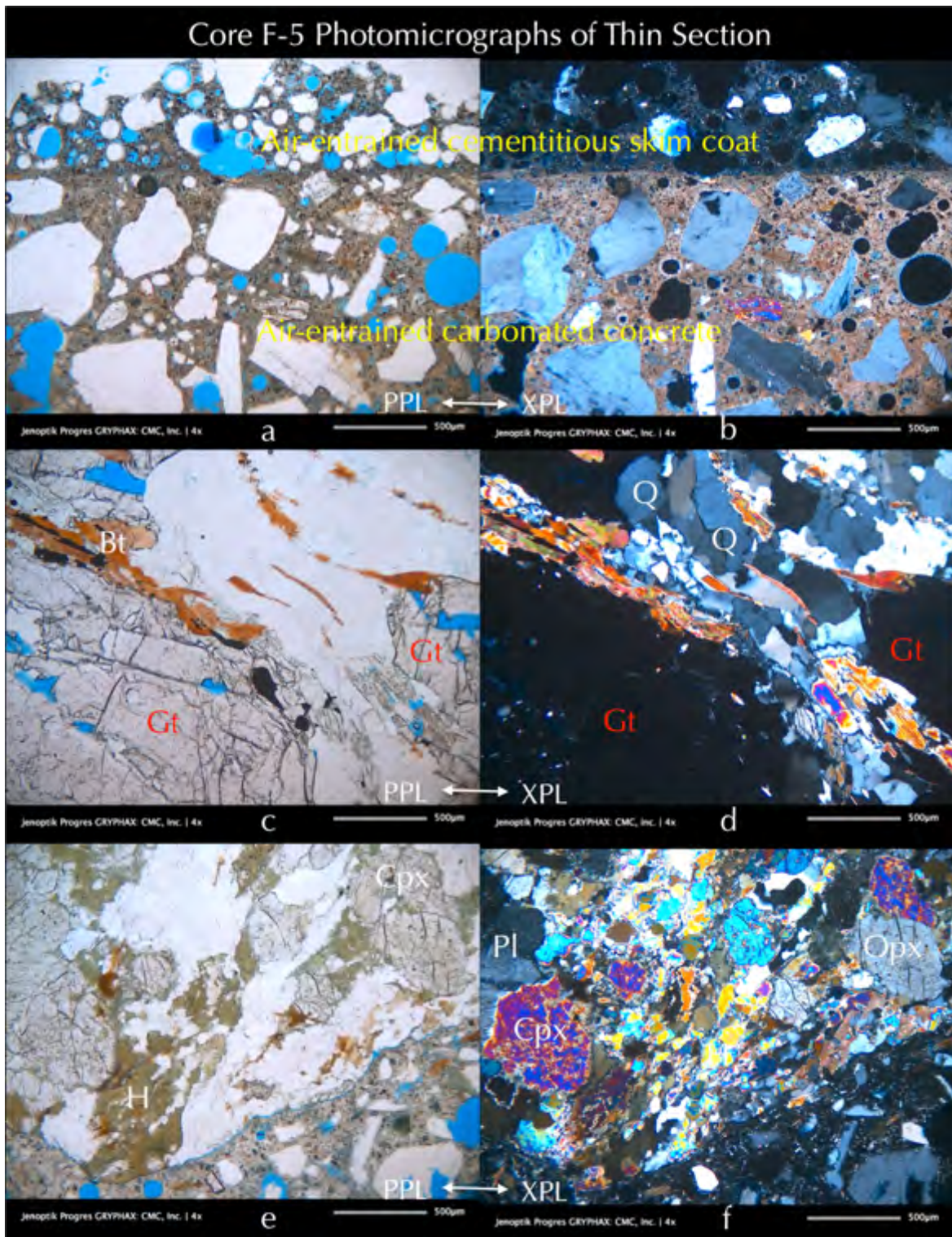


Figure D 40: Photomicrographs of thin section of Core F-5 showing mineralogies, textures, and microstructures of concrete and aggregates. Photos: a and b – thin air-entrained cementitious protective coating well-bonded to concrete beneath. Photos: c and d – garnetiferous (Gt) quartz (Q)-feldspar (albitic plagioclase, Pl)-biotite (Bt) gneiss where disseminated opaque (O) grains in dark are of iron sulfide (pyrrhotite) and iron-titanium oxide (ilmenite). Photos: e and f - metamorphosed gabbro (pyroxene granulite) consisting of pyroxene (Opx – enstatite, Cpx -augite, H - hornblende) and plagioclase (oligoclase, Pl). PPL-XPL photos of same microstructure taken in plane and crossed polarized-light modes with a petrographic microscope.

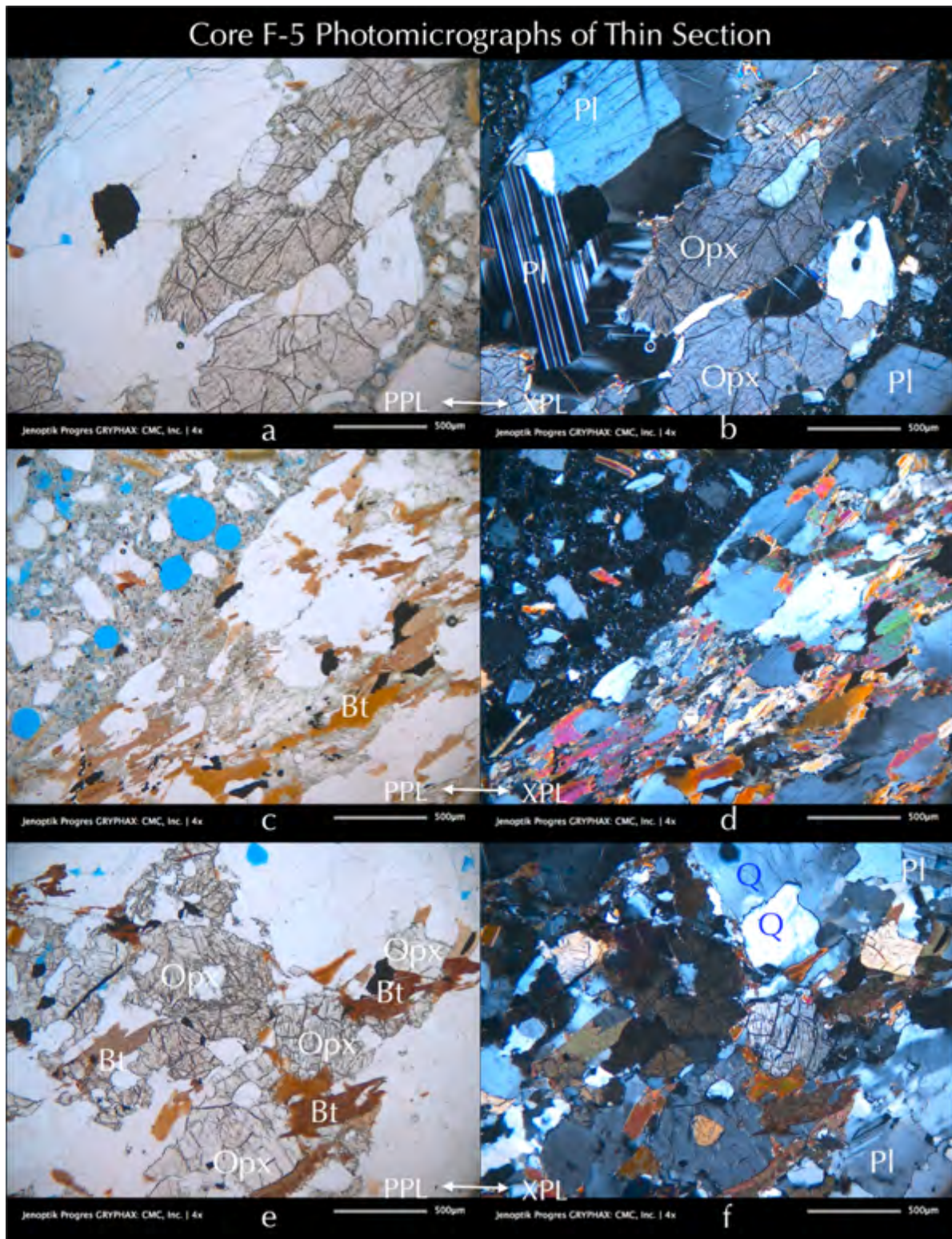


Figure D 41: Photomicrographs of thin section of Core F-5 showing mineralogies, textures, and microstructures of concrete and aggregates. Photos: a and b – metamorphosed gabbro (pyroxene granulite) consisting of pyroxene (Opx – enstatite, Cpx -augite) and plagioclase (oligoclase, Pl). Photos: e and f - garnetiferous (Gt) quartz (Q) -feldspar (albitic plagioclase, Pl) -biotite (Bt) gneiss where disseminated opaque (O) grains in dark are of iron sulfide (pyrrhotite) and iron-titanium oxide (ilmenite). PPL-XPL photos of same microstructure taken in plane and crossed polarized-light modes with a petrographic microscope.

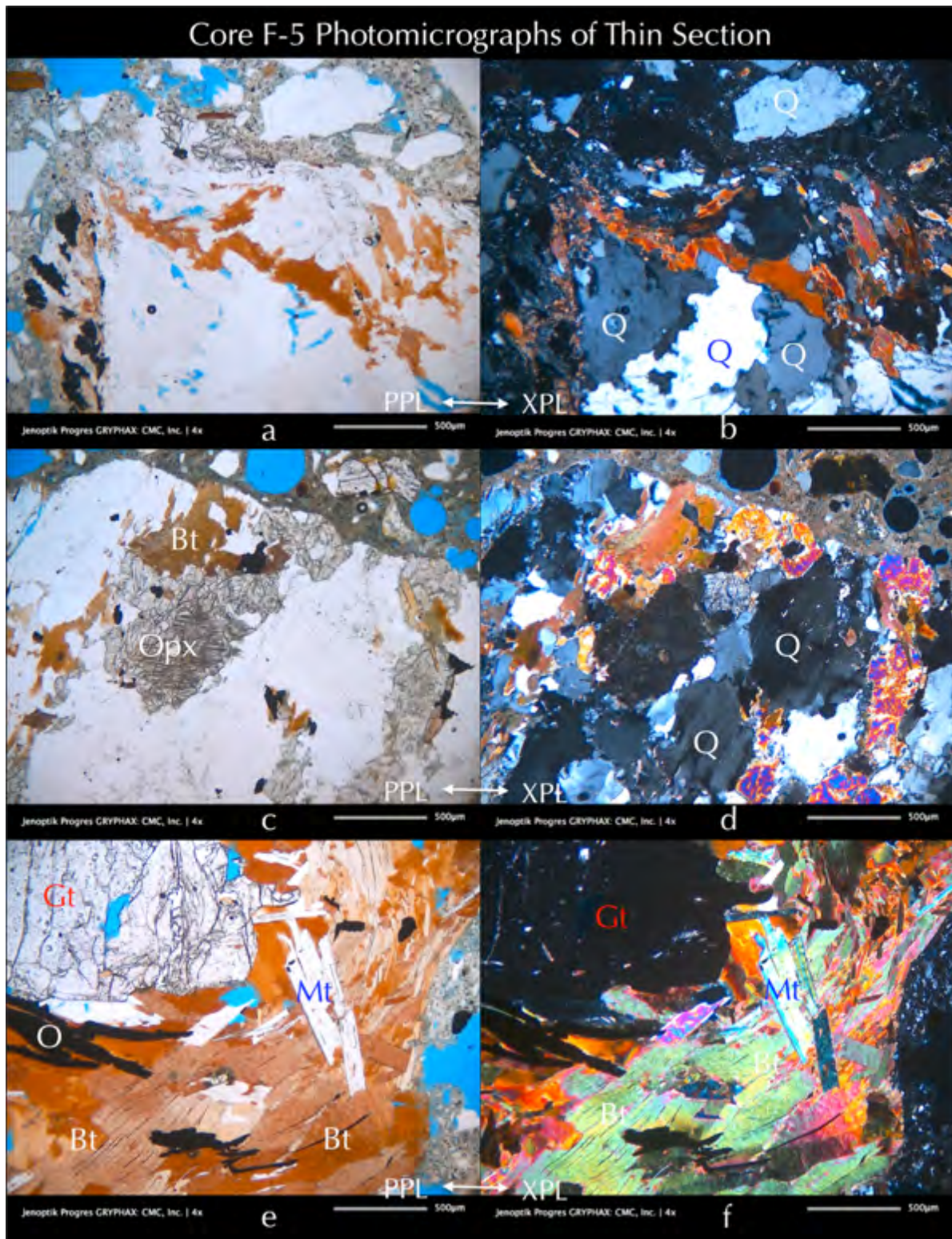


Figure D 42: Photomicrographs of thin section of Core F-5 showing mineralogies, textures, and microstructures of concrete and aggregates. Photos: a to f –garnetiferous (Gt) quartz (Q) –feldspar (albitic plagioclase, Pl) –biotite (Bt) gneiss where disseminated opaque (O) grains in dark are of iron sulfide (pyrrhotite) and iron-titanium oxide (ilmenite). PPL-XPL photos of same microstructure taken in plane and crossed polarized-light modes with a petrographic microscope.



# APPENDIX E

## Scanning Electron Microscopy & X-ray Microanalyses

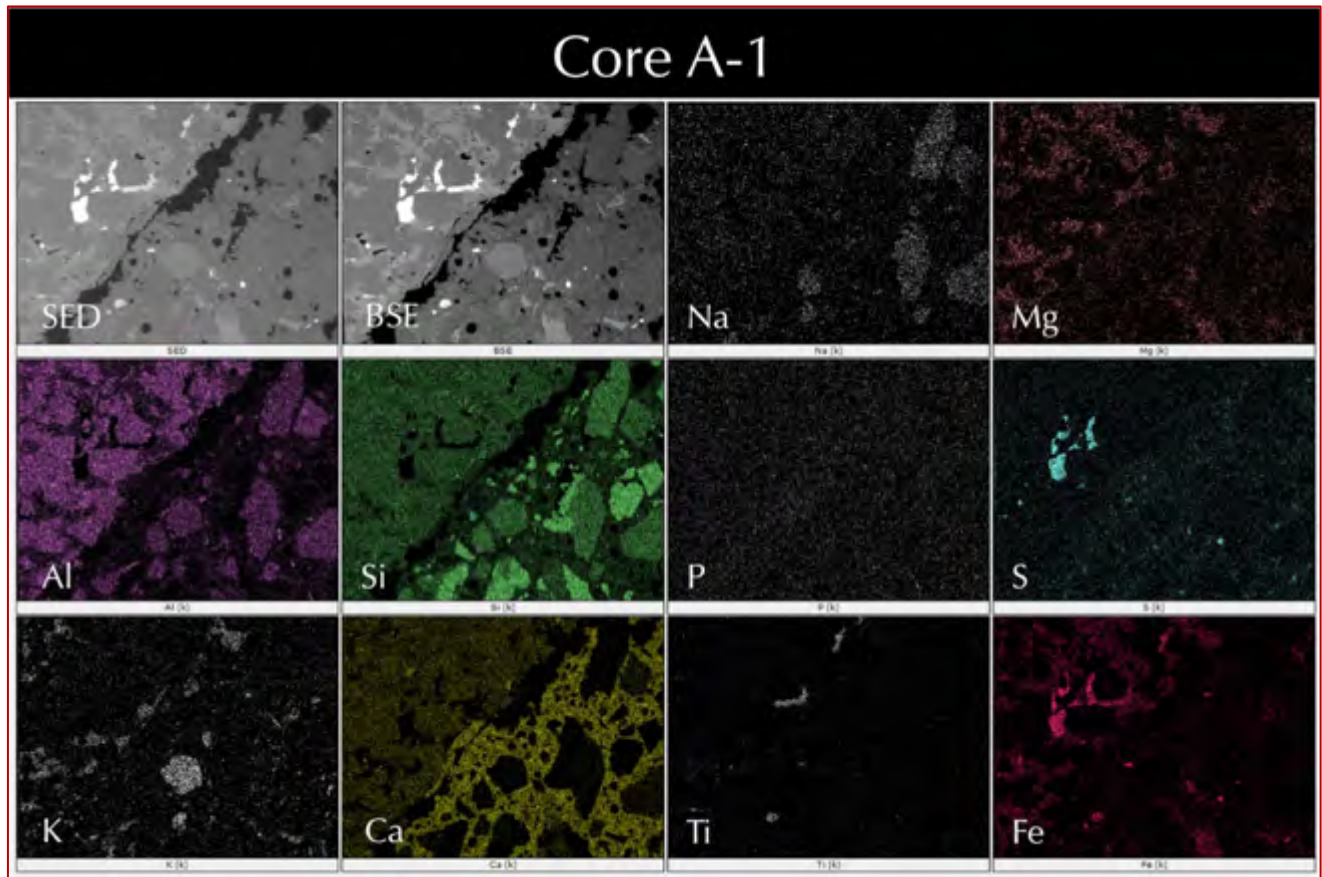


Figure E 1: Secondary electron image (top left), corresponding backscatter electron image (top 2<sup>nd</sup> from left), and corresponding X-ray elemental maps of sodium (Na), magnesium (Mg), aluminum (Al), silicon (Si), phosphorus (P), sulfur (S), potassium (K), calcium (Ca), titanium (TI), and iron (Fe) of microstructure of concrete in Core A-1 showing: (a) disseminated pyrrhotite grains in aggregate highlighted by Fe and S maps, (b) feldspar grains in gneiss coarse aggregate highlighted by Na, K, Al, Si maps, (c) calcium silicate hydrate paste from Portland cement hydration highlighted in Ca map, (d) siliceous sand fine aggregate highlighted in Si map, and (e) iron-titanium grains in aggregate highlighted in Fe and Ti maps.

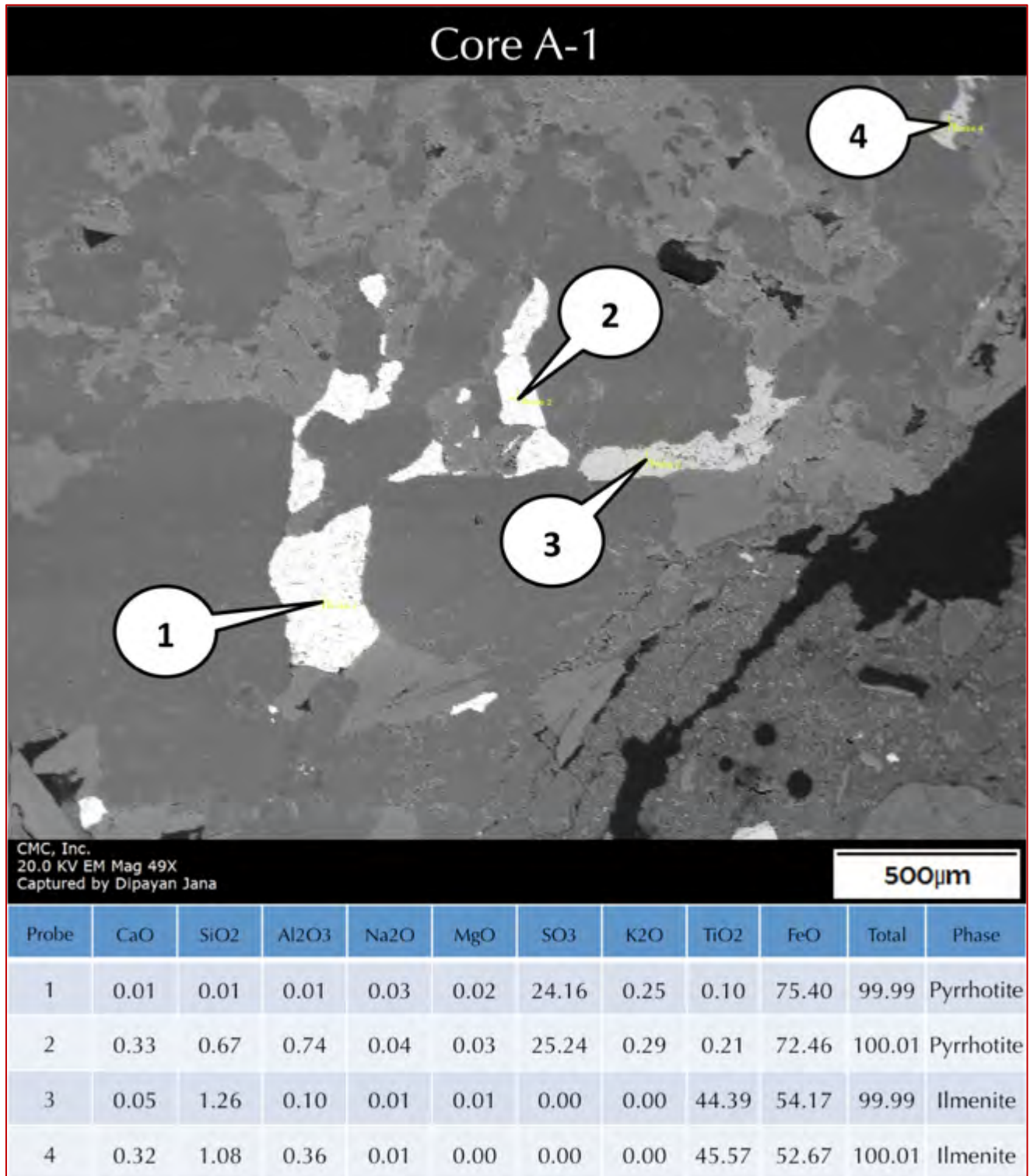


Figure E 2: Backscatter electron image (top) and compositional analyses of selected areas (at the tips of callouts) by energy-dispersive X-ray fluorescence spectroscopy of a portion of concrete microstructure in Core A-1 showing pyrrhotite and associated ilmenite opaque grains with their typical compositions of Fe-S and Fe-Ti-O, respectively.



Figure E 3: Backscatter electron image (top) and compositional analyses of selected areas (at the tips of callouts and in boxed areas) by energy-dispersive X-ray fluorescence spectroscopy of a portion of concrete microstructure in Core A-1 showing: (a) secondary ettringite deposits having characteristic calcium, aluminum, sulfur compositions, and (b) Portland cement paste having typical calcium silicate (hydrate) composition.

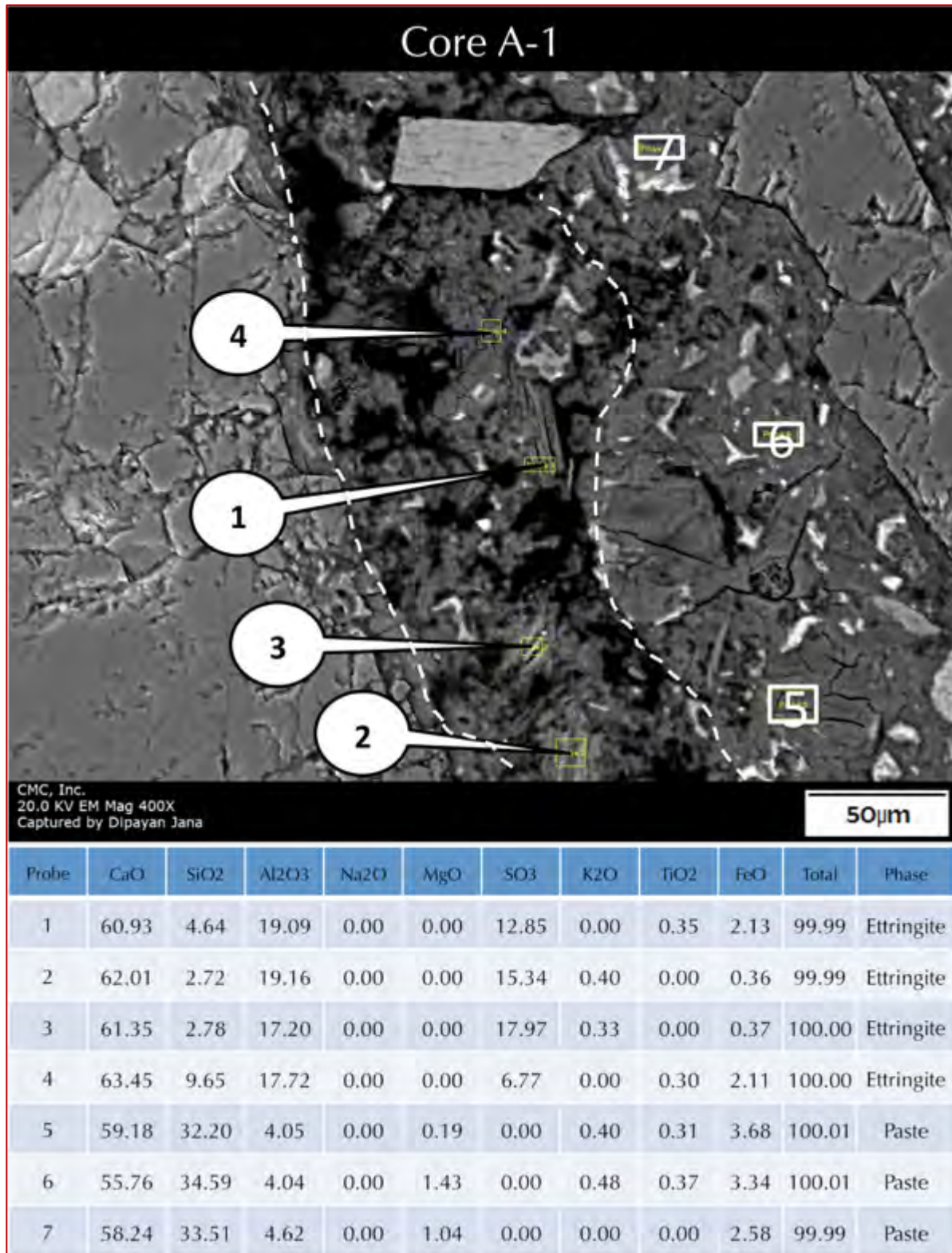


Figure E 4: Backscatter electron image (top) and compositional analyses of selected areas (at the tips of callouts and in boxed areas) by energy-dispersive X-ray fluorescence spectroscopy of a portion of concrete microstructure in Core A-1 showing: (a) secondary ettringite deposits along an aggregate-paste interface having characteristic calcium, aluminum, sulfur compositions, and (b) Portland cement paste having typical calcium silicate (hydrate) composition.

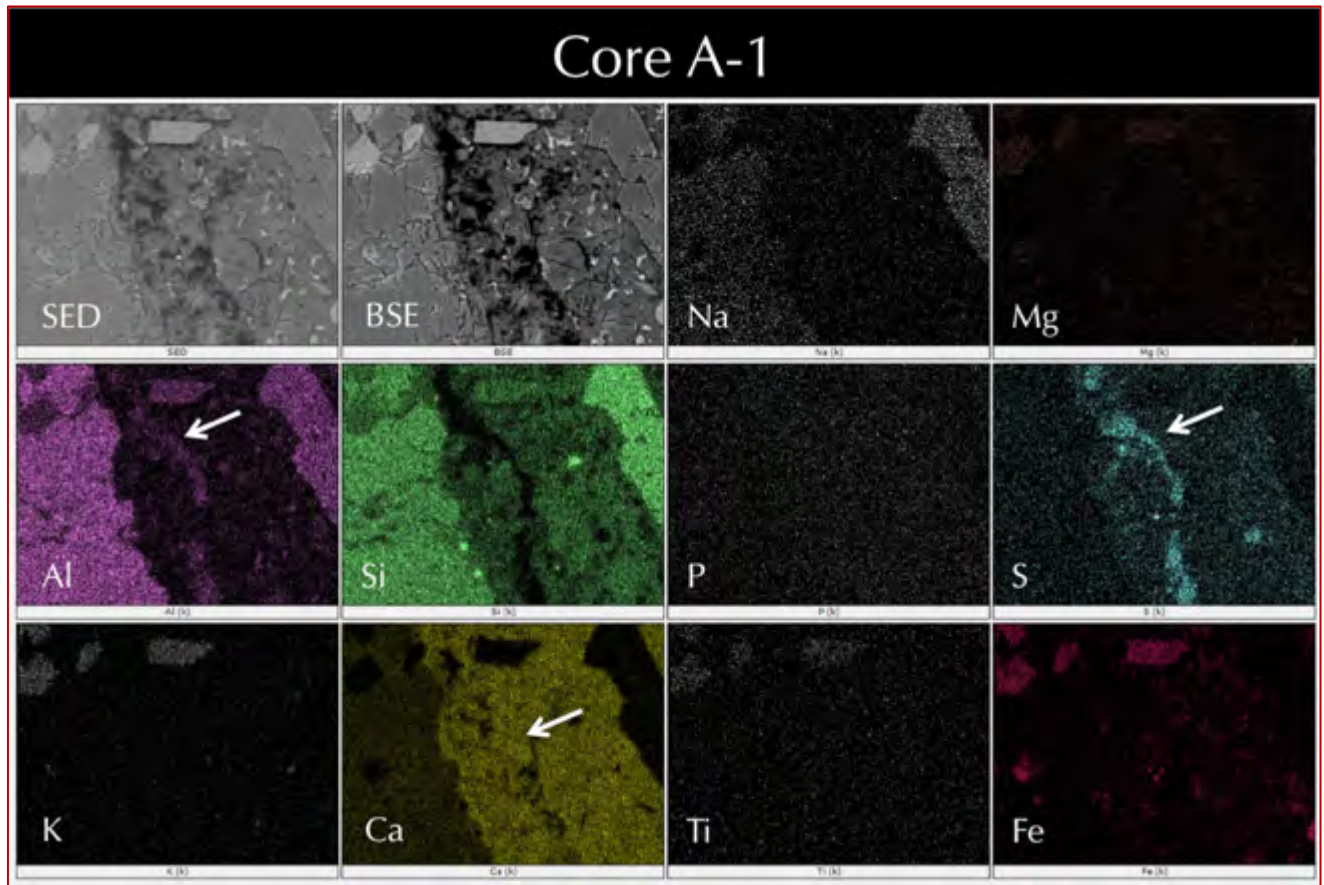


Figure E 5: Secondary electron image (top left), corresponding backscatter electron image (top 2<sup>nd</sup> from left), and corresponding X-ray elemental maps of sodium (Na), magnesium (Mg), aluminum (Al), silicon (Si), phosphorus (P), sulfur (S), potassium (K), calcium (Ca), titanium (Ti), and iron (Fe) of microstructure of concrete in Core A-1 showing: (a) disseminated pyrrhotite grains in aggregate highlighted by Fe and S maps, (b) feldspar grains in gneiss coarse aggregate highlighted by Na, K, Al, Si maps, (c) calcium silicate hydrate paste from Portland cement hydration highlighted in Ca map, (d) siliceous sand fine aggregate highlighted in Si map, (e) iron-titanium grains in aggregate highlighted in Fe and Ti maps, and (f) secondary ettringite deposits in microcracks (arrows) and in paste highlighted in Ca, Al, and S maps.

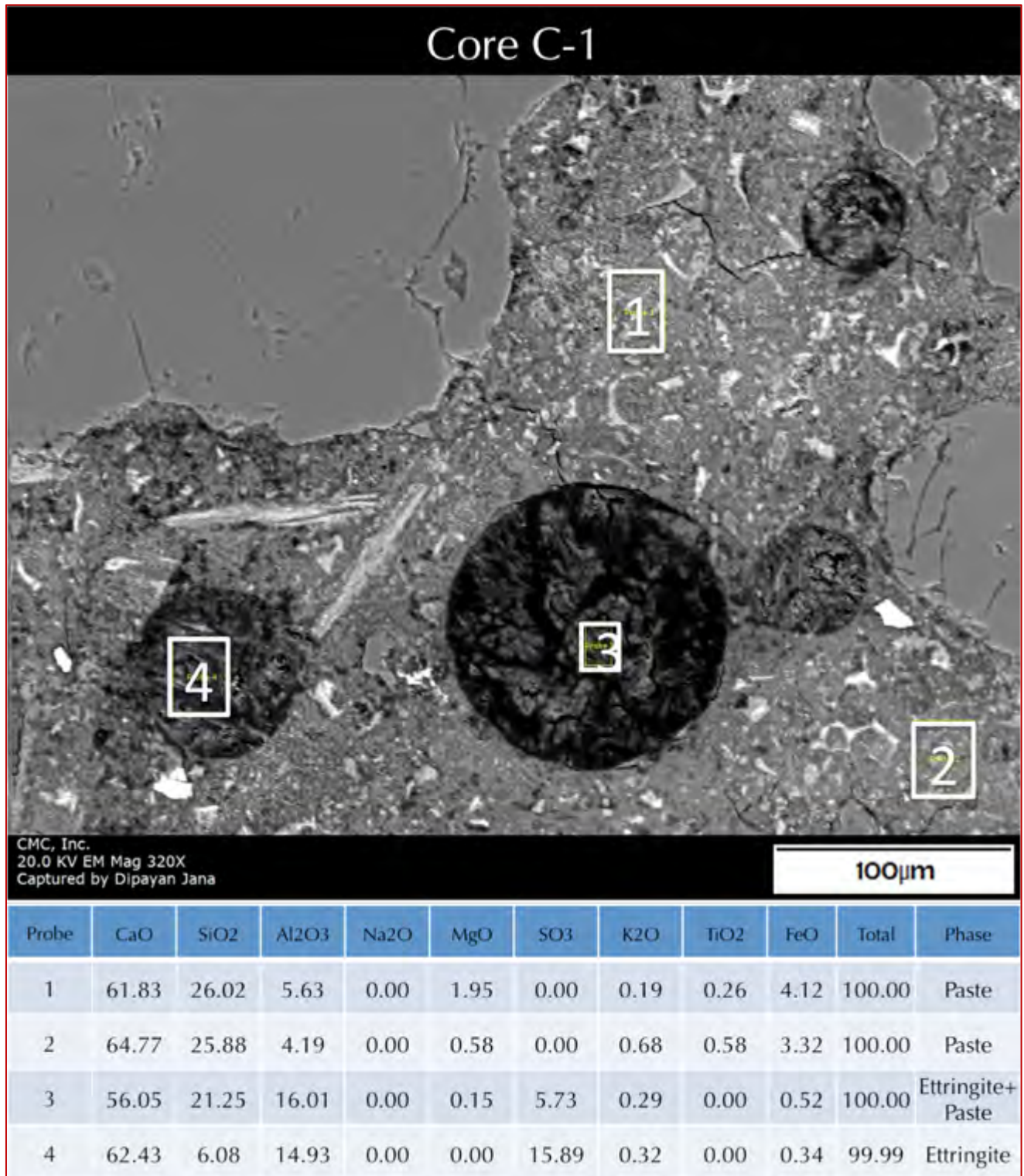


Figure E 6: Backscatter electron image (BSE, top) and compositional analyses of selected areas (at the tips of callouts and in boxed areas) by energy-dispersive X-ray fluorescence spectroscopy of a portion of concrete microstructure in Core C-1 showing: (a) secondary ettringite deposits having characteristic calcium, aluminum, sulfur compositions, and (b) Portland cement paste having typical calcium silicate (hydrate) composition. Scattered residual Portland cement particles having ferrite remains (appear bright in BSE image) are seen in the paste.

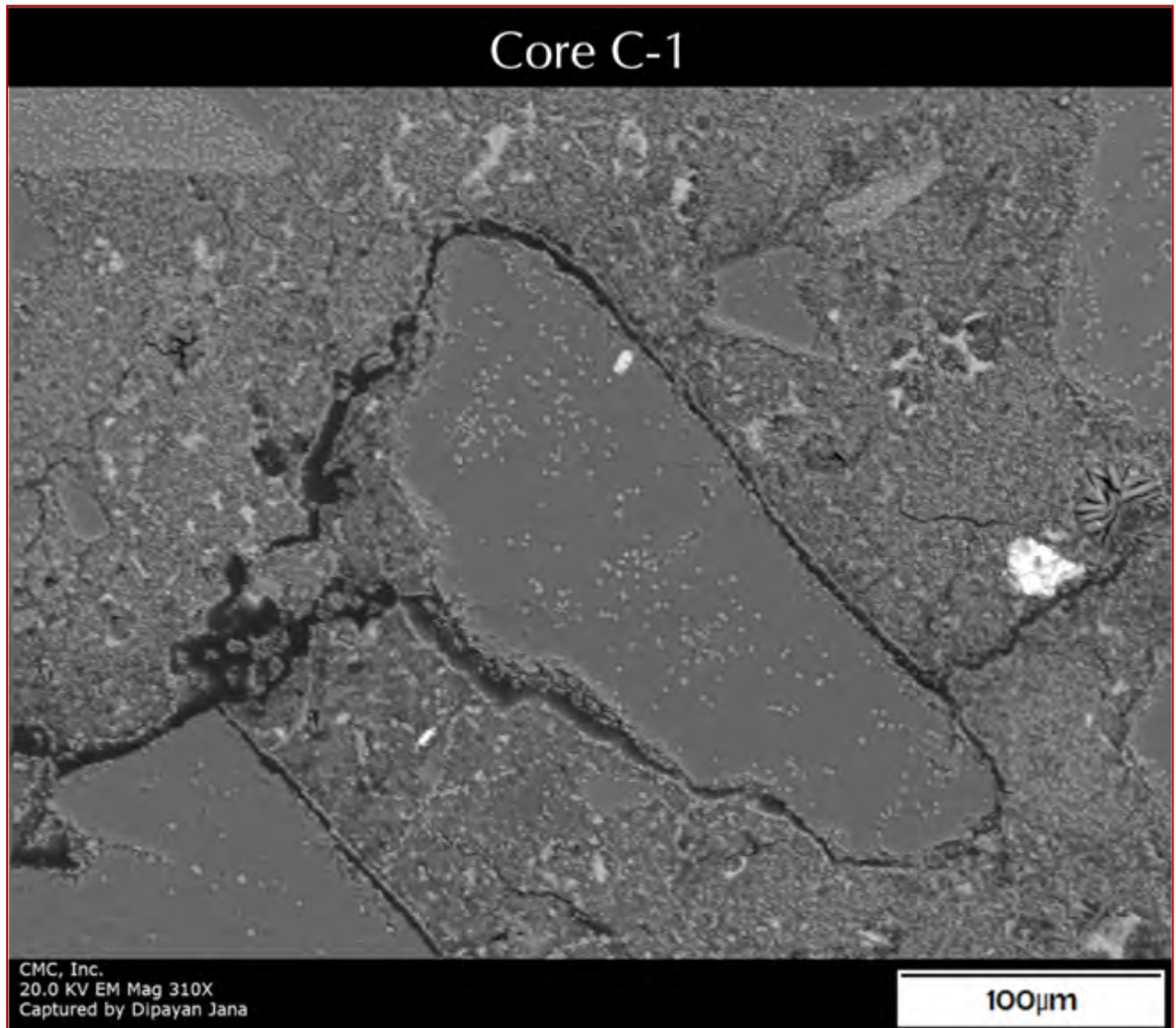


Figure E 7: Secondary electron image of a portion of concrete microstructure in Core C-1 showing gaps around aggregate, a typical feature found in many distressed concretes affected by delayed ettringite formation where paste expands relative to aggregates to form the gaps. Although present concrete does not show such features in abundance, expansion of paste still has occurred from sulfate attack in paste where sulfate was released from oxidation of pyrrhotite and formed such gaps.

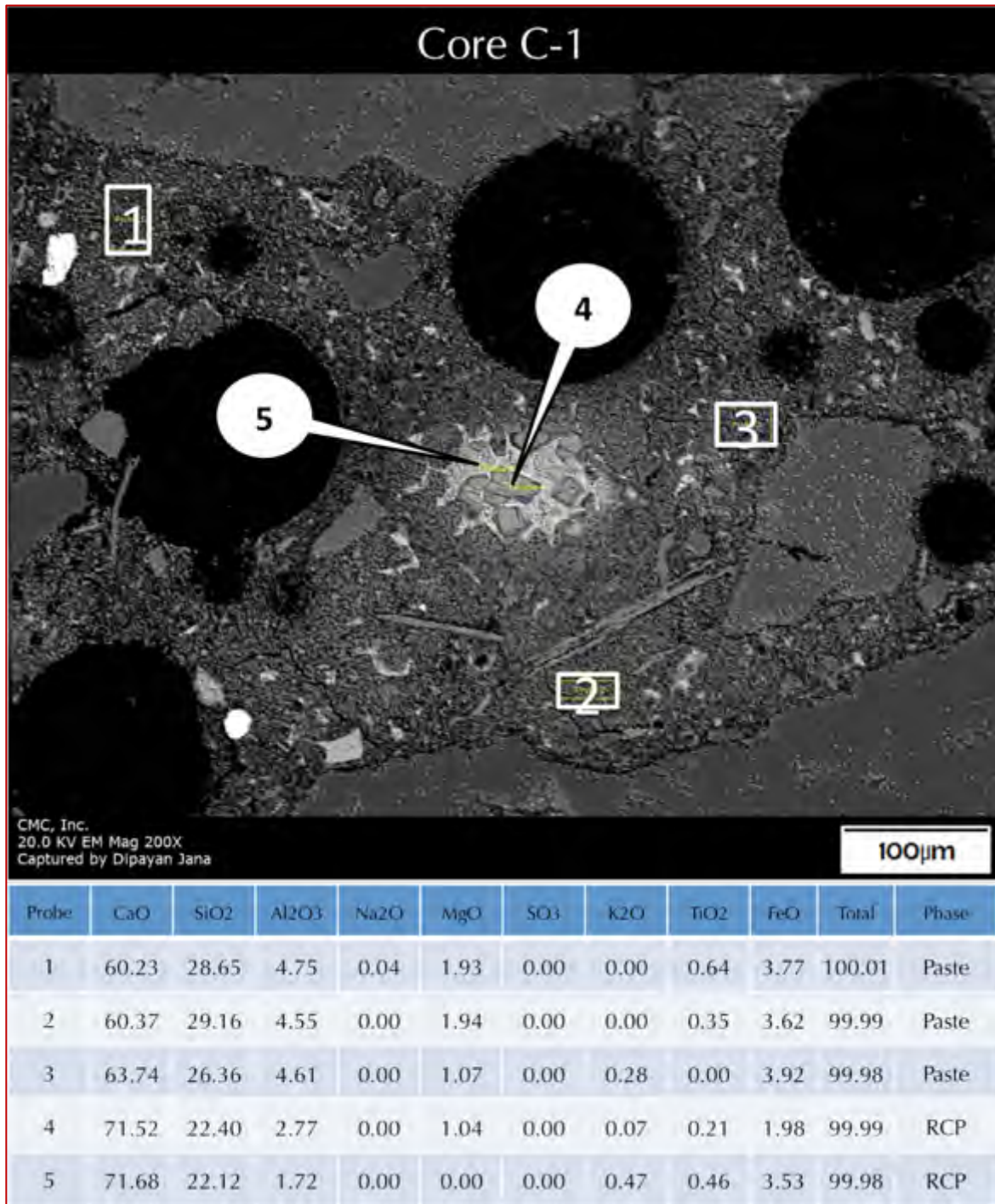


Figure E 8: Backscatter electron image (BSE, top) and compositional analyses of selected areas (at the tips of callouts and in boxed areas) by energy-dispersive X-ray fluorescence spectroscopy of a portion of concrete microstructure in Core C-1 showing: (a) a residual Portland cement particle (RCP) at the center having aluminate and ferrite remains (appear bright in BSE image) and subhedral alite crystals of cement, and (b) Portland cement paste having typical calcium silicate (hydrate) composition. Scattered residual Portland cement particles having ferrite remains (appear bright in BSE image) are seen in the paste.

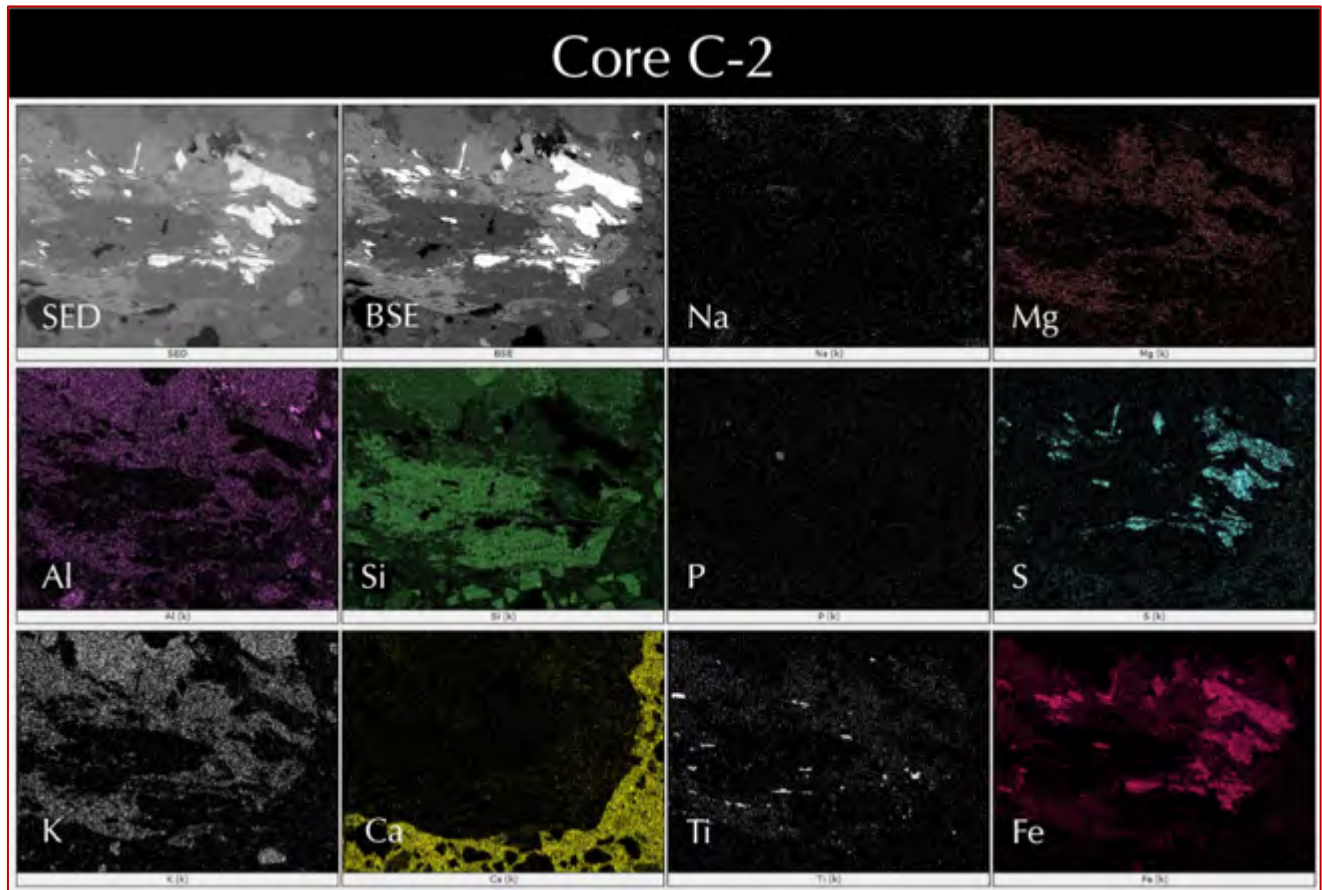


Figure E 9: Secondary electron image (top left), corresponding backscatter electron image (top 2<sup>nd</sup> from left), and corresponding X-ray elemental maps of sodium (Na), magnesium (Mg), aluminum (Al), silicon (Si), phosphorus (P), sulfur (S), potassium (K), calcium (Ca), titanium (TI), and iron (Fe) of microstructure of concrete in Core C-2 showing: (a) disseminated pyrrhotite grains in aggregate highlighted by Fe and S maps, (b) feldspar grains in gneiss coarse aggregate highlighted by Na, K, Al, Si maps, (c) calcium silicate hydrate paste from Portland cement hydration highlighted in Ca map, (d) siliceous sand fine aggregate highlighted in Si map, and (e) iron-titanium grains in aggregate highlighted in Fe and Ti maps.

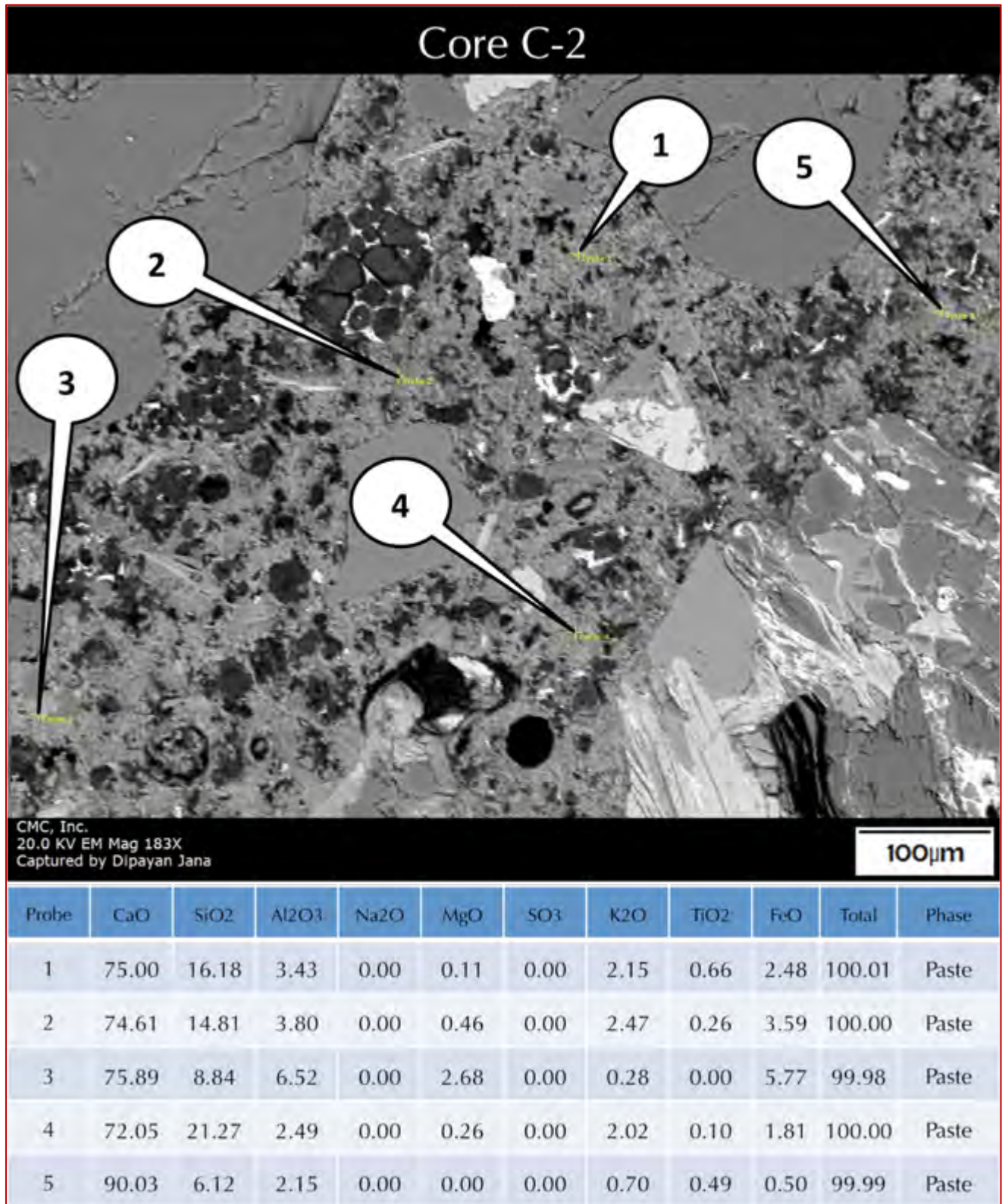


Figure E 10: Backscatter electron image (BSE, top) and compositional analyses of selected areas (at the tips of callouts) by energy-dispersive X-ray fluorescence spectroscopy of a portion of concrete microstructure in Core C-2 showing Portland cement paste having typical calcium silicate (hydrate) composition. Scattered residual Portland cement particles having subhedral alite grains, and ferrite remains (latter appear brighter in BSE image) are seen in the paste.

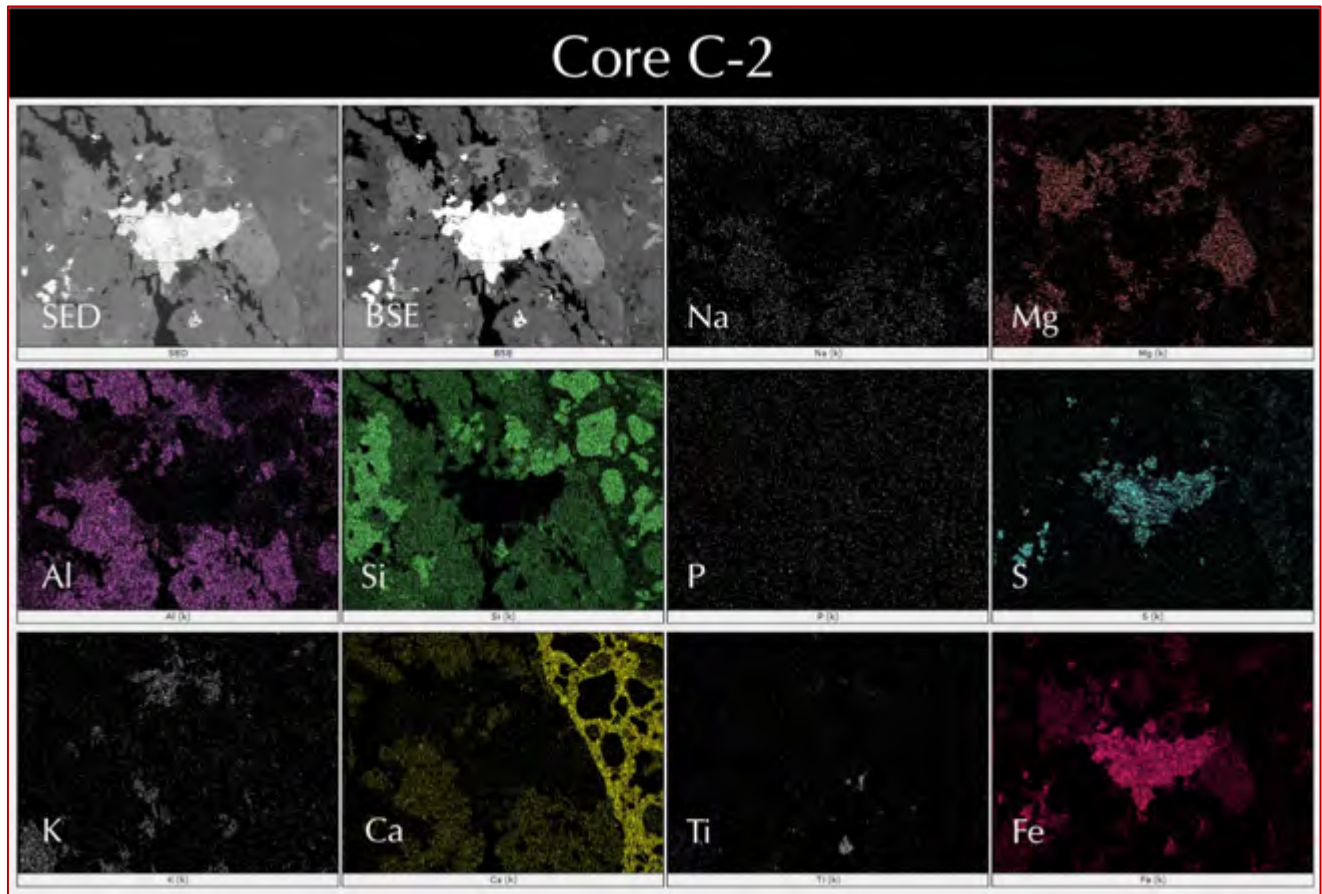


Figure E 11: Secondary electron image (top left), corresponding backscatter electron image (top 2<sup>nd</sup> from left), and corresponding X-ray elemental maps of sodium (Na), magnesium (Mg), aluminum (Al), silicon (Si), phosphorus (P), sulfur (S), potassium (K), calcium (Ca), titanium (TI), and iron (Fe) of microstructure of concrete in Core C-2 showing: (a) disseminated pyrrhotite grains in aggregate highlighted by Fe and S maps, (b) feldspar grains in gneiss coarse aggregate highlighted by Na, K, Al, Si maps, (c) calcium silicate hydrate paste from Portland cement hydration highlighted in Ca map, (d) siliceous sand fine aggregate highlighted in Si map, and (e) iron-titanium grains in aggregate highlighted in Fe and Ti maps.

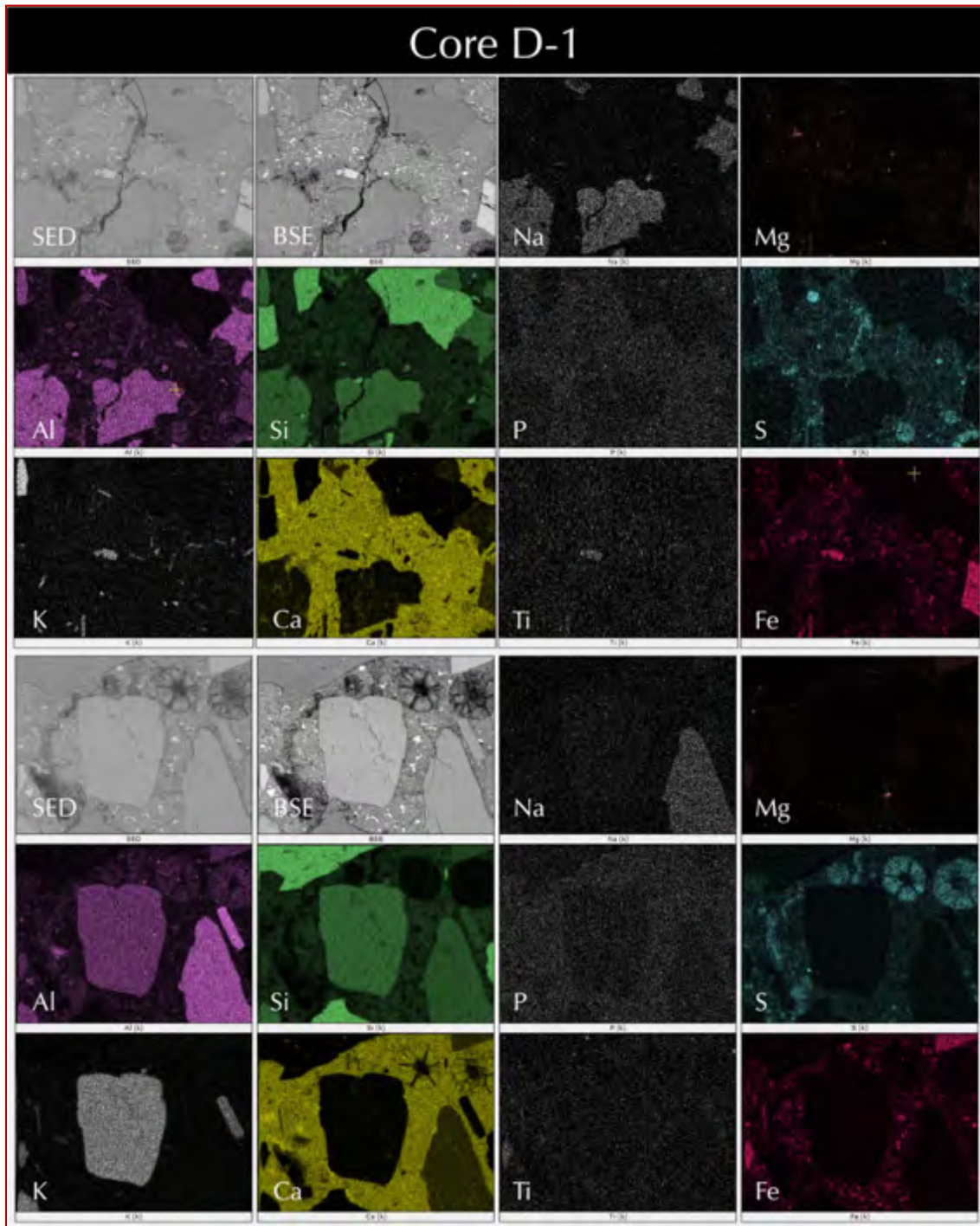


Figure E 12: Secondary electron images (top left), corresponding backscatter electron images (top 2<sup>nd</sup> from left), and corresponding X-ray elemental maps of sodium (Na), magnesium (Mg), aluminum (Al), silicon (Si), phosphorus (P), sulfur (S), potassium (K), calcium (Ca), titanium (TI), and iron (Fe) of microstructure of concrete in Core D-1 showing: (a) disseminated pyrrhotite grains in aggregate highlighted by Fe and S maps, (b) feldspar grains in gneiss coarse aggregate highlighted by Na, K, Al, Si maps, (c) calcium silicate hydrate paste from Portland cement hydration highlighted in Ca map, (d) siliceous sand fine aggregate highlighted in Si map, (e) iron-titanium grains in aggregate highlighted in Fe and Ti maps, and (f) secondary ettringite deposits in microcracks, voids, and in paste highlighted in Ca, Al, and S maps.

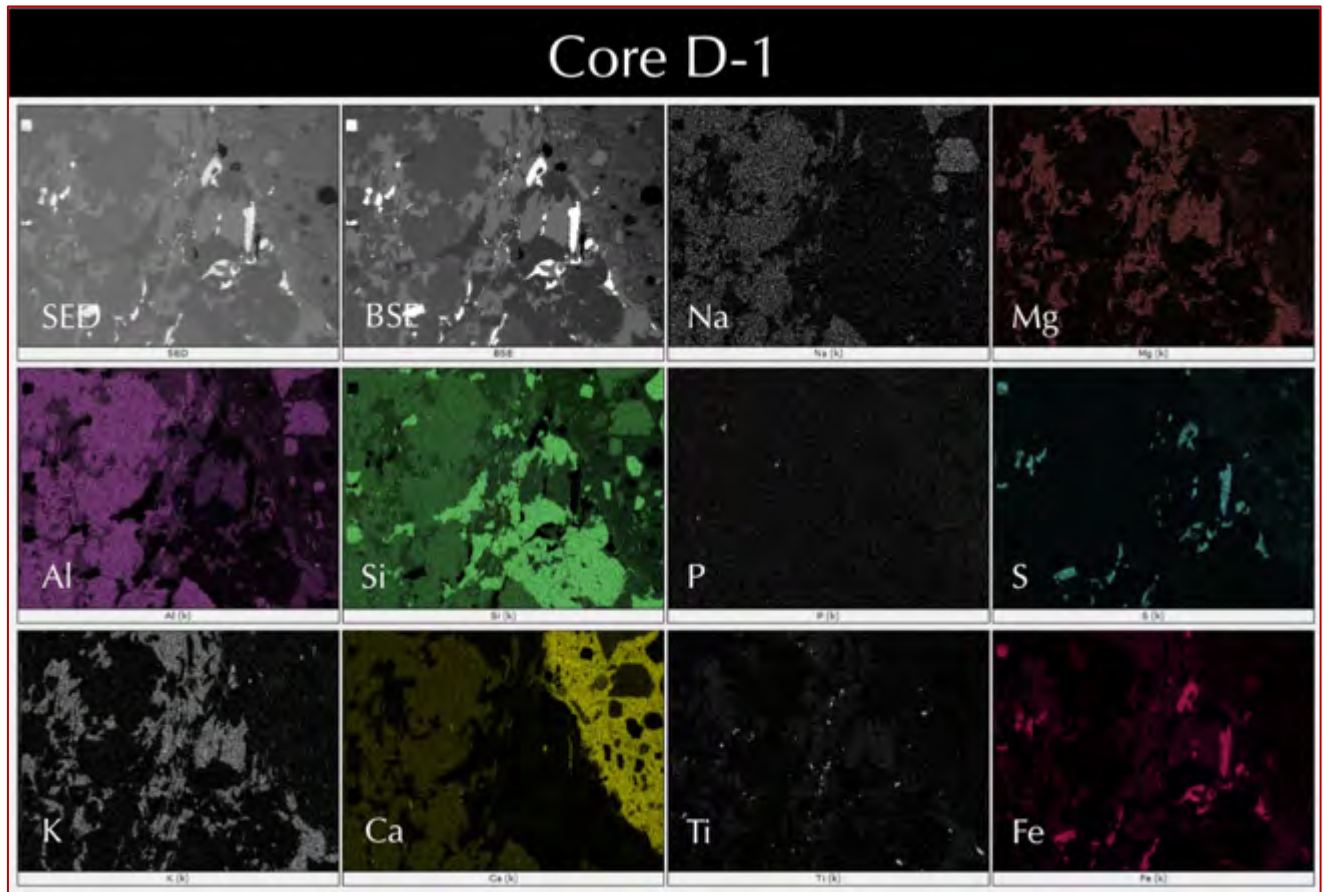


Figure E 13: Secondary electron image (top left), corresponding backscatter electron image (top 2<sup>nd</sup> from left), and corresponding X-ray elemental maps of sodium (Na), magnesium (Mg), aluminum (Al), silicon (Si), phosphorus (P), sulfur (S), potassium (K), calcium (Ca), titanium (TI), and iron (Fe) of microstructure of concrete in Core D-1 showing: (a) disseminated pyrrhotite grains in aggregate highlighted by Fe and S maps, (b) feldspar grains in gneiss coarse aggregate highlighted by Na, K, Al, Si maps, (c) calcium silicate hydrate paste from Portland cement hydration highlighted in Ca map, (d) siliceous sand fine aggregate highlighted in Si map, and (e) iron-titanium grains in aggregate highlighted in Fe and Ti maps.

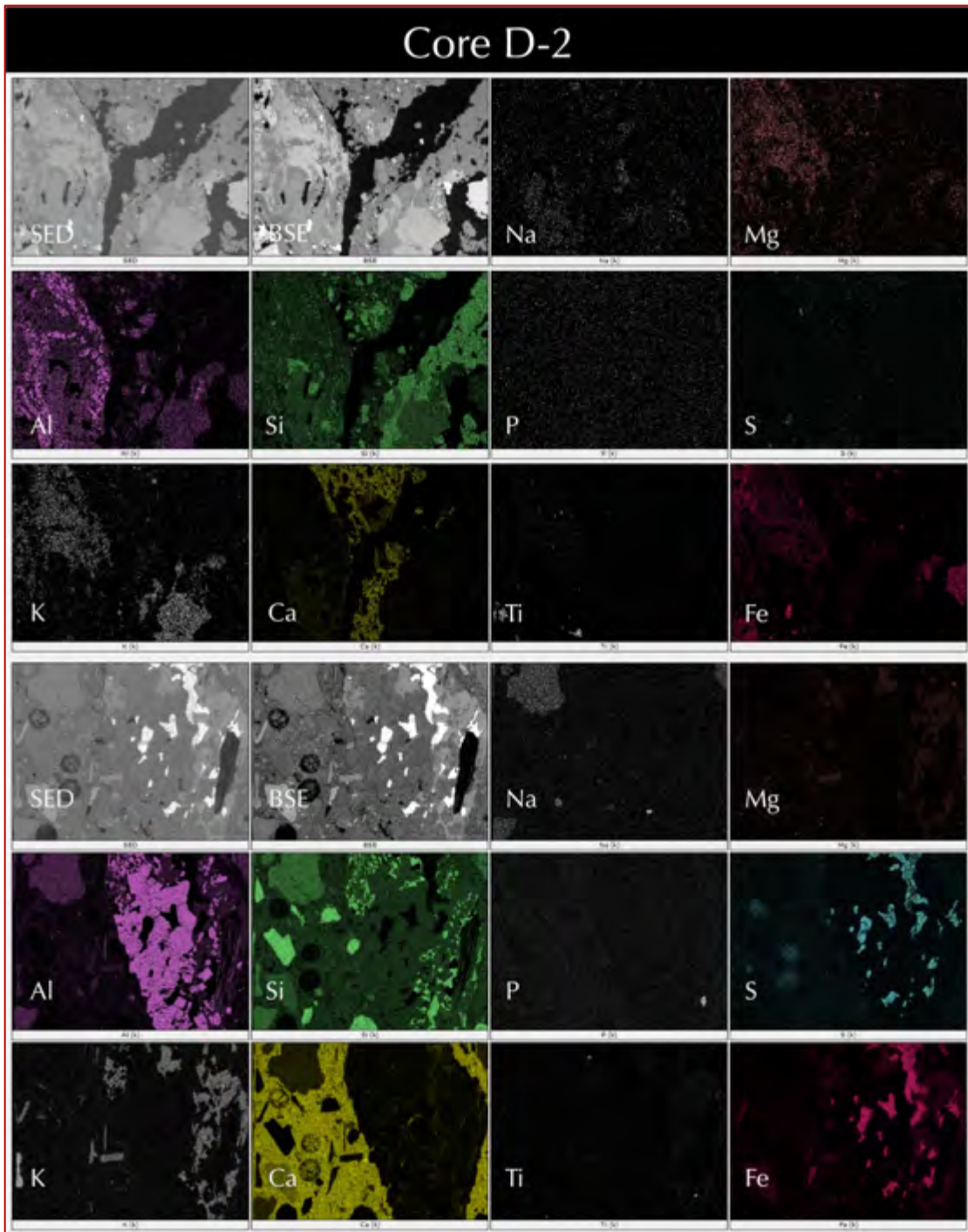


Figure E 14: Secondary electron images (top left), corresponding backscatter electron images (top 2<sup>nd</sup> from left), and corresponding X-ray elemental maps of sodium (Na), magnesium (Mg), aluminum (Al), silicon (Si), phosphorus (P), sulfur (S), potassium (K), calcium (Ca), titanium (Ti), and iron (Fe) of microstructure of concrete in Core D-2 showing: (a) disseminated pyrrhotite grains in aggregate highlighted by Fe and S maps, (b) feldspar grains in gneiss coarse aggregate highlighted by Na, K, Al, Si maps, (c) calcium silicate hydrate paste from Portland cement hydration highlighted in Ca map, (d) siliceous sand fine aggregate highlighted in Si map, and (e) iron-titanium grains in aggregate highlighted in Fe and Ti maps.

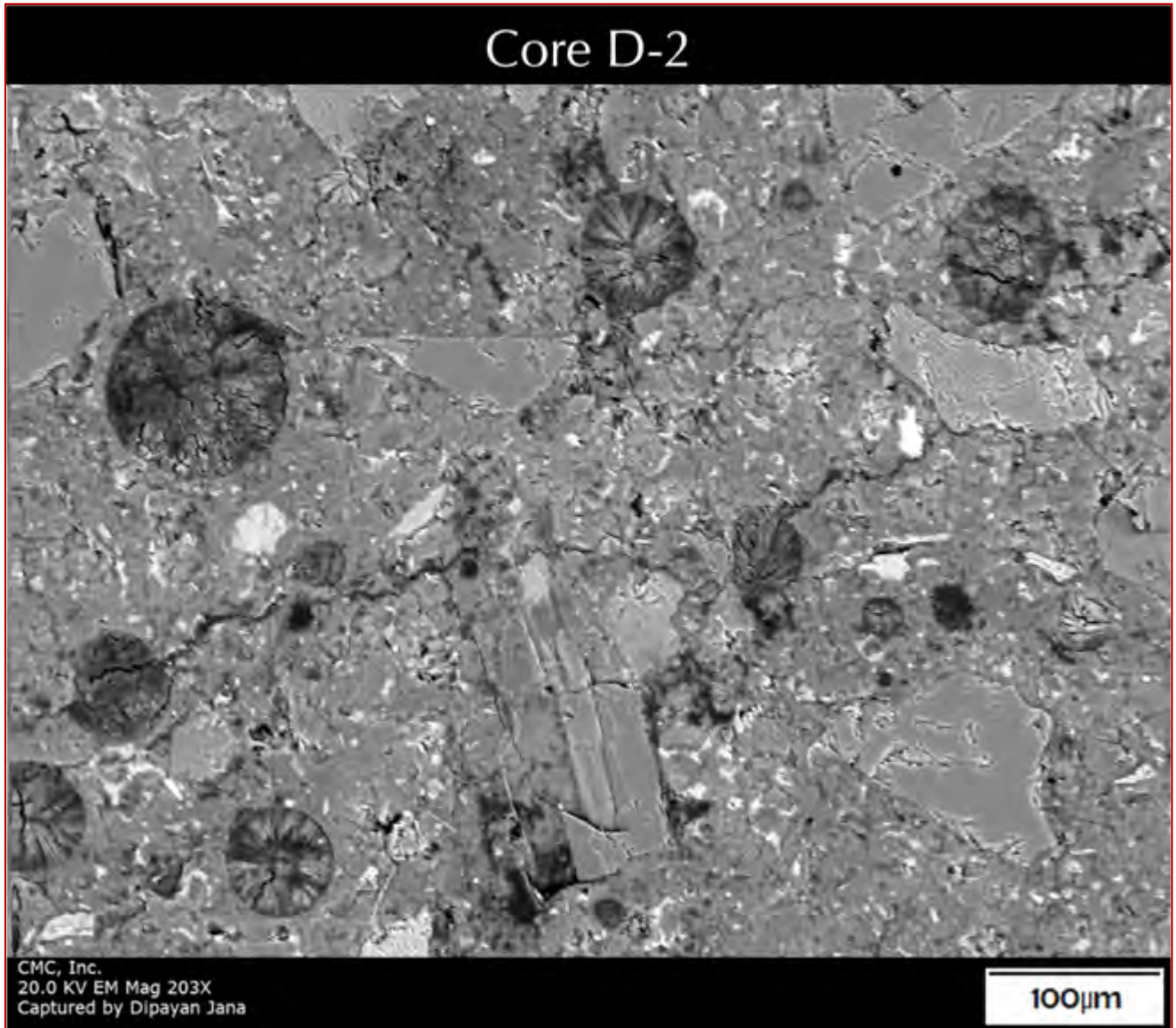


Figure E 15: Backscatter electron image of a portion of concrete microstructure in Core D-2 showing air voids filled with secondary ettringite deposits.

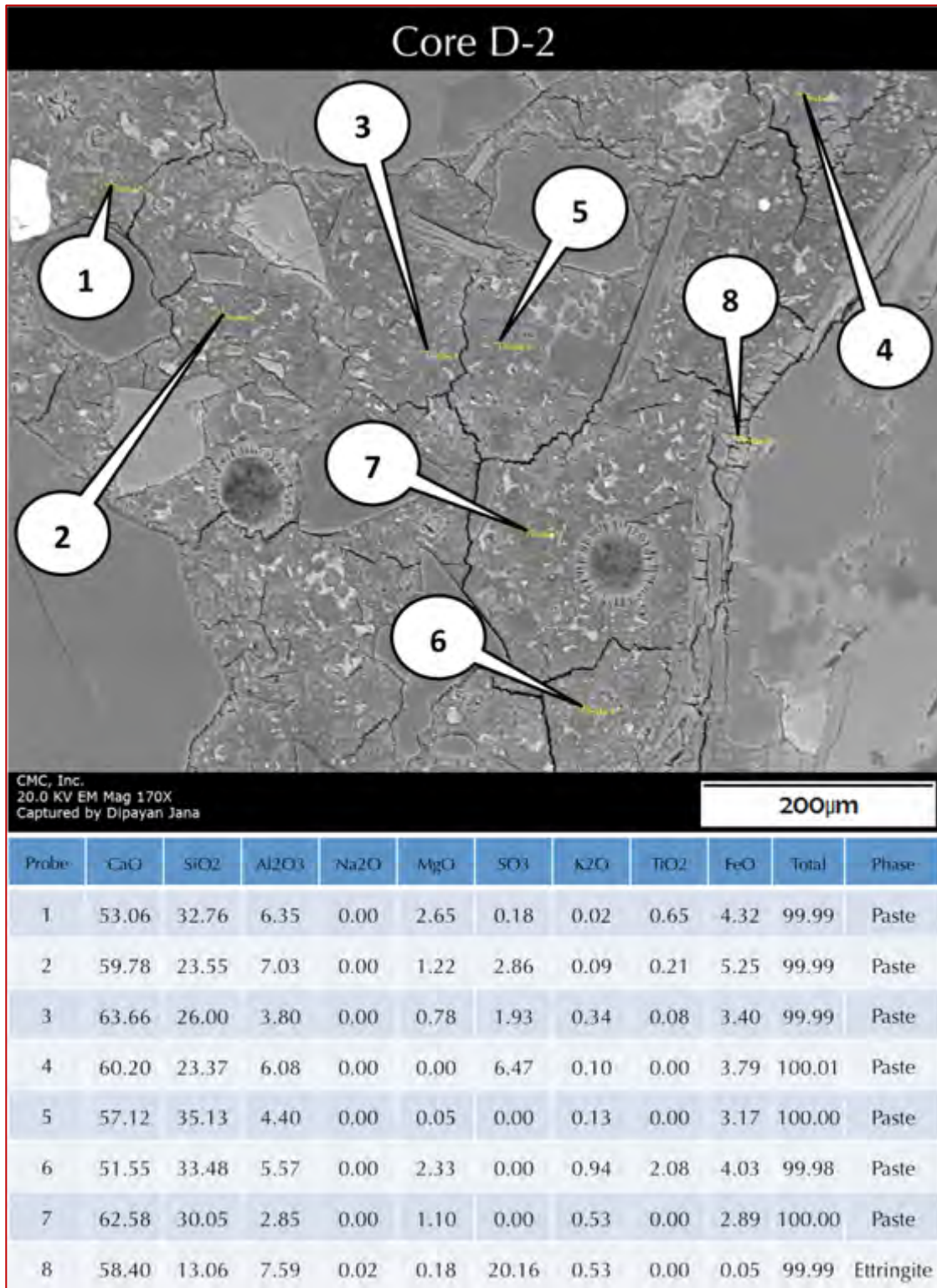


Figure E 16: Backscatter electron image (BSE, top) and compositional analyses of selected areas (at the tips of callouts) by energy-dispersive X-ray fluorescence spectroscopy of a portion of concrete microstructure in Core D-2 showing Portland cement paste having typical calcium silicate (hydrate) composition. Scattered residual Portland cement particles having subhedral alite grains, and ferrite remains (latter appear brighter in BSE image) are seen in the paste.

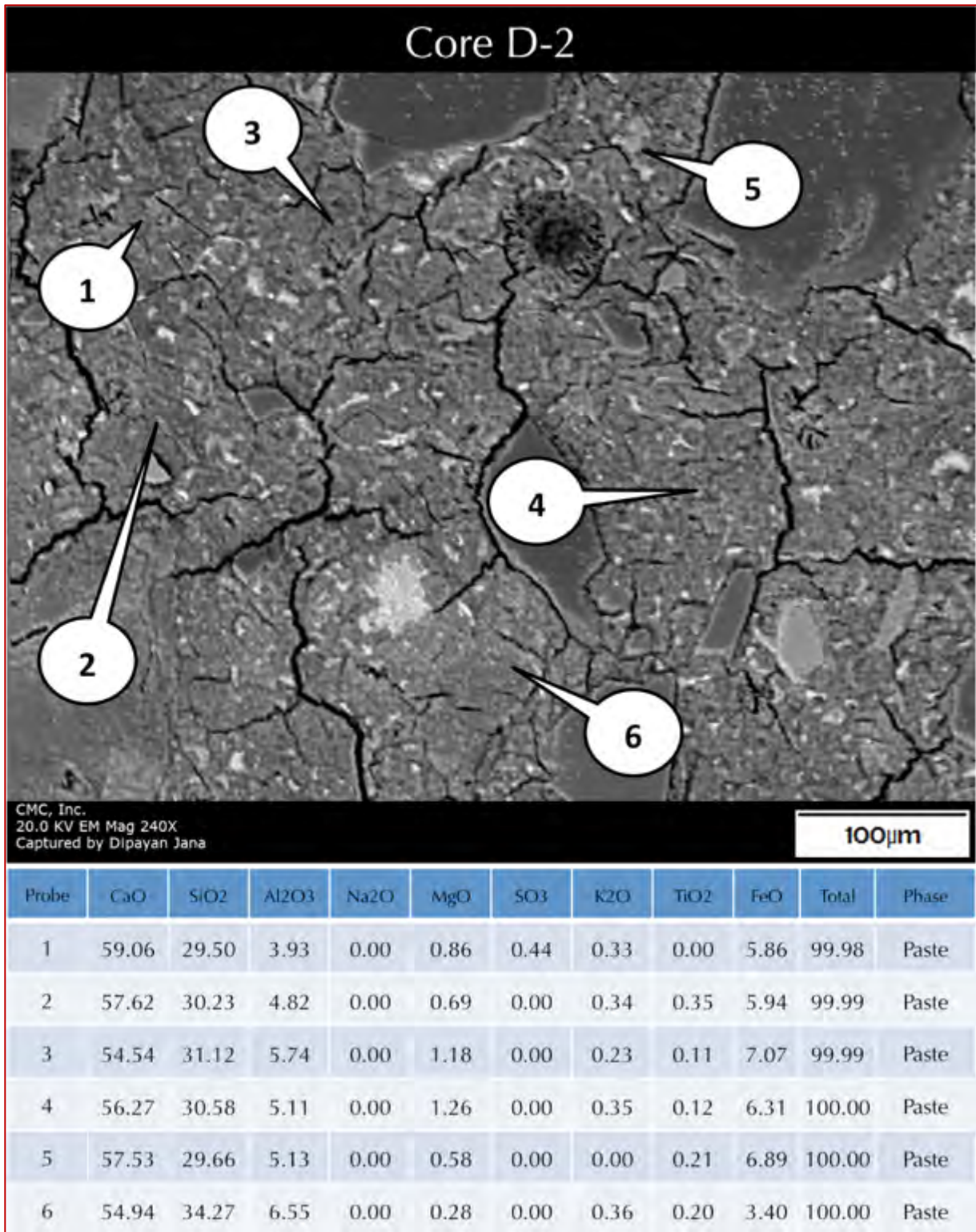


Figure E 17: Backscatter electron image (BSE, top) and compositional analyses of selected areas (at the tips of callouts) by energy-dispersive X-ray fluorescence spectroscopy of a portion of concrete microstructure in Core D-2 showing Portland cement paste having typical calcium silicate (hydrate) composition. Scattered residual Portland cement particles having subhedral alite grains, and ferrite remains (latter appear brighter in BSE image) are seen in the paste.

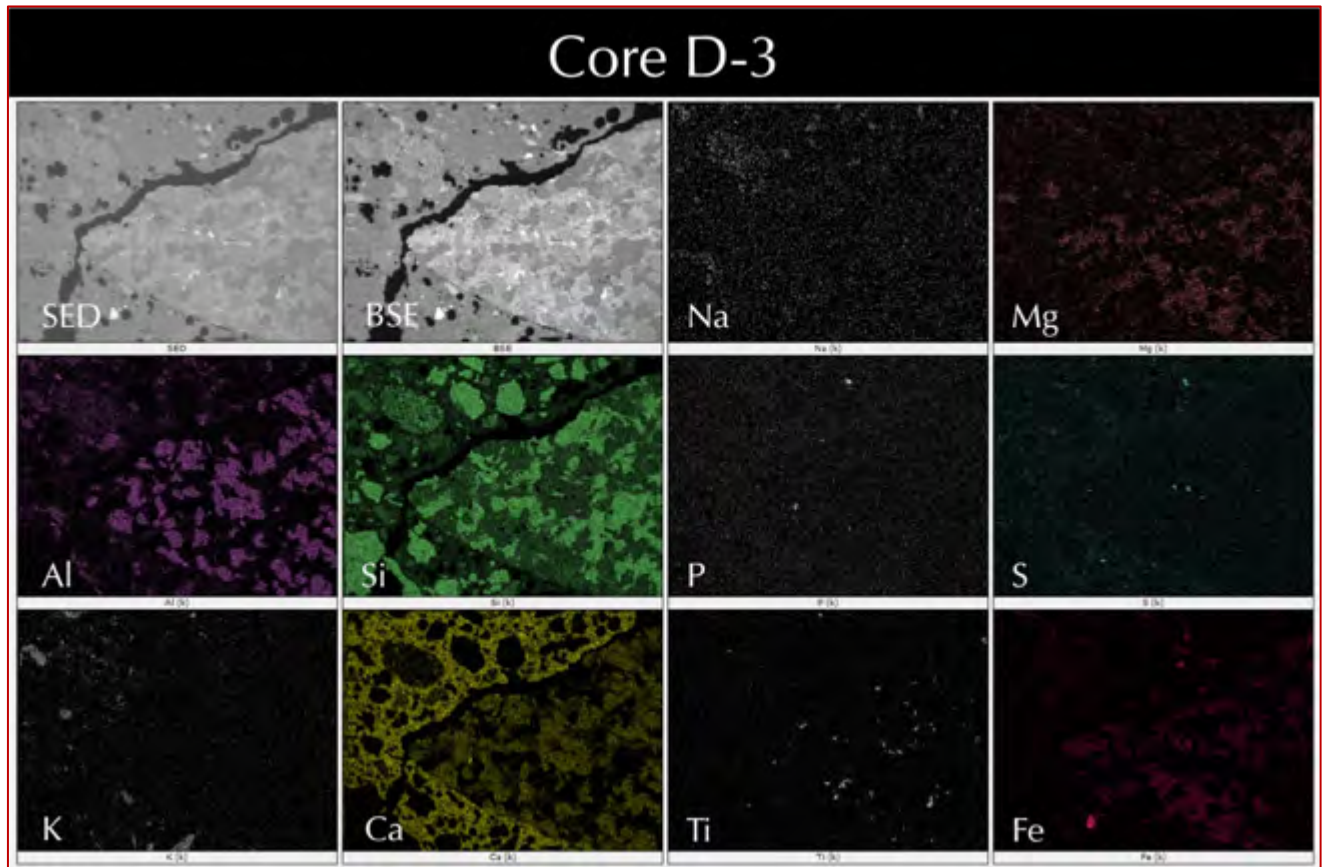


Figure E 18: Secondary electron image (top left), corresponding backscatter electron image (top 2<sup>nd</sup> from left), and corresponding X-ray elemental maps of sodium (Na), magnesium (Mg), aluminum (Al), silicon (Si), phosphorus (P), sulfur (S), potassium (K), calcium (Ca), titanium (Ti), and iron (Fe) of microstructure of concrete in Core D-3 showing: (a) disseminated pyrrhotite grains in aggregate highlighted by Fe and S maps, (b) feldspar grains in gneiss coarse aggregate highlighted by Na, K, Al, Si maps, (c) calcium silicate hydrate paste from Portland cement hydration highlighted in Ca map, (d) siliceous sand fine aggregate highlighted in Si map, and (e) iron-titanium grains in aggregate highlighted in Fe and Ti maps.

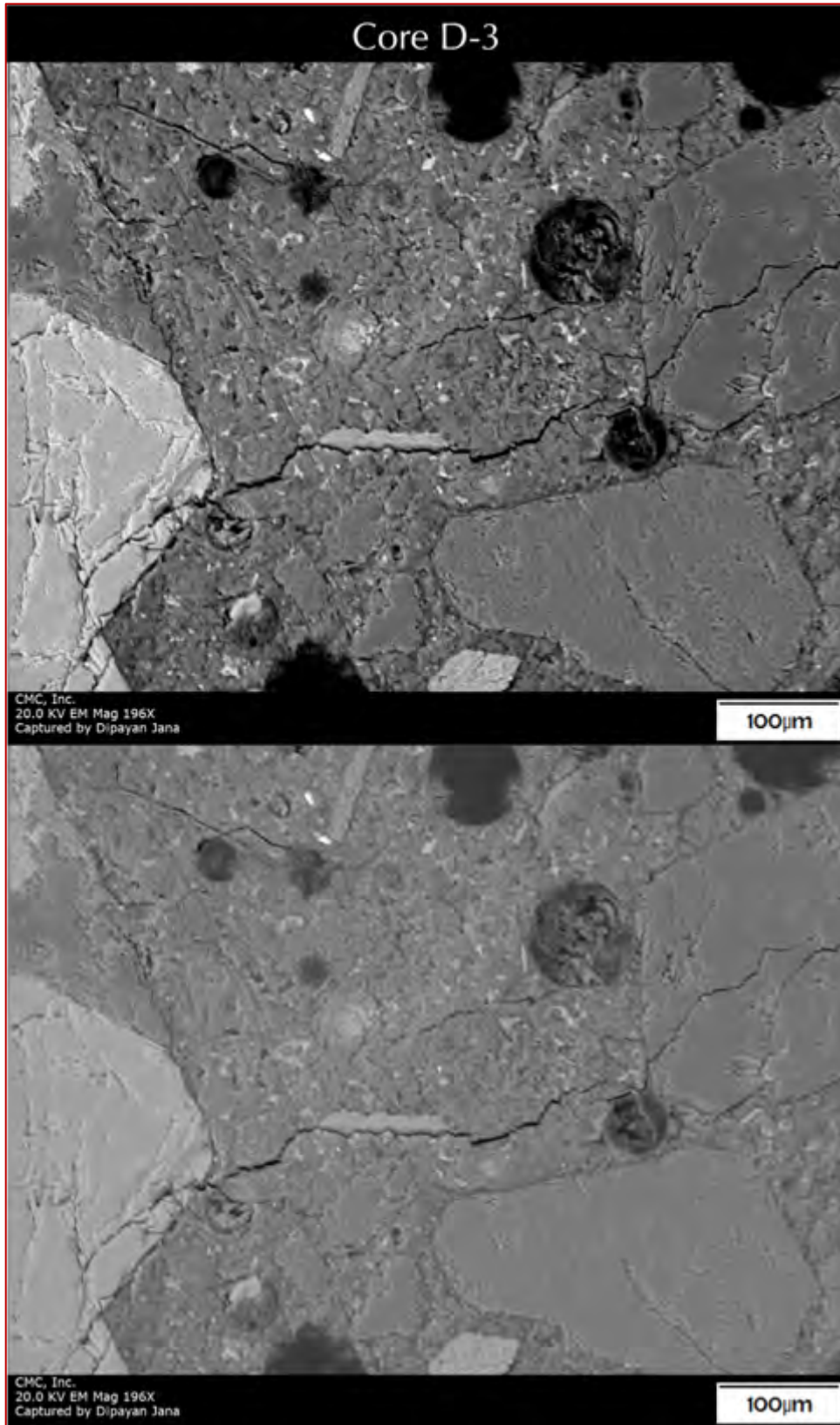


Figure E 19: Backscatter electron image (top) and corresponding secondary electron image (bottom) of a portion of concrete microstructure in Core D-3 showing air voids filled with secondary ettringite deposits.

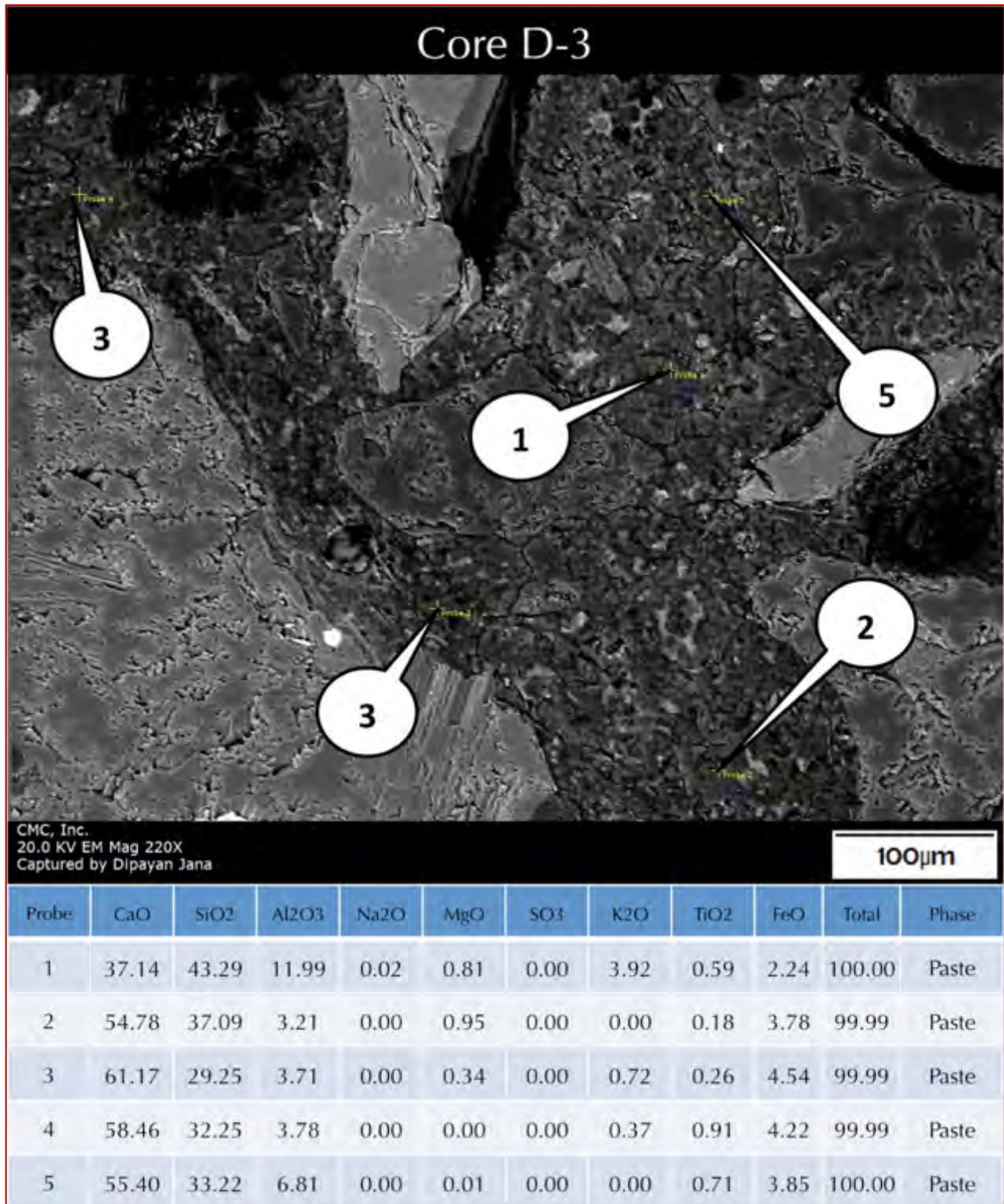


Figure E 20: Backscatter electron image (BSE, top) and compositional analyses of selected areas (at the tips of callouts) by energy-dispersive X-ray fluorescence spectroscopy of a portion of concrete microstructure in Core D-3 showing Portland cement paste having typical calcium silicate (hydrate) composition. Scattered residual Portland cement particles having subhedral alite grains, and ferrite remains (latter appear brighter in BSE image) are seen in the paste.

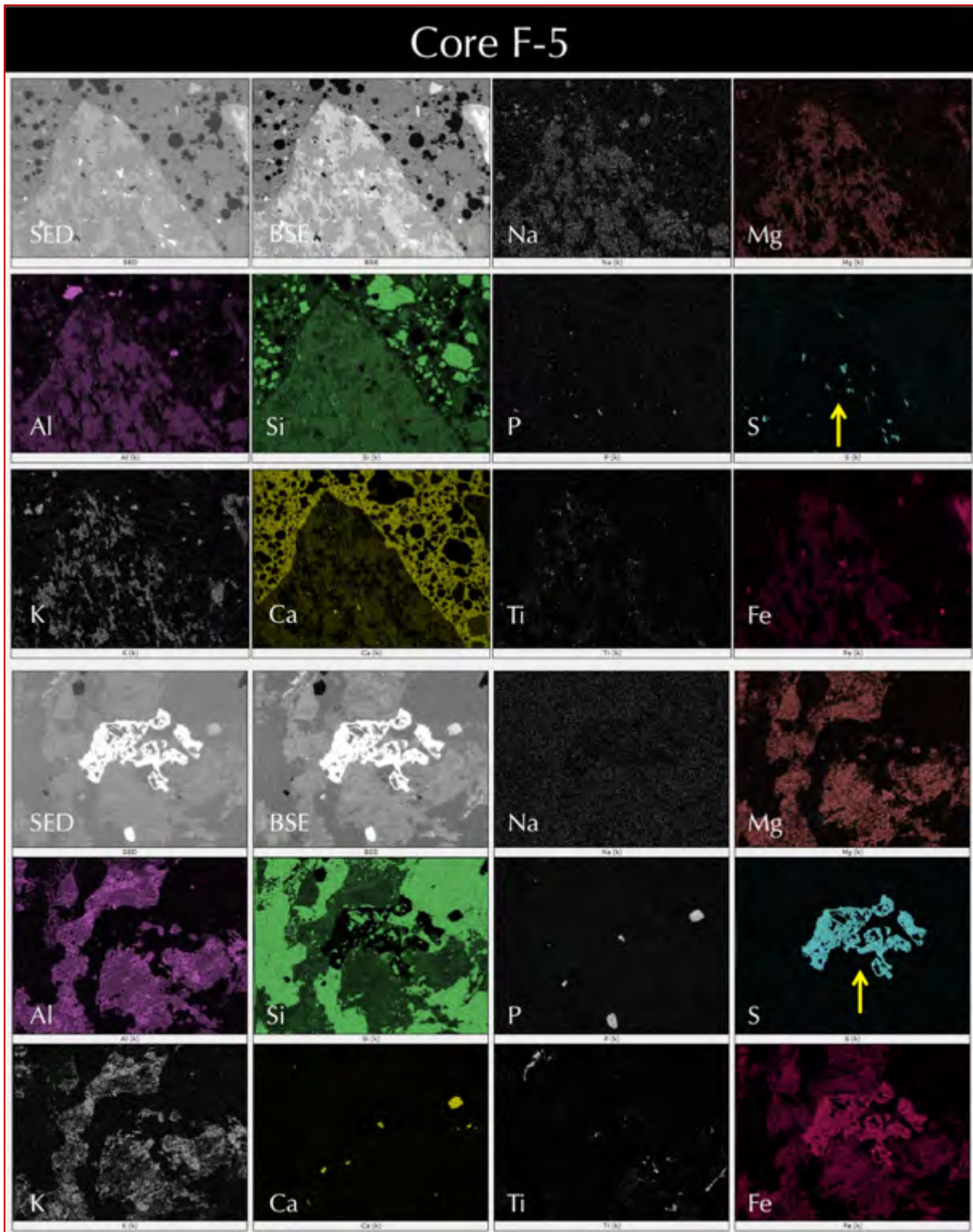


Figure E 21: Secondary electron images (top left), corresponding backscatter electron images (top 2<sup>nd</sup> from left), and corresponding X-ray elemental maps of sodium (Na), magnesium (Mg), aluminum (Al), silicon (Si), phosphorus (P), sulfur (S), potassium (K), calcium (Ca), titanium (Ti), and iron (Fe) of microstructure of concrete in Core F-5 showing: (a) disseminated pyrrhotite grains in aggregate highlighted by Fe and S maps (arrows), (b) feldspar grains in gneiss coarse aggregate highlighted by Na, K, Al, Si maps, (c) calcium silicate hydrate paste from Portland cement hydration highlighted in Ca map, (d) siliceous sand fine aggregate highlighted in Si map, and (e) iron-titanium grains in aggregate highlighted in Fe and Ti maps.



# APPENDIX F

## Mineralogical Compositions of Concrete & Aggregates From XRD

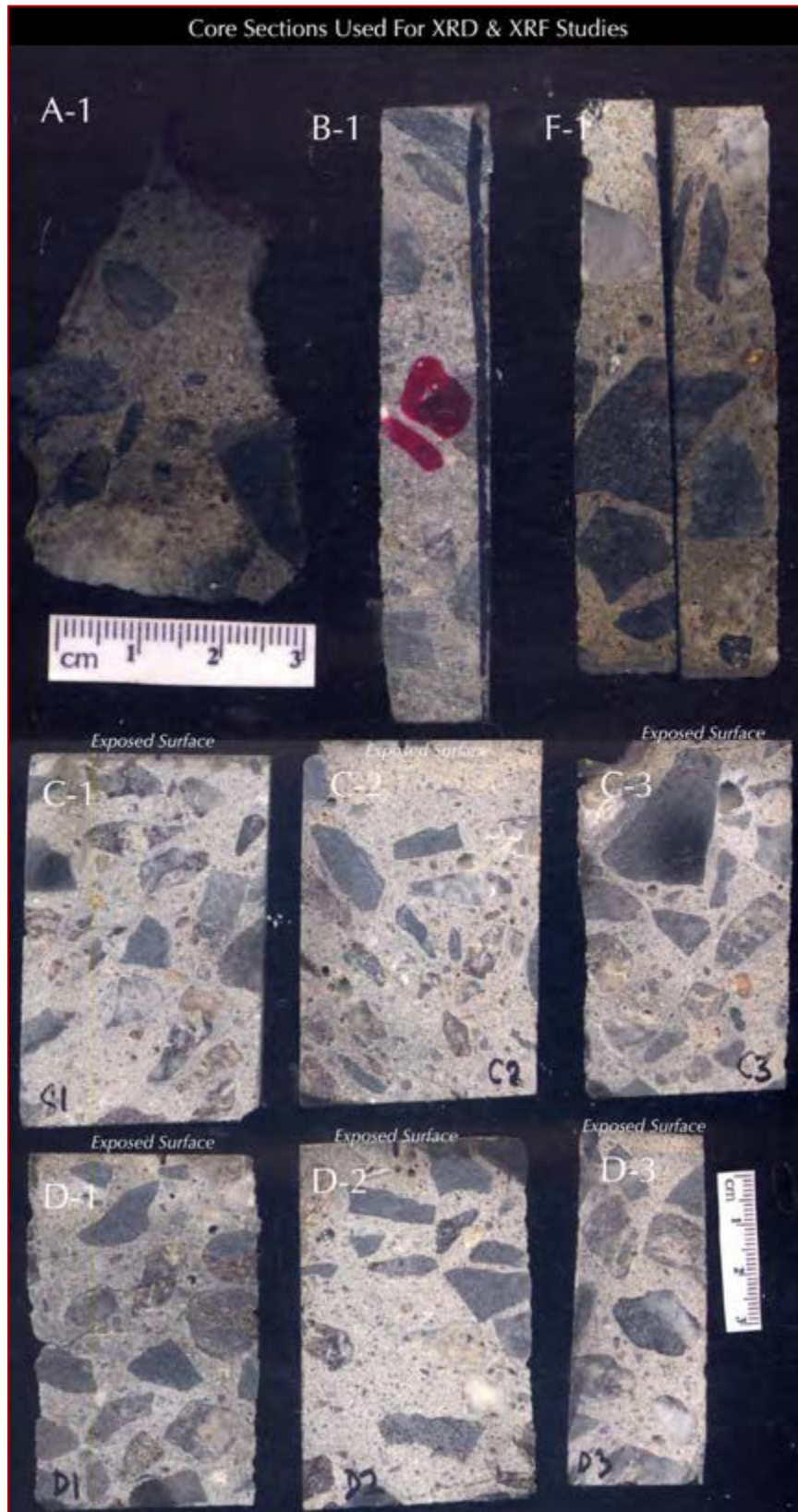


Figure F 1: Portions of cores selected for XRD and XRF studies. Each portion shown here was pulverized to pass No. 50 sieve and then further pulverized to finer than 44-micron for pressed pellets prepared for XRD and XRF studies.

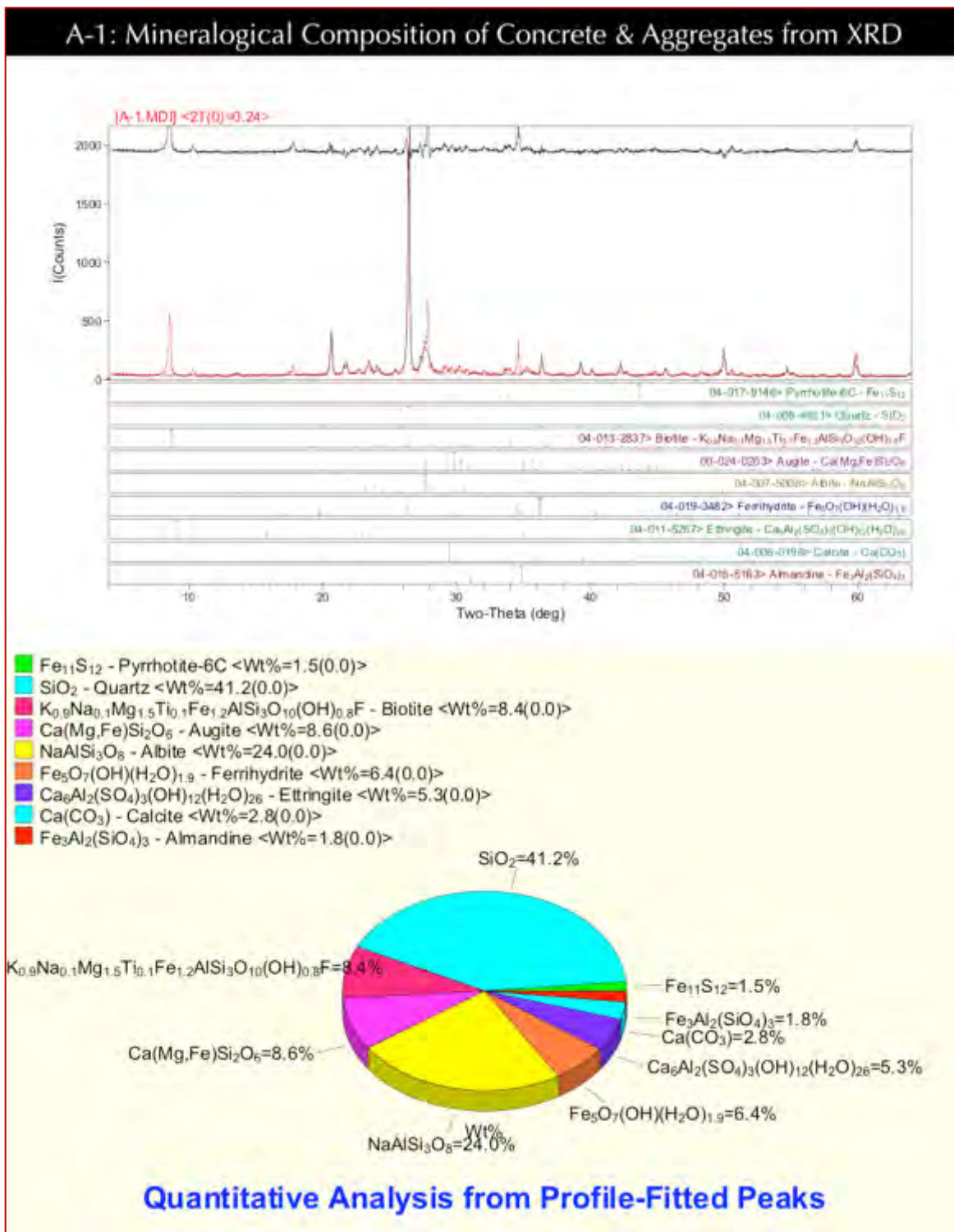


Figure F 2: X-ray diffraction pattern (top) and quantitative (Rietveld) mineralogical compositions presented as pie-graph (bottom) of concrete and its aggregates in Core A-1 showing: (a) the presence of pyrrhotite and its oxidation product ferrihydrite; (b) quartz, albitic feldspar and biotite from light pinkish-brown gneiss, (c) augite (clinopyroxene) from metamorphosed gabbro present as dark gray crushed stone; (d) red almandine garnet porphyroblasts in gneiss; (e) secondary ettringite formed from oxidation of pyrrhotite in the presence of moisture, most of which are deposited within the voids and cracks; and (f) minor secondary calcite from carbonated paste and other minerals.

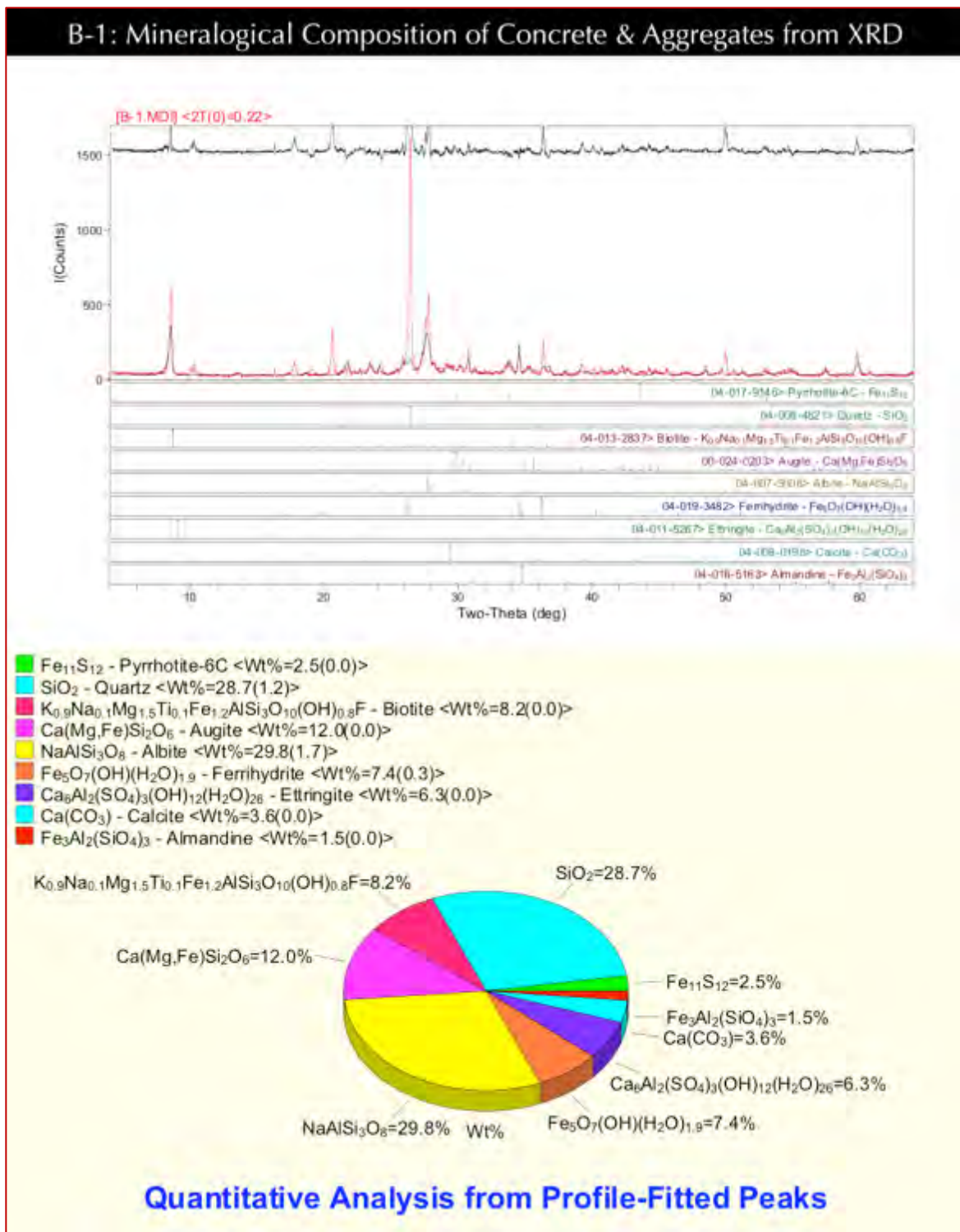


Figure F 3: X-ray diffraction pattern (top) and quantitative (Rietveld) mineralogical compositions presented as pie-graph (bottom) of concrete and its aggregates in Core B-1 showing: (a) the presence of pyrrhotite and its oxidation product ferrihydrite; (b) quartz, albitic feldspar and biotite from light pinkish-brown gneiss, (c) augite (clinopyroxene) from metamorphosed gabbro present as dark gray crushed stone; (d) red almandine garnet porphyroblasts in gneiss; (e) secondary ettringite formed from oxidation of pyrrhotite in the presence of moisture, most of which are deposited within the voids and cracks; and (f) minor secondary calcite from carbonated paste and other minerals.

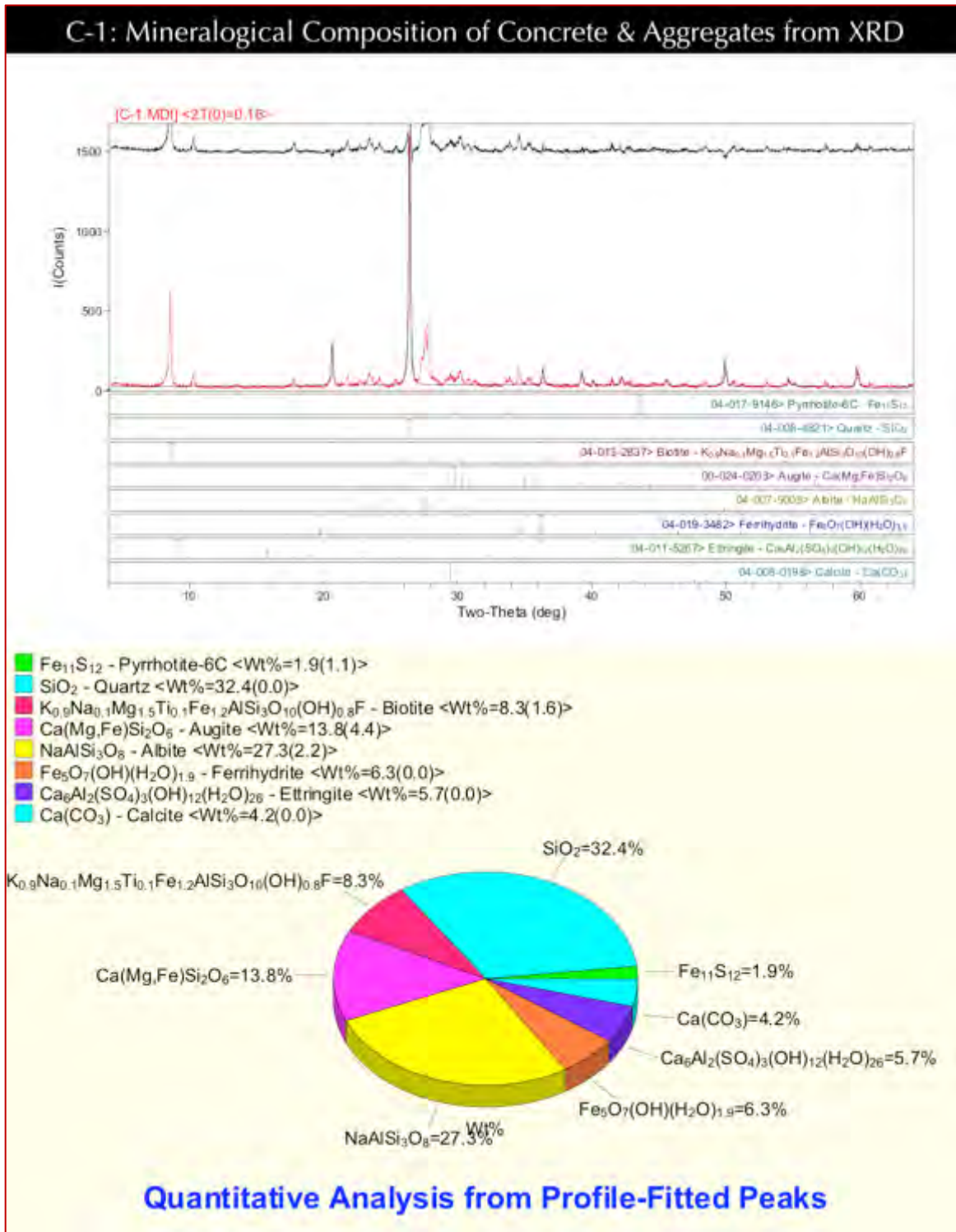


Figure F 4: X-ray diffraction pattern (top) and quantitative (Rietveld) mineralogical compositions presented as pie-graph (bottom) of concrete and its aggregates in Core C-1 showing: (a) the presence of pyrrhotite and its oxidation product ferrihydrite; (b) quartz, albitic feldspar and biotite from light pinkish-brown gneiss, (c) augite (clinopyroxene) from metamorphosed gabbro present as dark gray crushed stone; (d) secondary ettringite formed from oxidation of pyrrhotite in the presence of moisture, most of which are deposited within the voids and cracks; and (e) minor secondary calcite from carbonated paste and other minerals.

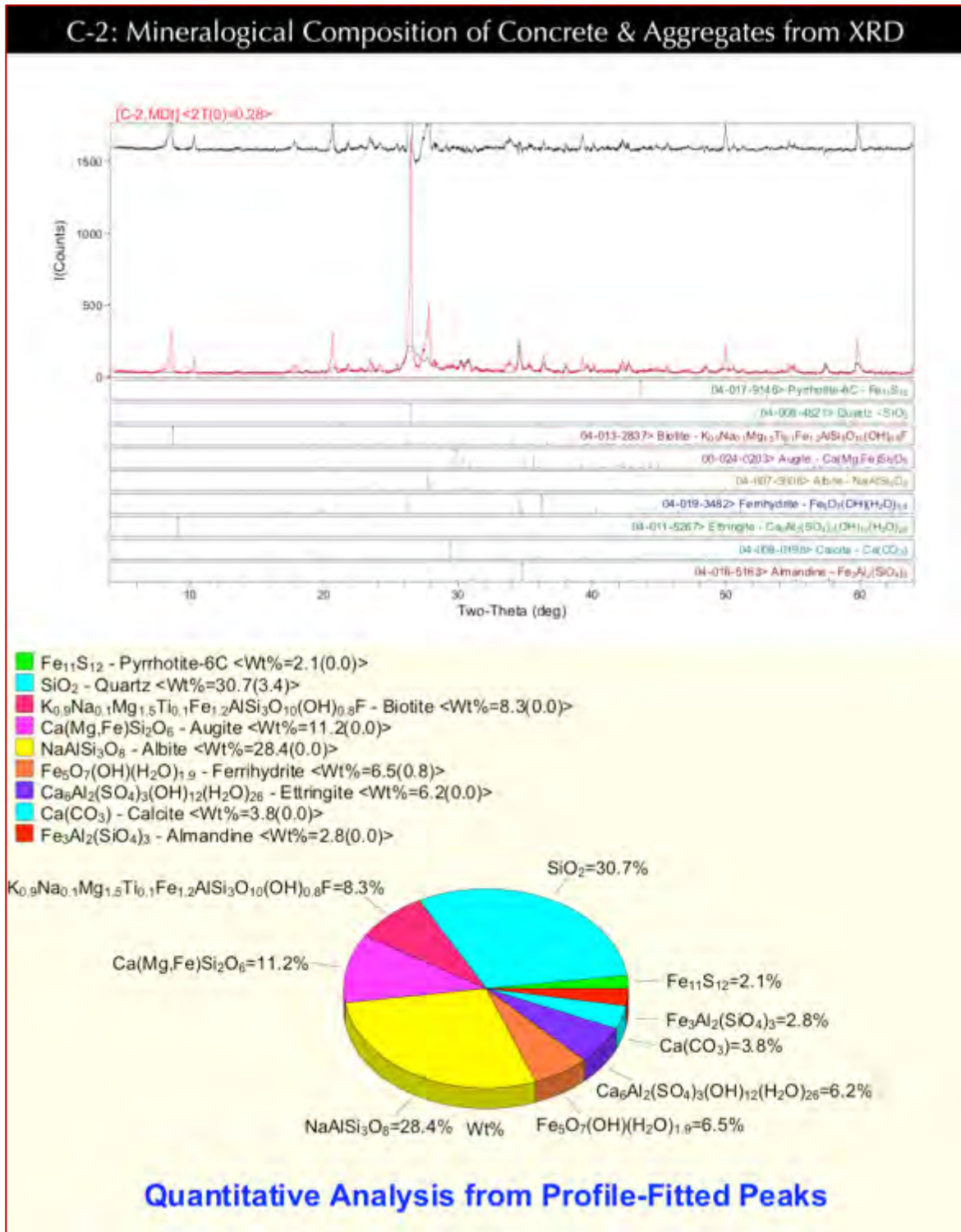


Figure F 5: X-ray diffraction pattern (top) and quantitative (Rietveld) mineralogical compositions presented as pie-graph (bottom) of concrete and its aggregates in Core C-2 showing: (a) the presence of pyrrhotite and its oxidation product ferrihydrite; (b) quartz, albitic feldspar and biotite from light pinkish-brown gneiss, (c) augite (clinopyroxene) from metamorphosed gabbro present as dark gray crushed stone; (d) red almandine garnet porphyroblasts in gneiss; (e) secondary ettringite formed from oxidation of pyrrhotite in the presence of moisture, most of which are deposited within the voids and cracks; and (f) minor secondary calcite from carbonated paste and other minerals.

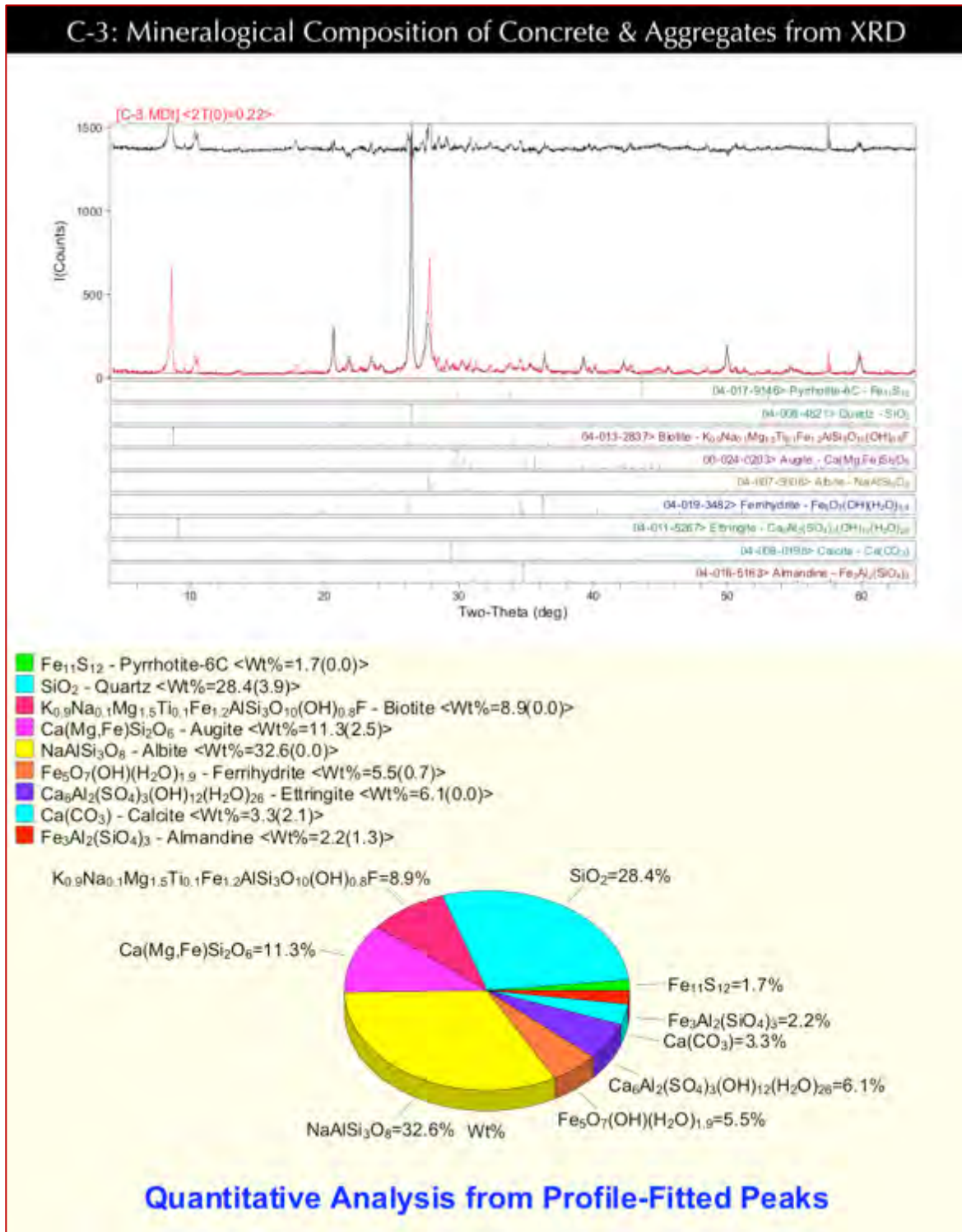


Figure F 6: X-ray diffraction pattern (top) and quantitative (Rietveld) mineralogical compositions presented as pie-graph (bottom) of concrete and its aggregates in Core C-3 showing: (a) the presence of pyrrhotite and its oxidation product ferrihydrite; (b) quartz, albitic feldspar and biotite from light pinkish-brown gneiss, (c) augite (clinopyroxene) from metamorphosed gabbro present as dark gray crushed stone; (d) red almandine garnet porphyroblasts in gneiss; (e) secondary ettringite formed from oxidation of pyrrhotite in the presence of moisture, most of which are deposited within the voids and cracks; and (f) minor secondary calcite from carbonated paste and other minerals.

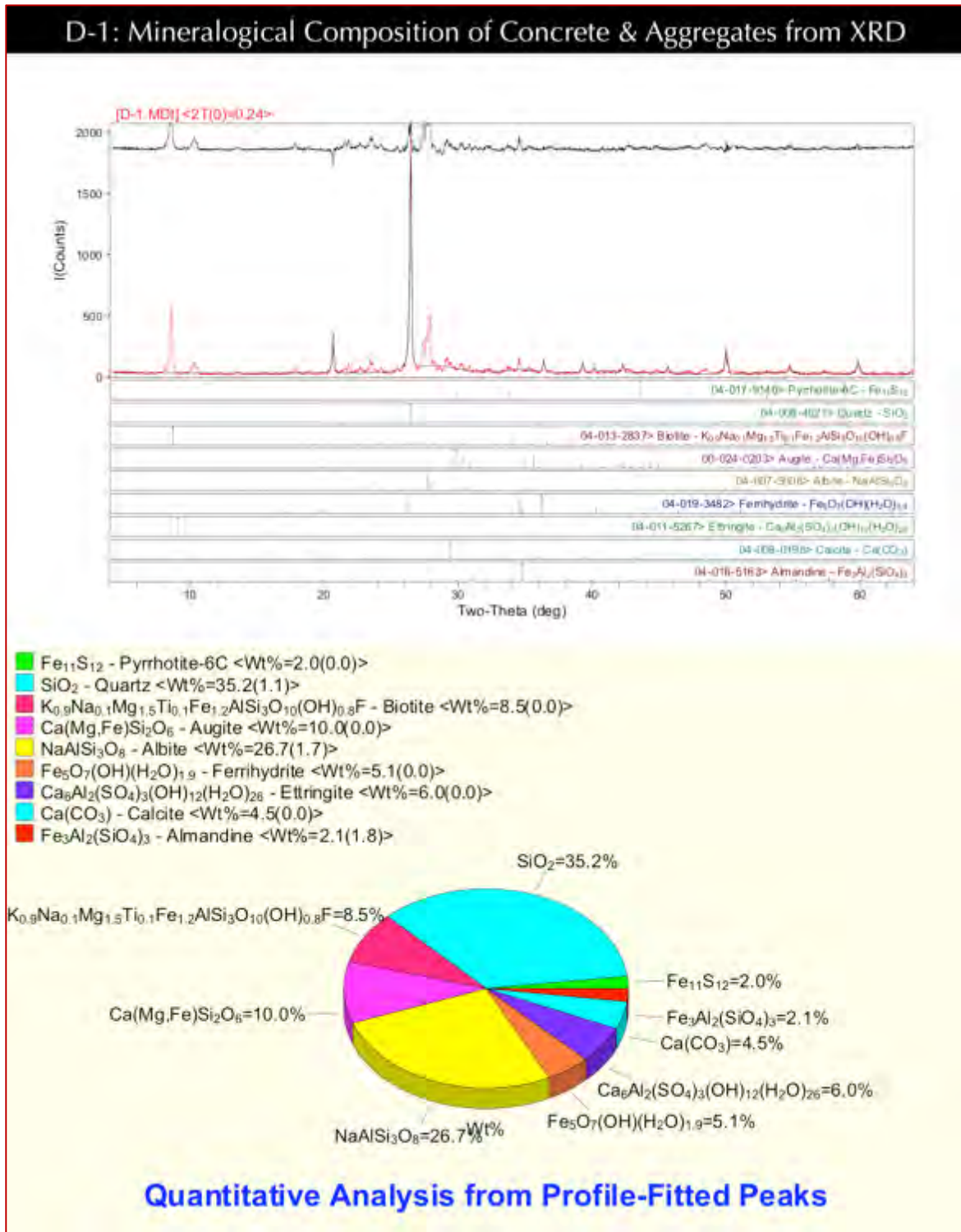


Figure F 7: X-ray diffraction pattern (top) and quantitative (Rietveld) mineralogical compositions presented as pie-graph (bottom) of concrete and its aggregates in Core D-1 showing: (a) the presence of pyrrhotite and its oxidation product ferrihydrite; (b) quartz, albitic feldspar and biotite from light pinkish-brown gneiss, (c) augite (clinopyroxene) from metamorphosed gabbro present as dark gray crushed stone; (d) red almandine garnet porphyroblasts in gneiss; (e) secondary ettringite formed from oxidation of pyrrhotite in the presence of moisture, most of which are deposited within the voids and cracks; and (f) minor secondary calcite from carbonated paste and other minerals.

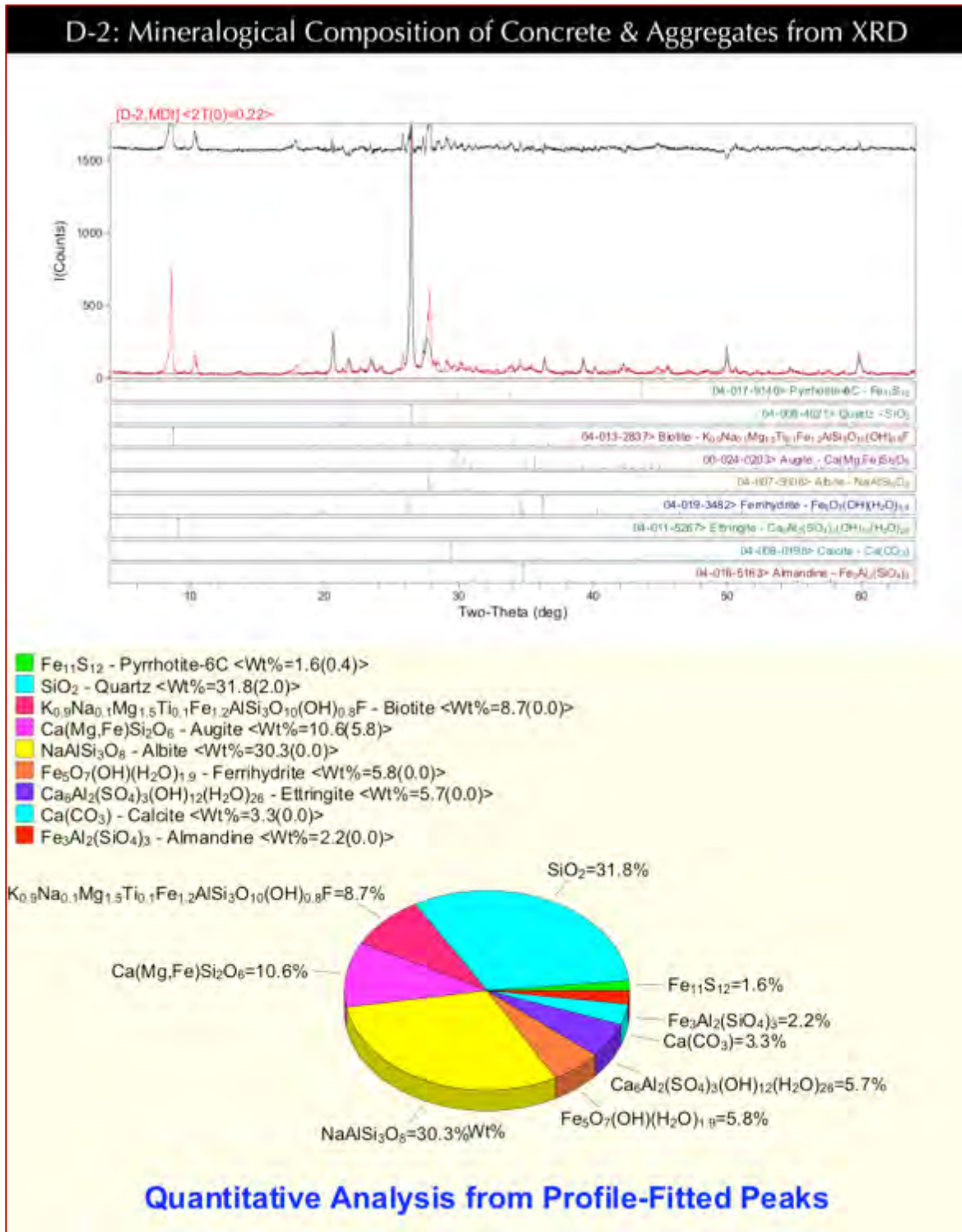


Figure F 8: X-ray diffraction pattern (top) and quantitative (Rietveld) mineralogical compositions presented as pie-graph (bottom) of concrete and its aggregates in Core D-2 showing: (a) the presence of pyrrhotite and its oxidation product ferrihydrite; (b) quartz, albitic feldspar and biotite from light pinkish-brown gneiss, (c) augite (clinopyroxene) from metamorphosed gabbro present as dark gray crushed stone; (d) red almandine garnet porphyroblasts in gneiss; (e) secondary ettringite formed from oxidation of pyrrhotite in the presence of moisture, most of which are deposited within the voids and cracks; and (f) minor secondary calcite from carbonated paste and other minerals.

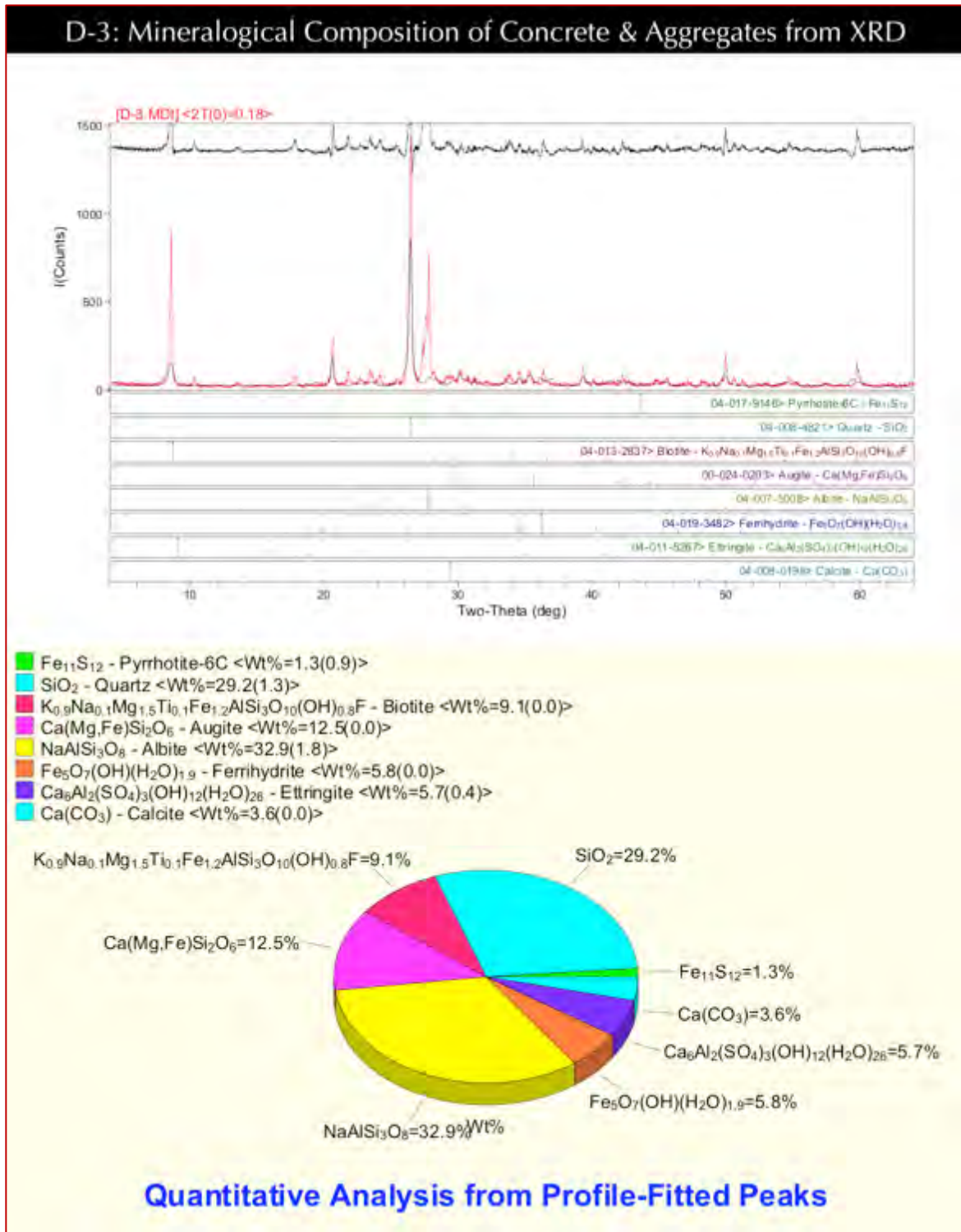


Figure F 9: X-ray diffraction pattern (top) and quantitative (Rietveld) mineralogical compositions presented as pie-graph (bottom) of concrete and its aggregates in Core D-3 showing: (a) the presence of pyrrhotite and its oxidation product ferrihydrite; (b) quartz, albitic feldspar and biotite from light pinkish-brown gneiss, (c) augite (clinopyroxene) from metamorphosed gabbro present as dark gray crushed stone; (d) red almandine garnet porphyroblasts in gneiss; (e) secondary ettringite formed from oxidation of pyrrhotite in the presence of moisture, most of which are deposited within the voids and cracks; and (f) minor secondary calcite from carbonated paste and other minerals.

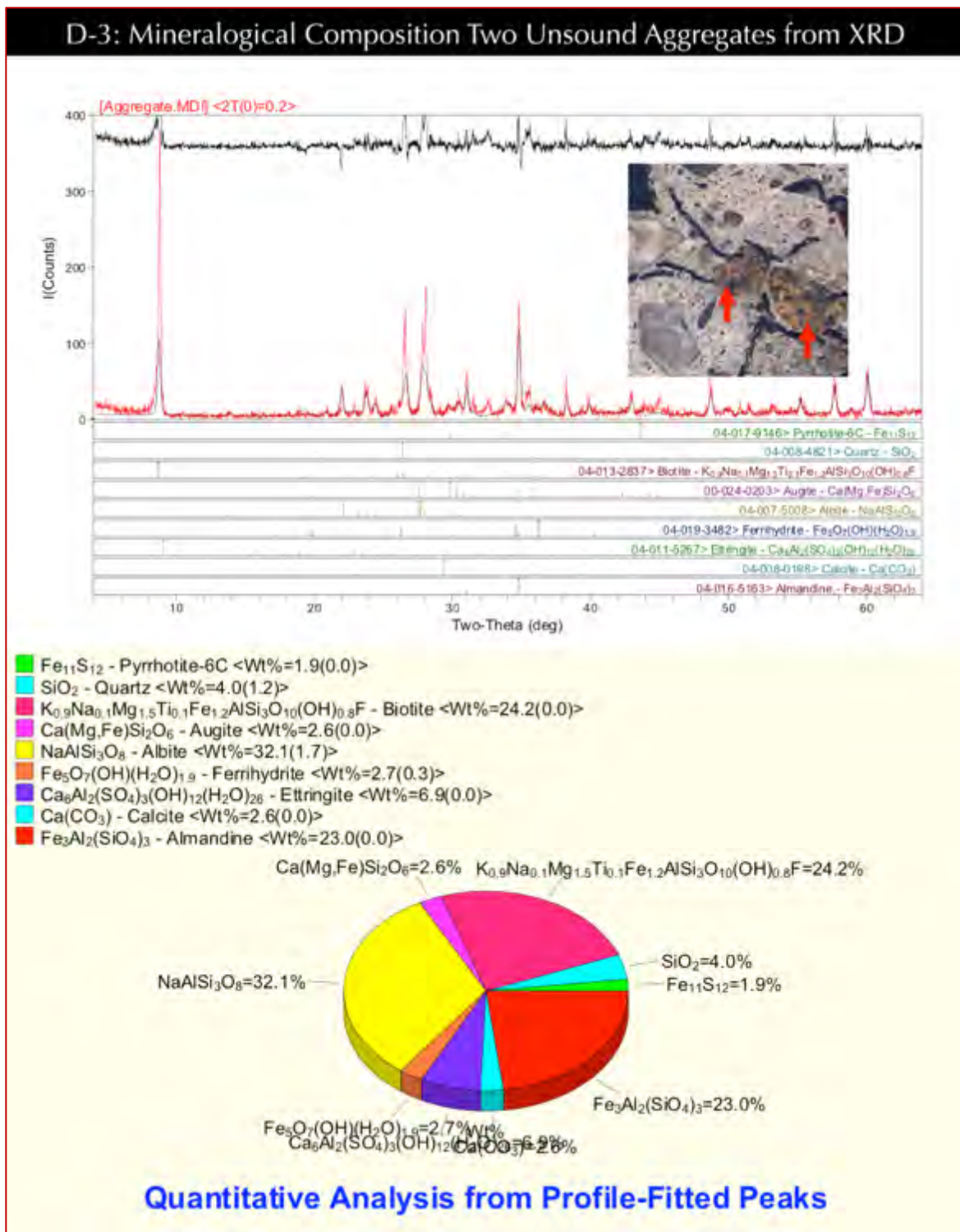


Figure F 10: X-ray diffraction pattern (top) and quantitative (Rietveld) mineralogical compositions presented as pie-graph (bottom) of two unsound aggregates in Core D-3 that have created radial and concentric cracks, showing: (a) the presence of pyrrhotite and its oxidation product ferrihydrite; (b) quartz, albitic feldspar and biotite, (c) minor augite (clinopyroxene); (d) red almandine garnet porphyroblasts in gneiss; (e) secondary ettringite formed from oxidation of pyrrhotite in the presence of moisture; and (f) minor secondary calcite from adhering carbonated paste and other minerals.

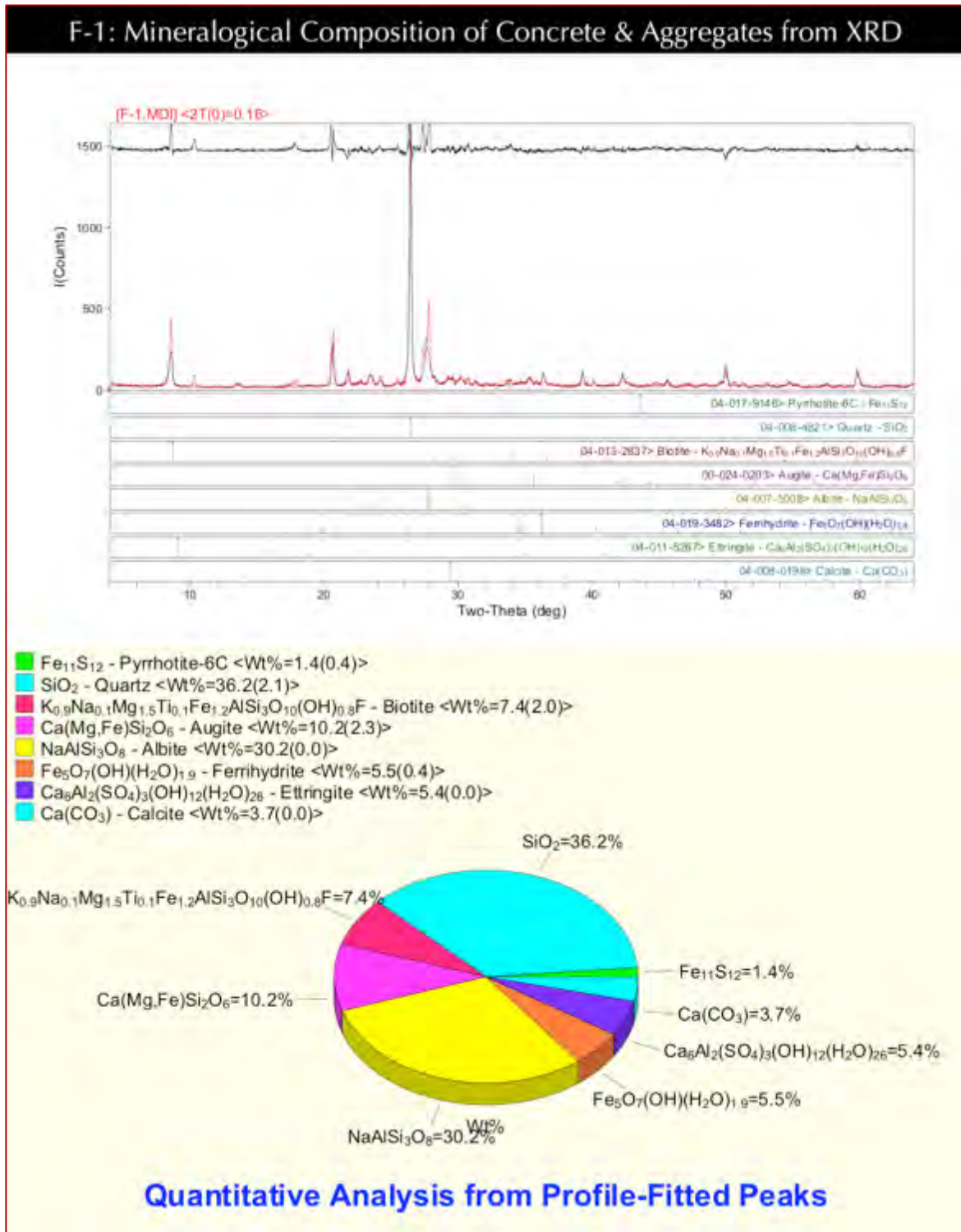


Figure F 11: X-ray diffraction pattern (top) and quantitative (Rietveld) mineralogical compositions presented as pie-graph (bottom) of concrete and its aggregates in Core F-1 showing: (a) the presence of pyrrhotite and its oxidation product ferrihydrite; (b) quartz, albitic feldspar and biotite from light pinkish-brown gneiss, (c) augite (clinopyroxene) from metamorphosed gabbro present as dark gray crushed stone; (d) red almandine garnet porphyroblasts in gneiss; (e) secondary ettringite formed from oxidation of pyrrhotite in the presence of moisture, most of which are deposited within the voids and cracks; and (f) minor secondary calcite from carbonated paste and other minerals.



# END OF REPORT<sup>2</sup>

---

<sup>2</sup> The CMC logo is made using a lapped polished section of a 1930's concrete from an underground tunnel in the U.S. Capitol.